An Investigation of Liquid Coating via the Contact Spreading Mechanism in Tumbling Drum and Fluidised Bed Coating Processes

By:

Norzaida Yusof

A thesis submitted in partial fulfilment of the requirements for the degree of Doctor of Philosophy

The University of Sheffield

Faculty of Engineering

Department of Chemical and Biological Engineering

May 2019

Declaration

The work presented in this thesis is, to the best of my knowledge and belief, original, except as acknowledge in the text, and has not been submitted in whole or in part, for a degree at this or any other institution.

<div align="right">

Norzaida Yusof

January 2019

</div>

Acknowledgements

I would like to thank my supervisors, Dr Rachel Smith and Dr Dennis Cumming for their guidance and support throughout my PhD journey at the University of Sheffield. I am lucky to have Rachel as my supervisor as she always encourages me with her humour and positive words. Thank you, Rachel, for giving me the opportunity to travel for conferences, workshops and chance to collaborate and join meetings with the Procter & Gamble (P&G) research team.

I also would like to thank the P&G team for their inputs and fruitful discussions regarding my first major experimental research part. Their advice and expertise are really appreciated. My thanks is also extended to the most efficient Post-Doctoral Research Associate in my group, Dr Kate Pitt, who always shared her time and knowledge throughout my research. Also, thanks to my group mate, Joshua Green, who helped me with my research by contributing his time, strength and input in my data analysis. Thanks also to Dr Andrew Campbell, who kindly developed the LabView coding and advised me on image analysis.

A special thanks to the awesome technical staff in the Chemical & Biological Engineering Department; Andy Patrick, Mario Dorna and Elliot Gunard who helped to design and manufacture the fluidised bed and tumbling drum for my research projects. Their expertise and ideas were highly appreciated. Many thanks to all my PhD friends, in particular, the Particle Technology Group members for your invaluable advice and technical help from early to the end of my research journey. The experiences I got during my PhD journey were excellent.

Thank you also to my family, especially my beloved husband, Asmadi Abdul Wahab, who has sacrificed a lot to accompany me to study in Sheffield. He has been a great supporter and has always had faith in me. Thank you also to my parents, Hj Yusof Mamat, Hajah Wan Zabidah Wan Abdullah and my mother in law, Wan Rohani Wan Mokhtar for the love, support, understanding throughout my PhD journey. Without all of you, I would not have been able to complete my PhD journey. Thank you, Allah, for all the achievements I have received in my whole life

Finally, thank you to the Ministry of Higher Education Malaysia and University Sultan Zainal Abidin for the financial support.

List of Publications

Yusof, N., Green, J., Pitt, K., Arjmandi-tash, O., Campbell, A. I., Ahmadian, H., Smith, R. (2019). A novel method for the analysis of particle coating behaviour via contact spreading in a tumbling drum : Effect of coating liquid viscosity. *Powder Technology*, 351, 102–114.

Abstract

The spray coating of particles is used in many industrial applications. One of the mechanisms involves the transfer of liquid between particles via liquid bridge formation and rupture; known as contact spreading. To date, there has been limited research into this mechanism. Indeed, the few studies reported have only been theoretical or modelling-based. In this thesis, a first experimental approach focusing on the liquid contact spreading mechanism is presented. Experimental data has been used to describe and quantify this mechanism, and this work will contribute to the design and scale-up of wet coating processes.

Two coating techniques, commonly used in industry, have been employed for this study; tumbling drum and fluidised bed. Experiments were conducted using model materials; spherical alumina particles and aqueous polymer solutions as the coating liquids with varying viscosities. For these studies, specially designed experiments were conducted to study the contact spreading mechanism only.

Of particular importance was the degree of coating uniformity within a batch of particles, quantified by the inter-particle coating variability (CoV). A new image analysis system, based on colorimetric measurement, has been developed to quantitatively determine the colour uniformity of particles coated with dyed solutions. Here, it is demonstrated that this novel method can analyse a large number of particles in a relatively small period of time and gives reproducible data with which to determine the CoV of a batch.

Contact spreading was seen to occur in all systems studied. This supports the concept that contact spreading plays an important role in the spray coating process. Indeed, in the both tumbling drum and the fluidised bed system under certain conditions, a near-uniform coating was ultimately achieved. The rate of contact spreading and, therefore, the time to complete the coating process, was highly dependent on both formulation and operational parameters. For example, the lower the coating liquid viscosity, the faster the rate of contact spreading. An increase in tumbling speed in the

drum and fluidisation velocity in the fluidised bed also resulted in an increase in contact spreading rate. The method of liquid addition in the fluidised bed was also found to affect the contact spreading process.

The findings are attributed to differences in the formation and rupture of liquid bridges between particles which influence the extent of liquid transfer via contact spreading. This study has demonstrated that the viscous Stokes number, St_v, and the critical Stokes number, St_c, as a function of collision velocity can be applied to predict the sticking criterion of the colliding particles in tumbling drum system. However, this is not the case for the fluidised bed system due to the large effect of drying in this system. In the fluidised bed systems, no correlation was found between the St_v and the time for coating completion, t_c, or the asymptotic CoV, which represents the extent of coating. However, in the tumbling drum system, a correlation was found between St_v and t_c; increases in St_v gave a decrease in t_c. In summary, this work has shown that the viscosity, collision velocity, the coating thickness and drying are the main parameters which influence the rate and extent of coating via contact spreading.

Table of Contents

List of Tables

List of Figures

Nomenclature

Uppercase symbols

Symbol	Definition
A	Amplitude of oscillation
AFM	Atomic Force Microscopic
Ar	Archimedes number (-)
Bo	Bond number (-)
Ca	Capillary number (-)
CFD	Computational fluid dynamics
CLSM	Confocal laser scanning microscopy
CoV	Coefficient of variation (-)
CoV_o	Initial Coefficient of variation (-)
CoV_∞	Asymptotic coefficient of variation (-)
CV_m	Coating mass variability (-)
D	Drum diameter (m)
DEM	Discrete element method
E_k	Kinetic energy (J)
ESEM	Environmental scanning electron microscopy
F	Fractional surface coating (-)
Fr	Froude number (-)
ID	Internal diameter (m)
L	Drum length (m)
LIBS	Laser-induced breakdown microscopy
MW	Molecular weight (Da)
NMR	Nuclear magnetic resonance
OD	Outer diameter (m)
Oh	Ohnesorge number (-)
U	Fluidisation velocity (m/s)
U_b	Bubbling rise velocity (m/s)
U_c	Collision velocity (m/s)

U_e	Entrainment velocity (m/s)
U_e	Excess velocity (m/s)
U_{mb}	Minimum bubbling velocity (m/s)
U_{mf}	Minimum fluidisation velocity (m/s)
U_s	Superficial velocity (m/s)
U_{tf}	Turbulence fluidisation velocity (m/s)
R	Drum radius (m)
R_a	Roughness
Re	Reynolds number (-)
S	Separation distance (m)
S_c	Critical separation distance (m)
St_c	Critical Stokes number (-)
St_v	Viscous Stokes number (-)
TPI	Terahertz pulsed imaging
V	Envelope volume (cm^3)
V_b	Liquid bridge volume (m^3)
V_c	Collision velocity (m/s)
V_w	Wall velocity (m/s)
We	Weber number (-)

Lowercase symbols

Symbol	Definition
d_b	Average gas bubble rise velocity (m/s)
d_p	Particle diameter (m)
$d_{3,2}$	Surface area mean diameter (m)
$d_{4,3}$	Volume moment mean diameter (m)
d_{10}	10th volume percentile size (m)
d_{50}	50th volume percentile size (m)
d_{90}	90th volume percentile size (m)
d_v	Diameter of equivalent sphere (m)

e_r	Particle coefficient of restitution (-)
g	Gravitational acceleration (m/s^2)
h_a	Thickness of coating layer (μm)
h_b	Particle surface asperity (-)
m_o	Initial particle mass (kg)
n_c	Critical speed (m/s)
rpm	Round per minute (-)
r_1, r_2	Radii of curvature (m)
t_c	Coating completion time (s)
v	Conversion factor (cm^3/mm)
v_o	Initial particle volume (m^3)
v_t	Terminal velocity (m/s)
w	Sample mass (g)

Greek symbols

Symbol	Definition
ρ_B	Bulk density (kg/m^3)
ρ_p, ρ_e	Envelope density (kg/m^3)
ρ_g	Air density (kg/m^3)
μ	Viscosity (Pa.s)
ω	Angular velocity (s^{-1})
ε	Gap distance
γ	Surface tension (mJ m^{-2})
δ	Dimensionless bubble space (-)
Θ_A	Advance contact angle (º)
Θ_C	Contact angle (º)
Θ_R	Receding contact angle (º)
β	Filling angle (º)
λ	Coating rate (s^{-1})
$\acute{m}$	Average coating mass (kg)

CHAPTER 1

1 Introduction

Spray coating of particles and powders is a commonly used process in many industrial applications, e.g. food, detergents and pharmaceuticals. It involves complex interactions which include three phases; solid, liquid and gas. Due to lack of reliable design rules and process understanding, the design and scale-up of the process are still largely based on trial and error. Tumbling drums and fluidised beds are typically used for particle coating processes, and the uniformity of the coating layer formed is very important when considering the quality of the final product.

1.1 Research Background

Spray coating can be conceptually divided into two distinct steps; drop deposition onto agitating particle surfaces (step 1), and the spreading of liquid between particles due to the formation and breakage of liquid bridges (step 2) as shown in Figure 1.1.
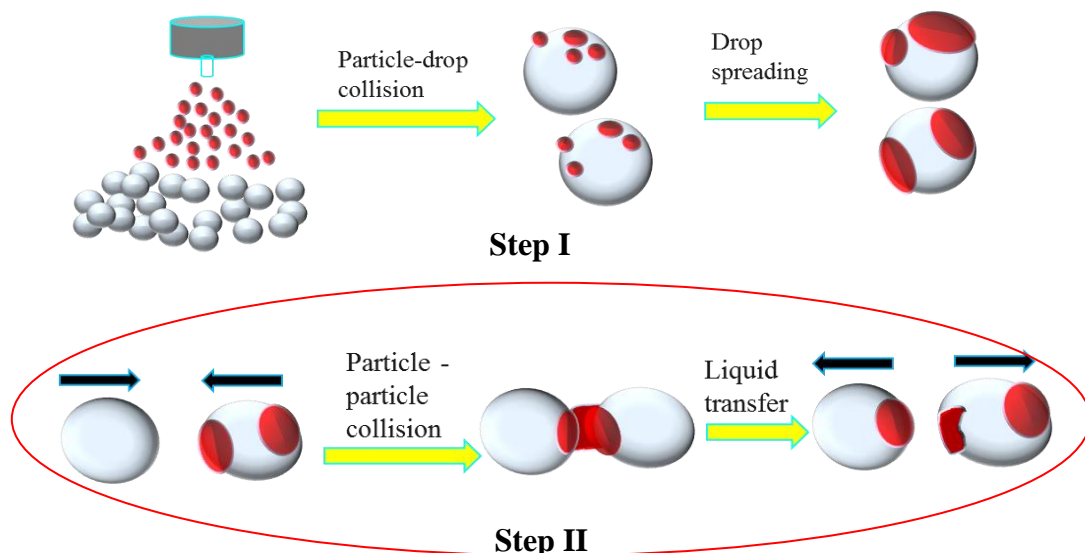
Figure 1.1. Schematic view of spray coating mechanisms: (step I) drop deposition, (step II) contact spreading.

Research to date has tended to focus on droplet deposition and spreading (step I) rather than liquid exchange between particles via contact spreading (step II) even though, for many systems such as rotating drums and fluidised beds, contact spreading is known to be a very significant process. Thus, this thesis will focus on understanding wet coating via the contact spreading process (step II) in both a tumbling drum and fluidised bed to assist in the design and scale-up rules for wet coating systems.

In the detergent and food industries, tumbling drums and fluidised beds are used to spray coat dried powders (generally porous powders) and active ingredients with active coating materials. In all cases, the characteristics of the coating layer, e.g. the desired thickness and coating uniformity, are key requirements in manufacturing processes to ensure that the active ingredients or core material have well-controlled delivery characteristics (Hilton *et al*., 2013). The uniformity and quality of the coating layer are strongly influenced by the level and distribution of the coating achieved. In many industrial processes, a certain level of liquid added to the coating systems often resulting in formation of agglomerates. This agglomerate is unfavourable in coating process because it could limit the spreading of liquid within particles and change the particles mixing behaviour in the system (Boyce *et al*., 2017a; McLaughlin and Rhodes, 2001).

To achieve coating uniformity, a balance between mixing and particle flow and operating conditions are of great importance in coating systems. In this study, the process of the contact spreading mechanisms in a tumbling drum and a fluidised bed will be analysed based on the coating uniformity of the coated particles.

1.2 Objectives

This study aims to understand the overall mechanisms of the liquid coating process via contact spreading in different coating systems. To achieve this, the research will focus on the following objectives:

1. To develop a novel method for the quantitative measurement of particle coating. The method will focus on the determination of the inter-particle coating uniformity within a batch of particles.

2. To develop experiments to study contact spreading only and reduce or remove the influence of the spray. The effect of formulation and operating parameters on contact spreading in a tumbling drum (drum speed/ tumbling regime, mixing time, coating liquid viscosity) will be studied.

3. To investigate the effect of liquid formulation and operating parameters on contact spreading in a small-scale fluidised bed (fluidisation velocity, liquid spray rate, nozzle height, coating liquid viscosity). This will involve the development of a small-scale fluidised bed with a spray system for initial liquid introduction.

4. To investigate different liquid loading methods in a fluidised bed (spray or pre-coating of particles), and the effect of operating parameters (mixing time, liquid coating viscosity and fluidisation velocity) on contact spreading.

5. To theoretically explain the distribution of liquid via the contact spreading mechanism using dimensionless numbers based on the experimental observations.

1.3 Structure of this thesis

In the following chapter, a thorough literature review of particle coating (wet coating) and coating equipment; tumbling drums and fluidised beds, is presented. Chapter 3 describes the materials, methods, the equipment set-up and techniques used in the study. The development of a novel image analysis system to quantitatively measure the degree of particle coating is explained and this is validated in Chapter 4. Chapter 5 investigates the effect of mixing time, coating liquid viscosity and tumbling regime on contact spreading only experiments in a tumbling drum. Chapter 6 describes experiments using a small-scale fluidised bed, where liquid is sprayed on fluidised particles and the spreading of liquid in the system is measured. In Chapter 7, a different liquid loading method for

the same fluidised bed is used. The effect of mixing time, coating liquid viscosity and fluidisation velocity on contact spreading are investigated, and the two methods compared. Chapter 8 contains a theoretical discussion on the contact spreading mechanism based on the overall experimental observations and findings. Finally, Chapter 9 of this thesis gives conclusions and recommendations for future works. An outline of this work is shown in Figure 1.2.

```
┌──────────────────┐      ┌──────────────────┐
│   Chapter 1:     │─────▶│    Chapter 2:    │
│  Introduction    │      │ Literature review│
└──────────────────┘      └──────────────────┘
                                   │
                                   ▼
                          ┌──────────────────┐
                          │    Chapter 3:    │
                          │  Materials and   │
                          │    methods       │
                          └──────────────────┘
                                   │
                                   ▼
                          ┌──────────────────┐
                          │    Chapter 4:    │
                          │  Image analysis  │
                          │   development    │
                          └──────────────────┘
```

┌───────────────────┐   ┌──────────────────┐   ┌──────────────────┐
│   Chapter 5:   │   │   Chapter 6:   │   │   Chapter 7:   │
│ Tumbling drum;   │   │ Fluidised bed; │◀─▶│ Fluidised bed; │
│ pre-coating method│   │   spray method   │   │   pre-coating   │
│   │   │   │   │   method   │
└───────────────────┘   └──────────────────┘   └──────────────────┘

```
                          ┌──────────────────┐
                          │    Chapter 8:    │
                          │   Theoretical    │
                          │    mechanistic   │
                          │   development    │
                          └──────────────────┘
                                   │
                                   ▼
                          ┌──────────────────┐
                          │    Chapter 9:    │
                          │  Conclusions and │
                          │ recommendations  │
                          └──────────────────┘
```
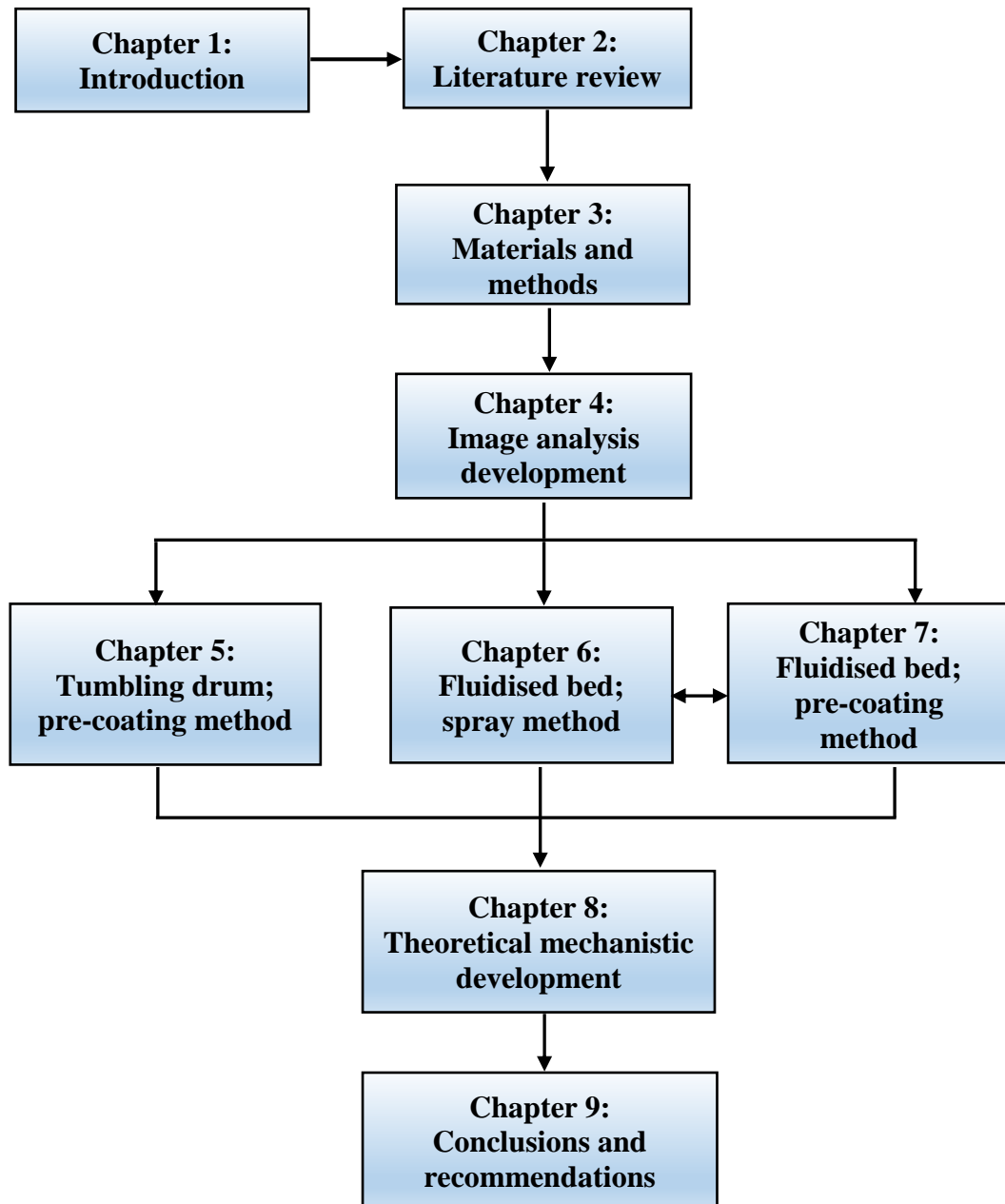
Figure 1.2. Flow chart of the work conducted in this thesis.

CHAPTER 2

2 Literature review

2.1 Introduction

Coating of particulate powders has gained great attention in recent years mainly in pharmaceutical, food and detergent industries. Coating is generally performed to achieve one or several of the following objectives:

a) protect powders from ambient factors such as moisture, oxygen and light (Fang and Bhandari, 2010),

b) delay and control the release of active agents (Haack and Koeberle, 2014),

c) increase the particle size (Donida *et al*., 2005),

d) improve product appearance, taste, or odour (Ribeiro *et al.,* 2007),

e) conserve nutrients contained in food products (Tatar *et al*., 2014),

f) functionalize powders (such as catalysts, enzyme-coated detergents) (Capece and Dave, 2011).

The coating process involves the deposition of coating material comprising one or multiple components onto solid particles. The coating material can be introduced by several methods as illustrated in Figure 2.1: a) powder form (dry powder coating); b) dispersed or dissolved in an easily evaporable solvent (wet coating) or as a melt (hot-melt coating). Each method can produce different properties of final products (Saleh and Guigon, 2007a). Nowadays, spray coating (wet coating) is the most widely applied coating process (Anwar *et al*., 2010; Dreu *et al*., 2012) and this will be the focus of this literature review.
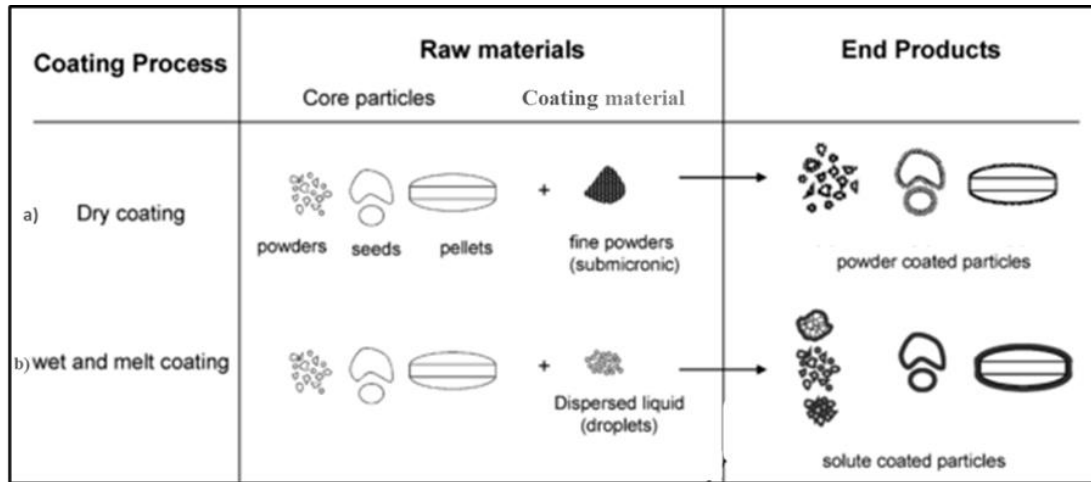
Figure 2.1. Schematic view of different coating methods. Adapted from Saleh and Guigon, 2007a.

In this chapter, an overview of literature relevant to this thesis is presented, with a focus on tumbling drum and fluidised bed coating systems. A description of both types of coating equipment is given followed by an explanation of the mechanisms involved in the spray coating in both systems. Current methods for the quantitative measurement of coating uniformity are also reviewed. Furthermore, contact spreading processes are discussed; an investigation into the characteristics and mechanisms of this process forms the objectives of this thesis.

2.2 Coating Equipment

In industry, many types of coating equipment are commercially used and can be classified into two categories: mechanical and pneumatic solid mixing systems. Tumbling drums and impeller mixers are examples of a mechanical mixing system while the fluidised bed is an example of a pneumatic mixing system, each of which has advantages and disadvantages. Among these, spray coating in the tumbling drum and fluidised bed are most widely used (Maronga, 1998). Thus, in the following sections, these two different types of coating system are compared.

2.2.1 Tumbling drums

Tumbling drums have a wide range of applications, mainly in the detergent, pharmaceutical and food industries, to form small coated particles or tablets. This mechanical solid mixing system is among the oldest industrial procedures, where the mixing of particles is achieved by the movement of the equipment itself or by using an agitator (Bansode *et al*., 2010; Kleinbach and Riede, 1995). Even though this coating system has been used for a long time, the problem with a high coating variability of the final product has still not been resolved.

In the tumbling drum coating system, most of the core particles are agitated by moving upwards, dragged by the drum wall with a small amount of the particles cascading down the free surface and therefore passing through the spray zone as illustrated in Figure 2.2. In the spray zone, the coating material is sprayed from the top onto the particle surfaces and subsequently forms a coating layer on the surfaces due to evaporation of the solvent facilitated by drying (hot air) which occurs simultaneously. Here, the number of spray nozzles can be more than one, depending on the drum design used. The cycle of spraying and drying is repeated until the desired properties of the final products are obtained, e.g. coating mass or uniformity (Turton, 2008).
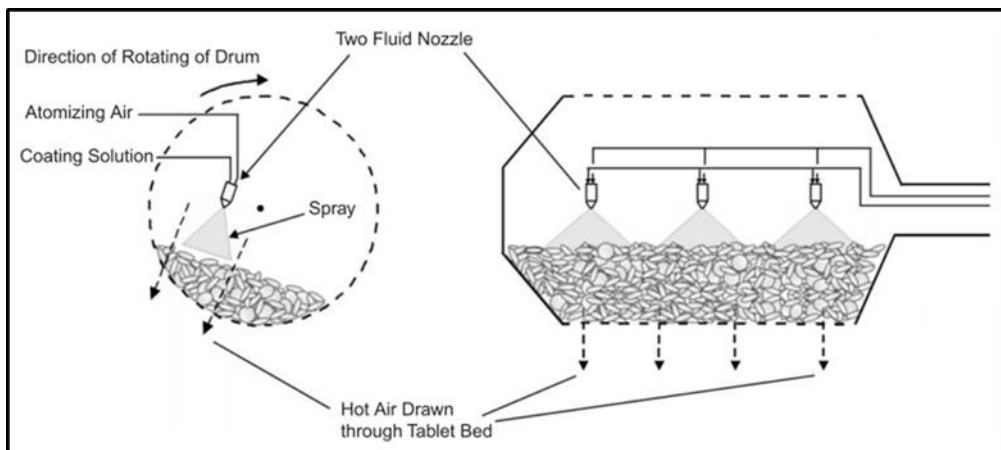
Figure 2.2. Schematic view of a typical drum coating process. Source: Turton and Cheng, (2005).

2.2.1.1 Types of Tumbling Drum Coater

Different types of drum coaters are available and have been used by previous studies such as side-vented Accela-Cota perforated pans (Kalbag and Wassgren, 2009), perforated drums fitted with baffles (Sandadi *et al.*, 2004; Kandela *et al.*, 2010) and side-vented drums with baffles (Smith *et al.*, 2003; Brock *et al.*, 2014). The basic elements of a drum coater are illustrated in Figure 2.2, and each drum can be differentiated by the drying air flow and the baffle designs and arrangement.

Baffles have been fitted inside drums by many researchers as they act as mixing elements and have been reported to reduce the residence and circulation time *(Kalbag et al.*, 2008), improve mixing efficiency (Smith *et al.*, 2003; Soni *et al.*, 2016) and increase the diffusion coefficients of the tablets (Sandadi *et al.*, 2004). Smith *et al.*, (2003) reported that the shape and type of baffles also influenced the mixing behaviour, where the time to reach uniformity of final product is shortest for rabbit ear followed by ploughshare and tubular designs.

2.2.1.2 Types of Tumbling Regime/Bed Behaviour

Knowledge of dynamic particle mixing and flow in a tumbling drum coater is critical to ensure the desired quality of the final product in terms of coating uniformity and process reliability are achieved. Typically, when the drum rotates, the particle bed has two regimes as shown in Figure 2.3: the active (cascading) layer which is composed of a thin layer of particles that flows down the free surface due to gravity, and the passive layer (quasi-static zone) which consists of the remaining particles that rotates with the drum wall and eventually enters the active layer. A previous study has reported that an increase in particle velocity in the active region leads to a higher possibility of transition to different flow regimes (Mellmann, 2001). Moreover, the mechanisms such as mixing, segregation, heat and mass transfer are also reported to occur in this active region (Ding *et al.*, 2001; Dubé *et al.*, 2013).
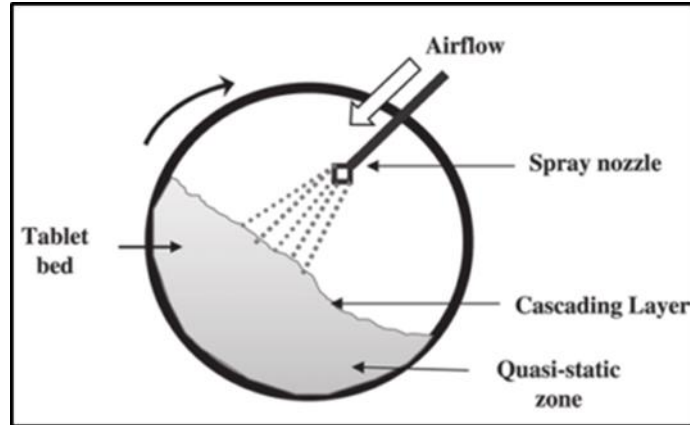
Figure 2.3 Schematic view of a tumbling drum coater showing a quasi-static and cascading zone in the bed as the drum rotates. Source: Sahni and Chaudhuri, (2012).

Numerous studies have numerically and experimentally investigated the transition of the regimes since process mechanisms may differ in different regimes (Henein *et al.*, 1983; Van Puyvelde *et al.*, 1999; Yang *et al.*, 2008). Depending on filling degree, particle properties and Froude number, Henein *et al.*, (1983) classified the flow behaviour in the tumbling drum into six different tumbling regimes in their discrete element method (DEM) study: slipping, slumping, rolling, cascading, cataracting and centrifuging as illustrated in Figure 2.4. These regimes change from slumping (Figure 2.4a) to the centrifuging (Figure 2.4f) as the drum rotational speed increases. Among these regimes, the rolling and cascading regimes are widely used in industry due to good particle mixing, low energy consumption and excellent heat transfer (Liu *et al.*, 2017; Santos *et al.*, 2014).

The slipping regime is an undesirable regime because the solid material only slips on the surface of the drum, resulting in little or no mixing. As illustrated in Figure 2.4f (the centrifuging regime), the solid particles remain fixed to the drum wall when the centrifugal force from the drum rotation exceeds the gravity force. The speed at this condition is regarded as the critical speed, n_c, (Eq. 2.1) and is set as a reference for other tumbling regimes which occur between zero and this critical speed (Sheritt *et al.*, 2003). In Eq. 2.1, *g* refers to gravity and *R* is the drum radius.

9

$$n_c = \frac{60}{2\pi}\sqrt{\frac{g}{R}} \qquad\qquad \textbf{(Equation 2.1)}$$
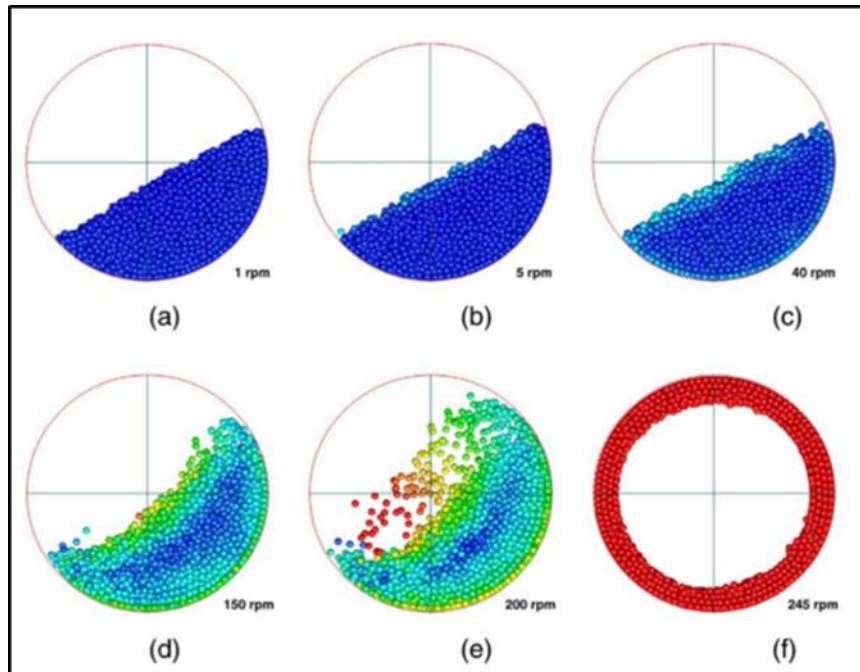
Figure 2.4. Different drum speeds showing different flow regimes: (a), slumping; (b) slumping-rolling transition; (c), rolling; (d), cascading; (e), cataracting; and (f), centrifuging. Source: Yang *et al.*, (2008).

A study by Santomaso *et al.*, (2003) has visually observed the difference in the bed surface shape of glass beads (25% fill level) as the drum speed increases from 0.6 to 52 rpm as shown in Figure 2.5. The lowest speed in Figure 2.5a (rolling regime) shows that the bed surface changes from flat to S-shaped (cascading, Figure 2.5b) and then to an ill-defined shape (cataracting, Fig. 2.5c) as the drum speed increases. This finding is supported by the flow behaviour observed from the DEM simulations in Figure 2.4.
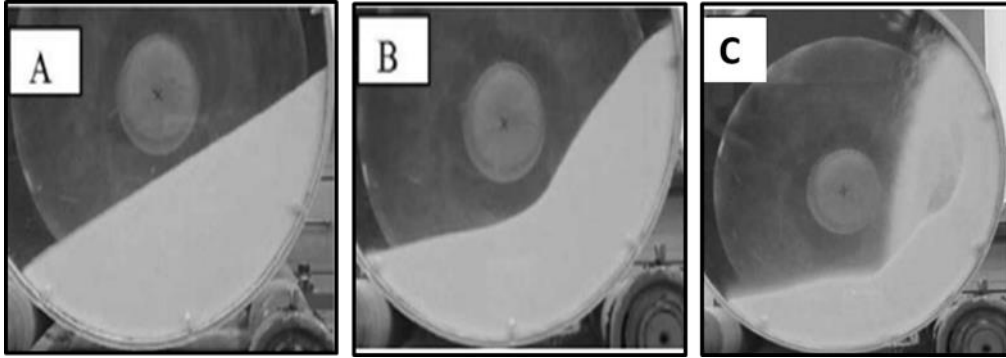
Figure 2.5. Bed surface shape as a function of drum speed: A) rolling; B) cascading and C) cataracting regime. Source: Santomaso *et al.*, (2003).

Furthermore, to maintain a similar dynamic behaviour in different drum geometries e.g. drum size, the pan speeds are set-up based on the Froude number, *Fr* (Pandey *et al*., 2006). This dimensionless number is the ratio of inertial to gravitational forces as shown in Eq. 2.2. In this equation, *ω* is the pan speed, *D* is the drum diameter, and *g* is the acceleration due to gravity. This similarity in dynamic behaviour ensures that the ratio of forces at certain points in the drum coater is constant across various scales. Numerous studies have attempted to relate the Froude number with the dynamic angle of repose, where it has been demonstrated that both are nearly linearly related: the angle of repose increases with Froude number (Khakhar *et al*., 1997; Komossa *et al*., 2014). In another study by Liu and Specht, (2010) it was found that the fraction or the thickness of the cascading layer also increases with the Froude number meaning that more mixing occurs in the drum.

$$Fr = \frac{\omega^2 D}{g} \qquad \textbf{(Equation 2.2)}$$

Dubé *et al.*, (2013) adopted the radioactive particle tracking (RPT) technique to observe the motion of non-spherical particles in both regions (active and passive) by using a tracer particle. The results obtained were then compared with spherical particles from other model studies. The findings found that the shape of particles influences the velocity in the passive layer. Spherical particles cascading down the bed surface with a larger

11

momentum caused a higher particle velocity in the passive layer. Due to a higher degree of spatial orientation for the non-spherical particles, core segregation and lower axial dispersion are observed in both the active and passive layers. Norouzi *et al*., (2015) found that in addition to filling level, Froude number and size, the particle shape also influences the transition of behaviour from rolling to the cascading regime. The thickness of the cascading layer is reported to be affected by the ratio of particle size (*d*)/drum size (*D*). At large *d/D* ratios, the active layer can be characterised by geometry of the drum, while for small *d/D* ratios, the active layer increases with the drum speed (Félix *et al*., 2002).

2.2.1.3 Mixing and Segregation

Particle mixing in the drum is characterised as either convective or diffusive and is observed to occur in two ways: mixing in transverse plane /radial and the axial direction (Figure 2.6). The former is more rapid and is caused by the rotation of the drum and a combination of both convection and diffusion which are regarded as the dominant mixing. The latter is caused by the bed height profile and the drum inclination and mixing occurs mainly by self-diffusion (Sheritt *et al*., 2003). Hogg *et al.,* (1966) point out that the axial mixing can be described by Fick's Law of diffusion and depends on particle and operating conditions: diffusivity increases with particle size, drum speed and drum size *(*Finnie *et al*., 2005; Parker *et al*., 1997) and decreases with fill level (Sheritt *et al*., 2003).
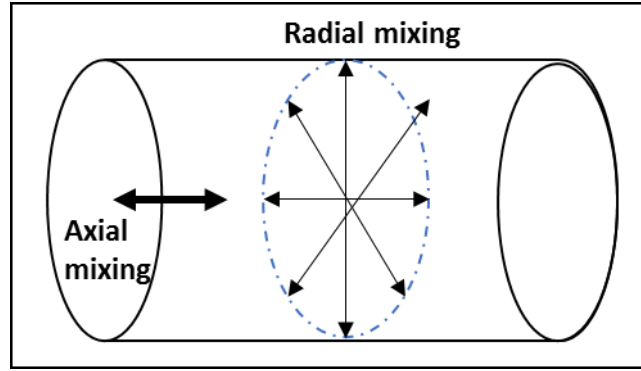
Figure 2.6. Schematic view of the axial and radial direction of mixing

Numerous studies have investigated particle mixing and segregation in tumbling drums by combining theoretical models and experimental results to enhance the coating performance. As summarised in Table 2.1, the material characteristics (particle size, shape, density) and the drum designs (drum size, fill level and drum speed) both influence the mixing and segregation behaviour in the tumbling drum of a dry system. Most of the studies have been carried out numerically since this method provides more precise data, and discrete element method (DEM) is commonly used (Sahni *et al*., 2011; Liu *et al.*, 2017; Nafsun *et al.*, 2017).

Table 2.1 Literature on mixing and segregation of particles in rotating drums

Authors	Parameters	Method	Findings
(Sahni *et al*., 2011)	Fill level, drum speed	Exp-DEM	• At the horizontal position, it is observed that radial convection is faster than axial dispersion in the pan coater, but axial mixing increases as the pan coater tilt increases (in both experiments and simulation) • Fill level and drum speed have minimal effect on mixing in a smaller pan coater under the ranges studied

(Sandadi et al., 2004)	Particle shape, size, drum speed	Exp.	• Circulation and surface times of tablets in the spray zone decreased as drum speed, drum loadings, and tablet size increased • The axial dispersion coefficient increased with the drum speed
(Liu et al., 2017)	Drum speed, drum length	Exp-DEM	• The surface mixing and whole mixing of mono-sized particles in the drum was compared by varying the drum speed and drum length • The short drum had no significant difference between the surface and whole mixing process compared to the long drum
(Nafsun et al., 2017)	Drum speed, fill level	Exp-DEM	• Thermal mixing time decreased with higher drum speed and lower filling level
(Alchikh-Sulaiman et al., 2015)	Drum speed, size, the initial loading method	Exp-DEM	• The degree of mixing of polydisperse particles was smaller as compared to monodisperse particles due to segregation phenomena • Addition of particles with intermediate sizes of smallest and largest particles improved the mixing and reduced the extent of segregation • For the bi-disperse and tri-disperse particles, best mixing was observed when the top (smaller)–bottom (larger) loading method was used

According to Alchikh-Sulaiman *et al.*, (2015), the degree of mixing of polydisperse particles is smaller compared to monodisperse particles due to the segregation mechanism, and the mixing of polydisperse particles was improved when an intermediate particle size range was added to the drum system. Liu *et al.*, (2017) experimentally validated a DEM model to investigate the difference between the surface mixing (active layer) and the whole mixing in the drum by using different drum length and speed. It was concluded that the drum length influences the surface mixing and the whole mixing as there was no significant difference for short drums (L = 26mm, L/D = 4.3) but a significant difference for longer drums (L ≥ 130mm, L/D >21). The particle

pattern in longer drums also shows that bed depth near both end walls is greater than that in the inner bed meaning that greater mixing is achieved due to the side-wall effect.

Most of these studies have focused on a dry system, in which particle-particle and particle-wall interactions and gravity dominate. However, when a small amount of liquid is added to the coating system, the mixing behaviour in the drum system changes. Thus, understanding the behaviour of wet particles in the drum system is important to the design or scale-up of the coating process. Despite this, there is still only a limited amount of research that has focused on this, and this will be reviewed later in this chapter.

2.2.2 Fluidised Beds

The fluidised bed coating technique has been extensively used in numerous industrial processes, for example, detergents, pharmaceuticals, food process technology and agriculture (Chan *et al.*, 2006; Palamanit *et al.*, 2013, 2016; Naz and Sulaiman, 2016). In the food industry, for instance, Palamanit *et al.,* (2016) applied the top spray fluidised bed to produce functional coated rice by adding curcuminoids that are present in turmeric rhizomes extract which possess high antioxidant activity and heat stability. Furthermore, there is a variety of food products that are treated in the fluidised bed during their production including milk, cocoa and coffee powders, and infant formula (Turchiuli, 2013).

In the fluidised bed coating system, particles are suspended or fluidised in a fluid-like state using gas introduced at the bottom of the bed. The fluidised bed chamber can be either cylindrical or conical in shape, and the air distributed through a distributor plate with an adequate partition and size of holes. At the same time, a coating solution or melt containing coating material is continuously sprayed onto fluidised core particles using a nozzle and the core will be coated every time they pass through the spray zone (Jacquot and Pernette, 2004). This process allows high coating rates and is known to be suitable

for a wide range of particle sizes (50 µm to 5 mm) and shapes. Generally, larger tablets (ca. more than 6.35 mm) are not suitable to be coated in a fluidised bed due to mechanical damage that occurs in the device. The types of fluidised bed can be classified according to the nozzle position or the ways in which the solution is sprayed (top, bottom or side) and to the operating conditions; either continuous or batch process (Teunou and Poncelet, 2002). There exist three types of basic batch fluidised bed coating systems and each coating system is different and summarised in the following section.

2.2.2.1 Types of Fluidised Bed

Top spraying is the oldest technique of spray coating technology. The coating material is introduced into this system from a spray nozzle placed at the top, and the coating is sprayed from top to bottom. The particles are fluidised by air from the bottom of the fluidised bed chamber (Figure 2.7a). The fluidised particles are coated in the spray zone and then fall back to particle bed, and the coating cycles continue until the desired coating quality is achieved. The final product quality is largely determined by the spray and bed characteristics, and the particle motion. According to Hede *et al.,* (2009) drop deposition occurs at the top of the fluidised bed. To prevent possible droplet drying and agglomeration during the coating process, the ratio of particles to droplets should be high enough in the coating zone, and the droplet size should be small enough to ensure coating success during collisions.

To improve the success of collisions between fluidised particles and the droplets, a bottom spray type is widely used (Figure 2.7b). The liquid is introduced from the bottom concurrently with the air, and this provides a shorter distance between the droplets and the fluidised particles, thereby reducing the drying of droplets before impact to the particle surface and leads to higher coating quality. Teunou and Poncelet (2002) found that the bottom spray type is efficient for coating tablets, but a higher concentration of wet particles than top spray type leads to the risk of agglomeration of small particles during the coating process.

In 1950, Wurster improved the bottom spray type to reduce the risk of agglomeration by adding a partition in the fluidised bed chamber (Figure 2.7c) with a new design of the distributor plate to control the fluidisation of the particles. This new design partition provides a high velocity air stream, hence improving the fluidisation of the particles. There are two zones observed: (i) inside the partition, where the spreading of the droplets is the most efficient and (ii) outside the partition, where gravity dominates, thus the fluidised particles slowly fall down the Wurster bed. This Wurster coater has been widely applied in the pharmaceutical industry to coat solid/tablet materials with a size range from 50-1000 µm due to greater coating uniformity, drying capacity and minimal risk of agglomeration.
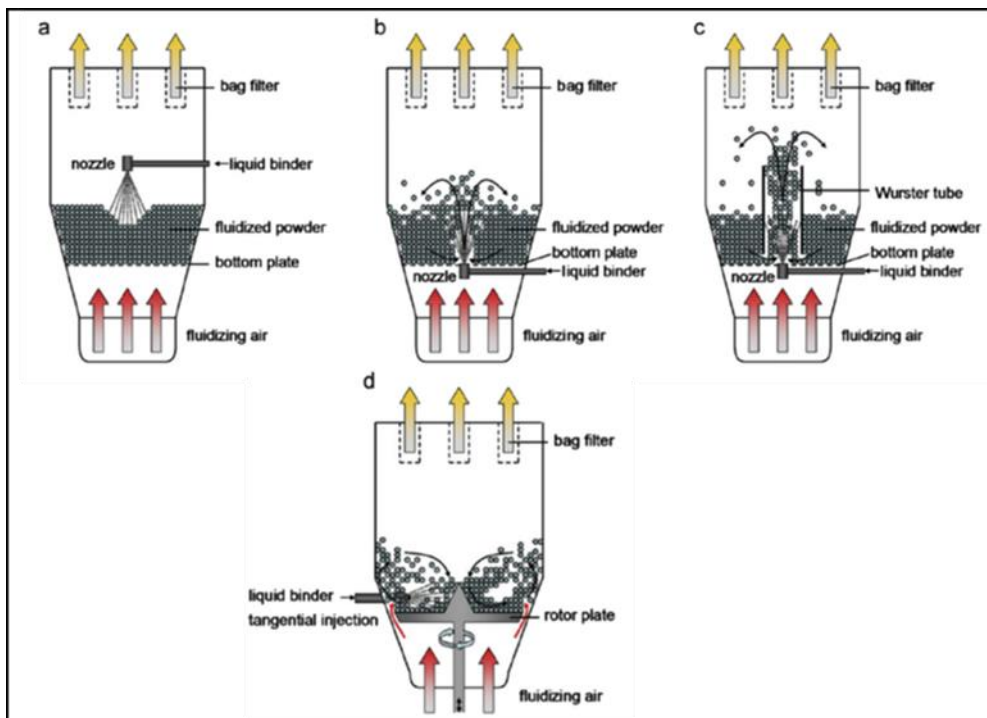
Figure 2.7. Different types of batch fluidised bed coating: a) top spray; b) bottom spray; c) Wurster coater and d) side/tangential spray with rotating disk. Source: Boyce, (2018).

Figure 2.7d shows a tangential/side spray fluidised bed. This type of device sprays the liquid directly from the side of the fluidised bed chamber, and a rotary plate is attached at the bottom of the chamber. The particles are fluidised from the airflow coming through

17

the space between the edge of the rotor plate and the inside chamber. The pattern of the fluidisation in this device can be described as a spiralling helix due to a combination of the centrifugal force, the air stream and gravity (Srivastava and Mishra, 2010). Similar to the bottom spray type, the final product from this device also produces a higher coating uniformity. However, since this technique applies high shear stress to the particles, it is not suitable for fragile materials.

2.2.2.2 Atomisation Principles

In the spray coating process, the atomisation of a coating material is the first stage (see Figure 2.15). This stage is very important, mainly to obtain a large and rapid increase in droplet surface area thus leading to an increase in the rate of evaporation (Hede *et al.*, 2008). Atomization is the process of producing droplets by the disruptive action of a high relative velocity between gas and the liquid stream. Here, the aerodynamic force exceeds the consolidating surface tension force and causes the liquid to disintegrate into droplets (Chen *et al.*, 2008). In addition, the optimum relative velocity achieved depends on the type of nozzles and sizes used. The nozzles can be divided into two main categories: (1) pressure or single-fluid nozzles, for which the pressurised liquid is the only stream fed to the device, and (2) pneumatic or two-fluid nozzles, in which two streams are fed; a liquid and a gas.

2.2.2.2.1 Two fluid nozzles

The most commonly used nozzles in the coating industry are two fluid nozzles or pneumatic sprays (Börner *et al.*, 2014; Naz *et al.*, 2014; Pacheco *et al.*, 2016). This type of nozzle can be further classified based on how both fluids come into contact (Figure 2.8): (i) internal mixing nozzles, where the air stream and the liquid are mixed inside the nozzle and (ii) external mixing nozzles, where both contact at the exit of the nozzle head,

and in the case of a pneumatic cup atomiser, both contact at the rim of rotating nozzle head.

Within these nozzles, in order to produce the same droplet diameter, the internal mixing is reported to be more energy efficient due to less air being required. However, its lifetime is shorter due to erosion when impurities are present in the liquid used. Compared to internal mixing, external mixing allows independent control of both liquid and air streams, and for that case, external mixing nozzles are typically desired for fluidised bed coating (Hede *et al*., 2008). Furthermore, nozzle clogging problems can be reduced because there is no interaction between the air and liquid in the nozzle device.
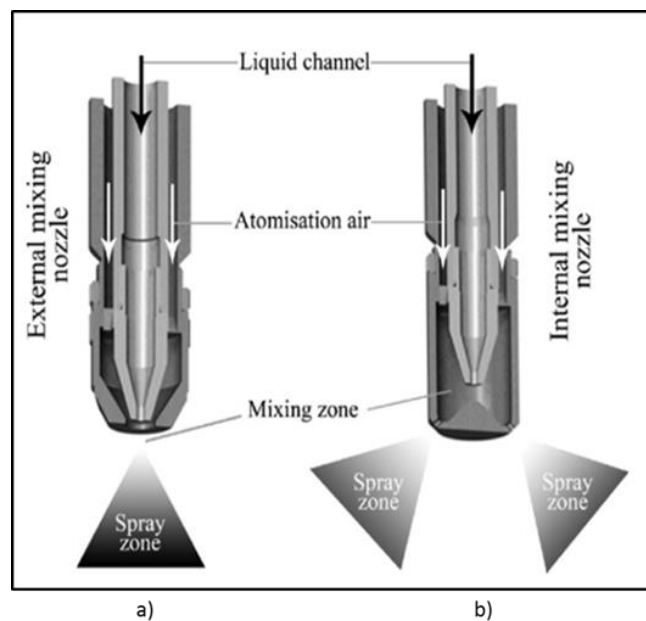
Figure 2.8. Schematic view of two fluid nozzle designs: a) external mixing nozzle; b) internal mixing nozzle. Source: Hede *et al*., (2008).

2.2.2.2.2 Spray Pattern

As previously mentioned, spraying nozzles play a critical role in fluidised bed coating, and there are many characteristics which should be considered to select an adequate nozzle; spray pattern, spray angle, spray rate and drop size. For spray pattern, as an example, in a conveyor belt applications, if dual or multiple nozzles are used, the overlapping liquid distribution pattern of the nozzles needs to be considered as the process may rely strongly on the spray relative to local volume flux (Hagers, 1997). Each nozzle might have different shape orifices and spray angles, thereby producing various spray patterns such as flat spray, full cone and hollow cone patterns (Figure 2.9).

With a flat spray nozzle pattern (Figure 2.9a), droplets are sprayed in tapered-edge shape or a flat-liquid layer with different thicknesses in relation to operating condition used to generate the spray. This type of spray nozzle is typically employed in narrow or rectangular enclosed spaces and used for dust prevention. In a full-cone spray (Figure 2.9b), droplets are distributed outward into a cone pattern, with its origin point at the nozzle orifice. Such a spray pattern is widely used in the food industry, for instance, the chocolate candies process, because it allows the droplets to distribute in the surface.
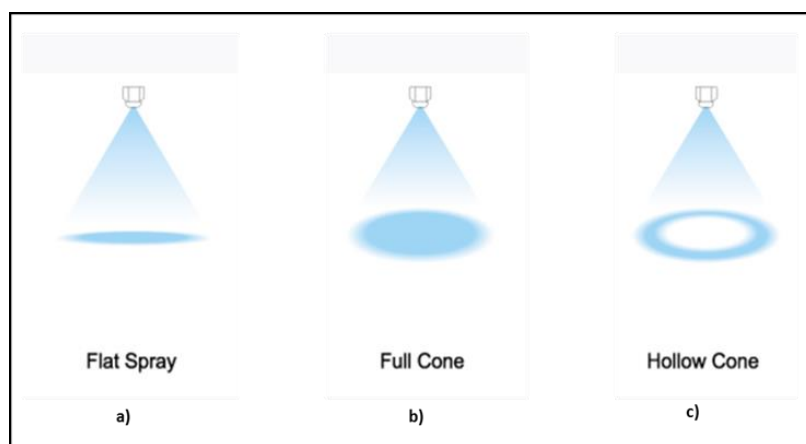
Figure 2.9. Different spray patterns for external mixing two-fluid nozzles: a) Flat-spray nozzles, b) Full-cone nozzles, c) Hollow-cone nozzles. Adapted from: BETE Fog Nozzle, Inc., (2017).

The third pattern is a hollow cone spray pattern (Figure 2.9c). This pattern looks like a circular ring and consists of droplets concentrated at the outer point of the conical shape volume with no droplets accommodated inside the conical shape. The liquid enters the nozzle at a right angle creating a centrifugal force which accumulates the droplets outside the cone. Compared to other two nozzles, it produces a smaller drop size, and it can be formed by a tangential or deflection nozzle (Co *et al*., 2000).

The spray pattern coverage area is dependent on the spray angle, θ, and the distance height from the particle bed, D. The spray angle of a nozzle is not constant, and it will diminish as the liquid moves from the nozzle due to gravitational effect. As demonstrated in Figure 2.10, the spray coverage varies with spray angle (below 180^0) and the spray distance. At certain spray distances, the spray angle of the liquid is affected by the viscosity, spray pressure and the flow rate (Andrade *et al*., 2012a).
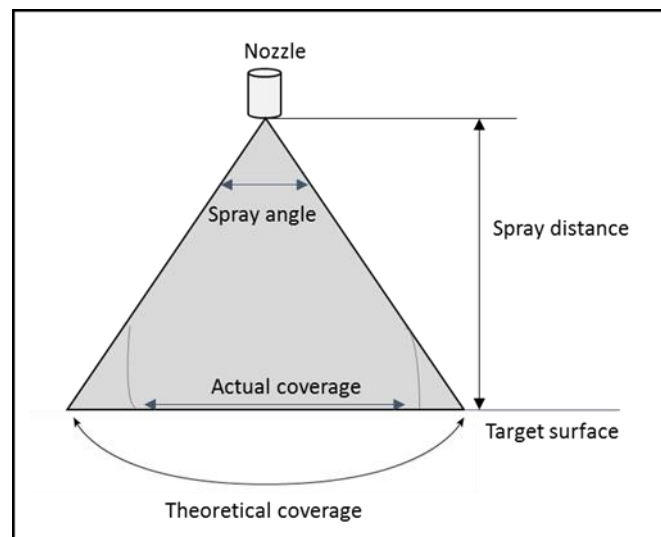
Figure 2.10. Spray angle and coverage of a nozzle. Adapted from: BETE Fog Nozzle, Inc., (2017).

2.2.2.3 Theory of fluidisation

Fluidisation of particles in the fluidised bed depends on the fluid and particle properties. To fluidise the solid particles, the fluid (either gas or liquid) is passed upwards through the bed by changing the flow rate. Different flow rates will reach different states of fluidisation regime; from the initial fixed state to pneumatic transportation. As indicated in Figure 2.11, at low air flow rate, the particle bed remains fixed. When the fluidisation flow rate increases gradually, the particles will start to move, and a small expansion of the bed is observed. This represents the incipient or minimum fluidisation regime. Then, when the flow rate is continuously increased, the following regimes can be observed sequentially: smooth, bubbling fluidisation, slugging, turbulent fluidisation, and pneumatic transport (Smith, 2007).

The fluidisation velocity, U, is commonly set between the minimum fluidisation velocity, U_{mf}, and the entrainment velocity, U_e, to maintain a recirculation of solid particles in the fluidised bed chamber. These two values are dependent on the properties of the particles (size, shape, and density), properties of the gas (viscosity, density) and also the porosity of the particle bed. Beside these two values, there are other fluid velocities in fluidised bed operations such as minimum bubbling velocity (U_{mb}) and turbulence fluidisation velocity (U_{tf}). However, not all these velocities need to be measured. It depends on the type of process used in the fluidised bed coater. In the case of the work involved in this thesis, the U_{mf} is the most important velocity which needs to be measured, and this is explained in the following section.
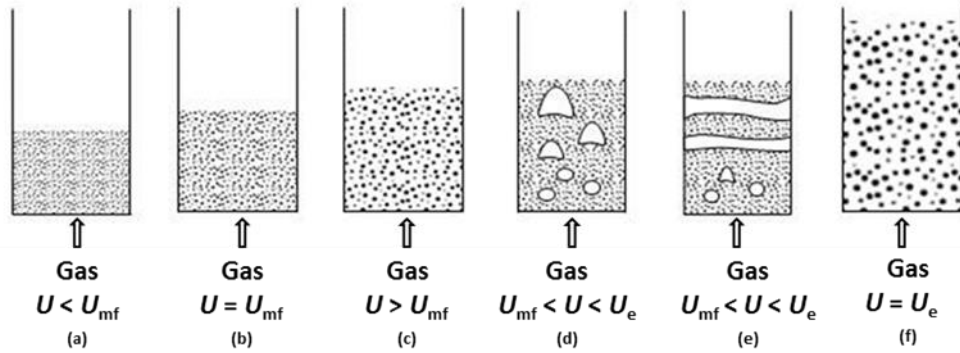
Figure 2.11. Fluidisation regimes: a) fixed bed, b) minimum fluidisation, c) smooth fluidisation, d) bubbling fluidisation, e) slugging fluidisation, f) lean phase fluidisation. Adapted from Rhodes, (2008).

2.2.2.4 Minimum Fluidisation Velocity

The minimum fluidisation velocity, U_{mf}, as abovementioned is the lowest velocity of the air needed for the particle bed to change from a fixed to a fluidised state, and depends mainly to the properties of solid particles used (see Section 2.2.2.5). Teunou and Poncelet, (2002) found that U_{mf} mainly depends on the particle diameter, d_p, the particle density, ρ_p, the fluid density, ρ_g, and viscosity, μ, as shown in Eq. 2.3- Eq. 2.4.

$$U_{mf} = \frac{(\rho_p - \rho_g)^{0.934} g^{0.934} d_p{}^{1.8}}{111 \mu^{0.87} \rho_g{}^{0.066}} \qquad \text{for } d_p < 100 \text{ µm} \quad \textbf{(Equation 2.3)}$$

$$U_{mf} = \frac{\mu}{\rho_g d_p} \left[(11135.7 + 0.0408 Ar)^{\frac{1}{2}} - 33.7 \right] \text{ for } d_p > 100 \text{ µm } \textbf{(Equation 2.4)}$$

The Archimedes number, Ar in Eq. 2.4 is defined as the ratio of gravitational forces to viscous forces. This dimensionless number has been used to describe the motion of fluid and solid particles in a fluidised bed due to density differences in two-phase flows and is shown in Eq. 2.5:

23

$$Ar = \frac{\rho_s \, d_v{}^3 (\rho_p - \rho_g) g}{\mu^2}$$
(Equation 2.5)

where d_v is the diameter of an equivalent sphere.

Although the U_{mf} can be observed visually, it is more accurate if measured experimentally and compared with the theoretical equation. There are a few experimental methods have been used to measure the U_{mf} such as bed pressure drop, bed voidage and the heat transfer method and the former is more commonly used.

For the bed pressure drop method, the U_{mf} is determined by plotting a graph of bed pressure drop as a function of superficial fluidisation velocity, U, as described in Figure 2.12 (Khan *et al*., 2016; Patnaik and Sriharsha, 2010). At lower superficial velocity, the fluidisation air is passed upward through the fixed particle bed without causing any particle motion. As the fluidisation velocity is further increased, the pressure drop also increases until a certain point, then the pressure drops became constant. This point is where the particle weight fully supports the drag force, thus the fixed bed starts to expand due to the particle motion. The superficial velocity point here is termed the U_{mf} at which the fluidisation starts to occur.

For the voidage method, the U_{mf} is measured based on bed expansions where the U_{mf} is considered when the voidage starts to increase as the fluidisation velocity increases. In the heat transfer method, the U_{mf} is determined at the point when the heat transfer coefficient starts to increase drastically as the fluidisation velocity increases. The bed voidage and heat transfer methods are not commonly used due to being more complicated and they also require a higher cost for the experimental set-up.
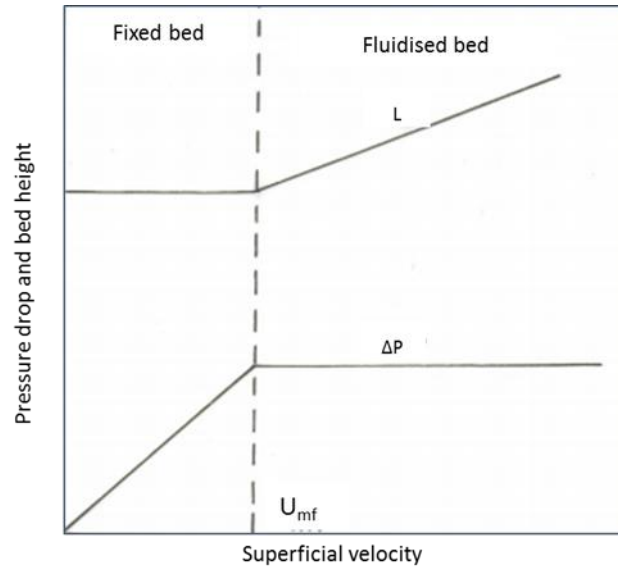
Figure 2.12. Schematic plot of bed pressure drop and bed height as a function of fluidisation velocity. Adapted from Patnaik and Sriharsha, (2010)

2.2.2.5 Powder Classification

Geldart, (1973) classified particles based on their properties into four groups to predict fluidisation behaviour: A, aeratable; B, bubble-ready/sand-like; C, cohesive and D, spoutable. These groups are characterised based on the density difference between the particles and the fluidising medium (ρ_p -ρ_f) and the particle size (d_p) as shown in Figure 2.13. The particle size ranges in Figure 2.13 shows that group C is the smallest (<30 µm) and referred to as cohesive powders. Due to high inter-particle forces of group C, the individual particles tend to form agglomerates which lead to defluidisation. Thus, for this group, generally, the particles are fluidised with external assistance such as baffles, microjets or mechanical vibration. A better fluidisation is also achieved when larger particles, e.g. group B particles, are added to the particle bed (Cocco *et al*., 2014).
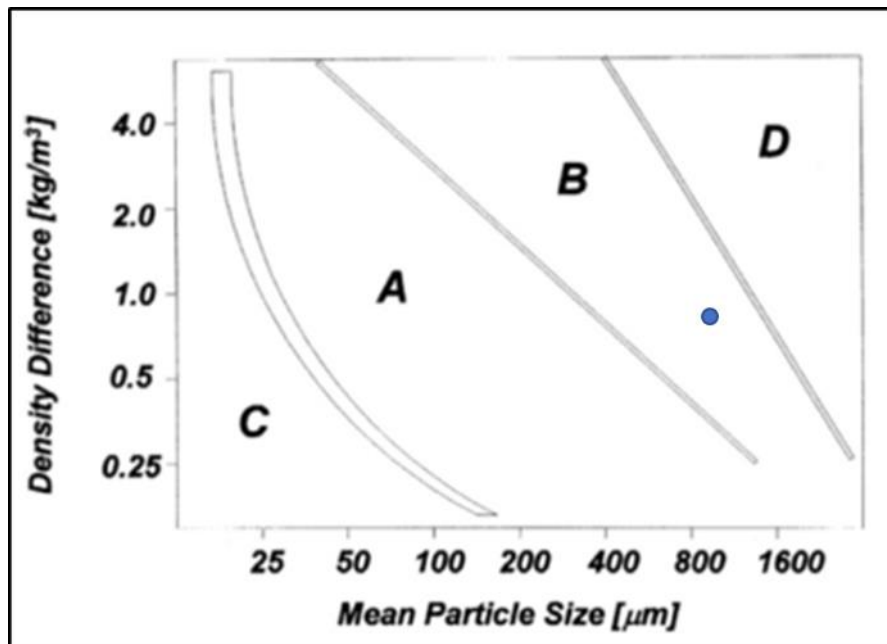
Figure 2.13. Geldart's classification of particles. Source: Geldart, (1973).

Note: • in the graph is referred to the group of alumina particles used in this study

The largest particles belong to group D (500 μm – several millimetres) with high particle density. Bubble formation can be observed when fluidising this group of particles. The large bubbles formed cause the particles to be swept upwards causing unstable operation. Thus, these particles are typically processed in spouted beds, which require lower gas flow than standard fluidised beds.

Geldart group A particles are referred to as being aeratable due to good fluidisation behaviour and form a uniform bed expansion as the fluidisation velocity increases more than minimum fluidisation velocity, U_{mf}. These types of particle range in size from 30 to 125 μm and have a particle density less than 1400 kg/m^3. Most of the particles used in the fluidised bed system are from this group, mainly because they can be operated at low gas flows which allow easier control of the growth and speed above the U_{mb}, where they exhibit the bubbling behaviour.

26

Group B particles are described as sand-like and range in medium size from 50–1500 µm and their particle density falls in the range of 1400–4000 kg/m^3. As shown in Figure 2.13, the alumina particles used in this study are belong to this group based on their density and size. In contrast to group A particles, this group of particles exhibit bubbling at the minimum fluidisation velocity ($U_{mb} = U_{mf}$).

2.3 Mechanisms of spray coating in tumbling drums and fluidised bed coaters

Although different types of coating systems are used in different industries, the underlying principles of spray coating for the abovementioned systems are the same (Figure 2.14). The differences primarily relate to the way particles move between the spray and drying zones and the method of removing the solvent. In both coating systems, spray coating is based on repeated exposure of particles (e.g. tablets, granules) to a spray containing solute and solvent as conceptually shown in Figure 2.14. After the spray region, the particles move into a drying region where the partial coating is solidified, typically via evaporation of the solvent facilitated by heated drying air. The drying air is directed towards the surface of the particle bed in order to achieve good heat and mass transfer. Then, the spraying and drying zone cycle are repeated multiple times until the desired coating mass and uniformity have been reached (Turton and Cheng, 2005; Turton, 2008; Suzzi et al., 2010; Sahni et al., 2011).
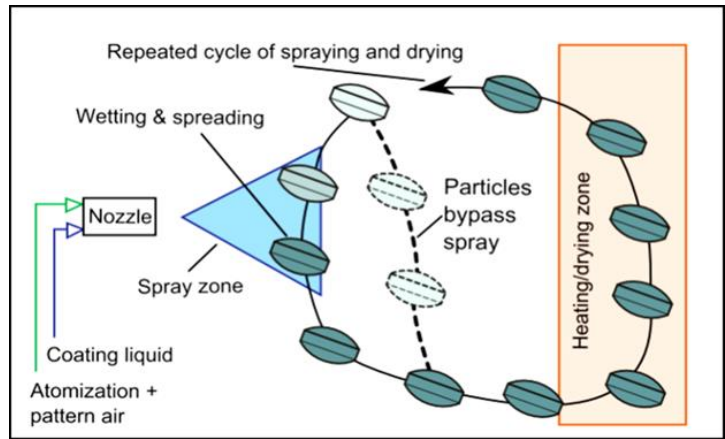
Figure 2.14. Schematic view of the coating mechanism in most types of coating equipment. Source: Turton, (2008).

As the bed is moving during fluidisation, particles spend a fraction of a second in the spray zone and receive a partial coating from the initial wetting and spreading (step 1 – drop deposition) mechanism with the amount and distribution depending on the local conditions in the spray zone. From here, the droplet may spread or penetrate to some extent over the particle, and in some cases, the liquid may be transferred to other uncoated particles (step 2 – contact spreading). These two possible mechanisms are illustrated in Figure 2.15.
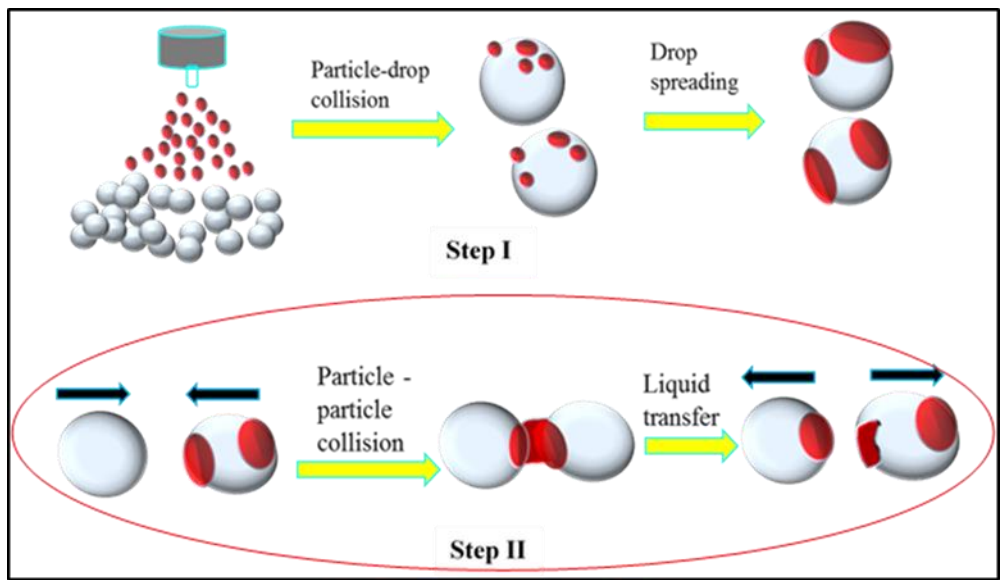
Figure 2.15. Schematic view of spray coating mechanisms: (step I) drop deposition, (step II) contact spreading.

There is potential for many processes to take place inside the bed depending on the operation conditions, core particle properties and the coating materials properties (Nienow, 1995). The possible mechanisms that could occur in a fluidised bed coater are shown in Figure 2.16. Nienow, (1995) points out that two main mechanisms should be controlled to ensure a successful coating is achieved: the success of collisions between droplets and particles and the collisions between a particle and a wet particle. The term success here refers to the breakage of the liquid bridge formed from the wet collision upon drying inside the bed.
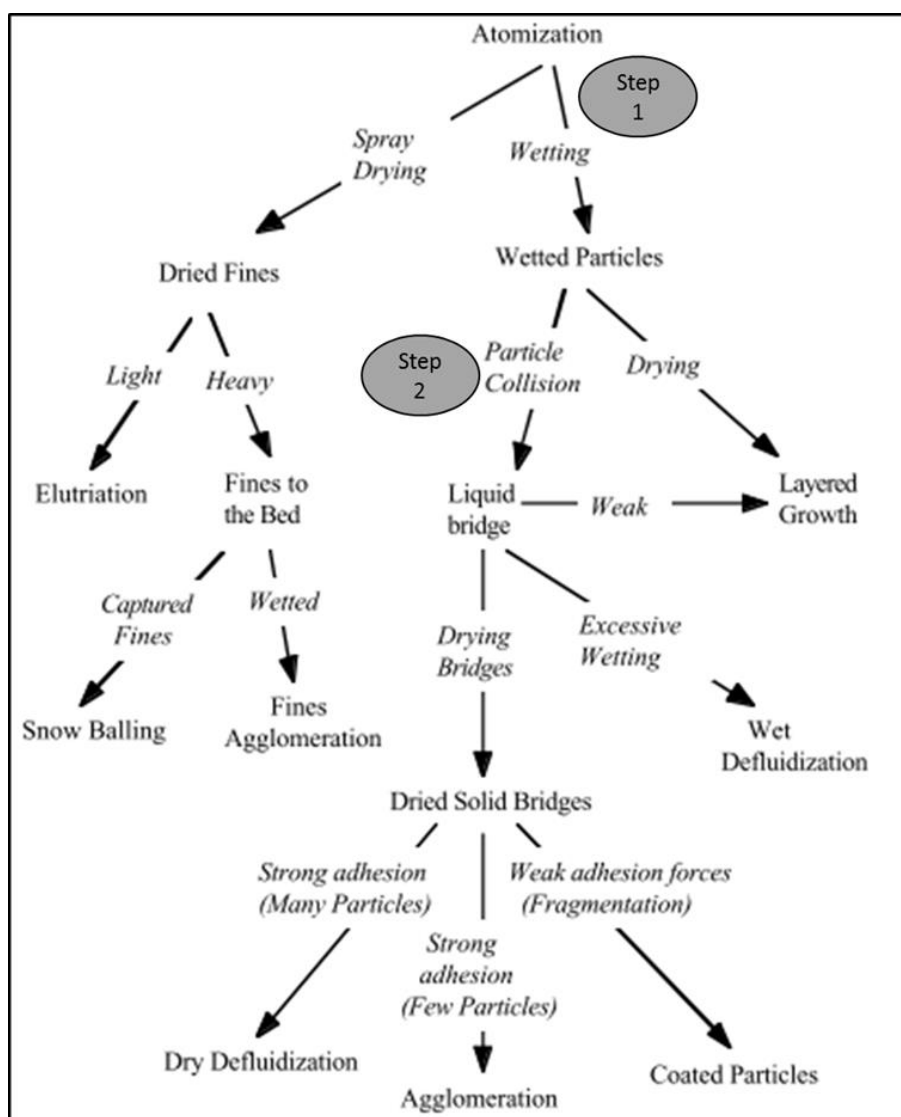
Figure 2.16. Possible mechanisms that could occur in a fluidised bed coater. Adapted from Nienow, (1995).

2.3.1 Drop Deposition and Spreading (Step 1)

Studies in the area of wet coating have largely focused on liquid atomisation and deposition or droplet impact on particles (step 1). This step of coating is clearly similar to distribution nucleation, one of the first stages in granulation, which begins with droplet formation, drop impact, wetting and spreading over the particle surface, secondary levelling of droplets, consolidation and drying of the coating layer (Figure 2.17) (Link and Schlünder, 1997; Kariuki *et al*., 2013; Karlsson *et al*., 2011; Panda *et al*., 2001; Ström *et al*., 2005). Clearly, from Figure 2.17, liquid deposition behaviour is strongly affected by interactions of the spray and the solid surface to be coated. Hence, several attempts have been made to understand the basic principles of the spraying and deposition processes on a single tablet or granule (Karlsson *et al*., 2011; Ström *et al*., 2005). However, most studies use a fluidised bed rather than a rotating drum, although the latter is also extensively used because of its simple operation.
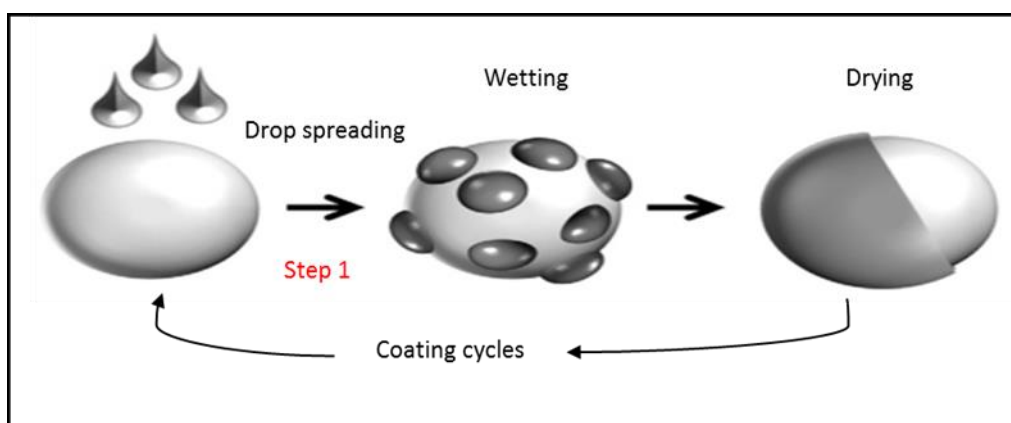
Figure 2.17. Schematic view of liquid atomization and deposition in single particle coating studies. Adapted from Suzzi *et al*., (2010) and Sondej *et al.*, (2015).

From the literature, several works highlight the important effect of particle surface wettability, surface roughness, density, size (Marston *et al*., 2010; Saleh and Guigon, 2007b), adhesion strength and liquid formulation (Pont *et al*., 2001; Yang and Leong, 2002; Andrade *et al*., 2012b) on coating efficiency and quality. Also, the interest in drop impact and spreading has been concerned with splashing, rebound and recoil, wetting

dynamics, maximum spread and final spread as the final coating quality is highly dependent on these phenomena (Werner *et al.*, 2007a, 2007c;. Andrade *et al*., 2012b).

The effects of wettability on the dynamics of the spreading can be characterised by a static (or equilibrium) contact angle, Θ_c. Static contact angles are measured when the droplet is in the static condition on a solid surface. Depending on the contact angle values, different wetting behaviour can be observed; wetting (contact angle < 90 º), complete wetting (contact angle = zero) and un-wetting (contact angle > 90 º), as illustrated in Figure 2.18a. The dynamic contact angle is measured when the three phases (droplet, solid and air) are moving, and these are referred to as advancing, Θ_a, and receding, Θ_r, angles. The drop starts to spread if the contact angle exceeds the static Θ_a, and de-wetting occurs if the contact angle is less than this value.
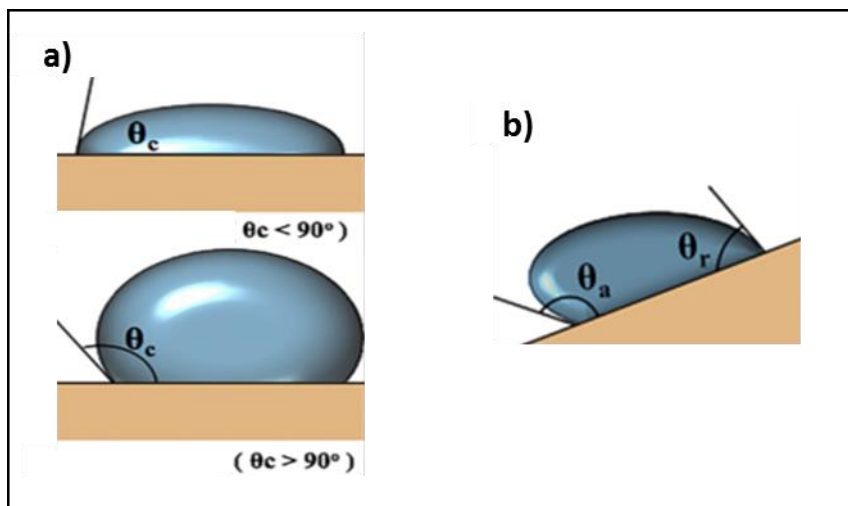
Figure 2.18. a) Different contact angles on a surface; b) Schematic of dynamic contact angle measurement by using the tilting cradle method. Adapted from: Zhao and Jiang, (2018).

The values for both Θ_a and Θ_r can be measured by using the tilting cradle or tilt plate method, as shown in Figure 2.18b. Using this method, the droplet is placed on the substrate which is then gradually tilted. The Θ_a is measured at the front of the droplet just before the droplet starts to move, while Θ_r is measured at the back of the droplet, at the

same time point. The difference between both contact angles is defined as contact angle hysteresis; it arises due to chemical heterogeneity, surface roughness, swelling and partial dissolution of the solid in the liquid (Andrade *et al*., 2013; Lazghab *et al.*, 2005). Other techniques, such as the Wilhelmy plate and capillary rising method have also been reported to determine the contact angle on flat surfaces. For fine single particles, the measurement methods can be based on microscopic visualization of the solid-liquid interface, and could include: sessile drop, atomic force microscopy (AFM), environmental scanning electron microscopy (ESEM) and floating particle methods (Alghunaim *et al*., 2016; Good, 1992; Lazghab *et al*., 2005; Mitra *et al*., 2013).

As shown in Figure 2.19, when a drop impacts on a solid (smooth or rough), impact behaviour can be divided into several sub-processes identified as spreading, splashing and rebounding (Yarin, 2006).
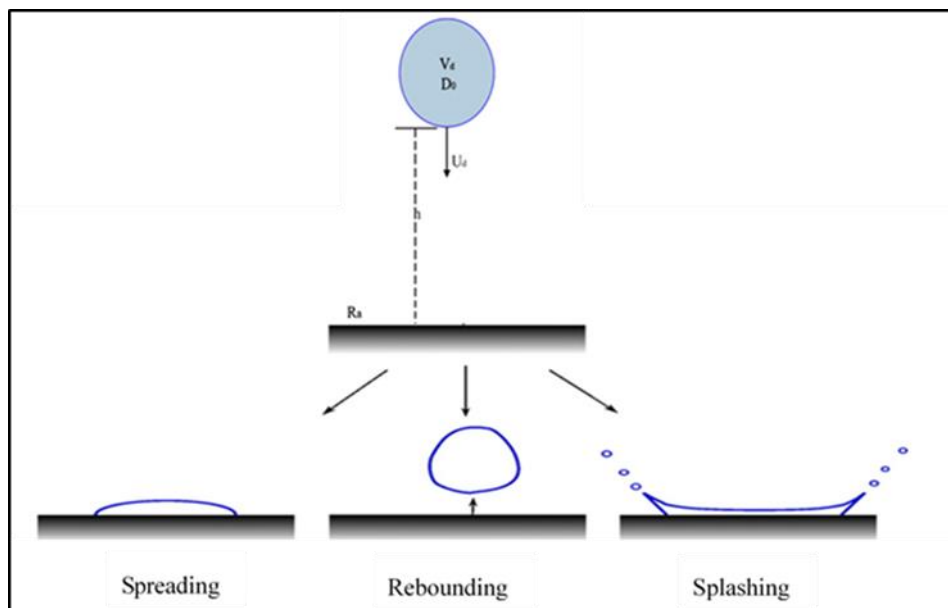
Figure 2.19. Impact of a drop on a solid surface: spreading, rebounding, and splashing. Source: Bolleddula *et al*., (2010).

According to a study by Bolleddula *et al*. (2010), for low kinetic energies (E_k) of drop impacts, after impact, the E_k is dissipated by viscous forces and the drop will deposit

32

over the surface and reach a maximum diameter after a finite spreading time. In some cases, inertia could also be negligible if the E_k is low enough. However, if the E_k is too large, inertia will take place to maintain the excess of surface energy upon impact, and the drop may partially recede and even completely rebound. Moreover, several works have suggested that the abovementioned phenomena represent a continual trade-off between inertial forces (associated with the mass of the drop and its impact velocity), capillary forces (which depend on the surface tension and the solid surface characteristics), gravitational forces and viscous dissipation (Cooper-White *et al*., 2002) and these studies are summarized in Table 2.2.

Furthermore, the drop impact behaviour also can be described using three main dimensionless parameters (Yarin, 2006):

The Reynolds number (Eq. 2.6) compares the droplet inertia and the viscous dissipation, meaning that the impact of highly viscous droplets (resulting in a low *Re* number) could lead to poor spreading.

$$Re = \frac{\rho D v_i}{\mu} \qquad \textbf{(Equation 2.6)}$$

The Weber number (Eq. 2.7) compares the inertia and surface energy. According to previous findings (Yarin, 2006), droplet rebound can take place when the *We* number is higher than unity and over a certain limit.

$$We = \frac{\rho D v_i^2}{\gamma} \qquad \textbf{(Equation 2.7)}$$

Another dimensionless parameter, the Ohnesorge number (Eq. 2.8) is obtained as a combination of the Reynolds and Weber number. It reveals the importance of the viscous force with the aerodynamic and capillary force and can be described to scale the

resisting force to the recoiling motion. It has been reported that increases in the *Oh* number will slow down the recoiling behaviour.

$$Oh = \frac{\mu}{\sqrt{\rho \gamma D}}$$
(Equation 2.8)

Here, ρ = liquid density; D = diameter; v_i = impact velocity; μ = viscosity; γ = surface tension.

Kariuki *et al.*, (2013) have developed a Bernoulli model to describe the fractional surface coating, *F*, which is important to accurately predict the strength of the liquid bridge formed from the collision of two particles. The strength of the liquid bridge is based on the volume of the liquid bridge. This information could add new knowledge to differentiate the process; particle coating or distribution nucleation. In this study, a new dimensional parameter, the particle coating number, ϕ_p, has been introduced which defines the ratio of the theoretical area coated by the drops (assuming no overlap) to the total surface area of the particle. Experimental results demonstrated that ϕ_p could be used to predict *F* using simple, known parameters and was able to account for differences in drop size and particle size. In addition, it could also be used to predict the effect of changing particle size, surface area, and liquid level or drop size on the coating fraction. Thus it is extremely valuable in a range of wetting and coating applications.

Table 2.2. Single particle/ drop impact behaviour studies

(Note: CM: Coating material; IV: Independent variables; DV: Dependent variables; CMC: Carboxymethylcellulose; D: Diameter; CA: Contact angle; PVA: Polyvinyl alcohol; PEG: Polyethylene glycol; HPMC: Hydroxypropyl methylcellulose; MD: Maltodextrin; ↑: Increase; ↓: Decrease; Re: Reynolds; We: Weber; Oh: Ohnesorge)

Author/ Year	Core/ Coating material	Parameters	Results	Method/Apparatus
Khoufech *et al.*, (2015)	-hydrophobic surface/ -water -CMC	IV -droplet size -liquid viscosity -drop velocity DV -max spreading -recoil velocity -max height of rebound	-as CMC ↑, all DV (max. spreading, recoil velocity & max. height rebound) decrease -max. spreading influenced by inertia & viscous dissipation -impact velocity ↑ spreading and receding -impact regime diagram based on Oh and We numbers established based on collected data	-high-speed camera and image analysis
Andrade *et al.*, (2015)	-banana and eggplant epicarps/ -gelatin, glycerol, cellulose nanofibers	IV -CM type -CM viscosity -surface energy DV -max spread D/ factor	-max. spread factor not effected by surface energy -but effected by viscosity	
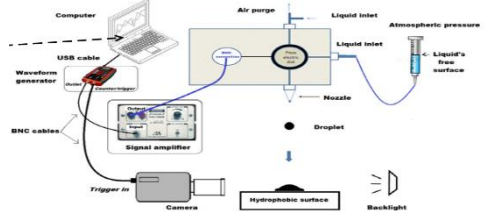
Šikalo *et al.*, (2002)	horizontal surfaces: -smooth glass, wax, PVC, rough glass/ -water, isopropanol, glycerine	IV -droplet We number -liquid types -CA/surface wettability DV -spreading D -apex/peak height of the droplet	-surface wettability strongly influenced droplet spreading - max spreading ↑ with ↑ Re and We number	
Bolleddula *et al.*, (2010)	-tablet (3 types)/ -opadry TMII white with varying content of: PVA, PEG, HPMC	IV -surface type (acrylic, mica, Teflon) -viscosity -drop velocity -CA DV -spreading D -centerline height of drop, h(t)	-when Oh values range are extended above 1, splashing and rebounding completely inhibited (highly viscous Newtonian) -role of wettability is negligible at an early stage of impact -max spreading D showed agreement with three models used	
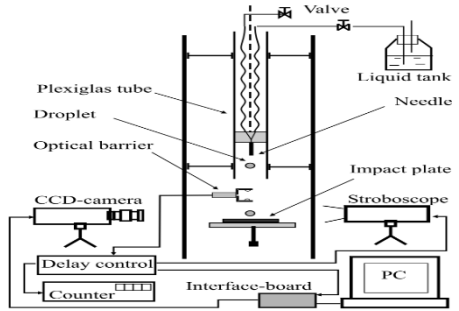
Mitra *et al*., (2013)	-spherical particle/ -water, isopropyl alcohol, acetone	<u>IV</u> -We number -surface temperature (20-250^0C) -CM types <u>DV</u> -droplet shape evolution -max spreading	-droplet spreading better predicted by dynamic CA than the static angle	
Werner *et al*., (2007c)	-smooth anhydrous milk fat surface/ -MD DE5, water	<u>IV</u> -drop velocity -CM viscosity -surface tension (adding surfactant) <u>DV</u> -max spreading D	-greater max spreading with higher drop velocity and lower viscosity -surfactants not significant on max spreading, limited droplet recoil -surfactants affect final spreading, coverage area 3 times higher	

2.3.2 Contact Spreading via Particle-Particle Collision (Step 2)

The collision of wetted particles which allows liquid bridges to form and solidify, as in granulation, is undesirable in the coating process (Boerefijn *et al*., 2009). Furthermore, if the flux of fluid is too high, this tends to over-wet the bed and increases the possibility of wetted particles agglomerating as demonstrated in Figure 2.20a (Hapgood *et al*., 2004). Thus, in order for particle coating to be successful, after the inter-particle collision occurs, the formation of liquid bonds between wetted particles have to be broken before the bridge solidifies (Figure 2.20b). More importantly, it is believed that there is also some redistribution of liquid from wet to non-wetted particles in the bulk of the bed as they return to the spray zone. This mechanism of coating is theoretically due to the liquid transfer via contact spreading within particles in the powder bed, and its rate of occurrence is expected to be a complex function of particle properties (size distribution, density, shape, surface roughness), liquid properties (viscosity, surface tension, density), particle/liquid properties (solid/liquid contact angle, liquid penetration rate) and the operating parameters (equipment type, speed, relative dimensions, load) (Sahni and Chaudhuri, 2011; Saleh and Guigon, 2007b; Toschkoff & Khinast, 2013). Despite the significance of liquid transfer between particles occurring in systems such as a rotating drum and fluidised bed, the way that liquids interact and spread through the powders is not well understood, and there is still little research conducted in this area.
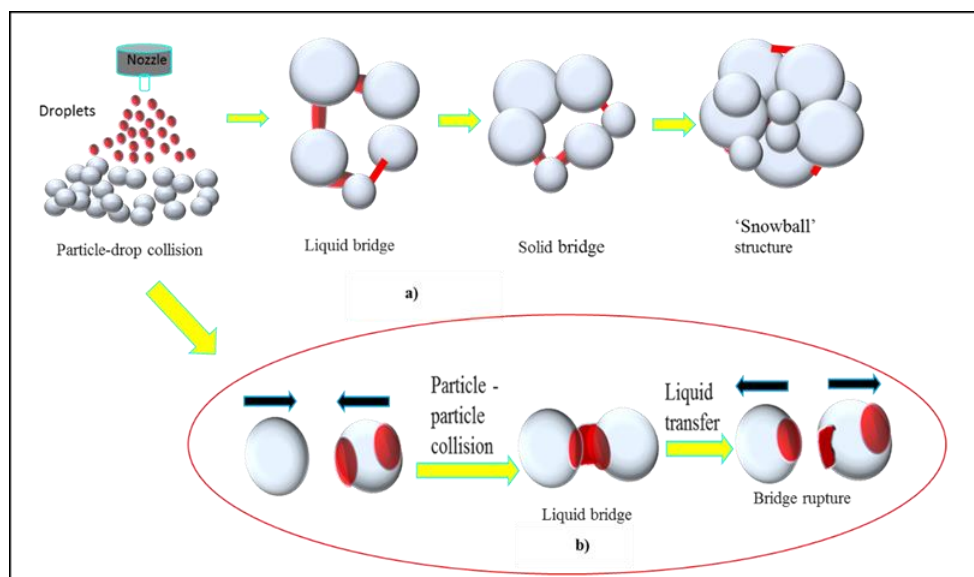
Figure 2.20. Schematic view of different mechanisms between a) granulation/agglomeration process and b) liquid transfer via contact spreading

2.3.2.1 Liquid Bridge Forces

In a wet particle-particle collision, the formation and rupture mechanisms of liquid bridges are important to understand the way liquids disperse through the powder. The liquid bridge consists of a cohesive force (static) due to surface tension and a viscous force (dynamic) due to the relative motion of particles. Based on the amount of liquid added to the system, previous studies claim that different types of liquid bridges can be formed, e.g, pendular (between two equal spheres or different sized particles), funicular (more than two particles with higher amount of interstitial liquid with some voidage) and capillary (more particles with all interstitial spaces filled with liquid, and thick liquid layers around the particles) as illustrated in Figure 2.21 (Zhou *et al.,* 2013). Most of the liquid bridging occurring in coating systems is found to be in the final capillary state (Wright and Raper, 1998).
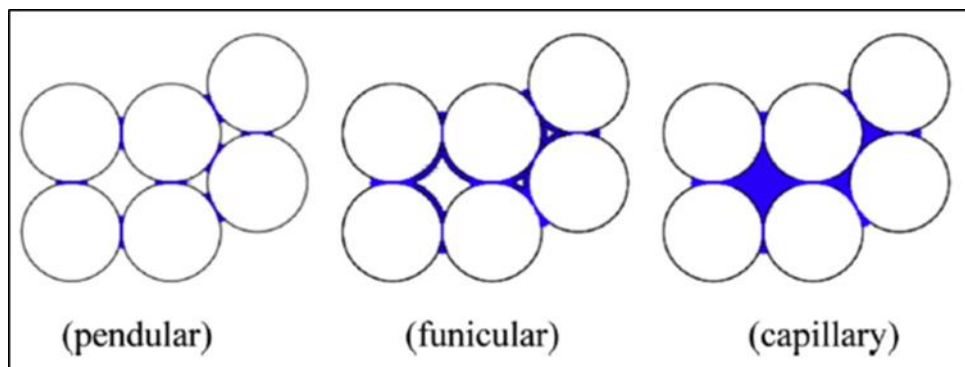
Figure 2.21. Different states of liquid bridging based on the amount of liquid in the system. Source: Zhou *et al.*, (2013).

Figure 2.22 illustrates that under static conditions, the cohesive force between the two spherical particles is caused by the surface tension and pressure difference due to the curvature of the air-liquid interface. Fisher, (1926) was the first to calculate this cohesive force by using the toroidal approximation and assumed that both sets of curvature are circular and shown in Eq. 2.9. The first term on the right-hand side of the equation refers to the pressure difference across the air-liquid interface and is described by the Young-Laplace equation as shown in Eq. 2.10, while the second term arises from the surface tension of the liquid:

39

$$F_l = \pi r^2 \gamma \left(\frac{1}{r_1} + \frac{1}{r_2}\right) + 2\pi r_2 \gamma \qquad \textbf{(Equation 2.9)}$$

$$\Delta p = \gamma \left(\frac{1}{r_1} + \frac{1}{r_2}\right) \qquad \textbf{(Equation 2.10)}$$

where γ is the surface tension of liquid, and r_1, r_2 are the radii of curvature of the liquid bridge surfaces.
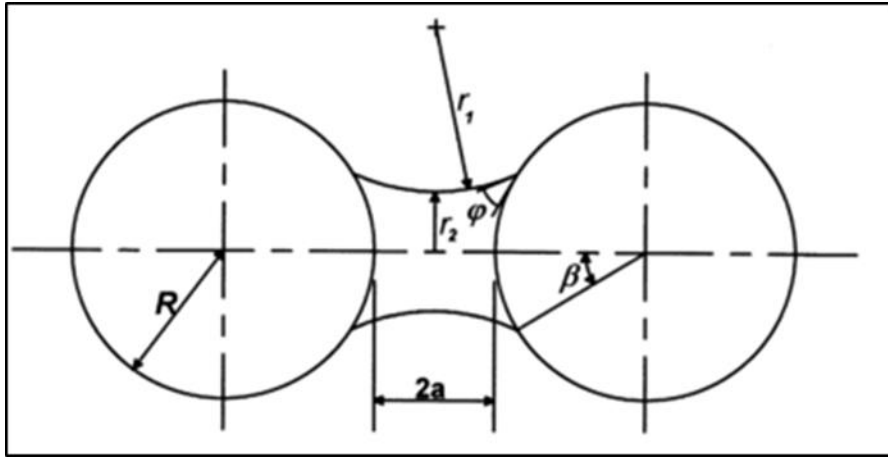
Figure 2.22. Liquid bridge between two equal spheres where a = half particle separation. Source: Lian *et al*., (1993).

Based on lubrication theory, which simplifies particle-particle adhesion by a dynamic pendular liquid bridge as an adhesion mechanism between two particles coated with a thin liquid film, the dissipative viscous force can be divided into two components: the normal and tangential viscous force as shown in Eq. 2.11 - 2.12 (Nase *et al*., 2001):

$$F_{v,n} = 6\pi\mu v_n R^* \frac{R^*}{S} \qquad \textbf{(Equation 2.11)}$$

$$F_{v,t} = \left(\frac{8}{15}\ln\left(\frac{R^*}{S}\right) + 0.9588\right) 6\pi\mu R^* v_t \qquad \textbf{(Equation 2.12)}$$

Here, $\qquad \frac{1}{R^*} = \frac{1}{R_1} + \frac{1}{R_2}$

where μ is the liquid viscosity, v_n, v_t are the normal and tangential components of the relative velocity between particles, R_1 and R_2 are the particle radii, and S is the separation distance. Most of the previous modelling works have neglected the tangential component of the viscous force for simplicity (Hsiau and Yang, 2003; Washino *et al.*, 2017).

Numerous studies on the liquid bridge force between particles have been carried out experimentally and numerically. For example, Mazzone *et al.,* (1987) investigated the rupture behaviour of the pendular liquid bridge and found that the shape of the liquid bridge was different and stronger as compared to the stationary condition. This indicates that models developed based on the static liquid bridge are not fit to be used for a dynamic liquid bridge. Ennis *et al.,* (1990) determined the normal viscous force by oscillating the particles relative to one another and found that at a capillary number, *Ca*, less than 10^{-3}, the static force dominated while at a *Ca* of more than 10^{0}, the viscous force dominated the liquid bridge force. Lian *et al.*, (1993) point out that after the collision, the liquid bridge ruptured when the critical separation distance, S_c, was greater than the rupture distance and conclude that S_c is proportional to the cube root of the liquid bridge volume, V_b, (Eq. 2.13). In the equation, $\varTheta$ is the solid-liquid contact angle in radians.

$$S_c = (1 + 0.5\theta)V_b{}^{1/3} \qquad \text{(Equation 2.13)}$$

Capillary number, as well as Bond number, are non-dimensional numbers used to characterise and map the behaviour of the system based on forces involved in the liquid bridge (Boyce *et al.*, 2017b; Donahue *et al.*, 2012; Ennis *et al.*, 1990). The bond number in Eq. 2.14 represents the ratio of the surface tension to the gravitational force, while the capillary number (Eq. 2.15) is the ratio of viscous to surface tension forces:

$$Bo = \frac{6\gamma}{\rho g D^2} \qquad \text{(Equation 2.14)}$$

$$Ca = \frac{\mu v_c}{\gamma} \qquad \text{(Equation 2.15)}$$

where g is the acceleration due to gravity, ρ is the particle density, D is the particle diameter, v_c is the characteristic collision velocity, μ is the viscosity and γ is surface tension. To determine the characteristic collision velocity, v_c, previous studies have used different methods depending on the coating systems used. For instance, in a fluidised bed system, v_c is chosen based on the terminal velocity of the particle or based on the bubble rise velocity (Ennis *et al.*, 1991; Boyce *et al.*, 2017a). However, in a tumbling drum system, v_c is based on the maximum collision velocity (ωD) (Ennis *et al.*, 1991; Iveson and Litster, 1998).

The influence of liquid bridges on the dynamic behaviour of a moving tablet colliding with a stationary tablet has been investigated by Song and Turton (2007) by incorporating a viscous liquid force model into DEM simulations. The parameters used for this were determined using high-speed videos of tablet collisions, where the tablets had been coated with different viscosities of thin liquid films at their surfaces. As a result, it was shown that the viscous force governs the capillary force for liquids with high viscosity and a linear relationship between S_c and viscosity has to be used in order to match the simulation and experimental results. Additionally, when only one surface is wetted with a very high liquid viscosity, liquid bridges could not be formed due to the short contact time for a single collision event.

2.3.2.2 Effect of Liquid Bridge on Bed Hydrodynamics

In recent years, there has been an increasing amount of literature on the behaviour of wet particles in tumbling drums and fluidised beds caused by liquid bridges. For example, a particulate flow taking into account the adhesive force which arises from capillary forces and surface tension effects due to the liquid bridge has been modelled by Muguruma *et al.*, (2000) using DEM. This study ignored the viscous effects of the liquid bridge, and the findings indicated that the motion of particles in a centrifugal tumbling granulator is largely affected by adhesion forces. In addition, they also compared the calculated components of the particle velocities with experimental measurements, and the results showed good agreement. Similar findings were observed by Liu *et al.*, (2013a)

and McCarthy, (2003) where the capillary force reduced the mixing performance in the drum.

Jarray *et al*., (2018) found that higher capillary forces between the particles decrease the width of the flowing region and the velocity of the particles at the free surface. Liao, (2018) and Chou *et al*., (2010) demonstrated that the liquid viscosity induced segregation due to the formation and rupturing of liquid bridges in a rotating drum. Moreover, the diffusive process observed in axial motion is described by Fick's law, where the particle diffusivity decreased with an increase in inter-particle cohesion and drum fill level, but increased with the drum rotation speed (Liu *et al*., 2013b).

For wet particle behaviour in a fluidised bed, Song *et al.,* (2017) found that when a small amount of liquid was added, the particles began to agglomerate and the bubbles became gas channels. Girardi, (2016) simulated the behaviour of wet particles using CFD-DEM and found that stronger capillary forces led to larger agglomerates being formed, thus a higher fluidisation velocity is needed to support the particles. A similar method has been used by Boyce *et al.,* (2017b) and they found that the minimum fluidisation velocity and the defluidised bed height both increased with the Bond number (Bo) due to inter-particle cohesion and inhomogeneity of the flow structures. He *et al.,* (2014) simulated the particles with and without liquid bridges in a bubbling fluidised bed and reported that the mixing of the dry system was quicker compared to the wet system and the mixing process took more time as liquid volume increased.

In both systems, when a small amount of liquid is added, the formation and rupture of agglomerates seem to have a strong impact on bed hydrodynamics. Thus, previous studies have characterised the agglomerate behaviour to assist in the scale-up of the coating process.

2.3.2.3 Agglomerate Behaviour

An understanding of the coalescence or rebound after the collision of primary particles is important to understand the behaviour of agglomerates (formation, growth and breakup). It can be summarised that there are three modelling approaches to describe the coalescence of wet particles; assume that capillary forces contribute significantly and neglect the viscous force, assume the viscous forces dominate and neglect the capillary force (Ennis *et al*.,1991), or assume both forces contribute significantly and both forces need to be considered (Darabi *et al*., 2009). It is reported that the coalescence of particles depends on the balance between the rupture energy of the liquid bridges and the kinetic energy of the particle collision particles (Simons *et al*., 1994).

Ennis *et al*., (1991) proposed the Stokes number (St_v) and critical Stokes number (St_c) to study the behaviour of agglomerates in the granulator with a dominant viscous effect. The Stokes number is defined as the ratio of the initial collisional kinetic energy to the viscous dissipation caused by the dynamic liquid bridge as shown in Eq. 2.16:

$$St_v = \frac{4\rho_p d_p U_c}{9\mu} \qquad \textbf{(Equation 2.16)}$$

where μ is the liquid viscosity, U_c is the particle collision velocity, d_p is the particle size, and ρ_p is the particle density. Then, critical Stoke's number, St_c, is a dimensionless number which represents the ratio of the initial collision kinetic energy to the energy dissipated by viscous lubrication forces as follows:

$$St_c = \left(1 + \frac{1}{e_r}\right) \ln\left(\frac{h_b}{h_a}\right) \qquad \textbf{(Equation 2.17)}$$

where e_r is the particle coefficient of restitution, h_b is the thickness of the coating layer and h_a is a measurement of the particle asperity height. According to this model, if the St_v < St_c, the two particles will coalesce (collision success), while if $St_v > St_c$, the particles will rebound, regardless of whether it is a normal particle-particle or oblique particle-wall collision (Kantak *et al*., 2005).

Other studies by Donahue *et al*., (2010) have applied St_v to attempt to predict the sticking or rebound behaviour of the collisions between two or three particles. Recent studies also have found that apart from the Stokes number, other dimensionless numbers can be applied to describe agglomerate behaviour. For instance, Boyce *et al*., (2017a) found that agglomerate growth required a high Bond number (ratio of surface tension forces to the gravitational forces) and low capillary number, where the capillary number here is defined as a ratio between the collisional and liquid bridge formation timescales. Even though many studies have reported on the agglomerate behaviour at the micro- and macro-scale level, there is a still lack of knowledge on how the formation and rupture of these agglomerates (liquid bridges) could influence the liquid distribution in both systems during the coating process.

2.3.2.4 Modelling and Measurement of Liquid Transfer

The first study incorporating a model for liquid transfer in DEM simulations was reported by Shi and McCarthy, (2008). The results indicated that liquid transfer through contact spreading is significant. The study performed numerical simulations of liquid transfer between particles in a rotating drum. The model was based on liquid bridges that form between two particles and included cohesive and viscous forces and the redistribution of liquid by the bridge rupture. This work aimed to determine the liquid bridge volume formed upon impact between two heterogeneous particles and to define liquid redistribution upon rupture of bridges. To achieve this, they made two assumptions. Firstly, the liquid bridge formed is composed of liquid from both contacting particles and is composed of the assembled liquid on the surface of a spherical cap near both contact areas (this volume can be used to calculate the capillary force and critical separation force, S_c). Secondly, the liquid bridge rupture at S_c is assumed to occur at the thinnest section, and it was these two 'halves' of the liquid bridge that were used to determine the redistribution of the liquid (Figure 2.23). Furthermore, the model was coupled with DEM simulations and, as a result, the model found that mass coating variability, CV_m, was inversely proportional to the square root of the coating time when the ratio of capillary force to particle weight, Bo_g, was less than 1. They also predicted that CV_m increases linearly with the square root of coating time when Bo_g was greater than 1.
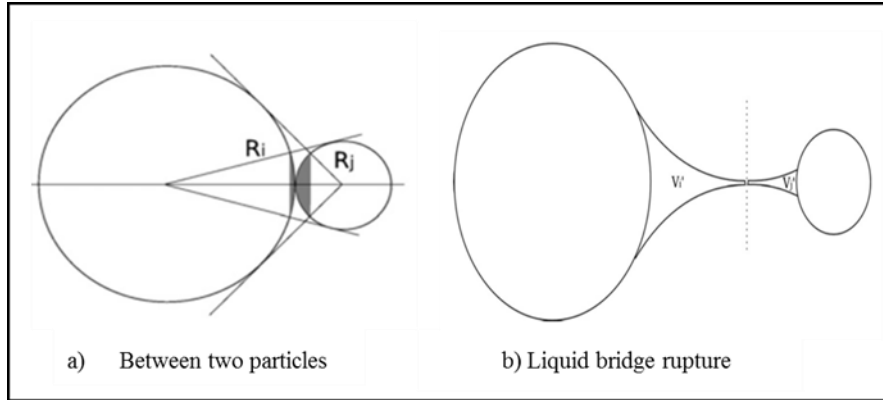
Figure 2.23. Schematics of: a) spherical cap contributing to liquid bridge between two particles, b) liquid bridge rupture at thinnest section. Adapted from Shi and McCarthy, (2008). Note: R_i: radius particle i; R_j: radius particle j; V_i: liquid bridge contribution from particle i; V_j: liquid bridge contribution from particle j.

In contrast to Shi and McCarthy, (2008), Darabi *et al*., (2010) performed computational fluid dynamics (CFD) simulations and developed a simplified mathematical model to predict the shape evolution, rupture distance, and liquid distribution of stretching liquid bridges between two equal-sized solid spherical particles with the same contact angle. They concluded that for a simplified model, several assumptions must be made. For instance, it was assumed that the surface tension effects dominate the viscous, inertial and gravitational effects and that the bridge has a parabolic shape. Nevertheless, for the CFD simulations, all the effects mentioned above were considered. As a result, both models showed good agreement, though the numerical simulations provided better results. In addition, the effects of contact angle and gravity were also investigated on liquid distribution with the aid of numerical simulations, and it was shown that more liquid is transferred to the particle with the smaller contact angle. The liquid transfer fraction increased as the Bond number, Bo_g or liquid bridge volume increased.

Mohan *et al.,* (2014) numerically studied the effects of four different liquid transfer models (Figure 2.24) on liquid spreading upon inter-particle collisions in sheared particle beds. The liquid transfer in Model A was assumed to occur when particle surfaces are in contact, similar to heat conduction between particles. Model B1 proposed the liquid transfer to occur immediately when in contact, based on the spherical cap assumption by Shi and McCarthy, (2008). Model B2 was similar to B1 but considered the re-distribution

46

of liquid caused by the formation and rupture of the liquid bridge. Model C was similar to Model B2 but considered there was a limited liquid exchange rate between the contact of the coating layer. This study concluded that the fraction of liquid flowing into the bridge was the main key to the liquid transfer rate. Furthermore, the study suggests that the best model, Model C, could be further improved by considering the initial liquid bridge volume (assumed zero in this work) or wetting effects since the rate of liquid spreading is also controlled by the dynamics of wetting.
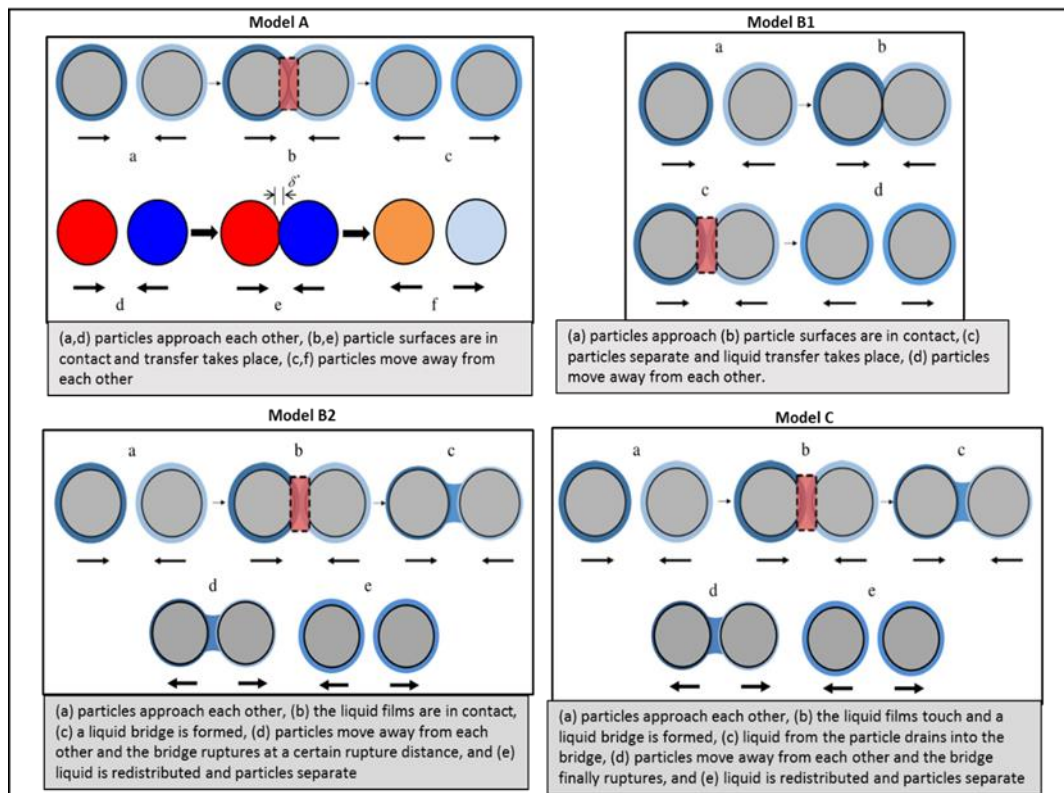
Figure 2.24. Schematic view of liquid transfer based on four different liquid transfer models. Adapted from Mohan *et al.,* (2014)

Given all the above, the assumption used in these models is that the particle surface is always uniformly coated with a thin liquid layer after contact. However, this assumption may not be suitable for hydrophobic particle surfaces and higher viscosities which produce a lower rate of liquid spreading. Thus, a new contact model has been proposed by Washino *et al.,* (2016) to investigate the liquid transfer considering a partial wetting of the particle surface upon contact using discrete element method (DEM). In this model, each of the particle surfaces are subdivided (Figure 2.25) and it is assumed that

the liquid transfer will only occur at these points and are tracked with time. This model was applied to simulate the spray drum system and it was then compared with the results from the Shi and McCarthy, (2008) study. It was found that the Shi and McCarthy model was valid only for lower viscosities while the Washino model was valid for both low and high viscosities.
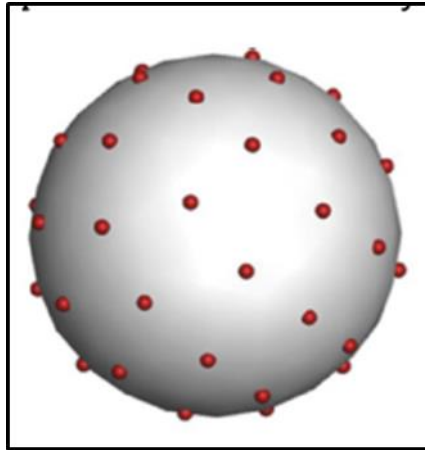
Figure 2.25. Sub-divided particle surfaces in the Washino model; red dots represent the centre of the sub-divided surface. Source: Washino *et al.,* (2016).

Until now, previous studies have only studied the liquid transfer mechanisms using modelling techniques (DEM, CFD, DEM-CFD) and future studies should seek to understand these dynamics experimentally in the coating system, where agglomerates might be formed during the coating process, and this is believed to also influence the liquid transfer mechanism via contact spreading.

2.4 Characterisation of the coating layer

There are two different types of coating quality to consider; (i) intra-particle uniformity which relates to the homogeneity of the coating layer on single particles, and (ii) inter-particle uniformity, which describes the coating homogeneity between different particles within one batch (Tobiska and Kleinebudde, 2003). The coating uniformity can be characterised based on the mass distribution, thickness or morphology of the coating

material (Turton, 2008), which depends on the purpose of the coating, and the mass distribution has been reported abundantly.

Both parameters are typically quantified using a relative standard deviation, or coefficient of variation, CoV (Sahni and Chaudhuri, 2011) and smaller values (i.e. higher coating uniformity) are desired for production coating processes. In some studies, intra-particle uniformity has been defined as the ratio of film thickness to the mean film thickness over the tablet's surface (Freireich *et al.*, 2015). Inter-particle coating variability has been defined in other work as the *CoV* of the coating mass between particles and is shown in Eq. 2.18 (Kumar and Wassgren, 2014);

$$CoV_{inter} = \frac{\sigma}{\bar{m}}$$ **(Equation 2.18)**

where average coating mass, $\bar{m}$, and its corresponding standard deviation, σ, are given, respectively, by Eq. 2.19 - Eq. 2.20:

$$\bar{m} = \frac{1}{N}\sum_{i=1}^{N} m_i$$ **(Equation 2.19)**

$$\sigma = \sqrt{\frac{1}{N}\sum_{i-1}^{N}(m_i - \overline{m})^2}$$ **(Equation 2.20)**

In Eq. 2.19 and Eq. 2.20, m_i refers to the coating mass on the *i*'th particle and *N* is the total number of particles in the bed.

In past studies, the characteristics of coating layers have been determined by multi-technique approaches. The simplest method reported was based on weight gain of the particles during coating (Abe *et al.*, 1998). The coating mass is obtained from the mass difference before and after the coating process. Sudsakorn and Turton (2000) evaluated the coating uniformity based on the amount of dyed coating material deposited on different particle size fractions. It was conducted by dissolving a coated particle in a known amount of water to determine the blue dye intensity using a spectrophotometer.

Other characterisation techniques have also been reported such as digital imaging (Mozina *et al*., 2010), X-ray tomography (Perfetti *et al.*, 2010; Sondej *et al*., 2016), terahertz pulsed imaging (TPI) (Ho *et al*., 2007; Maurer and Leuenberger, 2009), confocal laser scanning microscopy (CLSM) (Sondej *et al*., 2016), and scanning electron microscopy (Heinämäki *et al*., 1997).

However, the aforementioned methods do not adequately characterize the overall coating quality for each batch, e.g. inter-particle coating variability, which is a major concern, for example, in coating bioactive ingredients. There have been studies which have reported the methods for quantifying inter-particle coating uniformity within a batch of particles coated in tumbling drums and fluidised beds. For instance, a study by Li *et al*., (2013b) used a combination of weight gain and nuclear magnetic resonance (NMR) to determine the coating amount of one hundred coated particles. Here, NMR analyses were carried out by measuring a specific component in the coating solution. Dubey *et al.*, (2011) applied laser induced breakdown spectroscopy (LIBS) to investigate the influence of speed, loading and spray pattern on tablet coating uniformity in a pan coater and validated the results obtained using discrete element method (DEM). Kennedy and Niebergall, (1997) developed an image analysis system to evaluate the inter-particle coating uniformity based on the standard deviations of individual particles generated from the optical density data. Romero-Torres *et al.,* (2005, 2006) evaluated the feasibility of using Raman spectroscopy to determine inter-tablet coating uniformity. The findings indicated that this method is a simple and robust technique to quantitatively characterise the coating variability and coating thickness. Depypere *et al.,* (2009) have used confocal laser scanning microscopy (CLSM) to quantify the coating thickness and quality of protein coated microparticles produced in a fluidised bed. Table 2.3 summarises the inter-particle coating uniformity characterisation methods, including their advantages and disadvantages.

Although many of these techniques have proven to be able to determine the inter-particle coating uniformity, there are some drawbacks such as:

(i)   small number of particles that can be analysed within a reasonable time frame

(ii)   large-sized particles and/or high amounts of coating material required

(iii)   time-consuming sample preparation

(iv)   destructive techniques (e.g. LIBS).

Thus, a new, better method of quantitative analysis is required to determine the inter-particle coating variability which could contribute to a higher product quality of the coated particles.

To achieve final product uniformity and increase the process reliability in tumbling drum and fluidised bed coaters, a number of experimental and numerical investigations have focused on operating parameters (e.g. drum speed, fluidisation velocity, fill level) and particle properties (e.g, size, shape, hardness) which affect inter- and intra-particle uniformity (Werner *et al.*, 2007b; Suzzi *et al*., 2010; Sahni and Chaudhuri, 2012; Toschkoff and Khinast, 2013). Moreover, coating uniformity in drum and fluidised bed coaters is also influenced by particle mixing and flow and understanding both will aid in increasing the final product quality.

Ideally, particles should be exposed to the coating region or spray zone at the same rate to ensure coating uniformity. However, this is almost impossible to achieve in practice. To improve this, a balance must be achieved between the movement of particles within the coating systems, the frequency or average number of passes a particle makes through the spray zone, the duration of the particles in the spray zone, the orientation towards the spray nozzle and the rate of spray applied with the operating conditions (Kalbag *et al.*, 2008; Kalbag and Wassgren, 2009).

Table 2.3. Techniques used to characterise the inter-particle coating uniformity

Technique	Information	Advantages/ Disadvantages	Reference
Nuclear magnetic resonance (NMR)	• ~ 100 sample particles randomly selected for analysis • Specific component for each coating solution of each sample is measured	<u>Advantages</u> • Suitable for relatively large tablets ~ 1mm <u>Disadvantages</u> • Need large amount of coating material • Expensive technique	(Li, *et al.*, 2013b)
Laser-induced breakdown spectroscopy (LIBS)	• Twenty tablets from each batch were randomly selected for analysis • Based on atomic emission from the particle surface using a laser	<u>Advantages</u> • Minimal sample preparation <u>Disadvantages</u> • Restricted to certain amounts of sample • Sample destruction	(Dubey *et al.*, 2011)
Image analysis	• ~ 221 sample size used for analysis • Samples are captured using a digital camera and images are imported to the software, which allows the measurement of optical densities of individual particles	<u>Advantages</u> • Low cost • Large sample size can be evaluated • Rapid measurement <u>Disadvantages</u> • Limited in particle size for analysis	(Kennedy and Niebergall, 1997)
Raman Spectroscopy	• Used a combination of a revolving laser focus with partial least square (PLS) multivariate spectrochemical analysis	<u>Advantages</u> • Minimal sample preparation • Rapid and non-destructive <u>Disadvantages</u> • Provides information biased to the surface of the coating	(Romero-Torres *et al.*, 2005, 2006)
Confocal laser scanning microscopy (CLSM)	• ~50 microparticles are used for analysis • Able to optically section the microparticle at any desired position • a combination with image analysis allows for quantitative measurement of coating thickness	<u>Advantages</u> • Non-destructive • Rapid measurement <u>Disadvantages</u> • Restricted to small particle size ~200 µm	(Depypere *et al.*, 2009)

2.4.1 Inter-particle coating variability: Effect of process parameters

Qualitative information regarding the effect of drum speed on residence times and coating duration, and fill level, particle shape, size and spray rate on inter-particle coating variability are available in the literature. Studies by Tobiska and Kleinebudde, (2001) and Sandadi *et al*., (2004) reported that the residence time under the spray decreases as the pan speed and fill load increases. In contrast, Kalbag *et al*., (2008) and Denis *et al*., (2003) reported that the pan load does not affect the average residence time per pass. Studies by other researchers suggested that inter-tablet variability decreases with increased drum speed and fill level (Dubey et al., 2011) and axial mixing was found to be the most important parameter. In contrast, Chang and Leonzio, (1995) did not observe any distinct trends regarding the drum speed and the inter-tablet variability, and it was suggested that this was due to spray drying and coating transfer effects.

Compared to drum speed and fill level, not much work has been conducted to quantify the effect of spray characteristics on coating variability. Dubey *et al*., (2011) reported that coating variability was also affected by the fill level and spray patterns used; full surface spray and symmetric band spray produced much lower coating variability than ellipse and circular design patterns. In contrast, Pandey *et al*., (2006) mentioned that spray shape did not significantly affect the process, but an increase in the spray area led to lower coating variability. A study by Brock *et al*., (2014) revealed via the design of experiment (DoE) model that coating uniformity was beneficial at low drum load, high drum speed, low spray rate and high run duration. In addition, results also demonstrated that terahertz pulsed imaging (TPI) was a good method to measure inter-tablet uniformity and to evaluate critical process parameters (CPP) in an active pan coating process. In a process that involves perforated coating pans, the main parameters of interest are the fill level, the size and shape of the tablets, the rotation speed and the presence and shape of baffles (Kalbag *et al*., 2008). However, one of the most important parameters, the drum size, has not been studied in detail.

In a fluidised bed, the quality of the coated particles is largely affected by the spray characteristics and the particle motion (Vanderroost *et al*., 2011). Atarés *et al.,* (2012) used confocal laser scanning microscopy (CLSM) to quantify the coating

thickness and found that the coating thickness was affected by the particle size. A smaller particle size gave higher coating thicknesses because smaller particles can be fluidised more and move faster, compared to larger particles. Cheng and Turton (2000) reported that the inter-particle variability of coated particles was mainly due to variability in the amount of coating liquid deposited on particles in the spray zone.

It can be summarised that for both coating systems, numerous studies have related the inter-particle coating uniformity with the spray characteristics. The fraction of the particles in the spray zone compared to the whole system is considered small, and there might also be liquid transfer happening during the phase before particles re-enter the spray zone (outside the spray zone) and this might be also contributing to the coating uniformity of the final product. However, so far there is no experimental work reported in the literature regarding this mechanism, and work in this area could be very beneficial to industries which use coating techniques.

2.5 Summary

A number of theoretical and experimental studies have investigated the spray coating process in fluidised bed and tumbling drum coating systems. In wet coating systems, the distribution of the liquid amongst the particles in the system is important as the liquid is only sprayed at discrete points (top, bottom or tangential spray). Most of the studies have focused on liquid distribution via droplet deposition and spreading mechanisms at the micro- and macro-scale levels. This mechanism occurs in the spray zone, a small area compared to the whole system. When the particles travel from this area to the bulk particle bed, the wet particles will move through the bed, and liquid transfer may occur from wetter to drier particles. So far, the mechanism of liquid transfer between the wet collisions has been reported numerically. However, future experimental studies are needed to understand this mechanism.

The formation of agglomerates has also been investigated. This occurs mainly at initial stage of the coating process and has a strong impact on bed hydrodynamics.

However, no study has reported on how it impacts on liquid distribution in the system. Collision behaviour between granules can be predicted based on the liquid bridge forces formed by using the viscous Stokes number and other dimensionless numbers such as Capillary number (Ca) and Bond number (Bo). This thesis aims to contribute to our knowledge on the liquid distribution in a fluidised bed and tumbling drum coater via collisions of particles or in terms of the contact spreading mechanism. In addition, the liquid transfer via the contact spreading mechanism will also be related to the coating uniformity of the final coated particles.

Moreover, many techniques have been identified to quantify the inter-particle coating uniformity. However, each technique has its own drawbacks, such as the limitation in number of samples which can be analysed within a small-time frame. Many are also time consuming and cause damage to the sample. Thus, a new, improved method of quantitative analysis is required to determine the inter-particle coating variability of the product.

CHAPTER 3

3 Materials and Methods

In this study, different types of coating equipment have been designed to investigate the coating of particles via the contact spreading mechanism. In addition, the liquid spreading behaviour in the coating system is determined quantitatively by using a novel image analysis system set-up based on colorimetric measurement. This technique allows for the quantitative and qualitative determination of coating uniformity within a batch of particles. This chapter outlines details of all materials used, their characterisation, and the experimental procedures employed throughout this study. The development of the new colorimetric image analysis system with which to quantify coating behaviour will be described in following chapter (Chapter 4).

The first experimental method used a tumbling drum to study the contact spreading behaviour (Chapter 5). The second experiments were carried out in a small-scale fluidised bed with a spray system to observe the contact spreading behaviour in a different coating system (Chapter 6). Finally, the third experiments were carried out in the same fluidised bed system used in second experiments but without the spray system (Chapter 7). Here, a similar method to tumbling drum experiments (Chapter 5) was used and the objective was to study the different method of liquid supply (spray and pre-coated particles methods) to the fluidised bed system on contact spreading mechanism.

3.1 Particles

In this study, alumina particles were used to study the liquid distribution via contact spreading using three different coating techniques: tumbling drum (no spray) and fluidised bed (no spray and spray system). This section gives details of the particles used, their properties and their methods of characterization. For each of the experiments, alumina particles supplied by Anderman Ceramics Ltd, United Kingdom, were identified as the model particulate material. Images of the particles are shown in Figure 3.1. This

material was selected as a model material due to its properties; non-porous, good flowability, spherical shape and white in colour. A non-porous material is important in this study to avoid any liquid ingress into particles during coating, which could influence the coating behaviour and subsequent analysis of the coating layer on the particle surface. A flowable material was used to reduce the cohesive effect during experiments when the coating liquid is introduced into the coating system which could change the mixing behaviour. In addition, the material should be in white colour which is preferable for subsequent colorimetric image analysis.

Figure 3.1 Images of alumina beads

3.1.1 Particle Size Distribution

Two methods were used to determine the particle size distribution (PSD) of the alumina particles; sieving and dry cell laser diffraction (Malvern Mastersizer 3000, Malvern Instruments Ltd., UK). The PSD of the alumina particles was initially measured by sieving to obtain a size distribution based on mesh size. The dry sieving method (preferable for a size range 40 μm to 125 mm) with a vibrator sieve shaker (Retsch Sieve Shaker AS 200 Basic, Germany) was used to divide the samples into size fractions and their weight fraction. During sieving, the samples are thrown upward by the vibration from the sieve bottom and fall back down due to gravitational force. Here, an electromagnetic drive sets a spring/ mass motion and transfers the oscillations to the sieve stack, and the oscillation height of the sieve bottom is determined by the amplitude set-up. The relative movement between the samples and the sieve will spread the samples

uniformly across the sieve area. Depending on individual particle size, particles either pass through the sieve mesh or remain on the sieve surface. The possibility of the samples passing through the sieve is determined by the ratio of the sample size to the mesh size, the orientation of the particles and the number of encounters between the particles and the mesh openings.

The sieving method is based on equivalent sphere diameter, which is the diameter of a sphere passing through the same sieve aperture. This gives a mass distribution and a size which is known as the sieve diameter. The sieve diameter is dependent on the maximum width and thickness of the particles since the length does not hinder their passage through the sieve apertures. However, if the particles are extremely elongated, they may still remain on sieve surface even after an extended vibration time (Wills and Finch, 2016). However, in this case, where the particles are spherical, this method should give an accurate and realistic determination of the size distribution.

Approximately 40 g of the particles were sieved using a stack with a mesh sieve size of 1.18 mm to 750 µm at an amplitude of 1.5 mm / g for 3 min. Prior to and after analysis, each sieve and bottom pan was weighed, and the mass recorded. The retained sample weight and its percentage for each sieve were determined using Eq. 3.1 and Eq. 3.2:

$$\boldsymbol{w_3 = w_2 - w_1} \hspace{4cm} \textbf{(Equation 3.1)}$$

$$\textbf{\% retained sample on each sieve} = \boldsymbol{w_3/w \times 100} \hspace{1cm} \textbf{(Equation 3.2)}$$

where w is the initial sample weight, w_1 is the weight of empty sieve, w_2 is the weight of sieve and w_3 is the retained sample weight.

A frequency distribution was derived from the sieve analysis data. It was measured by dividing the mass fraction of particles on that particular sieve size with the width size of the sieve intervals and multiplied by 100 to get % frequency (Appendix A1).

Figure 3.2 gives the frequency distribution by mass of discrete size intervals against the midpoint of the interval size for the alumina particles by sieving analysis. It indicates a narrow unimodal distribution with a size range of approximately from 850 to 1200 µm.
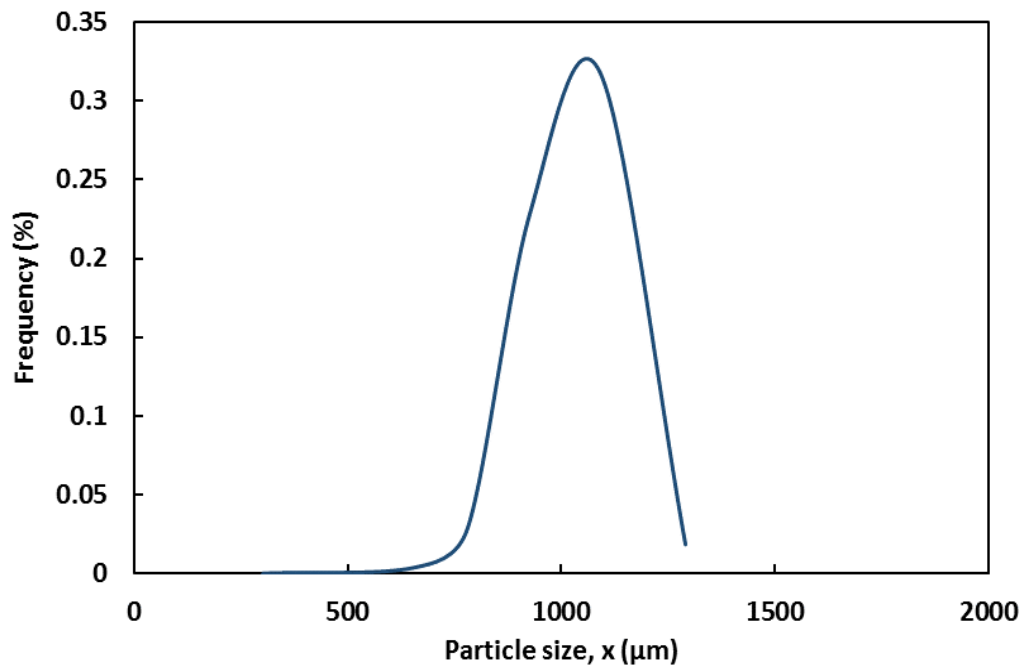
Figure 3.2. Size distribution of alumina particles determined by a sieve shaker

Following from the sieve analysis result, a dry dispersion laser diffraction (Malvern Mastersizer 3000, Malvern Instruments Ltd., UK) analysis was further conducted to determine the volume size distribution of the particles. This equipment was connected to a dry particle feeder and the size distribution of the sample was monitored during each measurement until successive readings became constant. This static light scattering technique consists of three main elements: optical bench, sample dispersion units and instrument software as shown in Figure 3.3.
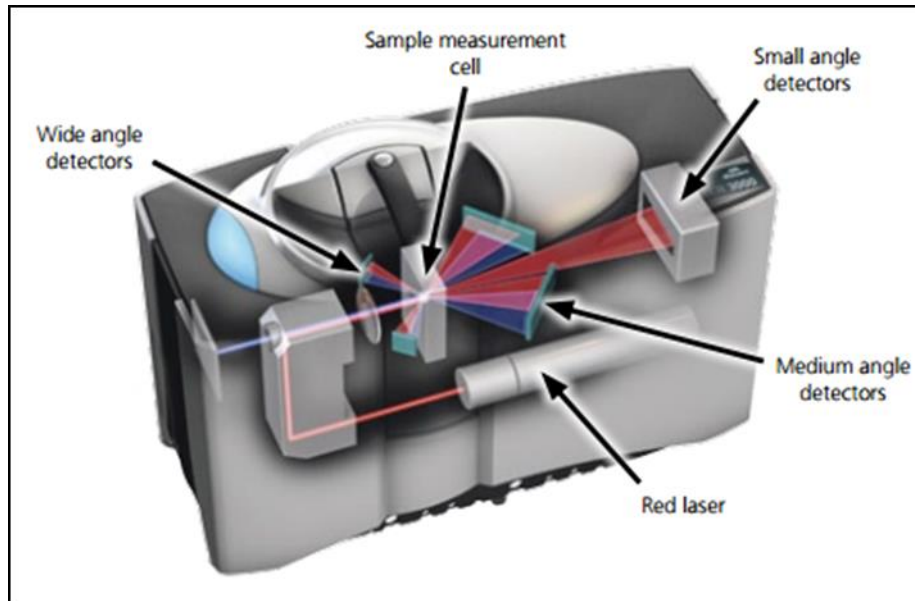
**Figure 3.3. Schematic view of the laser diffraction instrument
(Malvern Instruments, 2012)**

The particle size distribution obtained using this technique is based on measurement of the angular variation in the intensity of light scattered as a laser beam passes through a dispersed particulate sample (Malvern, 2012). As illustrated in Figure 3.4, the diffraction angle is inversely proportional to the particle size; large particles scatter at small angles, whereas small particles scatter at large angles. A series of detectors then accurately measure the intensity of light scattered by the particles. Eventually, the intensity data is analyzed using the Mie theory to calculate the particle size distribution, assuming a volume equivalent sphere model. For this theory, knowledge of optical properties (refractive index, RI, and imaginary component) of both the dispersant and the sample being measured are required. These data can be found either from published data, listed in the software library or can be directly measured.
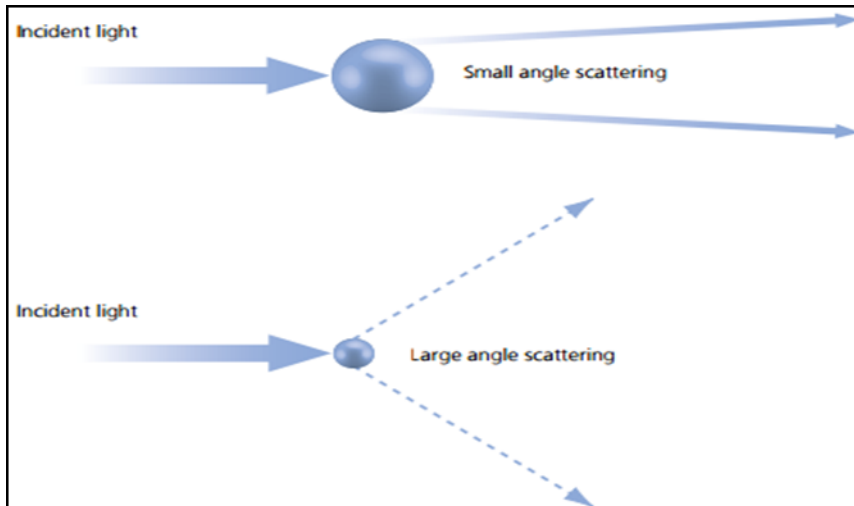
Figure 3.4. Laser diffraction principle: Scattering of light from small and large particles (Malvern Instruments, 2012)

The contribution of each particle in the distribution relates to the volume of that particle (equivalent to mass if the density is uniform). The results obtained from laser diffraction are illustrated in Figure 3.5. The size distribution of alumina particles shows a narrow unimodal distribution with the size range from 882 µm (d_{10}) − 1180 µm (d_{90}) and this result was consistent with the sieve analysis result. The size of alumina particles is expressed as $d_{4,3}$ (1020 µm), which is volume moment mean (de Brouckere mean diameter) diameter. The raw particle size data from sieve and laser diffraction can be found in Appendix A1. The alumina size properties from laser diffraction are summarized in Table 3.1.
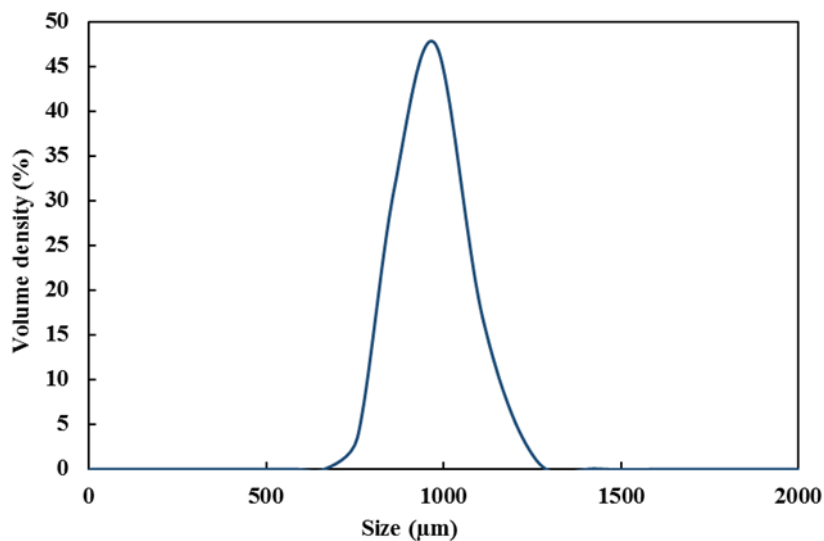
Figure 3.5. Size distribution of alumina particles determined by laser diffraction

Table 3.1. Size properties of the alumina particles obtained via laser diffraction

Properties	Particle size (µm)
$d_{4,3}$	1020
$d_{3,2}$	1010
d_{10}	882
d_{50}	1010
d_{90}	1180
Span	0.290

3.1.2 Particle Density

Here, the methods to determine bulk density, particle or true density and envelope density of the alumina particles are described. Bulk density is defined as mass per unit volume of a loose particle bed. The unit volume includes the interparticle spaces and intraparticle voids. The bulk density was measured based on Eq. 3.3, where the materials were weighed (m_o) and poured into a cylinder and the volume (V_o) was read directly to obtain the bulk density (ρ_B).

$$\rho_B = m_o/V_o \qquad \text{(Equation 3.3)}$$

In contrast to bulk density, true density is defined as mass over the volume of a particle, without considering pores in the particle. The true density was determined by helium pycnometry using an AccuPyc II 1340 Automatic Gas Pycnometer (Micromeritics, Norcross, USA) as shown in Figure 3.6a. Helium pycnometry allows the determination of the true density of powders, porous and irregularly shaped solids without considering the volume occupied by internal or open porosity. The pycnometer operates on the Archimede's principle by detecting the pressure change resulting from gas displacement by a solid sample. The displaced fluid is helium, which can penetrate the finest pores, thereby giving maximum accuracy. A quantity of helium at a known pressure is purged into an empty chamber. Measuring the pressure establishes a baseline. Then, a sample is placed in the chamber, which is resealed. The same quantity of helium is again purged into the sample chamber at the same pressure, and the resulting pressure is measured. The true volume of the sample can be determined by the difference between

the two pressures combined with the known volume of the empty sample. The true density then can be determined based on the known particle mass and true volume of particle measured.

Figure 3.6. Images of AccuPyc II 1340 Automatic Gas Pycnometer

Table 3.2. Densities of the alumina particles

Properties		Value
Density (g/cm^3)	Bulk	2.064
	True	3.62 ± 0.002

3.2 Coating Liquids

In this study, different coating materials were selected to study contact spreading behavior using three different coating techniques. The solutions used were polyethylene glycol (PEG) (Sigma-Aldrich, UK) for the tumbling drum coating system, while hydroxypropyl methylcellulose (HPMC) (Shin-Etsu Chemical Ltd., Germany) was used for fluidised bed coating system. Both of these coating materials were chosen as model coating materials because these materials have been commonly used for coating and agglomeration experiments in previous studies (Chua, *et al*., 2011; Dreu *et al*., 2012; Lee *et al*., 2011; Perfetti *et al*., 2011; Valizadeh *et al*., 2004). Viscosities of both liquids were varied by using the same concentration with a different grade (molecular weight) of PEG and HPMC.

Initially, to compare the contact spreading behaviour in different coating systems (tumbling drum and fluidised bed), the same type of coating solutions were to be used. PEG solutions proved to be a good coating solution for the studies in the tumbling drum system. However, when using PEG for preliminary experiments in the fluidised bed, there was no contact spreading observed even with long mixing times. Figure 3.7 shows the CoV as a function of mixing time for these preliminary experiments in the fluidised bed using a PEG 4000 molecular weight solution. This observation might be due to the fact that the drying rate in the fluidised bed is higher than in the tumbling drum system. Thus, even when increasing the mixing time, no contact spreading occurs. For this reason, the coating solution was changed to HPMC for fluidised bed experiments, where rapid drying was not so problematic with this material. This allowed coating behaviour to be investigated using this equipment.
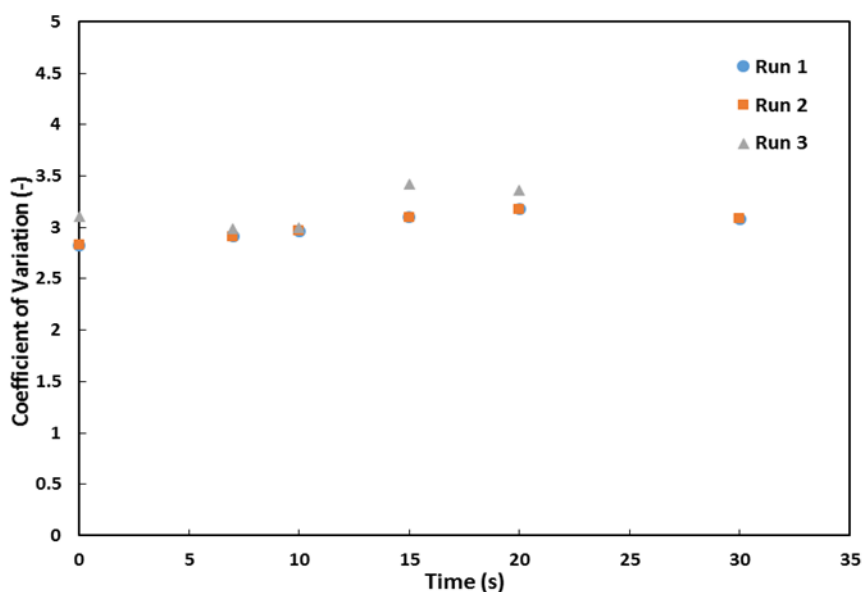
Figure 3.7. Coefficient of variation as a function of time for alumina coated with PEG 4000 in a fluidised bed

Polyethylene glycol (PEG) with different molecular weights (4000, 10000, 20000 and 35000 Da) at the same aqueous concentration (50% wt/wt) were used to investigate the contact spreading behaviour in a tumbling drum. First, acid red (Sigma-Aldrich, UK), 1% wt/wt was prepared to dye the coating solutions to allow for the colorimetric characterisation of the coating layer (see Chapter 4). Then, PEG was dissolved in the dyed

solution with the same percentage of mass (50% wt/wt). Three grades of hydroxypropyl methylcellulose, HPMC (Tylopur 603, Tylopur 606 and Tylopur 615, Shin-Etsu Chemical Ltd., Germany) with molecular weights of 16000, 35600 and 60000 Da, were used to investigate the contact spreading behaviour in the fluidized bed coating system. The HPMC solutions viscosities were varied by using the same concentration (5% wt/wt) with different grades. Acid red (Sigma-Aldrich, UK), 1% wt/wt, was also used to dye the coating solutions to characterize the coating layer (see Chapter 4). The HPMC was dispersed and dissolved first in 1/3 of the required amount of the dye solution, previously heated to > 80 °C using a magnetic stirrer. Then, the remaining cold dyed solution was added while vigorously stirring. The polymer completely dissolves when the temperature of the solutions falls to < 30 °C. The dyed aqueous solutions obtained were then allowed to de-foam and equilibrate at room temperature for several hours before use. The calculations for PEG and HPMC solutions preparation can be found in Appendix A2.

All liquid solutions were analysed to determine their properties; viscosity, surface tension, density and contact angle. The principles and operation of these characterisation methods are discussed in the following sections.

3.2.1 Viscosity Measurements

The viscosities of the solutions were measured using a rheometer (MCR 502, Anton Paar, Graz, Austria) fitted with cone + plate (2 ° cone angle, 50 mm diameter) as shown in Figure 3.8. The liquid is placed between the cone and a bottom fixed flat surface plate after which the torque as a result of the rotation of the cone is measured. In addition, this type of geometry was used so that the shear rate was independent of position for small angles, 2 ° or to ensure that a homogenous shear rate was applied to the sample. A stepped shear rate range between 0.1 and 1000 s^{-1} at 20 °C was used for the analysis. All measurements were repeated three times and the results were averaged.

Figure 3.8. MCR 502 Anton Paar Rheometer

In Figure 3.9, the viscosities of the dyed PEG solutions are plotted as a function of shear rate at a constant temperature of 25 °C. It shows that the solutions generally exhibit Newtonian behaviour, because the viscosities remain constant regardless of changes to the shear rate (although PEG 35000 did show a slight deviation from this behaviour at high shear rate). In addition, the viscosities also increase with an increase in molecular weight with the same concentration of solid PEG used from 137 mPa.s to 15489 mPa.s (Table 3.3). The change in viscosity with different molecular weight HPMC are summarized in Table 3.3. As expected, the viscosity increases substantially with molecular weight. In Figure 3.10, all the three solutions generally evidenced Newtonian behaviour, where the viscosity remained constant as the shear rate increased to 1000 s^{-1}. However, for HPMC 615, the viscosity was observed to decrease slightly at as the high shear rate approached 1000 s^{-1}, but in this work the shear rate is expected to be lower than this. Throughout this thesis, the different coating solutions will be referred to by their viscosity values.
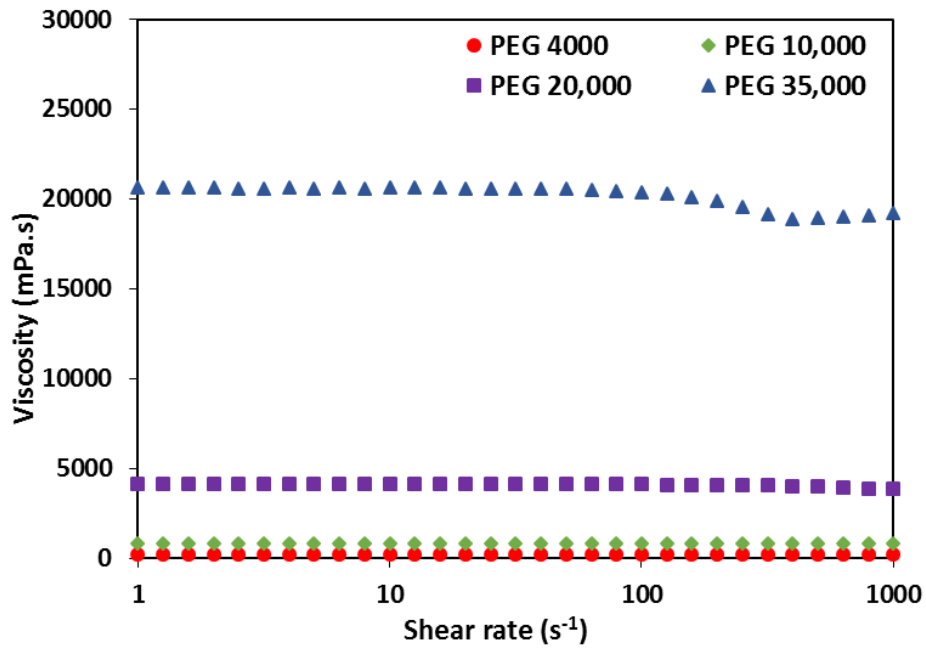
Figure 3.9. Viscosity of PEG solutions as a function of shear rate, shown on a logarithmic axis, at a constant temperature of 25 °C
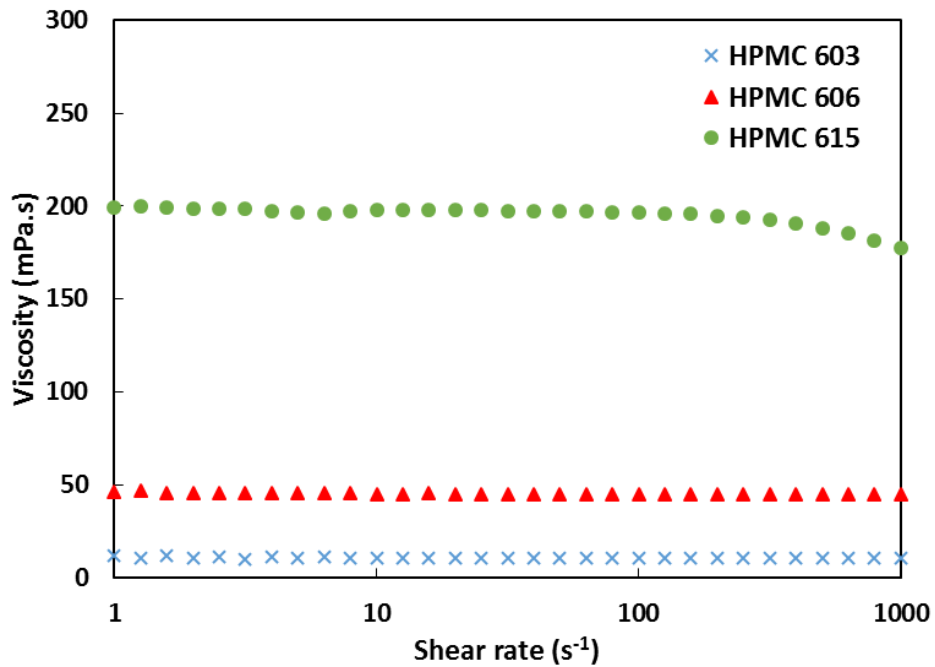
Figure 3.10. Viscosity of PEG solutions as a function of shear rate, shown on a logarithmic axis, at a constant temperature of 25 °C

Table 3.3. Viscosities of coating solutions

Coating Materials/ Molecular weight (Da)		Viscosity (mPa.s)
50% PEG	4000	137 ± 27
	10000	665 ± 90
	20000	3115 ± 496
	35000	15489 ± 3435
5% HPMC 603	16000	11 ± 0.55
5% HPMC 606	35600	44 ± 1.81
5% HPMC 615	60000	177 ± 18.8

3.2.2 Interfacial Tension Measurements

The interfacial tension for PEG solutions/air was measured with a Krüss K10ST tensiometer (Hamburg, Germany), equipped with a platinum plate; the Wilhelmy plate method (performed by Procter & Gamble, UK). The HPMC solutions were measured using a First Ten Ångstroms FTÅ200 goniometer. The interfacial tension measurements were important as interfacial tension will contribute to the liquid bridge formation and wetting behaviour of the coating solutions used. The Wilhelmy plate method was carried out by measuring the force exerted on a thin, wettable plate when it is brought into contact with the liquid. When the contact angle on the plate is zero, the interfacial tension can be calculated by divided the measured force with the perimeter of the plate.

For goniometer measurements (Figure 3.11), the pendant drop shape method was used (Woodward, 2008). This method is based on the Young-Laplace equation, and it uses the radii of curvature of the droplets and their density to calculate the surface tension. A needle of 0.41 mm diameter (22 G) was used to generate droplets. The captured images of the droplets were then stored on a computer in real time and software was used to convert these images into droplet profiles. All measurements were repeated ten times and the interfacial tension results were averaged.

For the PEG solutions, the difference in interfacial tension between the solutions is minimal which were in the range of 54-56 mN/m. The same was observed for HPMC

solutions; the difference in interfacial tension between the HPMC solutions was in the range from 46-49 mN/m (Table 3.4).
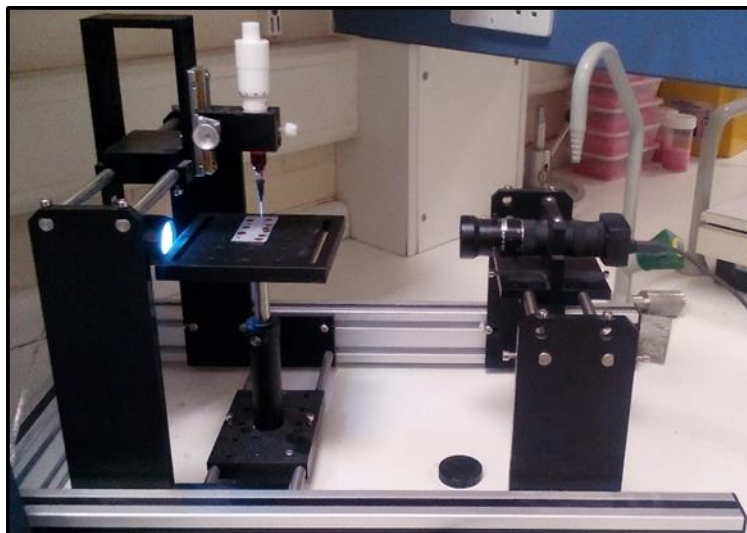
Figure 3.11. FTA 200 Goniometer

Table 3.4. Surface tension of coating liquids

Coating Materials/ Molecular weight (Da)		Interfacial Tension (mN/m)
50% PEG	4000	54.78 ± 0.21[a]
	10000	55.42 ± 0.20[a]
	20000	55.88 ± 0.22[a]
	35000	55.05 ± 0.24[a]
5% HPMC 603	16000	49.18 ± 0.08
5% HPMC 606	35600	46.89 ± 0.45
5% HPMC 615	60000	48.20 ± 0.80

[a] Measurements carried out by Procter & Gamble, Newcastle Innovation Centre, United Kingdom

3.2.3 Liquid Density Measurements

In order to measure the interfacial tension as discussed in Section 3.2.2, the liquid density needs to be known. For the measurement of liquid density, a graduated cylinder was used. The empty graduated cylinder was weighed and filled with the liquid of interest using a plastic pipette. Then, the filled cylinder was weighed again. The density was

calculated from the obtained liquid mass and the known cylinder volume. Table 3.5 shows densities for both PEG and HPMC solutions. It indicates that with an increase in viscosity, the density slightly increased for both solutions.

Table 3.5. Densities of coating liquids

Coating Materials/ Molecular weight (Da)		Density (g/cm³)
50% PEG	4000	1.049 ± 0.03
	10000	1.077 ± 0.01
	20000	1.110 ± 0.01
	35000	1.113 ± 0.02
5% HPMC 603	16000	0.979 ± 0.02
5% HPMC 606	35600	1.024 ± 0.01
5% HPMC 615	60000	1.022 ± 0.02

3.3 Particle-Liquid Characterisation

The determination of contact angle is of importance in this work to understand solid-liquid interactions mechanisms such as wetting and spreading. The wettability of particulate material can be characterised by the angle that is formed by the coating liquid on its surface. A common method to measure the contact angle is the sessile drop and this method was used in this work and the technique explained in the following sections.

3.3.1 Contact Angle Measurements

Measurement of the contact angle of powder-coating liquid systems was carried out by the sessile drop method using a First Ten Ångstroms FTÅ200 goniometer (Figure 3.11). First, a thin layer of alumina beads was prepared by crushing them using a mortar and pestle until a fine powder was obtained. This fine powder was used to obtain a flat particle bed surface to reduce the effect of excessive droplet penetration between large particles during the measurement. Then the fine powder was spread out and fixed on a microscope slide using double adhesive tape. Next, a 22 G (0.41 mm internal diameter)

blunt needle was positioned just above the bed, and a drop of the coating liquid allowed to detach from the needle to the powder bed. The shape of the drop profile was observed for up to 180 s with a 45-frame movie recorded. The FTA 200 software was used to determine the contact angle. However, previous findings (Woodward, 2008) reported that the software only could measure a contact angle $> 20°$ accurately. Therefore, in such cases, the baseline for the droplet had to be defined manually.

Table 3.6. Contact angle of all particle-coating liquid systems used in this work

Particle	Coating materials/ Molecular weight (Da)		Contact angle (°)
Alumina beads	50% PEG	4000	23.48 ± 1.49
		10000	42.50 ± 0.73
		20000	44.05 ± 1.21
		35000	69.62 ± 1.05
	5% HPMC 603	16000	$< 20°$ (4.38 ± 0.85)
	5% HPMC 606	35600	$< 20°$ (10.44 ± 2.67)
	5% HPMC 615	60000	27.15 ± 2.19

For this work, the contact angles for all coating liquids used were less than 70°, indicating that these liquids had a good wettability with the particles (Table 3.6). In addition, for both systems, a higher wettability was observed with a decrease in viscosity, as indicated by a lower contact angle value for lower viscosity. For HPMC-alumina systems, the liquid droplet spread almost instantly, making the contact angle so low that it could not be measured accurately by the software. For such systems, the contact angle is denoted as $< 20°$. The contact angle for each solution was measured at least five times and the mean value recorded.

3.4 Experimental Methods

This section provides a description of the experiments performed in this work. The experimental work was divided into three sections due to different coating techniques being used. However, in all systems, experiments were specially designed to study contact spreading only. The first part involved the contact spreading mechanisms in a tumbling drum without a spray system, where a portion of particles were pre-coated

before mixing with the remaining particle batch tumbling in the drum. The second part studied the contact spreading behaviour in a novel small-scale fluidised bed with a spray system to supply the liquid at the initial stage. Finally, the third part involved a method performed similar to tumbling drum experiments (i.e. no spray system), where particles were pre-coated before mixing with the remaining batch in the same fluidised bed system used in second set of experiments. These sets of experimental methods allow for the investigation of the contact spreading behaviour using different coating techniques.

3.4.1 Tumbling Drum Set-Up

A tumbling drum was manufactured 'in house' to study and understand the mechanisms of the liquid coating process via contact spreading in a rotating drum system. The set-up allowed for introduction of pre-coated particles to investigate liquid transfer from these particles to bulk particles in the drum. This system consisted of a horizontally positioned drum, a hand-held particle delivery device, a drum drive and control unit (Glen Creston Ball Mill, model CA3) as shown in Figure 3.12. The drum was made of stainless steel with dimensions of 325 mm x 210 mm. One end of the drum was removable, made from Perspex glass to allow for observation of the material within the drum, with a 65 mm diameter aperture in the middle for loading pre-coated particles. The other end plate was fixed to the body of the drum.
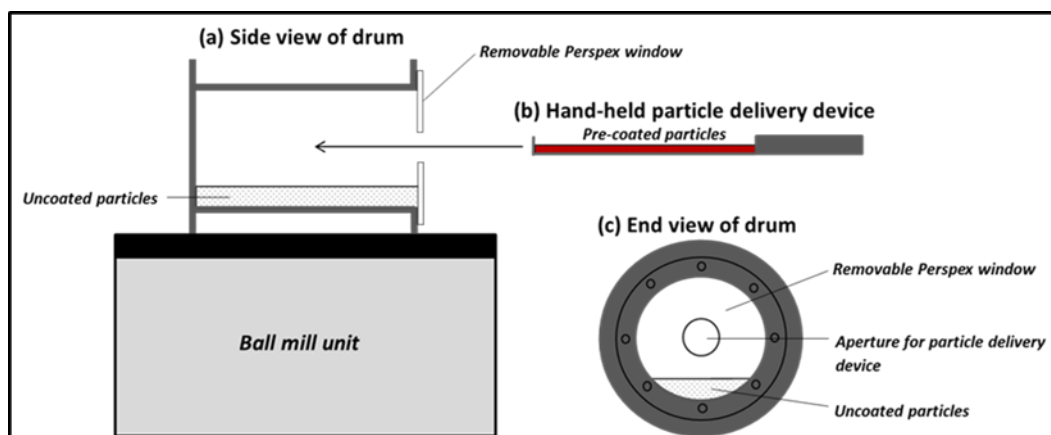
Figure 3.12. Schematic diagram of the tumbling drum system

The drum was placed on two 60 mm diameter and 735 mm long steel rollers with a 250 mm separation between them. The rollers were covered with a rubber layer to prevent slipping between the drum and the rollers (Figure 3.13). Both rollers were connected to a motor via a control unit, which was able to rotate the drum at speeds ranging from approximately 0 to 90 rpm or 0-0.951 in terms of the Froude number, *Fr* as shown in Eq. 3.6:

$$Fr = \omega^2 R/g \qquad\qquad\qquad \textbf{(Equation 3.4)}$$

where ω is the rotational speed in rad/s, R is the drum radius and g is the gravitational acceleration. This allowed the generation of five different tumbling regimes out of the six regimes of solid motions, although this work focused only on the rolling, cascading and cataracting regimes due to their industrial importance. Moreover, this system also can accommodate different sizes of drums with a range of fill levels (5-15% of the drum volume). However, a 10% fill volume was used throughout this work. Further details are given in Section 5.2.1.
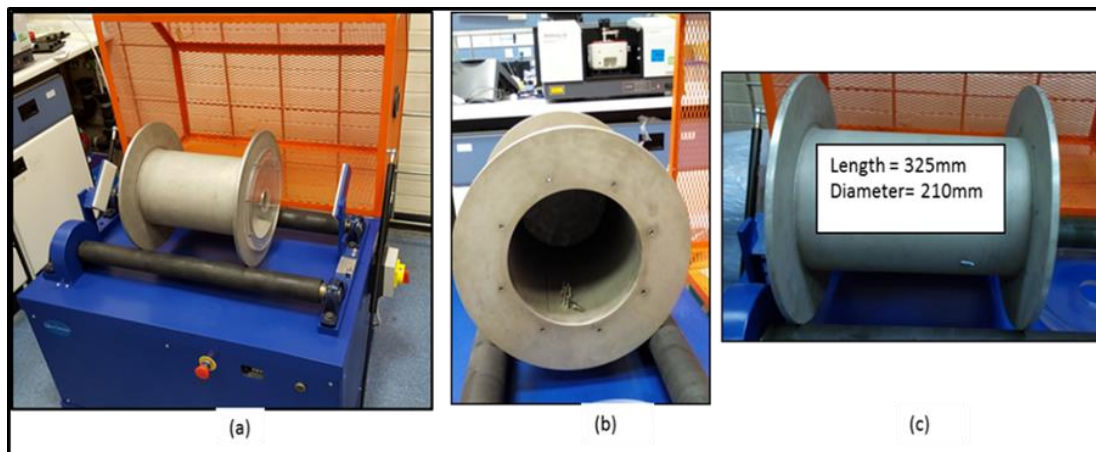
Figure 3.13. Tumbling drum experimental set up: a) the whole set-up view b) front view, c) side view

For each experiment, 10% of the alumina particles (232.37 g) from a 10% drum fill level (2323.69 g) were pre-coated with 50% wt/wt PEG solutions with different molecular weights (MW) to give different viscosity solutions. Five millilitres of the PEG

solutions were put in a plastic bag filled with the 10% portion of alumina particles using a plastic syringe. Then, the plastic bag was shaken manually until the particles were fully coated with the PEG solutions. Following this, the coated particles were added to the drum whilst tumbling using a hand-held particle delivery device (Figure 3.14). The particle delivery device was designed to apply the pre-coated particles evenly along the axial length of the drum (Figure 3.13 & 3.14). At this 10% fill level, a selected 50 rpm (Froude number = 0.294) speed was used to produce a 'cascading regime', allowing for an adequate flow of the particles within the drum.

Each experiment was carried out for a different tumbling time with intervals ranging from 0 s until a time when it was clear that the coating process was complete. Once stopped, the drum was emptied and the whole sample batches were put in a tray and dried at room temperature (21 °C) overnight prior to sampling for colorimetric analysis (see Chapter 4 for details). Experimental runs were then repeated and stopped at increasing time intervals, to give a series of coated batches at different times. In addition, for each series, an additional run was performed where the 10% of the pre-coated particles were added into the 90% of the uncoated particles in a static drum without any tumbling. The batch was then emptied out of the drum and collected. This was to consider if any additional liquid transfer had occurred during the procedure of emptying the drum and would provide an initial starting point from which the data would be analysed. This methodology will be described in more detail in Chapter 5, Section 5.2. A minimum of two experiments were performed at each condition to test the reproducibility of the data.
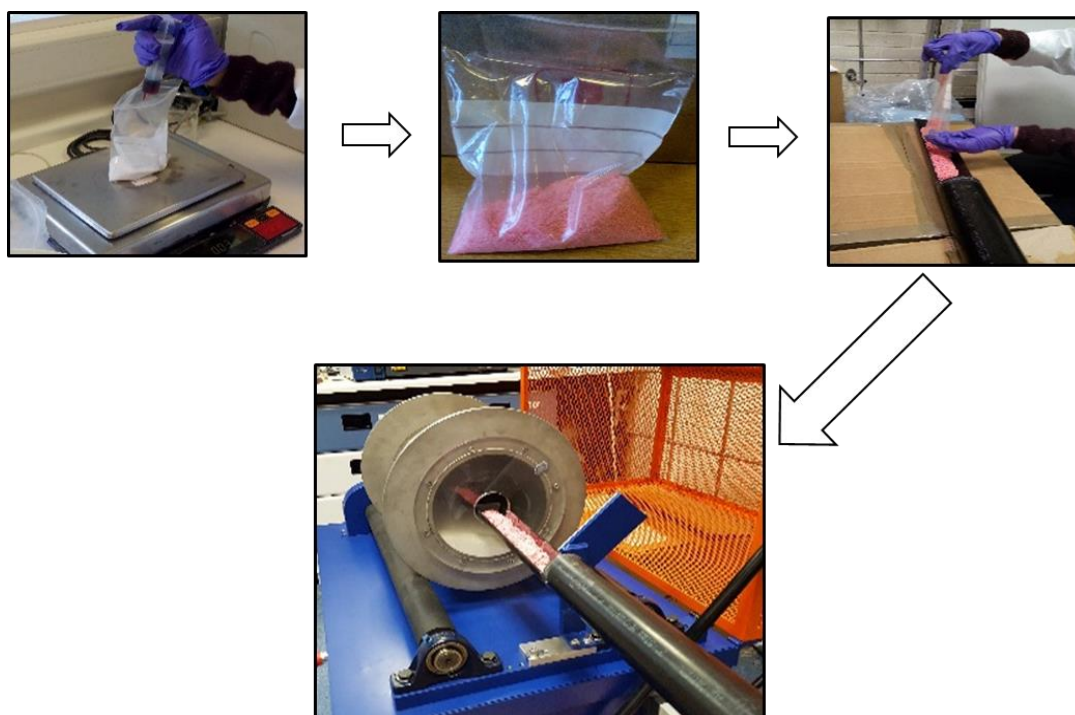
Figure 3.14. Method for introducing pre-coated alumina particles to the remaining particles in the drum: (a) Addition of PEG solution to particles; (b) Particles fully coated; (c) Pre-coated particles placed to particle delivery device; (d) Pre-coated particles added to remaining particles in the drum.

3.4.2 Fluidised Bed Coating Equipment Set-Up using the Spray Method

This section provides details of the development of a small-scale batch top spray fluidised bed which was manufactured 'in house'. This equipment consisted of three systems: fluidizing system, liquid dispensing system and spray nozzle atomizing system as shown in Figure 3.15. The fluidised bed tube was built with transparent acrylic material so that it was easy to observe the coating process within the tube. The tube had a diameter of 100 mm (outer), 90 mm (internal) and was 698 mm in height. To provide an even fluidizing air distribution, a distributor plate was used, manufactured from stainless steel wire mesh (w = 0.325mm) and the fluidized air flow was controlled by a rotameter (FTI 1750 Series Variable Area Flowmeter). This fluidised bed was designed to vary the position of the spray nozzle height based on the particle bed height and spray pattern used.
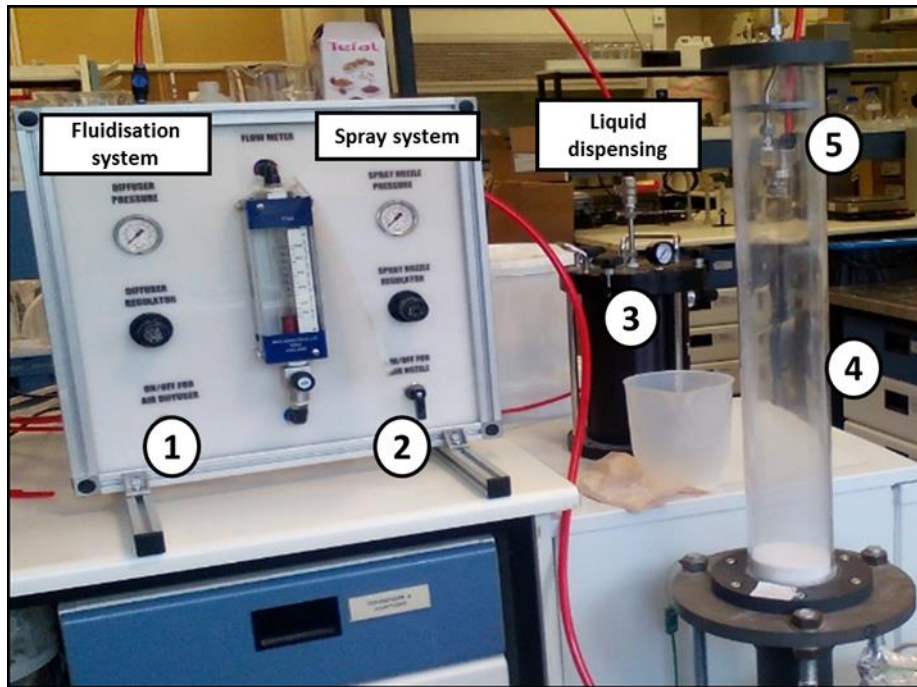
Figure 3.15. A schematic overview of the fluidised bed system set-up; 1: Fluidisation pressure control; 2: Spray atomisation pressure control; 3: High-pressure pot; 4: Fluidised bed chamber; 5: Spray nozzle

The coating solution was supplied by a high-pressure pot (TS1258, Adhesive Dispensing Ltd). A bottle containing the coating solution was placed inside the pot chamber and a feed stainless steel dip tube was pushed through the pot lid to reach the coating solution. The liquid was then pumped through this fitting to a 6.35 mm, internal diameter (ID) tube (Legris 8X6 Advanced Polyamide Calibre) linked to the fluid tube (stainless steel), attached to the nozzle. The liquid pressure was controlled by a pressure gauge (0 -7 bar) and pressure regulator located on top of the pot lid. The air was supplied to the pot through a fitted tube (Legris 8X6 Advanced Polyamide Calibre) located at the side of the body-pot, linked to the main air tap and controlled by a valve. The nozzle used for this study was a two-fluid external mixing nozzle (Spray System, PA64, PF1650), and the internal diameter (ID) and orifice diameter (OD) of the air cap and fluid cap used are described in Figure 3.16.

To spray the coating liquid, a top spray nozzle was inserted vertically inside the fluidised bed chamber. The spray nozzle was attached to the top plate of the fluidised bed chamber as can be seen in Figure 3.17.
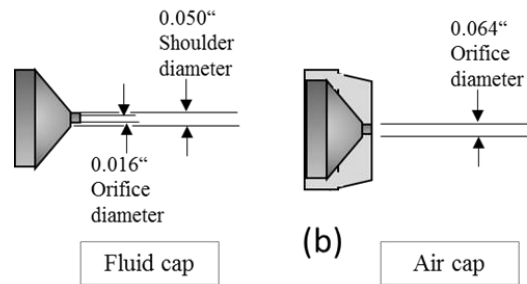
Figure 3.16. Images of a) the air cap and nozzle used and b) the dimensions of the air cap and fluid cap

The top plate consisted of four holes; for air outlet (3 holes) and a tube (middle) for leading through the air and liquid tube (attached to the atomized nozzle body). The nozzle tip was positioned in a range of 16-22 cm height from the distributor plate so that the spray was fully submerged when the particles were fluidized (Figure 3.17). The details of the operating conditions are explained in Chapter 6, Section 6.2.5. The nozzle (air cap and fluid cap) was fitted to the outlet of the atomizing nozzle body by tightening it using a wrench. A valve with a long stainless-steel holder was fitted at the liquid line close to nozzle inlet to control any dripping of the liquid supplied to the system once the liquid valve was shut off. The holder was designed long enough so that it was easier to control the on/off valve from the top of the fluidised bed chamber. The atomizing air pressure was controlled by adjusting the pressure gauge (0 -10 bar) and pressure regulator located at the spray nozzle control panel. In addition, this pressure could be varied to adjust the pattern and the droplet size of the atomized liquid spray.

With the development of this novel experimental set-up, contact spreading only experiments were now possible to investigate contact spreading in the fluidised bed system. In each experiment, a 10 cm particle bed height (1313.26 g) of alumina beads was loaded through a hopper to the fluidised bed chamber.
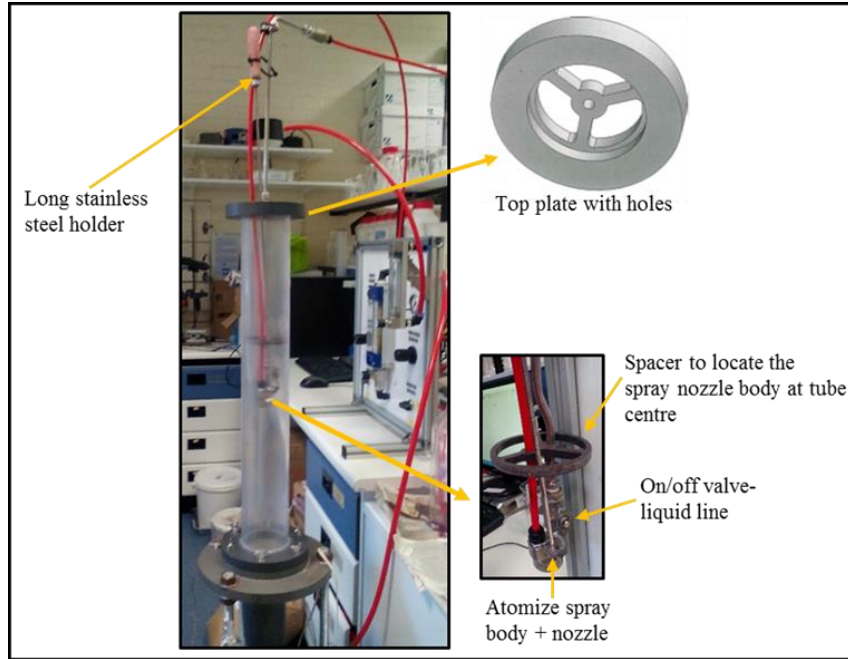
Figure 3.17. Images of the fluidised bed tube and the atomizing spray nozzle

The particles were first fluidised with the air at 2.5 bar fluidisation pressure and 320 L/min flowrate (1.5 U_{mf}). The measurement of minimum fluidisation, U_{mf}, for the particles is described in Chapter 6. Then, the nozzle height was set at 16 cm from the distributor plate. After a few seconds of fluidisation, the HPMC solution was sprayed from top of the tube at room temperature (21 °C) for 2 s. The liquid pressure was set up at 2.0 bar (2.0 g/s) and 1 bar atomization pressure to obtain a spray coverage area in the tube of approximately 6 cm. Once the spraying time had stopped, the mixing time was started until a predetermined interval time and at the same time, the top plate was removed from the tube to avoid any dripping of the liquid to the particle bed.

After the mixing time was completed, the fluidisation was stopped immediately. The tube was emptied and the whole batch was put in a tray and dried at room temperature (21 °C) overnight prior to sampling for colorimetric analysis. Experimental runs were then repeated and stopped at increasing time intervals, to give a series of coated batches for the selected conditions. Detailed conditions of all experiments performed can be found in Chapter 6, Section 6.2.5. In addition, for each series, an experimental run was performed where the particles were coated for the spray time only (2 s) (i.e. at 0 s mixing

time). The batch was then emptied out of the fluidised bed tube and collected. This batch was considered as liquid transfer occurring due to the spraying procedure only, and not contact spreading during mixing. This gave a starting point for the contact spreading only process. This same methodology was used for different HPMC viscosity solutions, nozzle heights, liquid spray rates, and fluidisation velocities, as described fully in Chapter 6. Duplicate experiments were performed at each condition to test the reproducibility of the method.

3.4.3 Set-up of the Fluidised Bed System Using the Pre-coated Particles Method

This section provides details of the contact spreading experiments in the same fluidised bed equipment developed in Section 3.4.2 with some modification. This was to allow the investigation of contact spreading using a different method of liquid introduction into the system. As compared to Figure 3.15, the set-up for these experiments was modified and only consisted of one system; the fluidising system and a fluidised bed tube as shown in Figure 3.18. This new set-up allowed for introduction of the coating liquid via pre-coated particles to investigate liquid transfer from these particles to bulk particles in the fluidised bed. The pre-coated particles method used here was similar to the method of liquid addition used in the tumbling drum experiments described in Section 3.4.1. However, here, the particles were pre-coated in a plastic container and poured directly to the system without using any particle delivery device as shown in Figure 3.19.

For each experiment, a 10 cm static bed height was used (1313.32 g). 10% of these alumina particles (131.32 g) were pre-coated with 5% wt/wt HPMC solutions with different molecular weights to give different viscosity solutions. The 90% of the remaining particles in the bed were first fluidised with the air at 2.5 bar fluidisation pressure and 400 L/min flow rate (1.8 U_{mf}).Four millilitres of HPMC solutions were put in a plastic container filled with the 10% alumina particles using a plastic syringe (Figure 3.19). Then, the container was shaken manually until the particles were fully coated (20 s) with the HPMC solutions. Once fully coated, these particles were added to the fluidised

particles directly from top of the tube at room temperature (21 °C) to imitate the top spray of liquid introduction as described in Section 3.4.2.
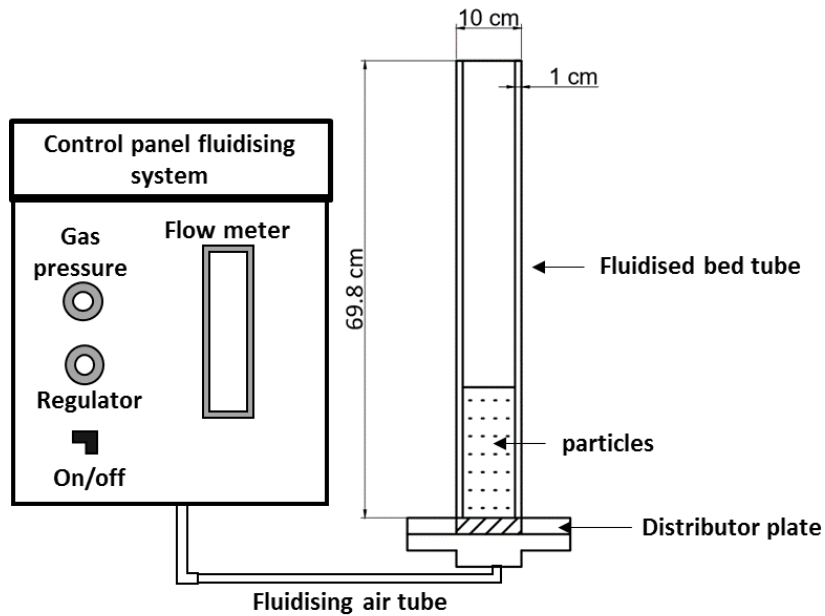
Figure 3.18. Schematic diagram of the modified fluidised bed setup for contact spreading by the pre-coated particles method. The fluidising air is supplied from the main air supply and is regulated using the control panel.
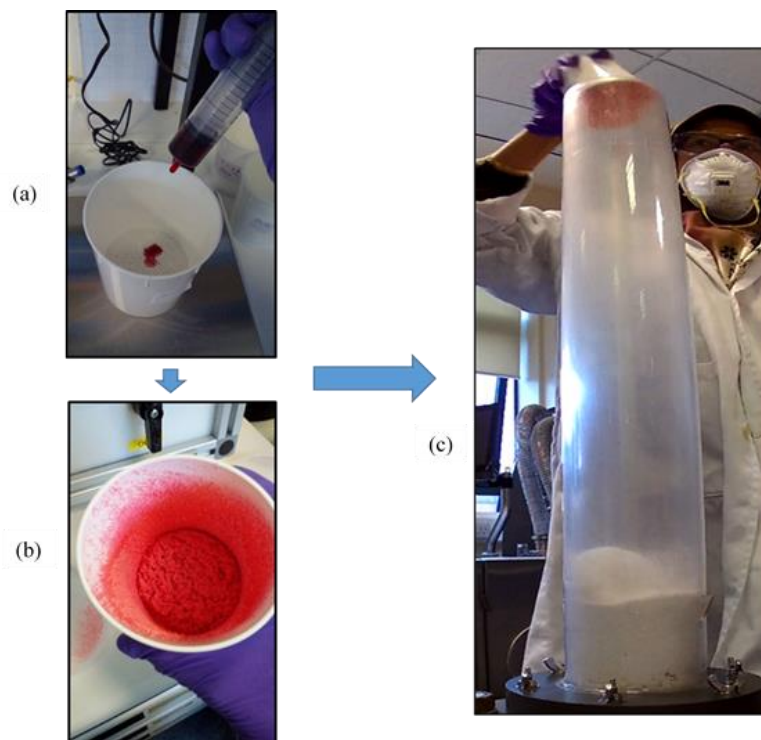
Figure 3.19. (a) and (b) pre-coating of 10% alumina particles and (c) pouring of the pre-coated particles into the remaining 90% uncoated particles in the fluidised bed

Each experiment was carried out for a different fluidisation time with intervals ranging from 0 s until the time that it was clear that the coating process was complete. Once stopped, the tube was emptied and the whole sample batches were put in a tray and dried at room temperature (21 °C) overnight prior to sampling for colorimetric analysis (see Chapter 4). Experimental runs were then repeated and stopped at increasing time intervals, to give a series of coated batches at different times. Moreover, for each series, an additional run was performed where the 10% of the pre-coated particles were added into the 90% of the uncoated particles in a static particle bed. The batch was then emptied out of the tube and collected. This was to consider if any additional liquid transfer occurring during the procedure of emptying the tube and this provided an initial starting point for subsequent analysis of coating with time. This same methodology was used for different HPMC viscosity solutions and is described in more detail in Chapter 7, Section 7.2. A minimum of two experiments were performed at each condition to test the reproducibility of the data.

3.5 Summary

In this chapter, a range of particle and liquid characterisation methods and three different coating equipment set–ups have been described for the study of liquid transfer via contact spreading. The experimental methods for each of the coating systems were also explained. However, the specific experimental conditions employed for each type of equipment will be described in detail in the relevant results chapters. In the following chapter, the development of newly developed image analysis system to quantitatively analyse coating behaviour based on the colorimetric measurement of the coating layer will be described in detail.

CHAPTER 4

4 Development of a Quantitative Colorimetric Method for Coating Characterisation

In order to investigate liquid coating distribution via contact spreading between particles, a new image analysis system, based on colorimetric measurement, was developed to quantitatively determine the inter-particle color uniformity of particles coated with dyed solutions. Here, a camera was used to capture images of the product samples, and the degree of coating on particles was evaluated based on the coefficient of variation (CoV) value measured from data generated by LabVIEW software. Preliminary assessment of this newly developed novel colorimetric image system was conducted by performing a contact spreading experiment in a tumbling drum and comparing the quantitative data generated from the LabVIEW software to visual images of the coating process. This chapter details the imaging system set-up and image capture, followed by the quantitative image analysis using the LabVIEW software. Finally, the validation and preliminary assessment of this technique to describe coating behaviour is discussed.

This method of quantitative analysis was used for all the experimental work throughout this thesis, and the liquid spreading via contact spreading mechanisms observed for different coating equipment based on data generated from the LabVIEW software.

4.1 Image Analysis System

This section presents an overview of the development a novel image analysis system to characterise inter-particle coating uniformity. The set-up is shown in Figure 4.1. The imaging system consists of five basic components: Lumenera Infinity 3 Camera, Navitar 12X zoom lens with light diffuser, lighting controller and a computer running Infinity Capture Software and LabVIEW software.
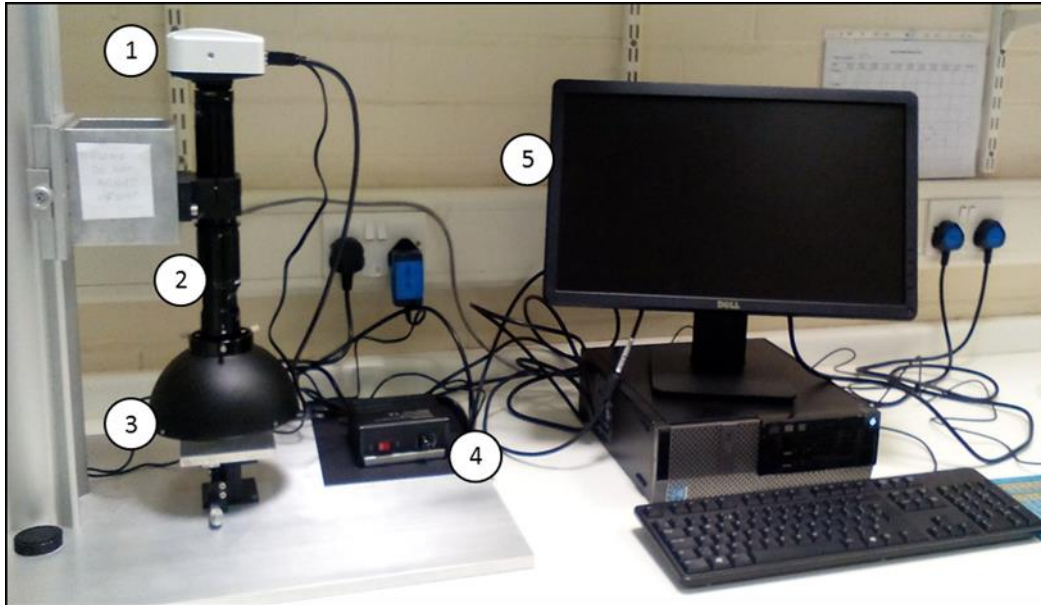
Figure 4.1. Image system set-up. 1. Camera; 2. Navitar 12X zoom lens; 3. Light diffuser; 4. Lighting controller; 5. Computer

To ensure proper identification and assessment of dyed coated particles, precise color measurement is required. The Lumenera Infinity 3 CCD Camera (Lumenera Corporation, Canada) with Infinity Capture software included was used to capture the images of coated particles; high quality images with extremely low noise and high dynamic range. Recently, CCD cameras have been frequently employed for quality classification, physical characteristic detection, and properties evaluation of food products (Andrade *et al*., 2012b; Zheng *et al*., 2006). The camera was fitted to a Navitar 12X zoom lens (Image Optics, UK) and a LGT.19.MF2D LED dome diffuser lamp (Honyu, China) attached to an adapter (ca. 57mm diameter) screwed to the lens. The attached light diffuser incorporates a ring with 120 LEDs which reflect onto a white dome to provide a completely shadow free incident illumination, thus reducing reflection on captured images. A lighting controller was also attached to this light diffuser to provide the right amount of light required.

4.1.1 Quantitative Image Analysis

To quantify the degree of particle coating based on colorimetric measurement, a series of self-written image processing algorithms in LabVIEW was used, developed at the University of Sheffield[1]. The algorithms created were based on color theory (Gonzalez & Woods, 2008). The 24-bit color images consist of three 8-bit arrays of pixel values for red, green and blue (RGB) intensities. By identifying the pixels forming the image of an individual particle, it is possible to calculate RGB intensity fractions (R + G + B = 1) for each particle and, therefore, how evenly distributed the coating is. For example, for perfect white particles, the same fraction of RGB value would be obtained (33.3% for each value) and for particles coated with red dye, those particles will have a higher fraction of red value (more than 33.3%). By measuring the relative intensity of the red fraction on individual particles in a batch sample, it is possible to quantify changes in the distribution of the coating with processing conditions.

4.1.2 Sampling

After the coating process, samples of the dyed coated particles from the whole batch were randomly collected with a riffle sample splitter (RT, Germany) as shown in Figure 4.2. This sampling technique enables in reducing the bulk sample size to a smaller sized sample as a representative of a sample batch. The bulk particles were poured evenly into the dividing head of the sample splitter and collected into two collecting receptacles under the dividing heads. This procedure was repeated (3 times) until the required quantity was obtained, approximately 10% of the whole sample batch. This random sample was then used for image analysis.

---

[1] Developed by Dr Andrew Campbell, Department of Chemical and Biological Engineering

Figure 4.2. A riffle sample splitter used for sampling

4.1.3 Image Capture

The randomly sampled particles were mounted on 5 mm x 5 mm double-sided adhesive black vinyl film (Anchor Magnets, UK) before images were taken using the Infinity Capture software. The software is supported by Windows and has a graphical user interface with standard pull-down menus, an icon-based toolbar and keyboard commands, which make it very simple to control the camera and take images (Figure 4.3). When capturing images, the camera settings were kept the same for all imaging. The mounted samples were placed on the sample stage in the field of view of the camera and 16 images taken for each sample batch, thereby measuring approximately 2000-4000 particles. Finally, the acquired images were stored as TIFF files for colorimetric analysis. This method utilizes a two-dimensional image and assumes that the coating uniformity of the posterior and the anterior views of the particles are not significantly different.
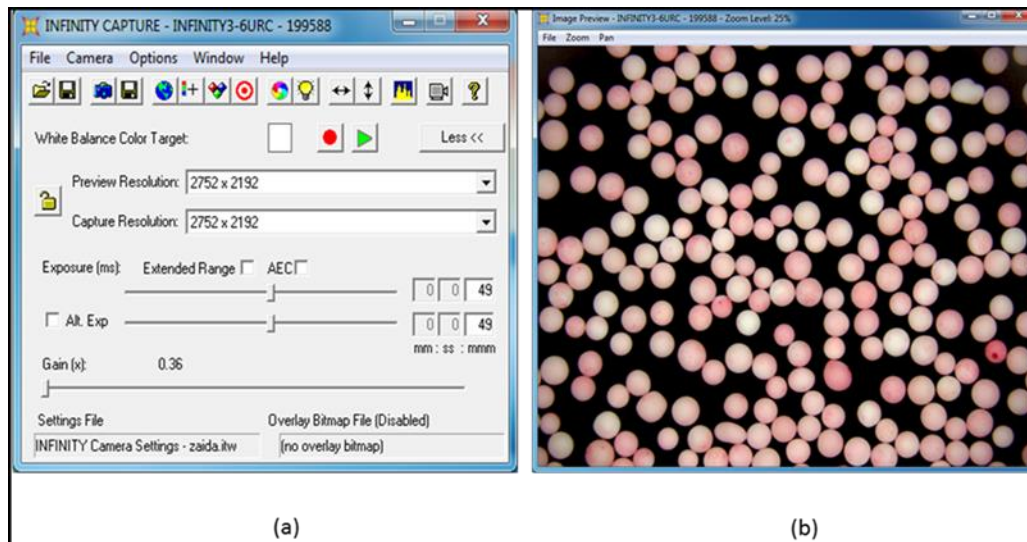
Figure 4.3. a) Infinity Capture main window with the camera settings and b) captured image in Live preview window

4.1.4 LabVIEW Software for Quantitative Determination of Contact Spreading

The images were imported into LabVIEW software for image processing. National Instrument's LabVIEW (Laboratory Virtual Instrument Engineering Workbench) version 15.0 (64-bit) was chosen as the programming language for the development of software for this research. It is a graphical programming language, G, using icons or graphics instead of typing a text. LabVIEW was chosen in this study for the following reasons:

• Programming uses a flowchart rather than being text-based, thus simplifying the process, and it is easier to visualize and debug a complex program.

• Dataflow in the program through the icons determines the execution order of the functions, allowing creation of a program that can execute multiple operations in parallel, which speeds up execution time.

• LabVIEW has an extensive toolset: Vision Assistant, which can be used to apply image-processing techniques directly and observe its effects on images. The

combinations of techniques that are found to be effective can then automatically be converted into executable LabVIEW programs.

Details of the LabVIEW software are further explained in Appendix B1. There are four main image processing steps after image capture input into the software (Figure 4.4). The details for each processing steps are described in the following sections.

Figure 4.4. Diagram of the main processing steps in image analysis using LabVIEW software

4.1.4.1 Smoothing

The image smoothing technique was developed as initial pre-processing of the input image data in LabVIEW for removing defects, e.g. improper focus, repetitive noise, or geometric distortions. As shown in Figure 4.5, to get a smoothed image, a Gaussian filter was adopted for noise reduction and to smooth the edges. It should be noted that the software has been designed such that the parameter values could be changed through the user interface. The most appropriate values for this alumina system were identified, so as to achieve colorimetric analysis for all particles present in the system. However, these parameters could be changed for samples with different characteristics, e.g. particle size and morphology.

4.1.4.2 Grey scale image

The second step of analysis began with separating the particles from the image background by converting the smoothed image to an 8-bit greyscale image. Grey-scale images are 2-D arrays that assign one numerical value to each pixel which are representative of the intensity at this point. It is generated from colored images by suppressing the RGB component to 1 and 0. Generally, the background is the 'white region' (value 1) and the value 0 is the 'dark region' which refers to the object pixels. In Figure 4.6, it is shown that all particle pixels have one grey level and all background pixels have another.
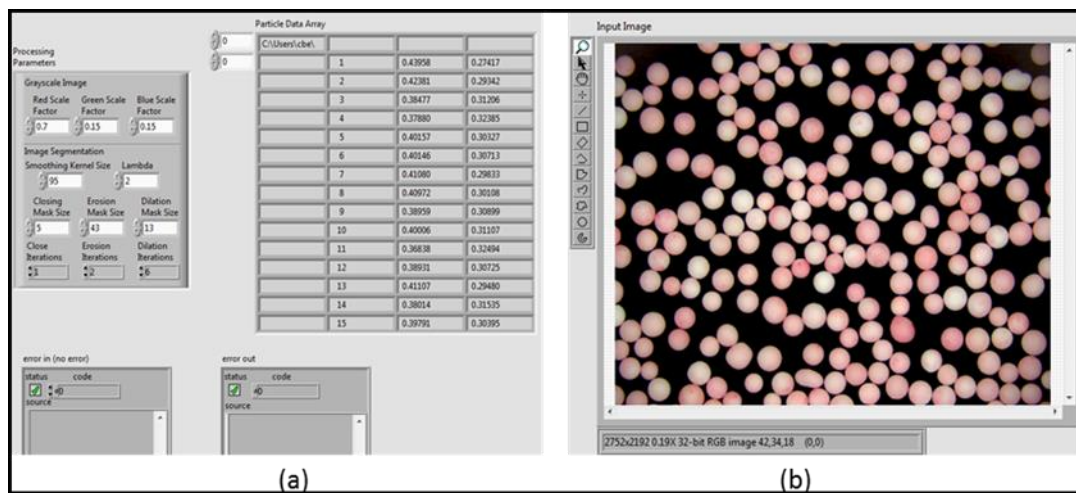
Figure 4.5. Front panel of a) input and b) smoothed image
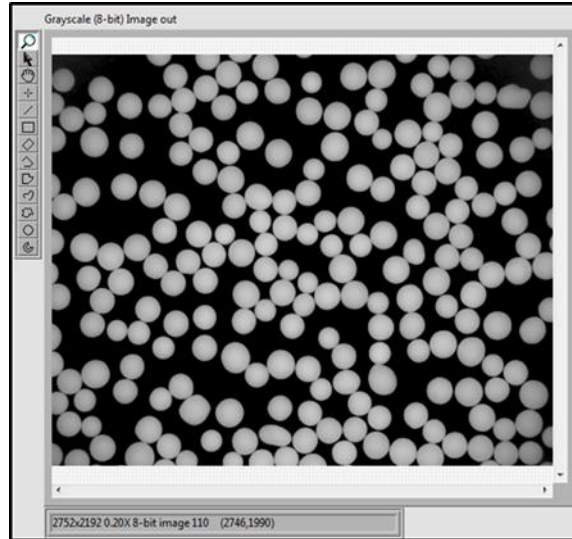
Figure 4.6. Front panel view for a grey scale image

4.1.4.3 Eroded Image

In the third step, a boxcar averaging background subtraction algorithm is applied (Crocker & Grier, 1996). This is an aid to subtracting the contrast gradients which might arise from non-uniform sensitivity among the pixels. The fundamental morphological 'opening' operation is then employed to ensure that the particles are separated from their neighbors in the image (Gonzalez *et al*., 2010). In morphological 'opening', the erosion (shrink the image) and dilation (expand an image) stages are applied generally to smooth the contour of an object, break the narrow isthmuses, and eliminate thin protrusions. Figure 4.7 shows an eroded image in the LabVIEW software.
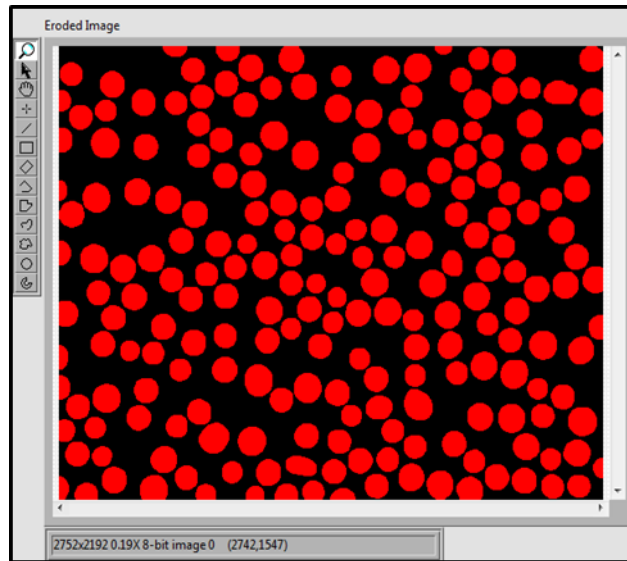
Figure 4.7. Front panel view of eroded image

4.1.4.4 Labelling

Finally, after removing the background and obtaining individual separate particles, LabVIEW's particle labelling function is applied. Here, an image is produced where each particle has a unique label (Figure 4.8). The labelled image is then used as a mask to isolate the pixels of each particle in the colour image from which the RGB intensity fractions are calculated. The LabVIEW software is created to export the data output to a spreadsheet (Microsoft Excel, Microsoft Corp.,) before the final determination of coating uniformity.
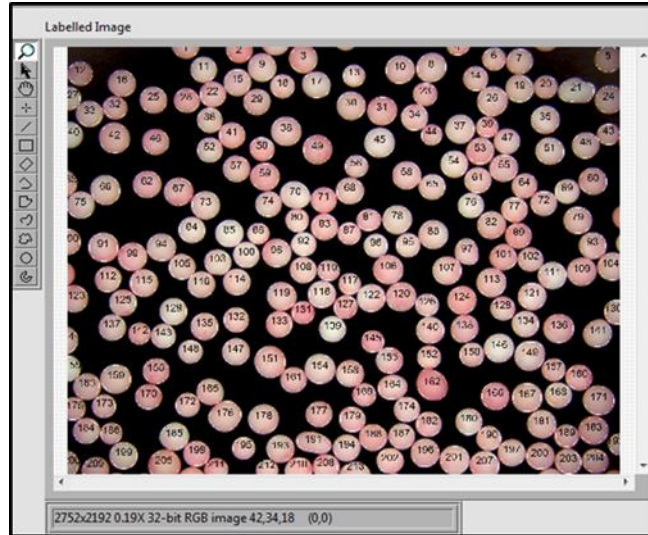
Figure 4.8. Front panel view of labelled image

4.2 Pre-assessment of the Image Analysis System

Prior to analysing data using the image system set-up and LabVIEW software, there is a need to validate the system. To validate the above-mentioned system set-up, firstly, coated samples supplied from Procter & Gamble Company (P&G), Newcastle Innovation Centre, United Kingdom have been tested (see Appendix B2) followed by coated alumina particles, a model material which will be used in this study. In the following section, the validation using coated alumina particles were explained. The details of raw materials used, and the experimental works are explained in Chapter 3 while the data analysis method is explained in the following sections.

4.2.1 Data Analysis Method

In this section, the data analysis of a typical data series are explained; in this case, 50% wt/wt aqueous PEG (molecular weight 10,000) was used as a coating solution. The coated particles were visualized using this novel imaging system and the LabVIEW software was used for analysing the inter-particle coating variability. Data analysis was based on the standard deviations and mean red values generated for the red intensity color

of individual particles in each sample batch. This data was then utilized to evaluate the inter-particle coating uniformity, explained in the following sections. In addition, the treatment of the data to fit an exponential curve to measure the decay constant, λ, and time for coating completion, t_c, are also discussed.

4.2.1.1 Coating evolution

The image analysis focuses on measuring the red values of the red-dyed coated particles. The coating evolution of dyed coated alumina particles are shown in Figure 4.9. The coating evolution can be described by plotting a graph of frequency as as a function of percentage red. The developed LabVIEW software sums the values for each pixel in a particle and returns the total value for each colour in a particle. Analytically, for perfect white particles, it will have 33.3% blue, 33.3% red and 33.3% green fraction, whereas particles with red dye will have a higher % red value (more than 33.3%).
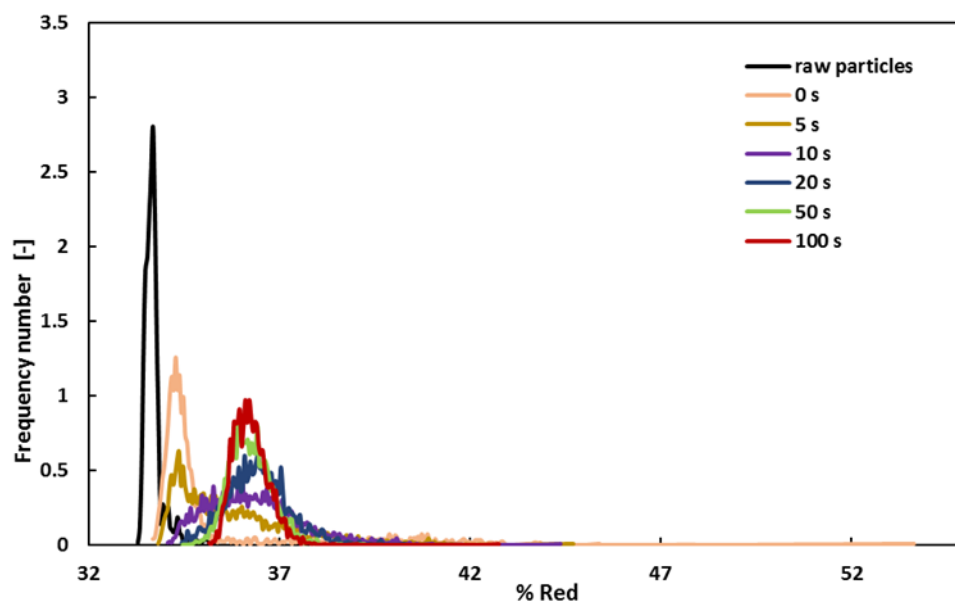
Figure 4.9. Coating evolution of alumina particles coated with PEG 10000 solution (note that not all time series for this graph are shown for visualisation purposes)

From Figure 4.9, it can be observed that an increase in tumbling time from 0 s to 50 s produces a slightly higher percentage of red dye and the distributions became sharper

92

and narrower. The raw particles show a relatively narrow peak at approximately 33.6 % red, indicating that they are almost white in colour (pure white particles would yield a value of 33.3 %). For the 0 second run, where the 10% pre-coated particles are added to the drum without any tumbling, a large distribution of % red between approximately 33.8 – 53 % is observed. The small peaks at the high % of red are attributed to the 10% of pre-coated particles while the large, relatively narrow peak at approximately 34.5% is attributed to the initial 90% uncoated particles. However, compared to the peak of raw particles, there is a shift in the peak of these particles to a slightly higher % red, indicating that there is some liquid transfer between particles occurring whilst the drum is being emptied. After 5 seconds mixing time, there is a further shift to higher red intensity, with a still relatively large distribution of % red. However, as the mixing time increases, the distributions become narrower indicating a lower degree of coating variation with time, i.e. the colour of the batch becoming more uniform, due to liquid contact spreading.

The average % red dye and the standard deviation of coated particles for all the samples were further calculated based on data produced by the LabVIEW software, where each labelled particle has its own % red dye value. The mean percentage red of all the particles at a specific time point as a function of mixing time is plotted in Figure 4.10. It can be seen that an increase in mixing time produced a very slightly higher mean % of red dye at lower mixing time. This correlates with the plot in Figure 4.9. It would be expected that the mean % red should be the same throughout mixing times. The reason for slightly lower values at lower mixing time could be due to the color analysis. At lower mixing time, particularly at 0 seconds, a percentage of the particles will be relatively thickly coated, and the color value may not quite reflect the amount of dye present on these particles. As the mixing time proceeds and contact spreading occurs, the color will be more evenly distributed across the batch of particles and this phenomenon will diminish; indeed after 10-20 seconds mixing time, the % red value appears to remain relatively constant.
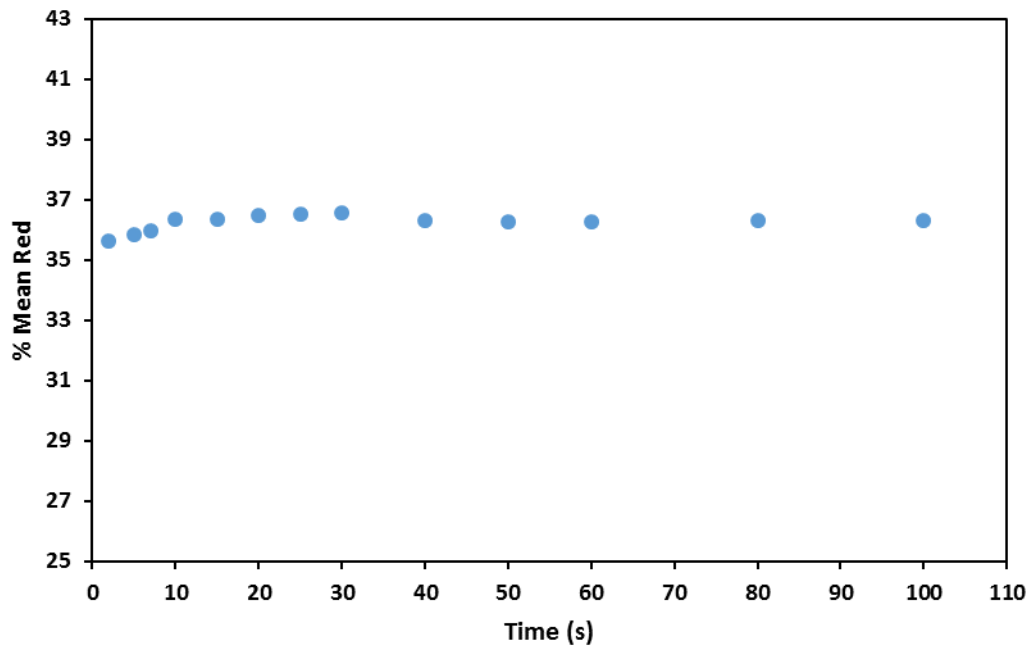
Figure 4.10. Mean % red as a function of mixing time

To follow the change in inter-particle coating variability between particles in a batch, the coefficient of variation (CoV) value for each time point was calculated based on Eq. 4.1 and plotted as a function of time as shown in Figure 4.11.

$$CoV = \frac{\sigma}{\mu} \; x \; 100 \qquad\qquad \textbf{(Equation 4.1)}$$

In Eq. 4.1, *CoV* is coefficient of variation, σ is the standard deviation of the distribution of % red dye intensity and μ is the % mean red intensity for each time point. Figure 4.11 indicates that the coating variability decreases with the mixing time, indicating that the process of contact spreading is occurring within the drum. The CoV value for this series also appears to reach an asymptotic value of ~1.4% at approximately 60 seconds.
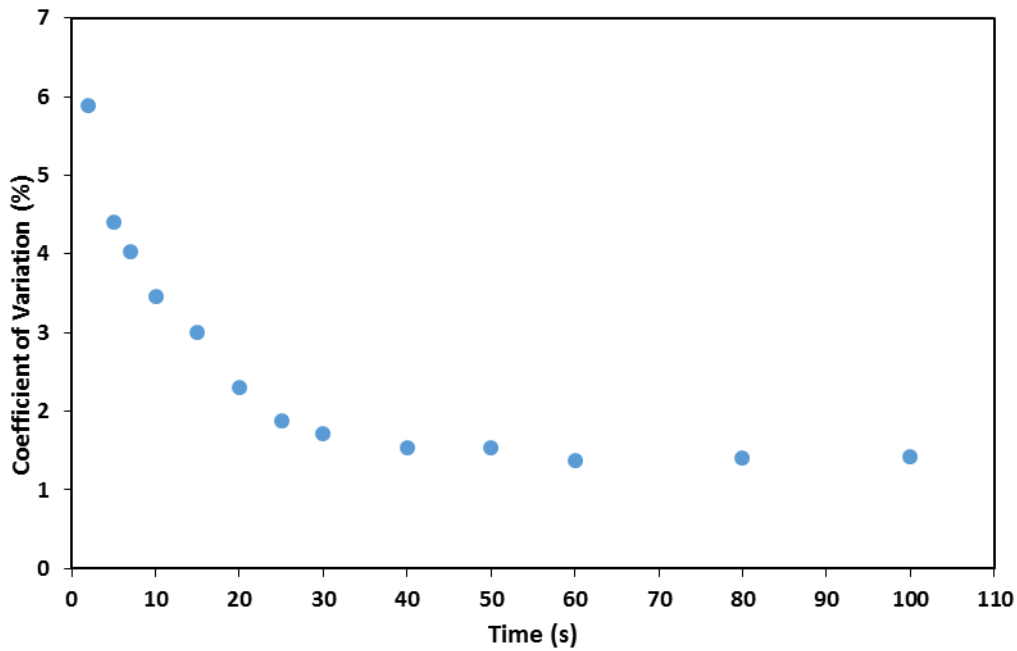
Figure 4.11. Coefficient of variation (CoV) as a function of mixing time

4.2.2 Treatment of Data

Figure 4.11 indicates that the CoV decreases with tumbling time until it reaches an asymptotic value and it appears to follow an exponential decay curve. The method used in this work to fit a curve to this data, followed the same procedure as that is described in Green, (2017). To fit the data, a function of the form given in Eq. 4.2 was used:

$$\boldsymbol{CoV\ (t) = CoV_\infty + (CoV_0 - CoV_\infty)e^{(-\lambda t)}} \qquad \textbf{(Equation 4.2)}$$

where CoV_∞ represents the asymptotic variation in the coating, CoV_0 represents the variation at the time 0 seconds, λ is the coating rate constant, and t is the mixing time.

The curve fitting based on Eq. 4.2 is dependent on the λ value; if it is too big, the function will over-predict the rate at which the data approaches the asymptote, if it is too

small, the function will under-predict the rate at which the data approaches the asymptote. Thus, to ensure the best fit was found in each case, a Solver add-in Excel was used. The Solver was used to find the best value of λ that will minimise the sum of the chi-squared value. The chi-squared value is an indicator to evaluate the difference between the real data and predicted data for each time point, where the smaller the value, the higher the correlation between the two sets of data. The asymptotic value is taken as an average of the CoV values at the final time points, where there is no clear decrease in CoV values (in this case, the CoV at 60, 80 and 100 s).

Moreover, to confirm the accuracy of the fitting and the relationship between the two variables, the coefficient of determination, also commonly known as R-squared is determined. The R-squared value can be presented in the range of 0 to 1, where closer to one indicates a better fit. In this case, the R^2 value is 0.99 (Figure 4.12), which means that 99% of the dependent variable (y-axis) is predicted by the independent variable (x-axis), thus confirming that the distance between the line and the data is very small.

As shown in Figure 4.12, an exponential decay curve was fitted based on Eq. 4.2 with a λ value of 0.095, which represents a coating rate constant. In addition, the time taken to complete the coating, t_c, can also been calculated. As the exponential decay function will reach infinity for the time taken to complete the coating process, in this work, the time for 98% of the coating to be completed is used (i.e. (CoV- CoV∞)/(CoV0-CoV∞) = 0.02. Eq. 4.2 is then rearranged to determine the t_c and Eq. 4.3 is obtained:

$$t_c = \frac{ln\frac{CoV\ (t) - CoV_\infty}{CoV_0 - CoV_\infty}}{-\lambda}$$ **(Equation 4.3)**
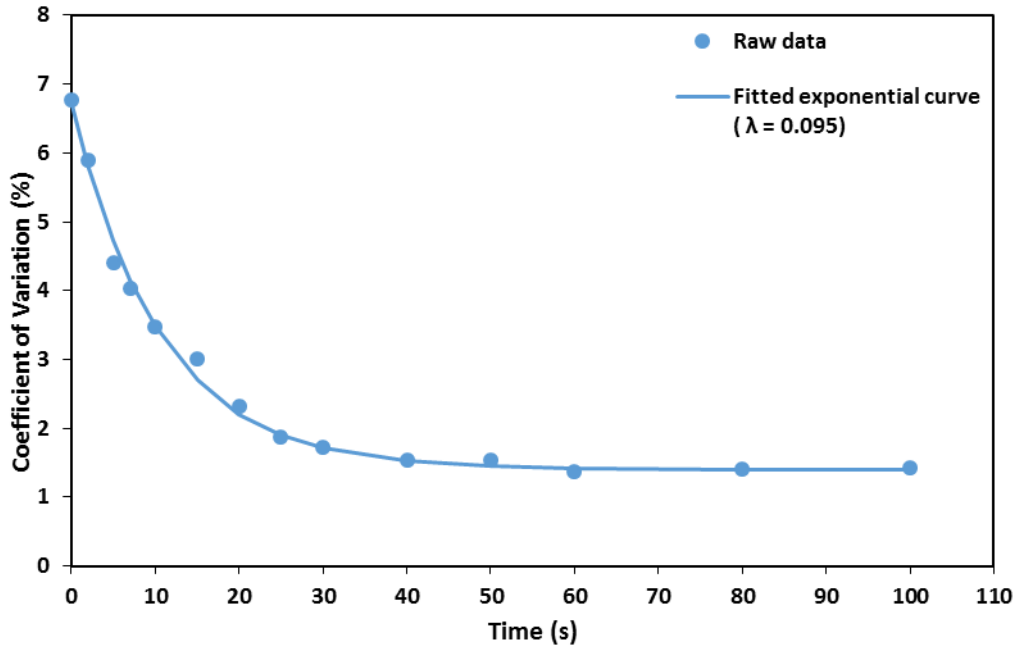
Figure 4.12. Exponential decay curve fit to the raw data for a typical data set

In Eq. 4.3, *CoV(t)* now refers to the time at which 98% of the coating is completed, assuming that CoV_∞ represents 100% and CoV_0 represents 0%. Based on this, the following Eq. 4.4 is obtained:

$$CoV(t) = 0.02(CoV_0 - CoV_\infty) + CoV_\infty \qquad \textbf{(Equation 4.4)}$$

By substituent Eq. 4.4 into Eq. 4.3, Eq. 4.5 and Eq. 4.6 are obtained and the t_c value then calculated. In the case of this data series, this yields a t_c of 41.17 seconds.

$$\mathbf{t_c} = \frac{\ln\frac{0.02(CoV_0 - CoV_\infty) + CoV_\infty - CoV_\infty}{CoV_0 - CoV_\infty}}{-\lambda} \qquad \textbf{(Equation 4.5)}$$

$$\therefore \quad \mathbf{t_c} = \frac{\ln(0.02)}{-\lambda} \qquad \textbf{(Equation 4.6)}$$

In the following results chapters, this same procedure is used to obtain plots and fit exponential curves for the whole data series. However, when comparing data series obtained using different conditions (viscosity, tumbling regime, fluidisation velocity,

flow rate, and nozzle height), the raw data is normalised by rescaling the data between the values 0 to 1. Normalisation enables the t_c and λ to be more easily compared between different experimental conditions due to different initial values of CoV obtained. The initial CoV value of each data set is dependent on the conditions used, e.g. viscosity of solutions, the rate of spray, and these are discussed in the relevant results chapters. The data is normalised according to Eq. 4.7, which is a normalised version of Eq. 4.2 and can be seen in Figure 4.13.

$$CoV_{normalised} = \frac{CoV\ (t) - CoV_\infty}{CoV_0 - CoV_\infty}$$
(Equation 4.7)
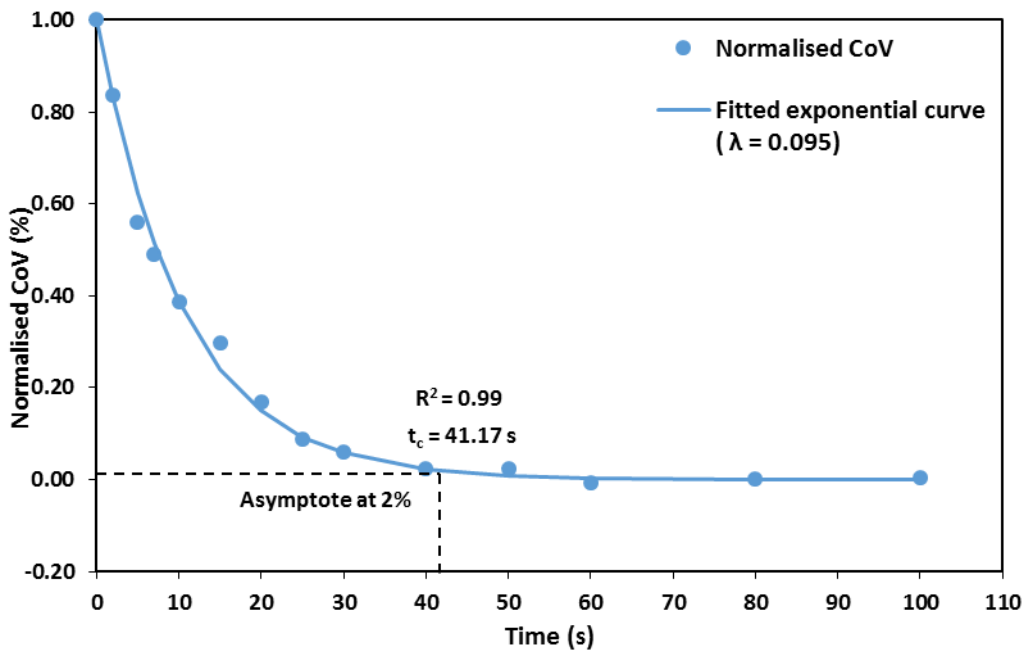
Figure 4.13. Exponential decay curve model fit to the normalised data for a typical data set

Figure 4.13 shows a rapid decay occurs mainly at lower mixing time. The physical mechanism occurs here might be due to the liquid transfer caused by the rapid formation and rupture of the wet agglomerates. As the time progresses, the coating rate nearly constant even the contact spreading occurs as the coating layer already dried due to evaporation occurs simultaneously in the system. The values for t_c and λ obtained from normalised and raw data appeared to be similar and this indicated that this fitting curve

method is reliable to determine the coating rate, λ, the asymptotic CoV value, and the time to reach this value, t_c. These values then will be determined and compared throughout this work using this method for each of the experimental conditions investigated.

Further to this, the quantitative data produced from this novel image analysis was also compared to the qualitative images. Figure 4.14 illustrates the images of alumina particles coated with 50% PEG 10,000 solution as a function of mixing time from 0 to 60 seconds. It is observed that the variation in inter-particle coating decreases with tumbling time. These visual studies agree with the quantitative data obtained from the image analysis software, where the t_c measured was 41.17 s.

0 second
(CoV = 6.76)

15 second
(CoV = 3.00)

30 second
(CoV = 1.72)

60 second
(CoV = 1.37)
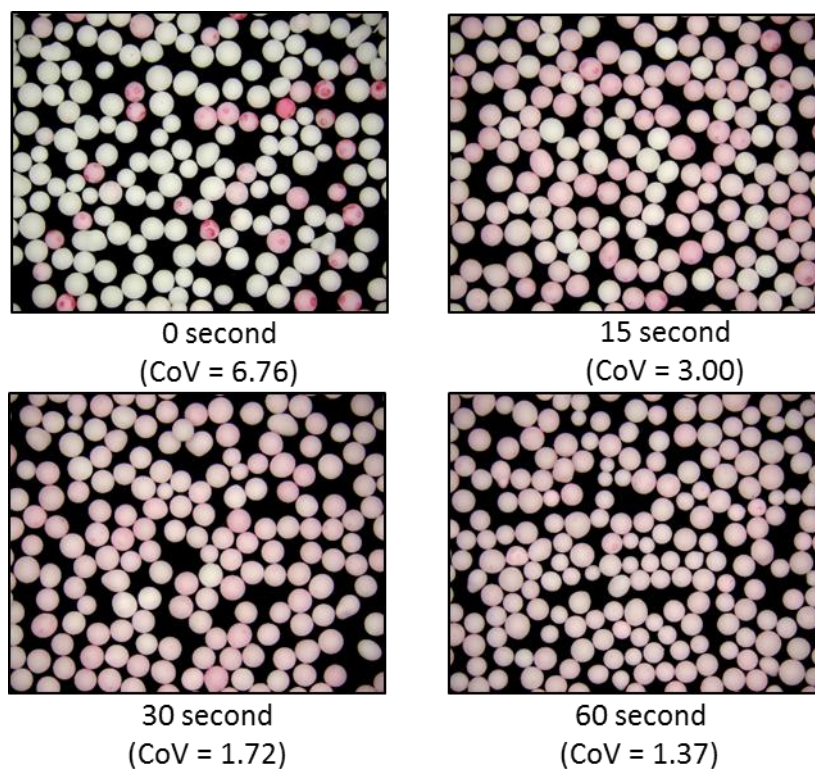
Figure 4.14. Images of coated alumina particles as a function of time

4.3 Summary

A novel image analysis system has been developed to assess and measure the liquid distribution during particle coating which has resulted in improvements being made to characterize the inter-particle coating uniformity of the coating layer compared to existing techniques (see Chapter 2, Section 2.4). This novel imaging system is accurate, easy to handle a lot of sample particles (ca. 2000 - 4000 particles per batch), and measurements and analyses can take place in a short period of time (approximately ten minutes per batch). Three main outputs can be obtained from this quantitative data analysis: (i) the extent of the liquid spreading in the system in terms of asymptotic CoV value, CoV_∞, (ii) the rate of the liquid spreading in terms of coating rate, λ and (iii) the time to reach the end of the liquid spreading in terms of the time to reach the asymptote, t_c.

By using this method, the effect of a range of formulation and operating variables on coating behaviour via contact spreading can be assessed to aid further understanding of the coating process. Furthermore, most of the pharmaceutical, food and detergent products are coloured and thus, a technique for assessing the quality of the coat based on the colour development of a coating layer could be achieved with this novel method.

CHAPTER 5

5 Investigation of the Contact Spreading Mechanism for Particle Coating in Tumbling Drums

5.1 Introduction

In this chapter, a large-scale tumbling drum was manufactured to study and understand the mechanisms of the liquid coating process in a rotating drum system. For these contact spreading only experiments, no spray system was used. Here, a proportion of a batch of particles was initially coated and added directly into the tumbling drum containing the remainder of the batch particles. This method allows for the sole study of the liquid contact spreading mechanism without the complication of the spray deposition/spreading mechanism occurring simultaneously.

These experiments used alumina particles and dyed polyethylene glycol (PEG) solutions as model materials and were designed to:

° Investigate the effect of mixing time and coating liquid viscosity on contact spreading behaviour

° Investigate the effect of the tumbling regime, by changing the drum speed, on contact spreading behaviour

5.2 Experimental Methods

5.2.1 Large-scale Tumbling Drum Experiments

Here, the experimental procedure and materials used are summarised. A more detailed description is given in Section 3.4.1. For each experiment, 10% of a batch of alumina particles (232.37 g) was coated with PEG solutions of a certain viscosity and placed in a running tumbling drum containing the remaining 90% of the particles using a powder applicator (see Figure 3.14). The drum was run with a Glen Creston Ball Mill

model CA 3 and the drum dimensions used for these experiments were 325 mm x 210 mm (see Figure 3.13). Each experiment was run for a different tumbling time ranging from 0 s – 280 s and experimental conditions for all data sets are shown in Table 5.1. A total of 21 datasets were collected comprising 275 individual experiments.

The experimental work for the effect of viscosity on contact spreading experiments were all carried out at 50 rpm. This drum speed was selected as a cascading regime was observed at this speed. This cascading regime was preferred as most industrial drums operate in this regime due to low energy consumption and providing good mixing (Norouzi, *et al*., 2015). The viscosity was varied by using the same concentration of dyed PEG solutions with different molecular weights (MW) of PEG: 4000 MW, 10000 MW, 20000 MW and 35000 MW.

For effect of tumbling regime on contact spreading behaviour, the experimental work performed was split into two sets. The first set used the lowest PEG viscosity, PEG 4000 MW, as a coating solution while the second set used the highest PEG viscosity, PEG 35000 MW solution. Both sets of experiments were carried out at three different drum speeds to produce three different tumbling regime behaviours: rolling (20 rpm), cascading (50 rpm) and cataracting regime (85 rpm).

|Rolling regime
(20 rpm, Fr = 0.047)|Cascading regime
(50 rpm, Fr = 0.294)|Cataracting regime
(85 rpm, Fr = 0.848)|
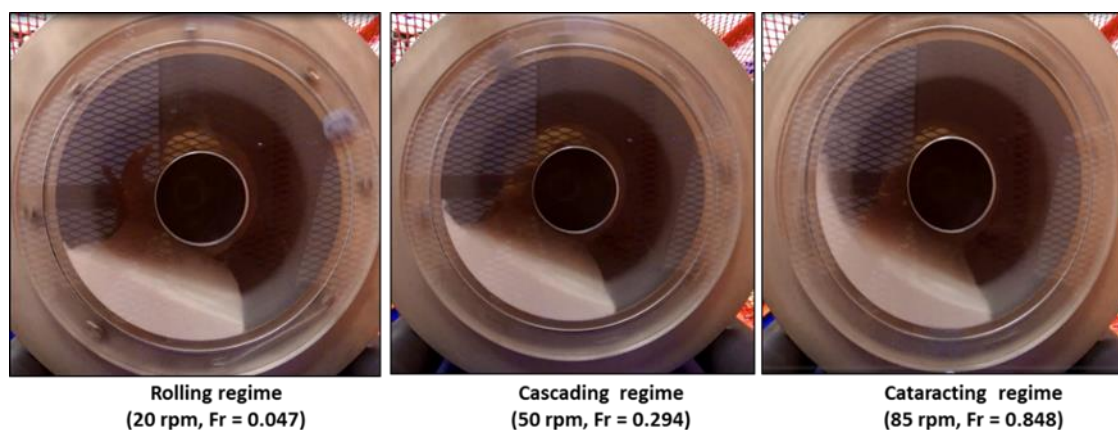
Figure 5.1. Bed surface shape as a function of tumbling regimes

Figure 5.1 depicts typical cross-sectional views of bed surface shape as a function of tumbling regime. It can be seen that different tumbling regimes showed a different bed

surface shape. In the rolling regime, the bed surface is approximately flat compared to the other two regimes, where the bed surface appears more curved and the radius of the curvature decreases with the drum speed. It is also can be observed that with an increase in the drum speed, the slope of the right (lower) half of the bed decreases, whereas the slope of the left (upper) half of the bed increases. This behaviour of the particle bed is similar to previous findings when the drum speed was changed at a constant fill level (Delele *et al*., 2016; Santomaso *et al*., 2003).

Table 5.1 lists all the experimental conditions used for all the data sets. In the results and discussion section, Section 5.3, all liquids will be described in terms of their viscosity values, while the different tumbling speeds used will be described in terms of their tumbling regime (Table 5.1).

Table 5.1. Operational parameters and conditions for all data sets of tumbling drum contact spreading experiments

Experiment run	Coating liquid (mPa.s)	Drum speed/regime (rpm)	Froude number (-)	Fill level (%)	Tumbling time (s)
1 (3 runs)	50% PEG 4000 (137)	50 (cascading)	0.294	10	0 – 60
2 (3 runs)	50% PEG 10000 (665)	50 (cascading)	0.294	10	0 – 100
3 (3 runs)	50% PEG 20000 (3115)	50 (cascading)	0.294	10	0 – 140
4 (3 runs)	50% PEG 35000 (15489)	50 (cascading)	0.294	10	0 – 200
5 (2 runs)	50% PEG 4000 (137)	20 (rolling)	0.047	10	0 – 120
6 (2 runs)	50% PEG 4000 (137)	85 (cataracting)	0.848	10	0 – 40
7 (3 runs)	50% PEG 35000 (15489)	20 (rolling)	0.047	10	0 – 280
8 (2 runs)	50% PEG 35000 (15489)	85 (cataracting)	0.848	10	0 – 120

5.2.2 Image Analysis

Samples for image analysis were prepared and analysed as described in Section 4.1. The coated particles were visualized using the imaging system. LabVIEW software was used for analysing the inter-particle coating variation give a quantitative determination of coating behaviour, i.e. the coefficient of variation (CoV).

5.3 Results and Discussion

5.3.1 Effect of Coating Liquid Viscosity on Contact Spreading

Figure 5.2 shows the results of a typical data series for the frequency distribution of alumina coated with a different viscosity of PEG solutions; 137 mPa.s, 665 mPa.s, 3115 mPa.s and 15489 mPa.s, all dyed with 1% Acid Red. Note that, for each graph, not all-time series are shown for visualisation purposes. The full data series are given in Appendix C1. Figures 5.2 (a-c) show a similar distribution trend; with an increase in a mixing time from 0 s to 10 s, there was a shift in the % of red dye to slightly higher values. It is also seen for all PEG solutions that an increase in mixing time leads to narrower distributions, indicating a more uniform coating. Figure 5.2d also shows a similar trend, however, the shift of the % red dye to slightly higher value seems to be slower (0 s to 20 s) until it reaches narrower distribution.

To determine the inter-particle coating uniformity within a batch of particles, the standard deviation and average % red dye of coated particles are used. First, all data sets for mean % red dye of coated alumina with 4 different viscosities of PEG solutions as a function of mixing time are shown in Figure 5.3. From Figure 5.3, the % mean of red dye for all different viscosities seems to reach a uniform value within approximately 10 - 20 seconds. This correlates with the distributions seen in Figures 5.2. It is expected that the % red should be the same throughout the mixing time. However, in Figure 5.3, there is a slight increase in % red value for all viscosities at low mixing times.
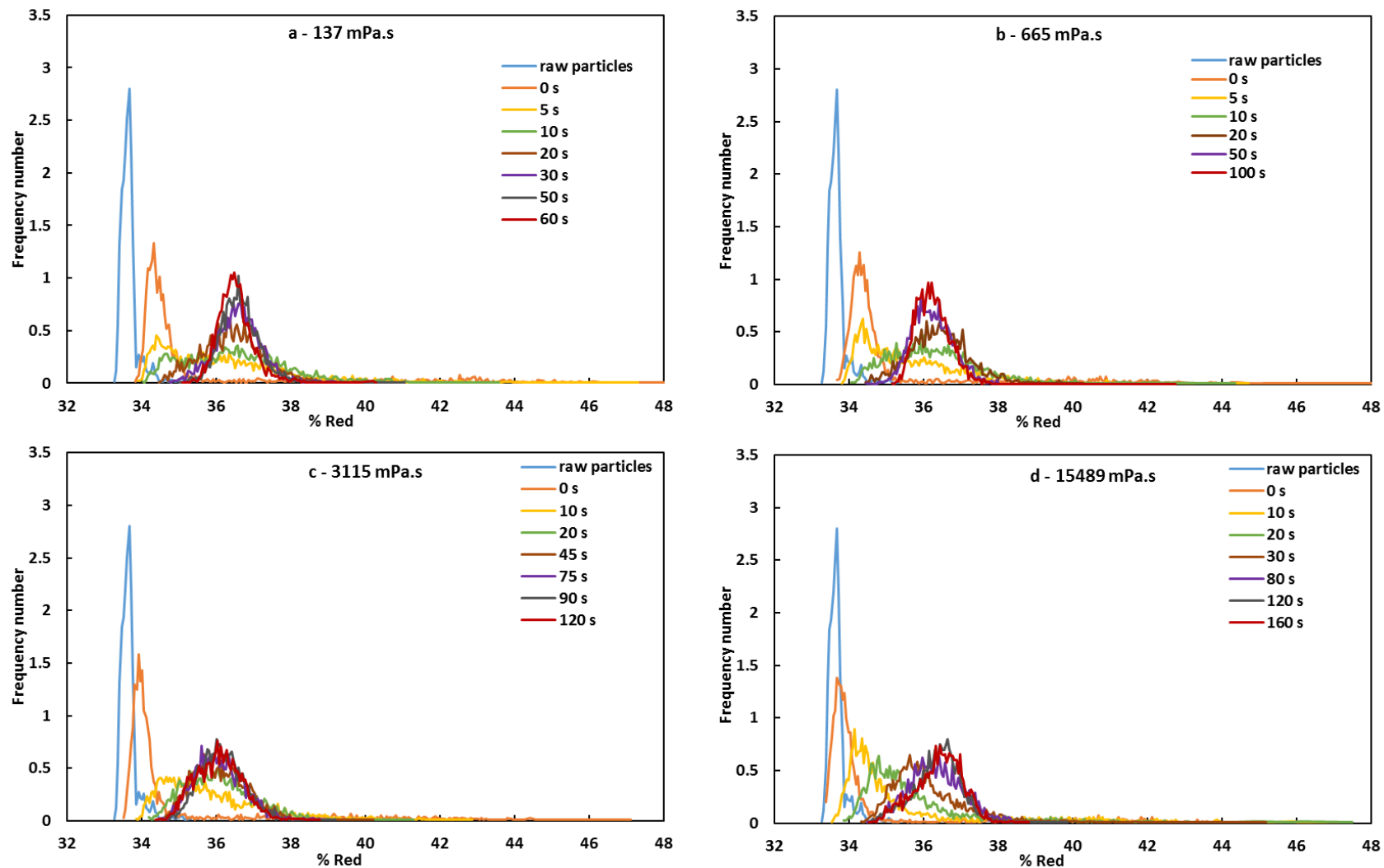
Figure 5.2. Coating evolution of alumina particles coated with different viscosity PEG solutions, a: 137 mPa.s ; b: 665 mPa.s ; c: 3115 mPa.s and d: 15489 mPa.s

The reason for slightly lower values at lower mixing time could be due to the color analysis. At lower mixing time, particularly at 0 seconds, a percentage of the particles will be relatively thickly coated, and the color value may not quite reflect the amount of dye present on these particles. As the mixing time proceeds and contact spreading occurs, the color will be more evenly distributed across the batch of particles and this phenomenon will diminish; indeed, after 10-20 seconds mixing time, the % red value appears to remain relatively constant.
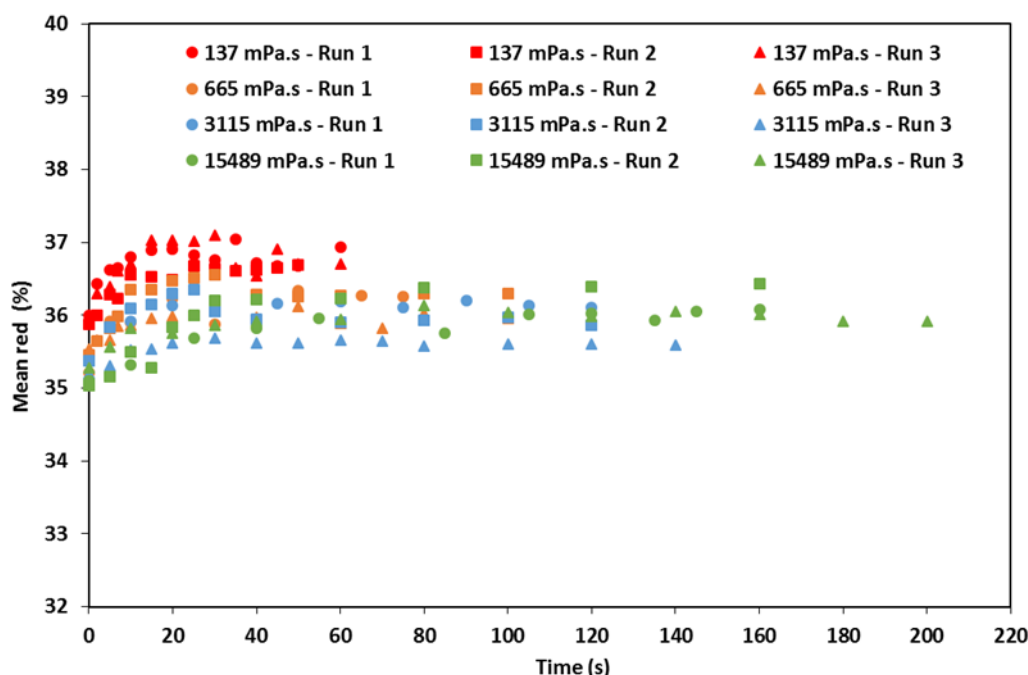
Figure 5.3. Mean % red dye as a function of mixing time

Moreover, different values of mean % red dye data series for different PEG viscosities were also revealed (Figure 5.3); higher mean % red values are recorded for the lower viscosity PEG solution. This is also shown in Figure 5.4, which shows images of the pre-coated particles. The mean % red of 10% pre-coated alumina particles decreases with PEG viscosity even though the same concentration of solid PEG and dye are used for each solution. This is due to the different PEG molecular weights used contributing to the slight changes in the red intensity of the solutions.
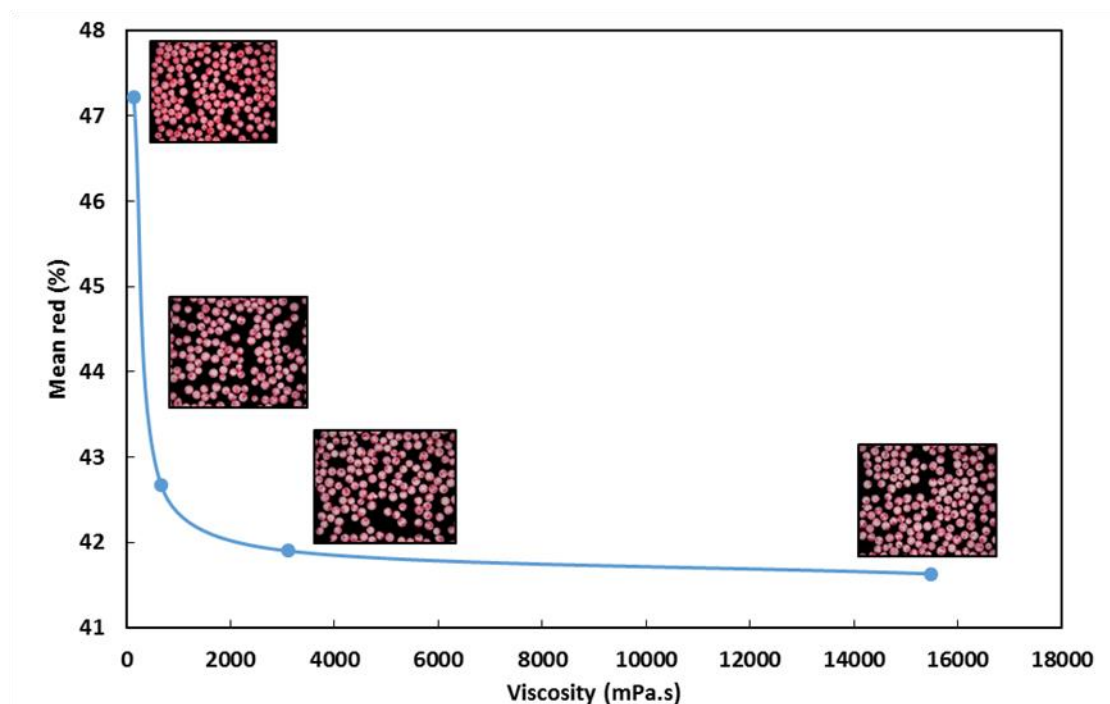
Figure 5.4. Mean % red dye and corresponding images as a function of PEG solution viscosity for 10 % pre-coated alumina beads

To quantify the degree of liquid spreading in the particle bed, the coefficient of variation, CoV, was determined based on Eq. 4.1 as explained in Section 4.2.1.1. A low CoV value infers more uniformity between coated particles. Figure 5.5 (a-d) shows the coefficient of variation (CoV) plotted as a function of mixing time for each viscosity. All the data series are presented in triplicate for each viscosity to check for the reproducibility of the data. From the graphs, it is seen that all the data at specific viscosities are reproducible. Kalbag and Wassgren (2009) simulation findings reported that the CoV decreases as the coating fraction increases and the coating time increases. This result was consistent with actual experimental data (contact spreading only) and previous works which have investigated non-contact spreading only experiments with the effect of spray zone area (Pandey *et al*., 2006; Sahni and Chaudhuri, 2011; Toschkoff and Khinast, 2013). The fact that coating fraction increases with mixing time means that the fraction of red dye-coated particles is larger than uncoated particles, thus the uniformity of coating increases. The results show (Figure 5.5) that as mixing time increases, the coating variability for alumina particles coated with different viscosity liquids decreases. This indicates that the coating becomes more uniform with time and the liquid distributes via

107

contact spreading within the drum. Moreover, the CoV value for all the data series appears to reach an asymptotic value at different mixing time.

Figure 5.6 shows all the data series for all viscosities plotted together and the asymptotic CoV value appears to be similar for all viscosities used. However, the initial CoV values for each data series are slightly different. There are two likely causes for the differences in CoV value at early time points; the difference in initial red intensity color (see Figure 5.4) and also the wetting properties of different solution viscosities. Therefore, for proper comparison of coating rates, all the data are normalised based on Eq. 5.1 and shown in Figure 5.7. This type of normalisation is referred to as the relative CoV throughout this thesis to differentitate between the other type of normalisation based on Eq. 4.7 as described in Chapter 4, Section 4.2.2.

$$Relative\ CoV(t) = (CoV\ (t)/CoV_0) * 100 \qquad \text{(Equation 5.1)}$$

where *CoV (t)* represents the variation at the mixing time, *t*, and *CoV$_o$* is the variation at time = 0 seconds.

As can be seen in Figure 5.7, the relative CoV data series for different viscosities of PEG solutions reach a similar asymptotic CoV value after a certain mixing time. However, the CoV values exhibited with time depended on the viscosity of the PEG solution; a lower viscosity showed a quicker decrease in CoV value and the curves are steeper compared to higher viscosity. This could be related to the effect of viscosity on liquid bridge strength and rupture mechanisms which influence the contact spreading process. Findings by Mazzone *et al*., (1987) found that the strength of the dynamic bridge is dominated by viscous forces and the magnitude order is stronger than a static bridge (attraction by surface tension only), especially for higher viscosity. Thus, it needs a higher force to rupture the bridge between particles.
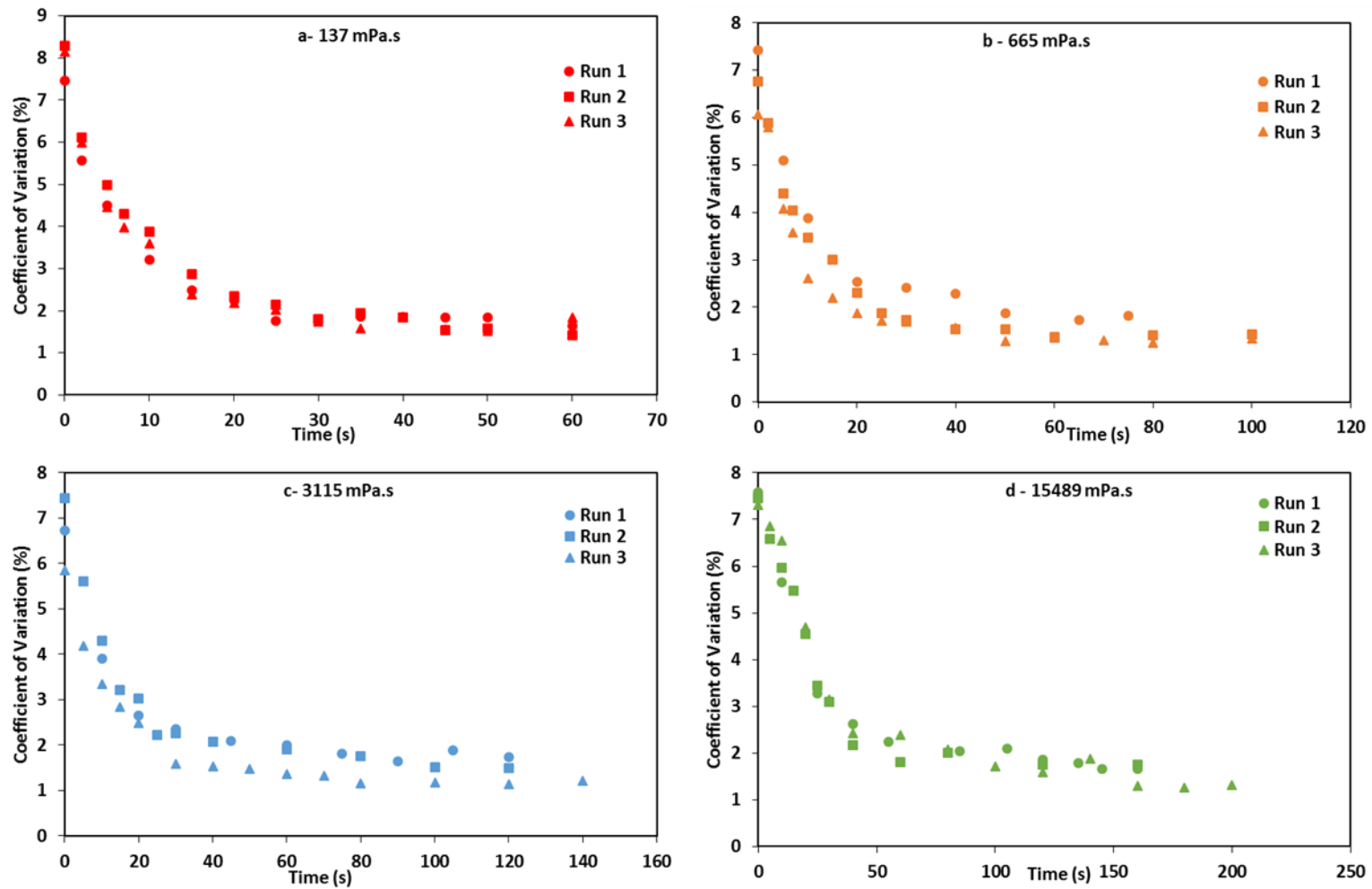
Figure 5.5. Coefficient of variation as a function of mixing time for alumina particles coated with different PEG viscosities for all data series, a: 137 mPa.s ; b: 665 mPa.s ; c: 3115 mPa.s and d: 15489 mPa.s
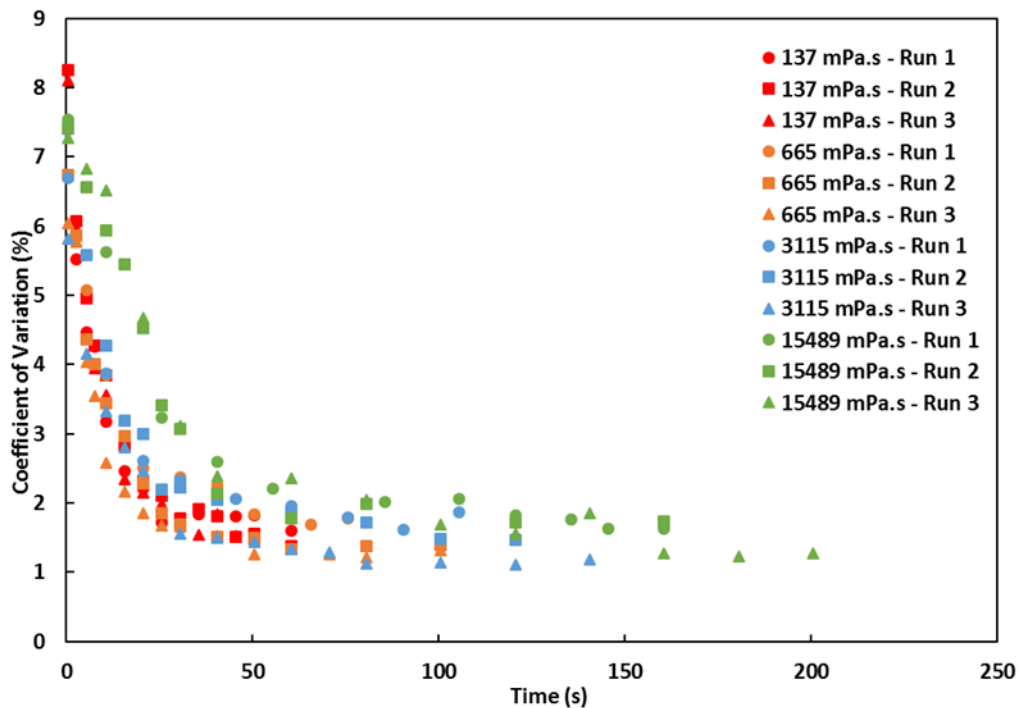
Figure 5.6. Coefficient of variation as a function of mixing time for alumina particles coated with different PEG viscosities
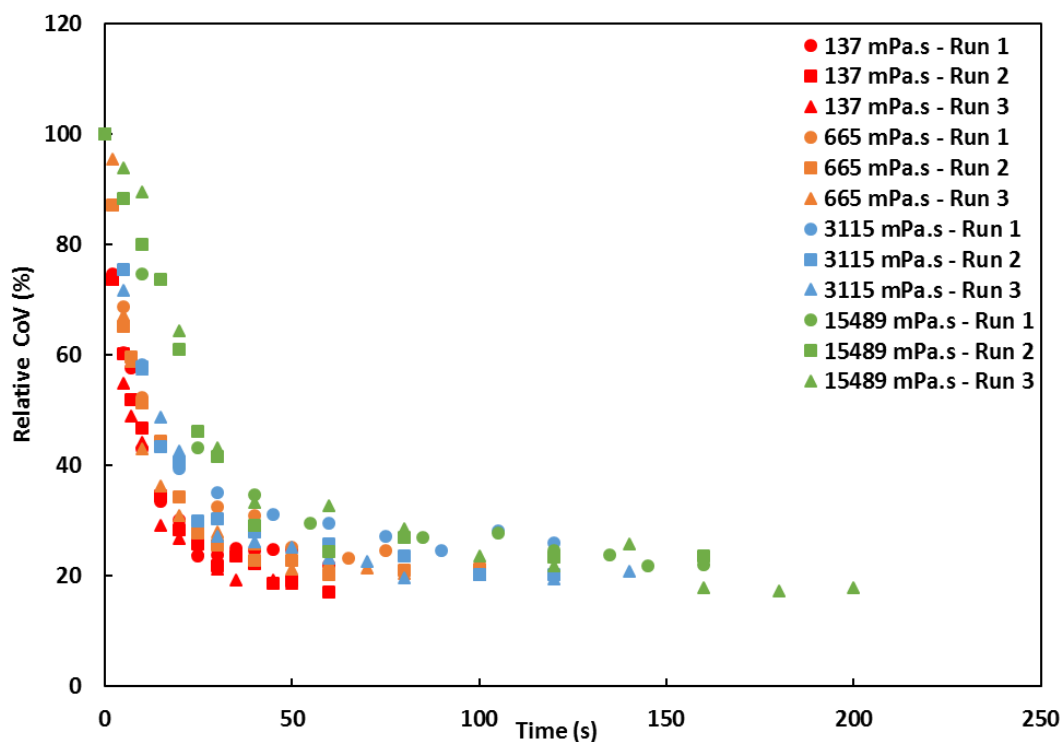
Figure 5.7. Relative coefficient of variation as a function of mixing time for alumina particles coated with different PEG viscosities

To determine the time to reach an asymptotic CoV value, t_c, and the coating rate, λ, an exponential decay curve, was fitted to each data set, normalised between CoV_o and the average CoV_∞ (Eq. 4.7). This curve fitting method was applied as the relative asymptotic CoV reaches a similar value for all viscosities used (Figure 5.8). The fitting method was based on Eq 4.2 and Eq. 4.7 as explained in Section 4.2.2 and shown in Figure 5.8. From this figure, all data series appeared to fit well with the fitting curve, supported by a reasonably high regression coefficient of determination, R^2 value. All the measured parameters are summarised in Table 5.2.
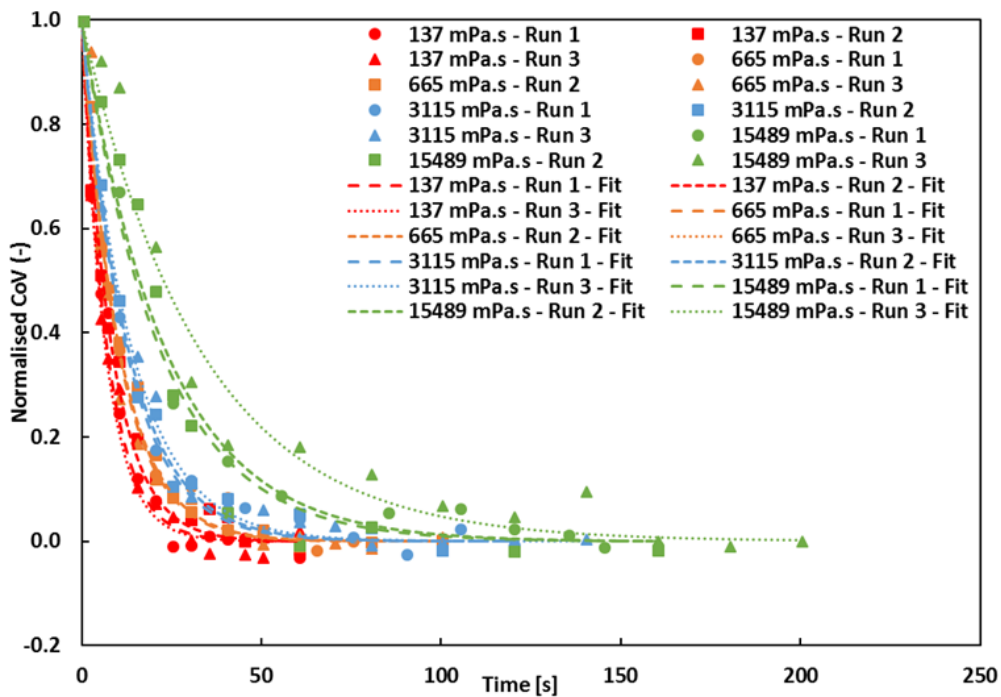
Figure 5.8. All data series of the normalised (between CoV_o and average CoV_∞) coefficient of variation and fitted decay curves as a function of mixing time for different PEG viscosities

Figure 5.9 shows an average normalised CoV and fitting curve for all viscosities used plotted as a function of time. The error bars represent standard deviations of repeated values of CoV obtained after repeated experiments. It shows that some data are presented with large error bars or with no errors bars due to insufficient sample particles to repeat the exact same mixing times for each data series. The mixing times for the second and third experimental runs were defined and repeated based on the maximum time needed for each viscosity to reach the end of the coating process (i.e. longer mixing time needs

for higher viscosity). The error bars for highest viscosity in Figure 5.9 are higher compared to lower viscosity might be due to the variation in fraction of wet agglomerates formed mainly at initial mixing time. A higher viscosity formed a stronger wet agglomerate, and the contact spreading mechanisms are highly depends on the rupture of these wet agglomerates in the system.
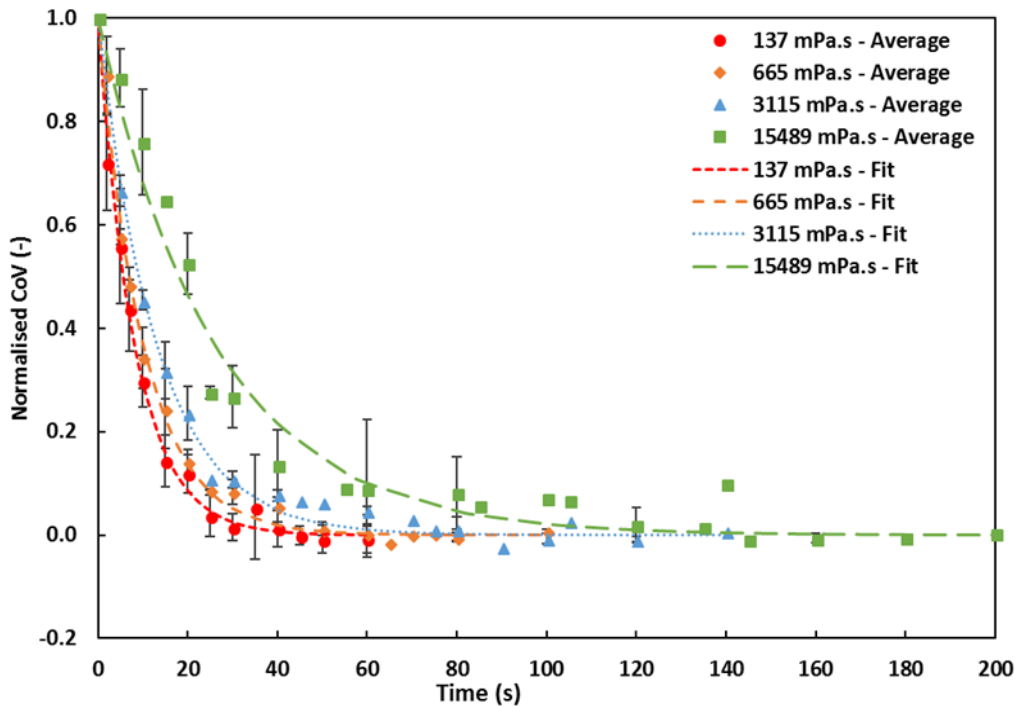
Figure 5.9. Average normalised (between CoV$_o$ and average CoV$_\infty$) coefficient of variation and fitted decay curves as a function of mixing time for different PEG viscosities. Error bars represent standard errors

According to Table 5.2, when comparing all the PEG solution viscosities used, the coating rate clearly decreases with an increase in viscosity, indicating that the contact spreading process is slower at higher viscosity. Thus, the time taken to reach the asymptote value, t_c also appears to be longer at higher viscosity. Furthermore, to point out the effect of viscosity on t_c, and λ, the mean of these values is plotted as a function of viscosity and shown in Figure 5.10 and Figure 5.11. Figure 5.10 shows clearly that the λ decreases logarithmically as viscosity increases and Figure 5.11 shows that the t_c increases with an increase in viscosity.

112

Table 5.2. Fitting constants and time taken for coating completion for all data series

Viscosity (mPa.s)	Run	Coating rate constant, λ (s^{-1})	R^2	Time for 98 % coating completion, t_c	CoV % asymptote
137	1	0.14031	0.987	27.88	1.790
	2	0.11825	0.979	33.08	1.510
	3	0.15019	0.987	26.05	1.696
	Mean	**0.13625**	-	**29.00**	**1.665**
665	1	0.09746	0.991	40.14	1.803
	2	0.09502	0.994	41.17	1.404
	3	0.10561	0.983	37.04	1.292
	Mean	**0.09936**	-	**39.45**	**1.500**
3115	1	0.08052	0.993	48.58	1.762
	2	0.07689	0.992	50.88	1.586
	3	0.07152	0.992	54.70	1.174
	Mean	**0.07631**	-	**51.39**	**1.507**
15489	1	0.0304	0.990	85.46	1.704
	2	0.04291	0.964	91.16	1.839
	3	0.04578	0.969	128.68	1.289
	Mean	**0.03969**	-	**101.77**	**1.611**

Note: The asymptotic CoV value is taken as an average of the CoV values at the final time points, where there is no clear decrease in CoV values
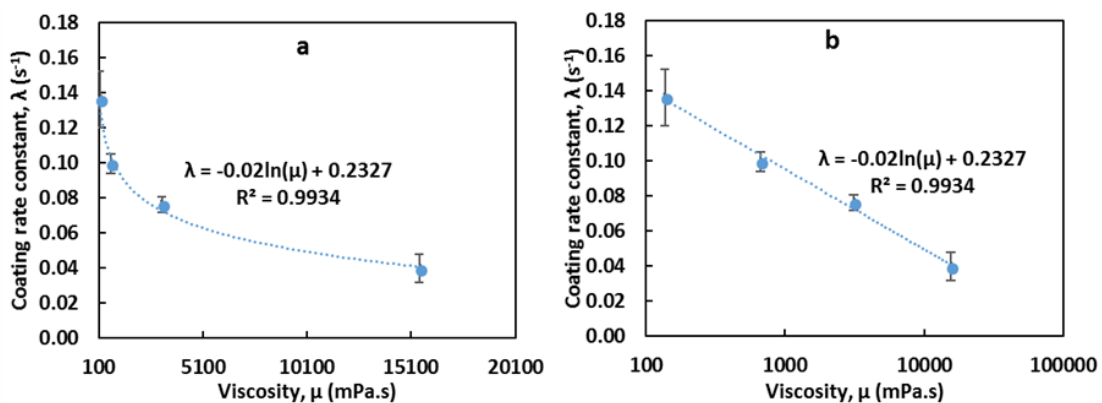
Figure 5.10. Coating rate constants plotted as a function of PEG viscosity, a) normal viscosity and b) log viscosity. Error bars represent standard deviation.
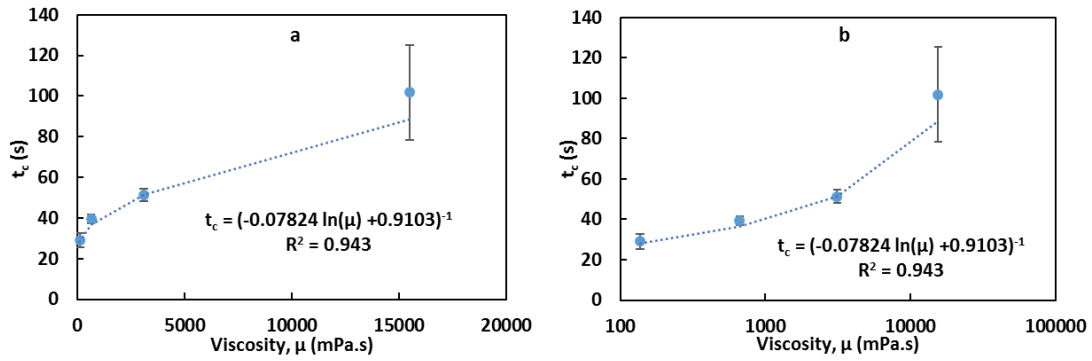
Figure 5.11. Time taken for coating completion, t_c as a function of PEG solution viscosity, a) normal viscosity and b) log viscosity. Error bars represent standard deviation.
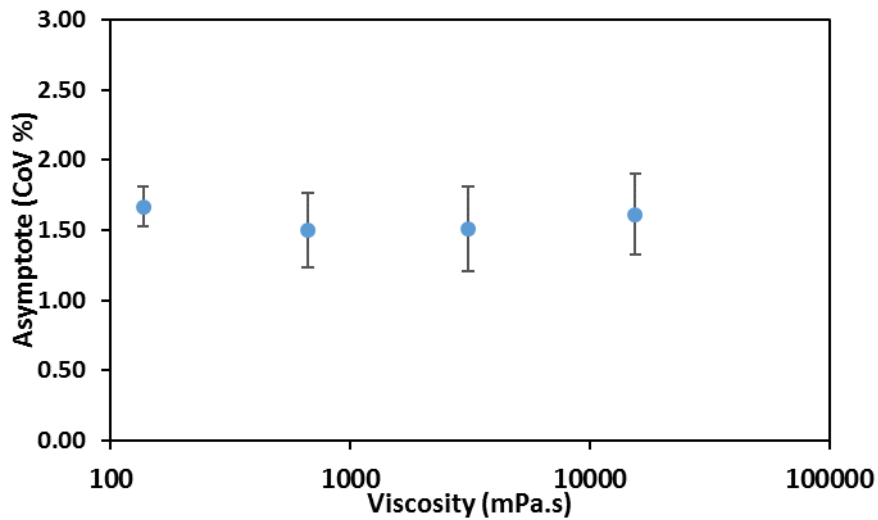
Figure 5.12. Asymptotic CoV (%) values as a function of PEG solution viscosity. Error bars represent standard deviation

Regarding the asymptote CoV value, CoV_∞, the viscosity did not significantly affect this value, which was nearly constant at 1.5-1.7% for all the PEG solutions and shown in Figure 5.12. In an ideal case, when the coating fraction is equal to one, all of the particles could be considered as equally coated and there is no variability in the coating (Kalbag *et al.*, 2008). The CoV_∞ obtained in these findings shows a minimal variation from the ideal case.

Also, based on the abovementioned results, the fitting methods used based on exponential decay curves seems to fit well with all the data sets. This fitting method is

compared with those used by previous authors (Pandey *et al.*, 2006; Shi and McCarthy, 2008; Freireich and Li, 2013) who fitted their CoV data as a function of time with a power law function. These works have been carried out in a tumbling drum with the spray system. For this, as the power law function does not hold below 1 s, the curves were only fitted above 1 s. Moreover, an extra fitting parameter was also used. A power law function was also fitted to the current data sets from 2 seconds (the earliest time considered in these experiments) and the R^2 values compared to the exponential function (this time adjusted from 2 seconds coating time) . An excel solver was used to minimise the sum of the squared difference between the theoretical and actual data points by varying the coating rate constant and thereby determining the best fit for each of the functions. Table 5.3 summarises the R^2 values for both fitting methods which were tested on one dataset for each PEG viscosity used. Both fittings gave good fits to all datasets tested ($R^2 > 0.9$). However, 10 out of 12 data sets tested show that the exponential function fits the decay of the CoV with time better where the R^2 values were slightly higher.

Figure 5.13 shows the exponential and power law function fitted to the CoV data with time for one data set for each PEG solution used. It can be seen that the exponential decay curve fitted better compared to power-law function for all PEG viscosities used. This might be related to the different system used. In this study, there was no spray involved and the spray zone can be considered constant referring to the 10% initially coated particles. The CoV might change with time depending on turnover time of this 10% wet particles within the particle bed and transfer the liquid via contact spreading. Moreover, Easo, (2017) found an exponential relationship using population balance modelling, where it is reported that exponential fit reasonably at large dimensionless times while a power law fit accurately at smaller times. In this case, it can be seen that at asymptotic CoV values, the exponential curve fit better compared to power law. Therefore, using the exponential function to fit curves to the data was considered the most appropriate and was employed throughout his work.

Table 5.3. The comparison of R² values for different fitting methods

Viscosity (mPa.s)	Run	R²	
		Exponential fit	Power law fit
131	1	0.975	0.934
	2	0.959	0.944
	3	0.971	0.959
665	1	**0.973**	0.986
	2	0.990	0.961
	3	**0.974**	0.987
3115	1	0.963	0.957
	2	0.982	0.977
	3	0.983	0.969
15489	1	0.974	0.977
	2	0.951	0.897
	3	0.957	0.939

Note: Text in bold is referred to the R² values for exponential function slightly lower than power law function
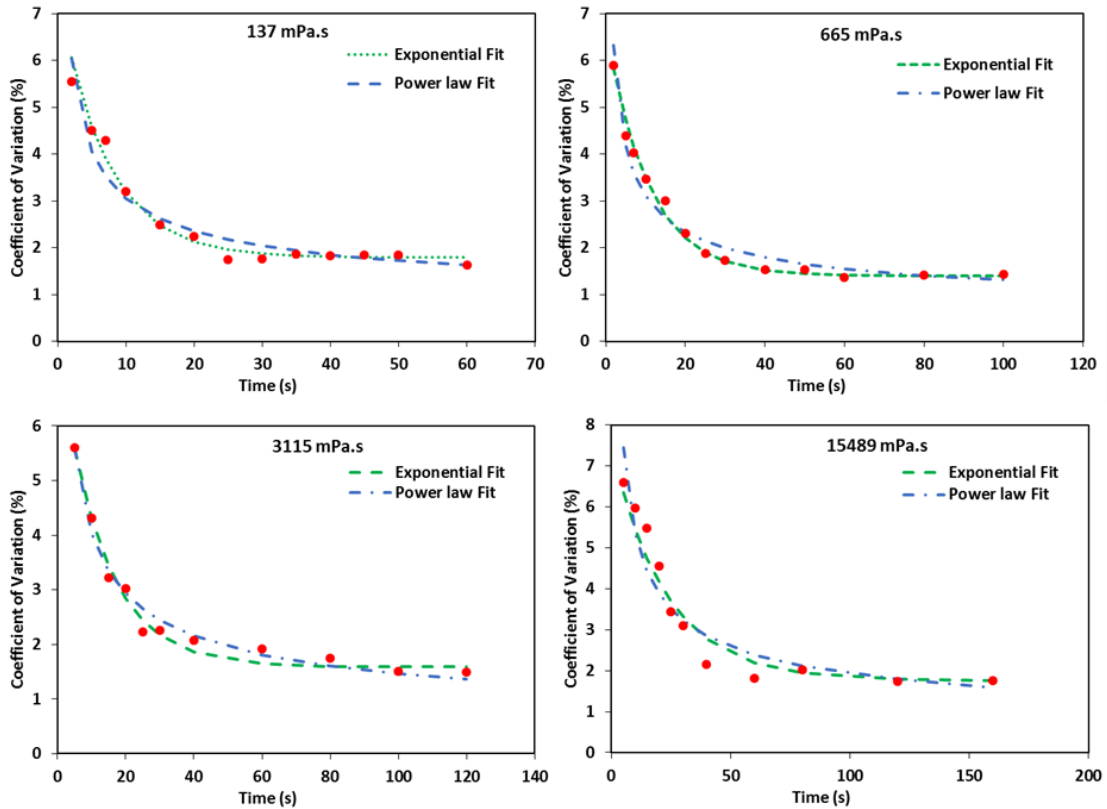
Figure 5.13. Exponential and power law function fitted to the CoV data with time for different PEG viscosities

Figure 5.14 illustrates the images of red dye-coated particles as a function of mixing time with two different PEG viscosities; 131 mPa.s from 0 – 40 s and 15489 mPa.s from 0 – 160 s. Each image captured at a different tumbling time gives visual information on coating variability of each batch. As observed in Figure 5.14, when both PEG solutions were used as a coating material, an increase in mixing time showed an increase in coating uniformity. However, it shows that a longer time was needed to reach a uniform coating uniformity for the higher viscosity solution, which revealed a slower coating process via contact spreading for higher viscosity. These visual studies correlate with the quantitative results obtained from the image analysis system.

The probable reason for this may be due to the behaviour of liquid bridge force formed during wet collisions. The overall strength of a liquid bridge consists of two distinct forces: adhesive force and viscous force. The adhesive force arises from capillary and surface tension effects while the viscous force is dependent on the viscosity of the liquid and always resists the motion of the colliding particles (Song and Turton, 2007). A capillary number (Ca) can be defined as the ratio of viscous to capillary forces (Eq. 5.2) and was calculated for all the PEG solutions as shown in Table 5.4.

$$Ca = \frac{\mu V_c}{\gamma} \qquad \text{(Equation 5.2)}$$

Here, V_c is the characteristic velocity (the linear velocity at the periphery of the drum), μ is the liquid viscosity, and γ is the liquid surface tension. According to Ennis *et al.* (1990), for low capillary number ($< 10^{-3}$), the maximum liquid bridge strength, F_{max} is dominated by the capillary force, whereas for high capillary number ($>10^0$), the viscous force dominates. In this case, Table 5.4 shows that the capillary number for majority of the solutions is more than 1, indicating that bridge strength is dominated by viscous forces, thus eliminating the dependence on capillary and surface tension. Based on the dynamic liquid bridge, viscous force here is a result of either high liquid viscosity or large relative velocity between the particles. However, the capillary number for 137 mPa.s solution is only slightly higher 1. Thus, in this case, the capillary and viscous forces are equally important, and the capillary force cannot be neglected.
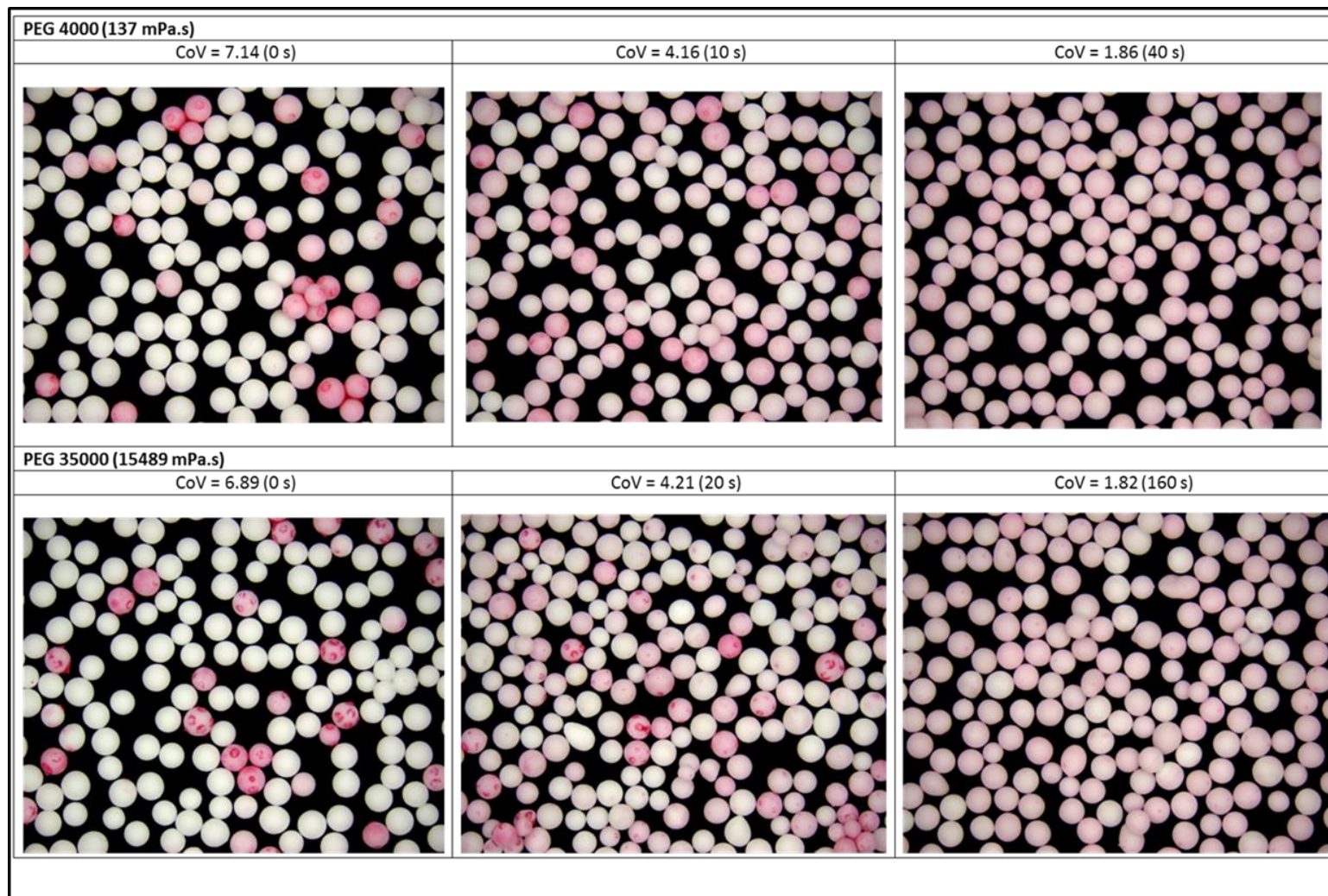
Figure 5.14. Images of coated particles as a function of tumbling time at two different PEG viscosities (137 mPa.s and 15489 mPa.s)

Table 5.4 Capillary number for each PEG solution viscosity

Viscosity (mPa.s)	Capillary number (-)
137	1.37
665	6.59
3115	30.65
15489	154.71

As the capillary force can be neglected for the three highest viscosity solutions, the liquid bridge strength is approximated by its viscous component, which can be predicted using lubrication theory (Ennis *et al.*, 1990). This force consists of components in both the normal and tangential directions given by Eq. 5.3 (normal direction) and Eq. 5.4 (tangential direction) (Shi and McCarthy, 2008).

$$F_{v_n} = 6\pi\mu R^* v_n \frac{R^*}{S} \qquad \text{(Equation 5.3)}$$

$$F_{v_t} = \left(\frac{8}{15} ln \frac{R^*}{S} + 0.9588 \right) 6\pi\mu R^* v_t \qquad \text{(Equation 5.4)}$$

Here, $1/R^* = 1/R_1 + 1/R_2$, μ is the fluid viscosity, v is the relative velocity of the spheres (normal and tangential), R_1 and R_2 are the radii of the two particles, and S is the separation between particles. This first order dependence shows that liquid viscosity can have a large impact on the liquid bridge strength, the contact spreading and, therefore, the ultimate CoV of the system. In addition, Eq. 5.3 also shows a squared dependence on the particle radius, however, for this system the effect of particle size was not investigated. Figure 5.15 plots the coating rate constant, λ, and time to complete the coating process, t_c against the liquid bridge force multiplied by the separation distance ($F_{vn}*S$). It shows that as $F_{vn}*S$ values increases, the λ decreases, while the t_c increases. This observation supports the fact that the viscosity contributes to the liquid bridge strength, thus influencing the contact spreading behaviour.
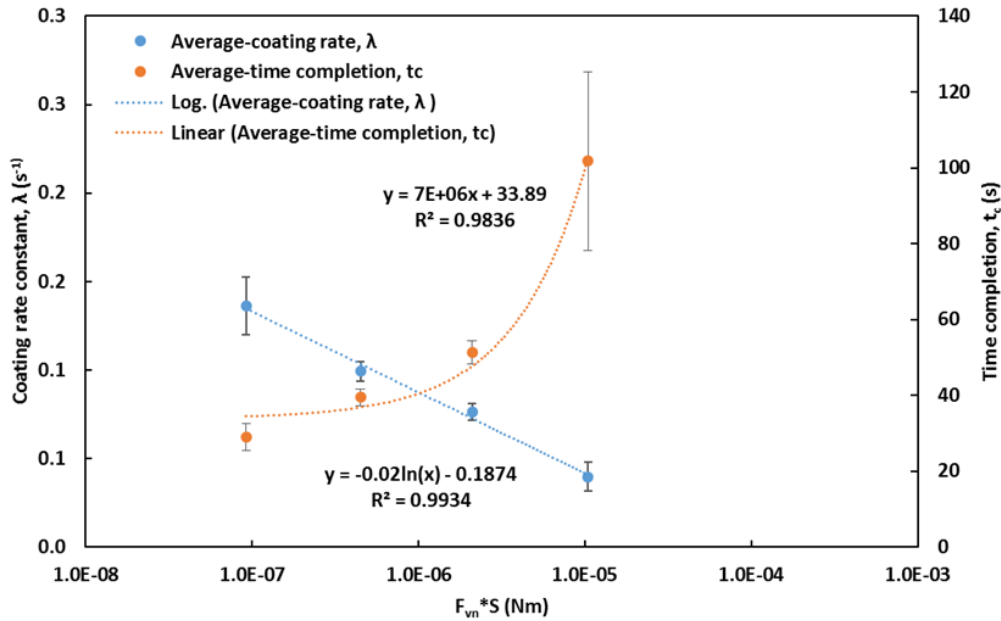
Figure 5.15. Coating rate constants and time completion plotted as a function of liquid bridge force multiplied by the separation distance of two particles. Error bars represent standard deviation.

For the higher viscosity solution, at a similar tumbling time, the images indicated higher intra-particle coating variability based on the localised spots of intense red color observed. This could be linked to agglomerate formation and liquid bridge rupture mechanisms occurring in the early stage of the process. The localised red spots can also be seen at 0 s for lower viscosity, but these disappeared more quickly with time. This might be due to higher wetting properties of the lower viscosity solution (indicated by a lower contact angle, see Section 3.4.1), where it will wet the solid surface more efficiently after liquid bridge rupture and not leave localised spots of the coating solution.

The wettability of the different PEG solutions used on a layer of fine alumina particles are illustrated in Figure 5.16. This figure shows that with an increase in viscosity, the base width of the droplet decreases while the drop height increases meaning that a higher viscosity reduces the maximum spreading diameter of the drop. Based on this, when the liquid bridges are formed from the collision of wet particles, it is possible that the higher viscosity solution does not spread on the particle surface as well as the lower viscosity solution and if this is followed by rapid drying, more liquid binder will be trapped within the agglomerates. When these particles separate, more viscous energy

dissipation occurs during the elongation of the bridge. Thus, at lower mixing time, once the bridge ruptured, more localised red spots can be seen (Figure 5.14) compared to lower viscosity. Moreover, it is also reported that rupturing of the liquid bridge happens at a larger inter-particle distance for higher contact angle (Hoornahad *et al*., 2015).

As a conclusion of this section, it appears that mixing time, coating liquid viscosity and wetting properties influence the liquid transfer through contact spreading in the tumbling drum. The difference in coating behaviour observed when using different viscosities is most likely due to the effect of viscosity on liquid bridge strength, in terms of the formation and rupture of the liquid bridges. The knowledge of these mechanisms could contribute greatly to understanding more about contact spreading. Therefore, investigating the effect of tumbling speed will be important, as higher tumbling speeds may favour quicker rupture of the bridges. The results for the effect of tumbling speed (tumbling regime) are presented in the following section.
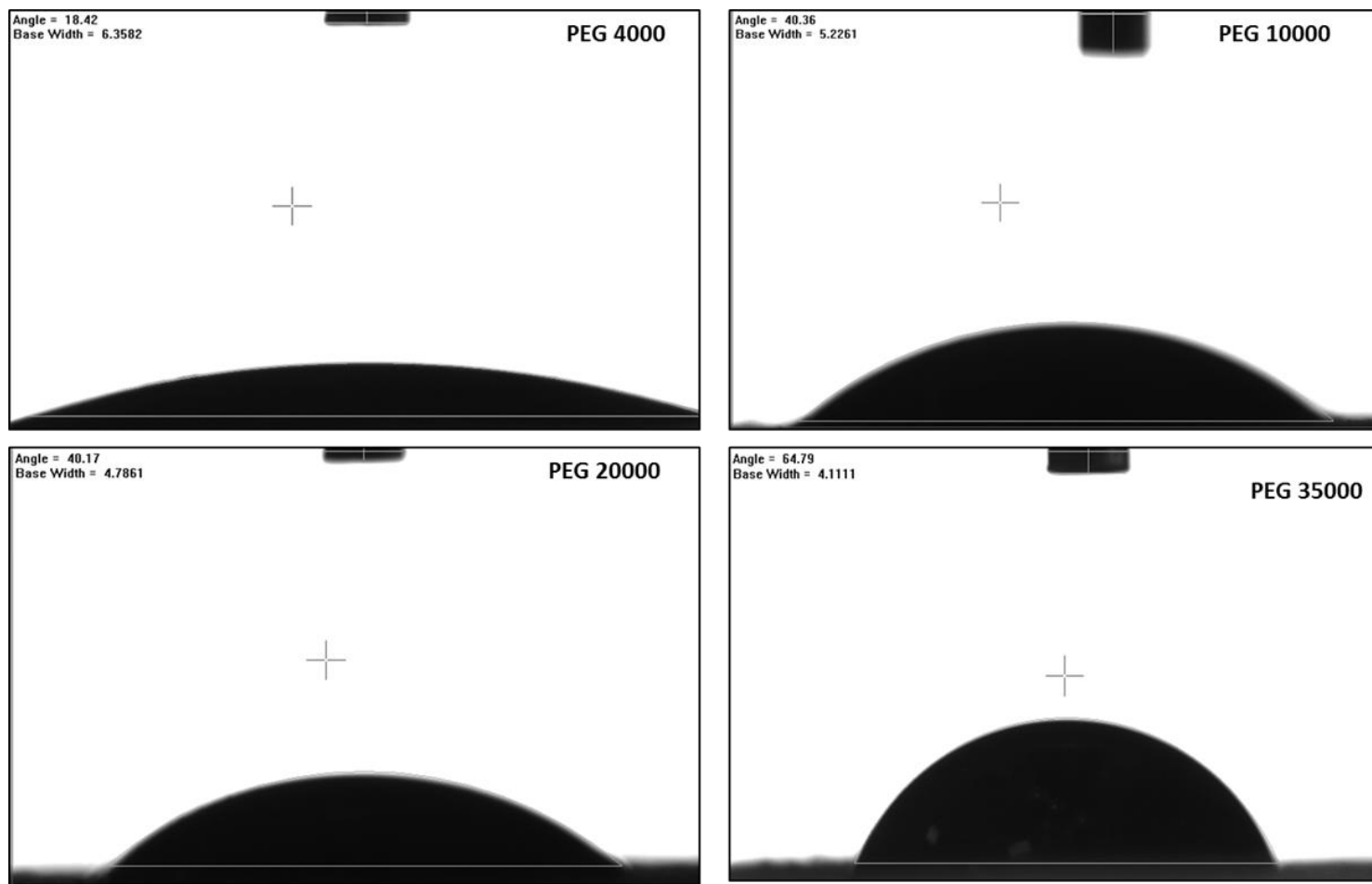
Figure 5.16. Snapshot of alumina fine particle layer-PEG solution after 3 minutes measurement. The contact angles are (2 - 5 $^\circ$) lower than the originally measured contact angle (see Section 3.4.1). Note: PEG 4000 MW (angle =18.42°, base width =6.3582 mm); PEG 10000 MW(angle=40.36°, base width=5.2261 mm); PEG 20000 MW (angle=40.17°, base width=4.7861 mm) and PEG 35000 MW (angle=64.79°, base width=4.1111 mm)

122

5.3.2 Effect of Tumbling Regime on Contact Spreading

In this section, results for effect of different tumbling regimes on contact spreading in a tumbling drum are discussed. Here, only two different PEG viscosities were chosen from the previous study; the lowest and the highest viscosity (137 mPa.s and 15489 mPa.s) due to time constraint and insufficient sample particles.

Figure 5.17a-c and Figure 5.18a-c show the results of a typical data series for the frequency distribution of alumina coated with two dyed PEG solutions (137 mPa.s and 15489 mPa.s) at three different tumbling regimes; rolling, cascading and cataracting regimes. For each data series, not all time points for that series are shown for visualisation purposes. The results for all data series are given in the Appendix C2. From both figures, a similar pattern to the effect of viscosity parameter can be observed here. It shows that with an increase in mixing time, the coating evolution shifts to a higher % red intensity and eventually reaches a constant distribution. When considering the same viscosity of PEG solution used, an increase in tumbling speed contributes to a narrower distribution and reaches a constant % red distribution faster. This shows that the coating uniformity between the particles in a batch increases with the tumbling speed (Appendix C4).
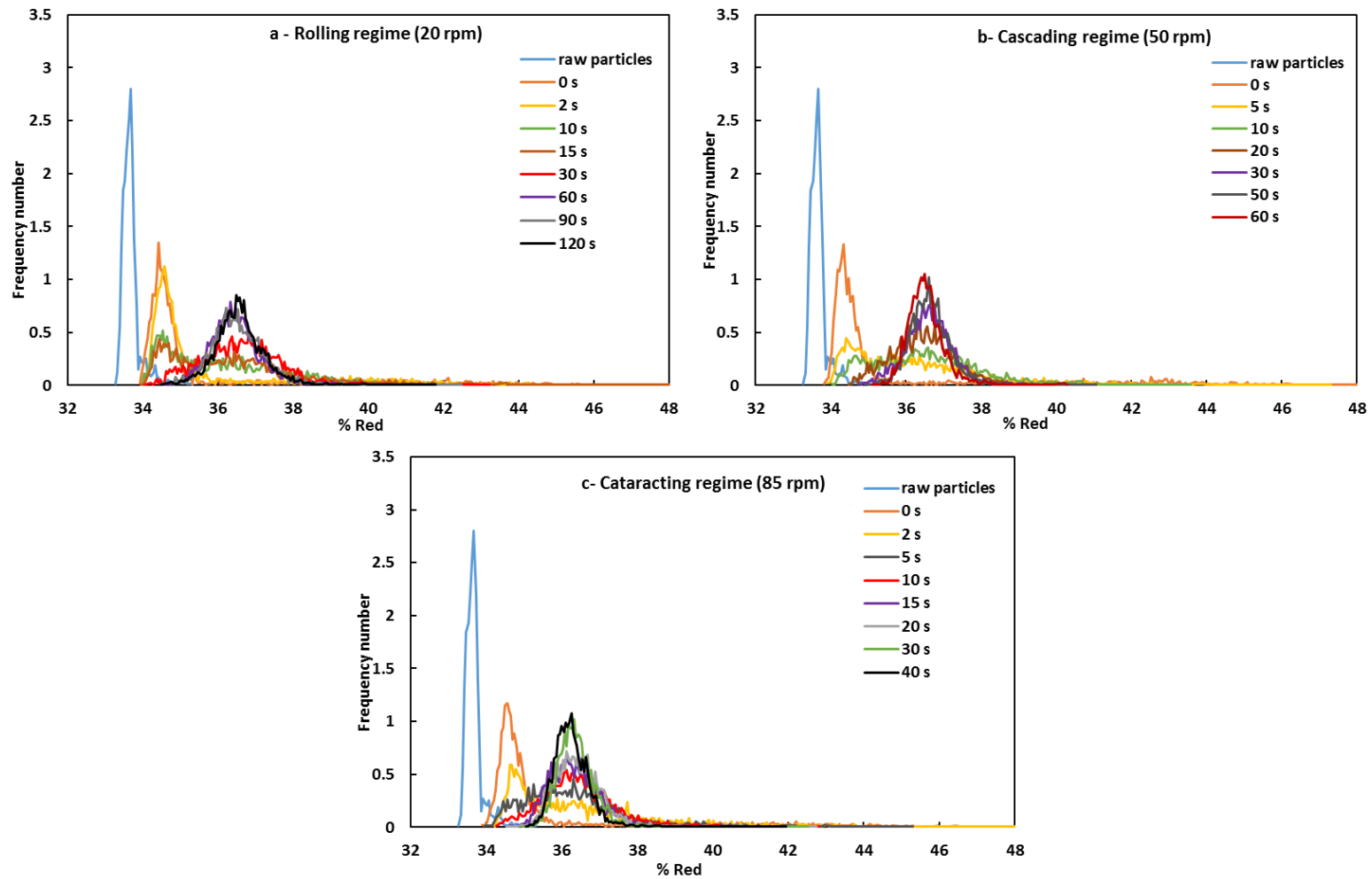
Figure 5.17. Coating evolution of alumina coated with PEG 4000 MW (137 mPa.s) at different tumbling regimes, a: rolling regime; b: cascading regime and c: cataracting regime (note that not all time points for each data series are shown for visualisation purposes)
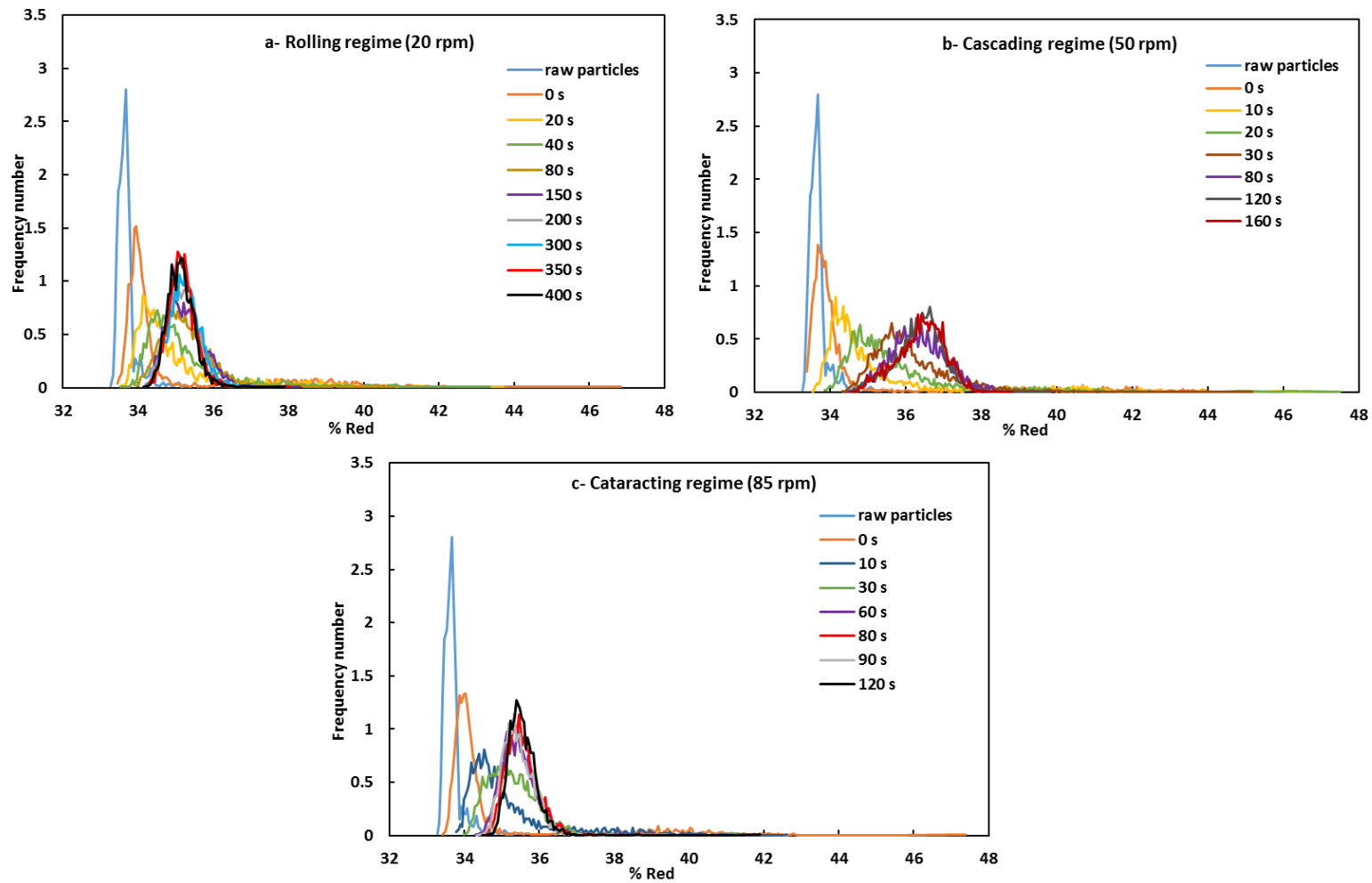
Figure 5.18. Coating evolution of alumina coated with PEG 35000 MW (15489 mPa.s) at different tumbling regimes, a: rolling regime; b: cascading regime and c: cataracting regime (note that not all time points for each data series are shown for visualisation purposes)

Figures 5.19 and 5.20 show the coefficient of variation, CoV and relative CoV plotted as a function of time. The CoV was determined based on Eq. 4.1 as explained in Section 4.2.1.1. All the data series for each tumbling regime are presented for both PEG viscosities; 137 mPa.s and 15489 mPa.s. From Figure 5.19a and 5.20a, it can be seen that the raw CoV data for both PEG viscosities used at different tumbling regimes decrease as time progresses and eventually plateau to a similar CoV value after a certain time. Normalisation of the data to give the same initial CoV values at 0 s (Figure 5.19b and 5.20b) also follow this trend.

It can be clearly seen from the data series for both PEG viscosities (Figure 5.19b, 5.20b) that the coating variability decreases more rapidly with increasing tumbling speed. All viscosities are observed to reach similar asymptotic CoV value. For both PEG solution viscosities, even though all the data series do not significantly differ between tumbling regimes, a similar trend is observed, where the coating variability for the rolling regime indicates the highest variability followed by cascading and cataracting regime (see Figures 5.19b and 5.20b). In order to determine the coating rate, λ, and t_c, the exponential decay fitting procedure described in Chapter 4, Section 4.2.2 was used. The value of the fitting constant (coating rate) obtained from the decay curve fitted to the all normalised data series (Figure 5.21) is summarised in Table 5.5.

The fitting curves largely fit well to the raw data series as the R^2 values obtained are in the range from 0.964 to 0.992, approaching 1, meaning that the accuracy of the fit approaches 100% (Table 5.5). From Table 5.5, it is shown that the coating rate constant, λ, significantly increased with the speed of the drum (see Figure 5.23). Note also that the effect of increasing speed also depends on the liquid viscosity. At the same tumbling regime, as expected, the lower viscosity shows a higher coating rate (Figure 5.23) and this behaviour can be related to the effect of viscosity described in the previous section. Images of the coated particles as a function of tumbling time for both viscosities at different tumbling regimes also show these trends and are given in Appendix C4 and C5.
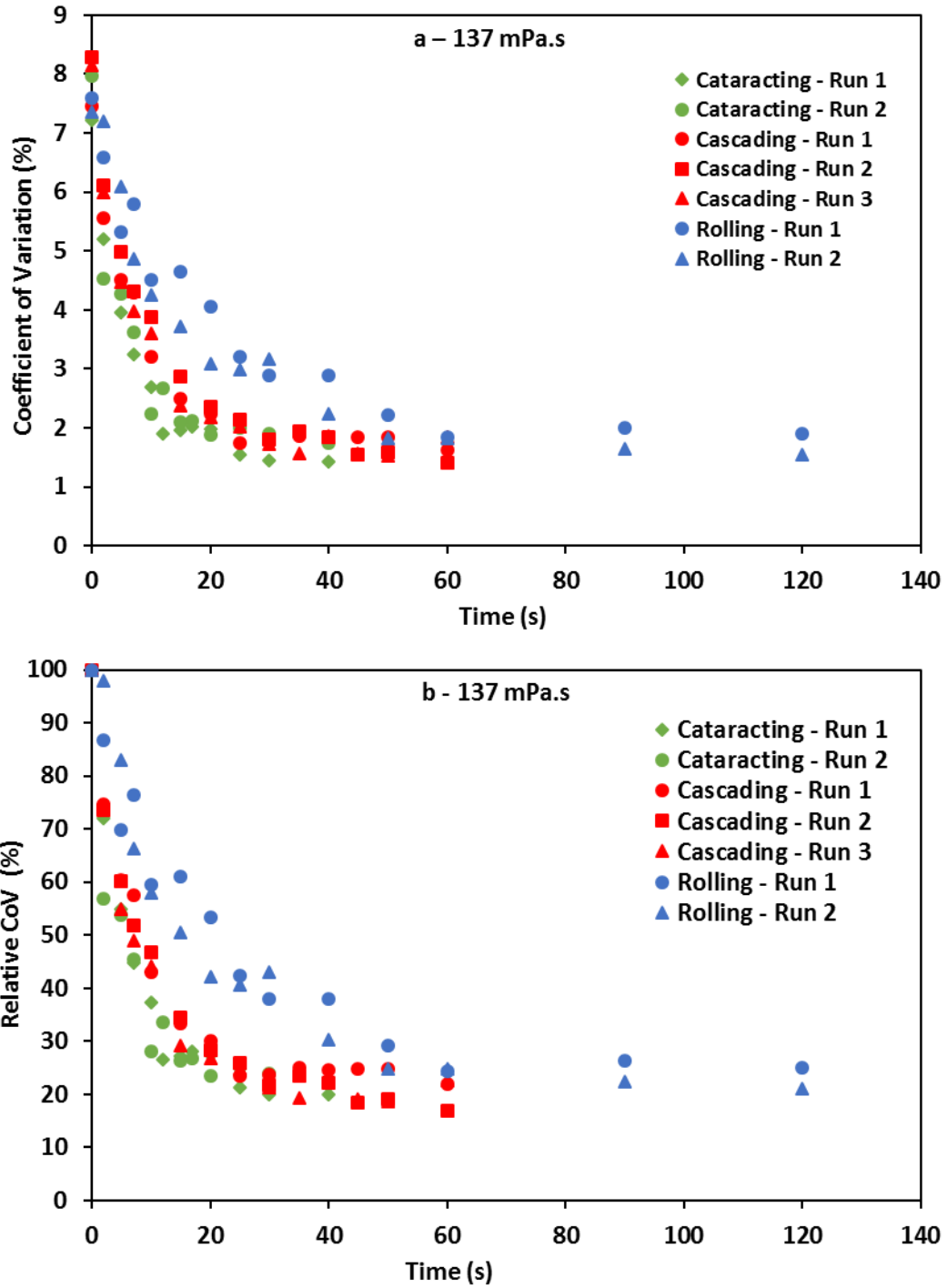
Figure 5.19. a) Coefficient of variation (CoV) and b) Relative CoV as a function of mixing time for alumina particles coated with PEG 4000 MW (137 mPa.s) at different tumbling regimes
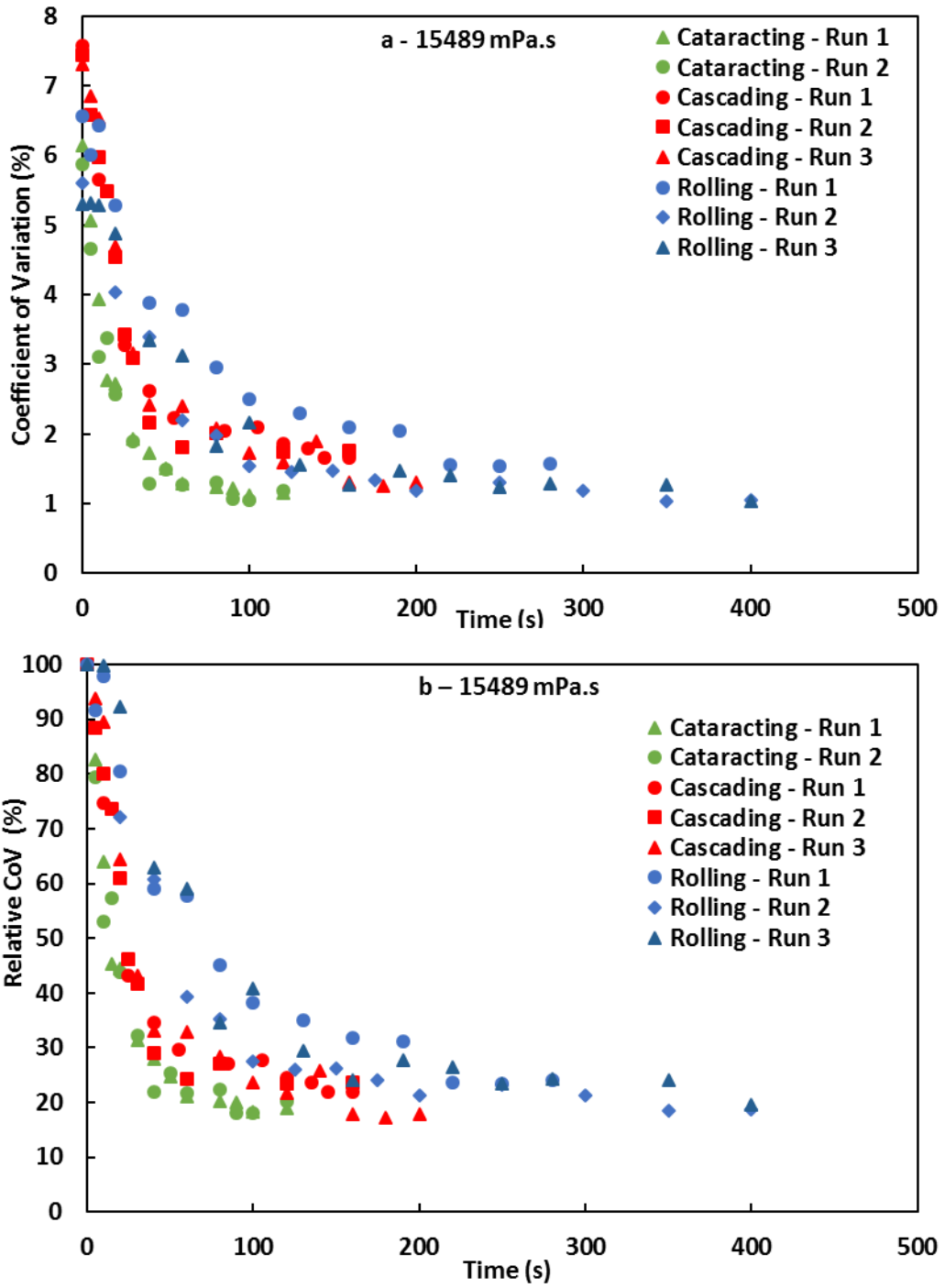
Figure 5.20. a) Coefficient of variation (CoV) and b) Relative CoV as a function of mixing time for alumina particles coated with PEG 35000 MW (15489 mPa.s) at different tumbling regimes
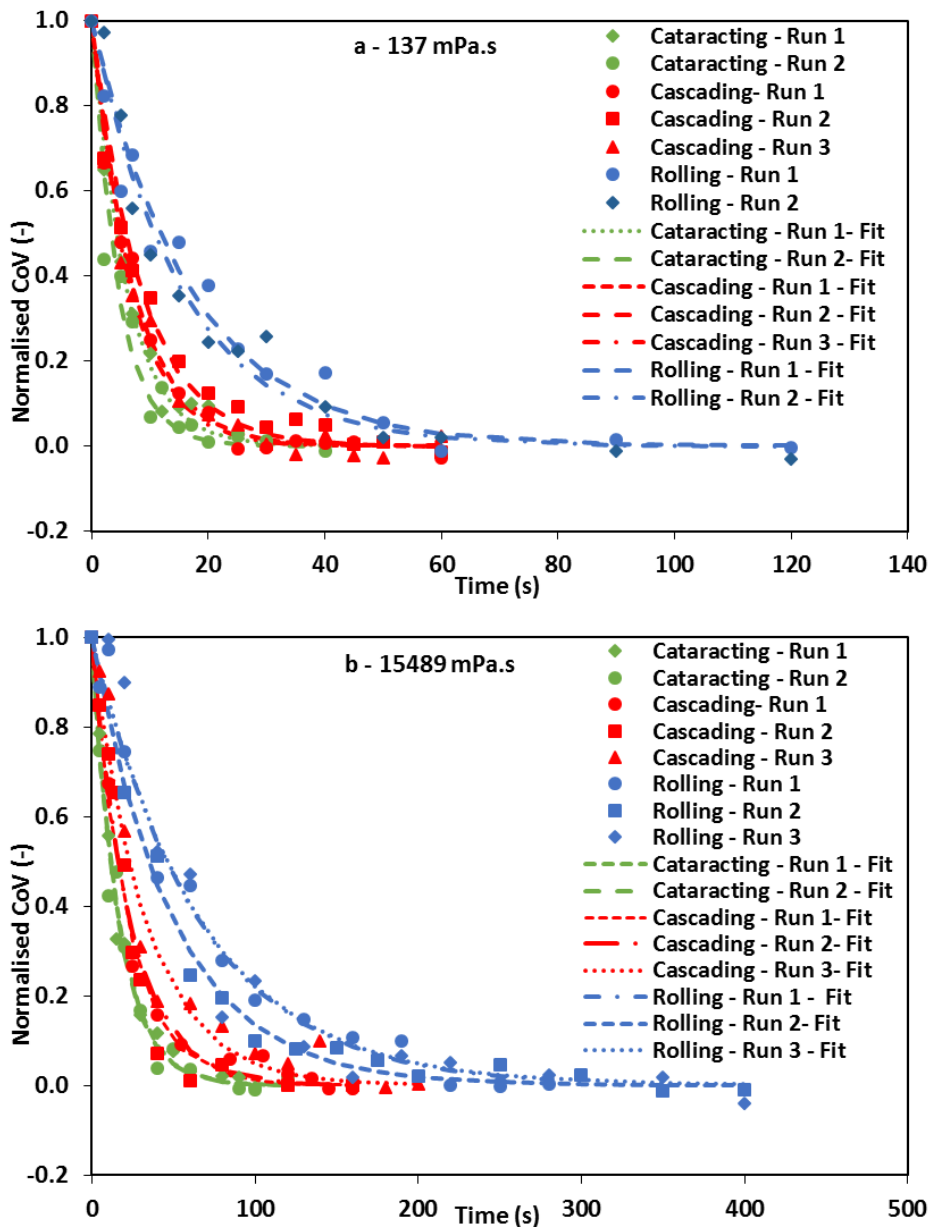
Figure 5.21. All data series of normalised (between CoV_o and average CoV_∞) coefficient of variation and fitted decay curves as a function of mixing time for a) PEG 4000 MW (137 mPa.s) and b) PEG 35000 MW (15489 mPa.s) at different tumbling regimes.

Figure 5.22 shows the average normalised CoV plotted as a function of mixing time and fitted with the decay curves for both PEG solutions used. Similar to the effect of viscosity data in Section 5.3.1, only some data in Figure 5.22 are presented with average values (error bars). Some of the data was added without a repeat (without error bars) to make sure that all the conditions reach the final point where the coating process is completed (fully coated particles).

Table 5.5 Fitting constants and time taken for coating completion for all data series

Viscosity (mPa.s)	Tumbling regime	Run	Coating rate constant, λ (s^{-1})	R^2	Time for 98 % coating completion, t_c	CoV asymptote (%)
137	Cascading (50 rpm)	1	0.1403	0.987	27.88	1.775
		2	0.1182	0.979	33.08	1.509
		3	0.1501	0.987	26.05	1.696
		Mean	**0.1362**		**29.00**	**1.660**
	Rolling (20 rpm)	1	0.0591	0.962	66.15	1.913
		2	0.0648	0.976	60.30	1.71
		Mean	**0.0620**		**63.22**	**1.81**
	Cataracting (85 rpm)	1	0.1685	0.987	23.22	1.441
		2	0.2215	0.937	17.66	1.82
		Mean	**0.1950**		**20.44**	**1.63**
15489	Cascading (50 rpm)	1	0.0304	0.990	85.46	1.704
		2	0.0429	0.964	91.16	1.752
		3	0.0458	0.969	128.68	1.289
		Mean	**0.0397**		**101.77**	**1.582**
	Rolling (20 rpm)	1	0.0202	0.989	193.99	1.090
		2	0.0154	0.984	254.84	1.557
		3	0.0151	0.965	258.38	1.201
		Mean	**0.0169**		**235.74**	**1.283**
	Cataracting (85 rpm)	1	0.0602	0.992	64.94	1.139
		2	0.0618	0.979	63.28	1.102
		Mean	**0.0610**		**64.11**	**1.120**

Note: The asymptotic CoV value is taken as an average of the CoV values at the final time points, where there is no clear decrease in CoV values
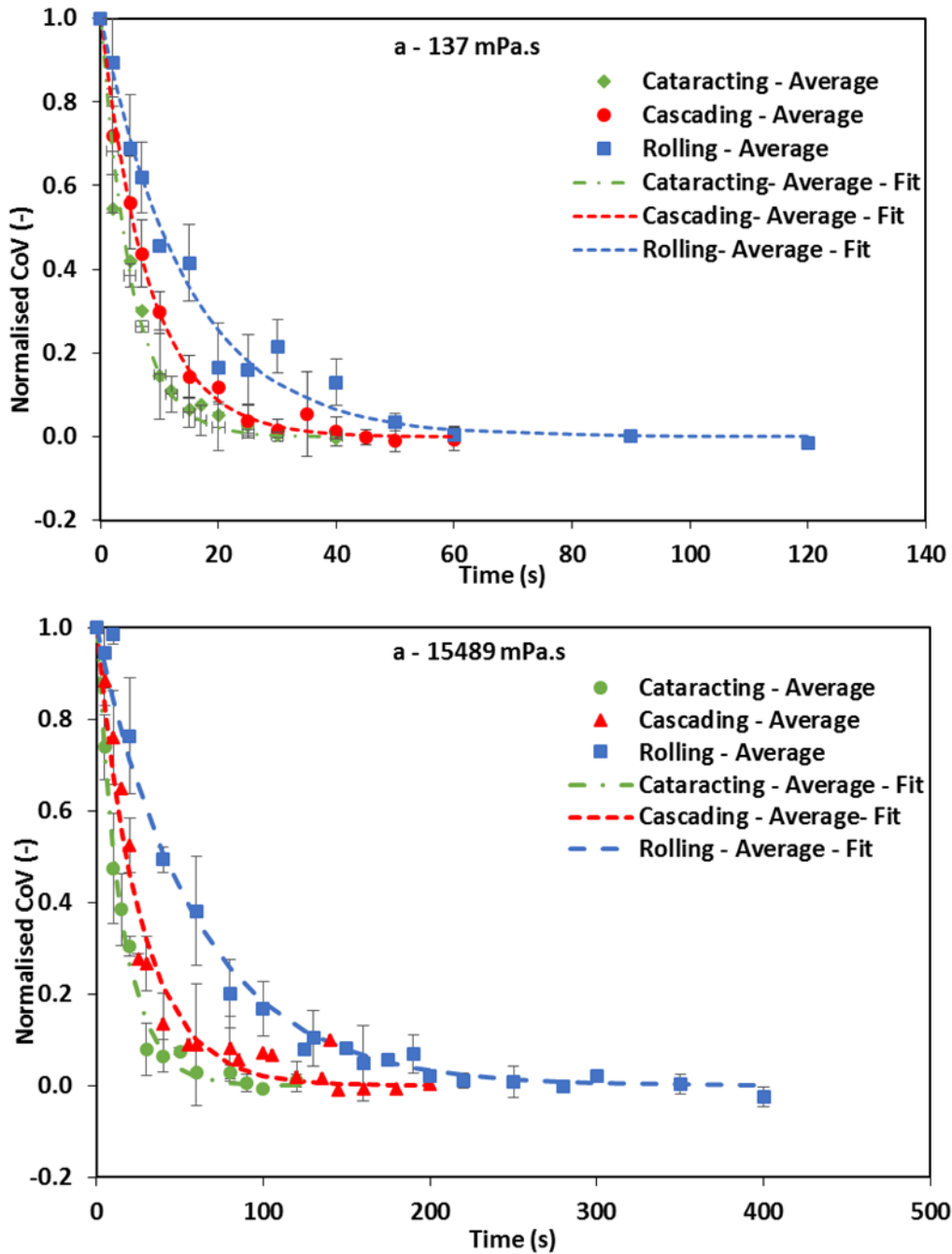
Figure 5.22. Average normalised (between CoV₀ and average CoV∞) coefficient of variation and fitted decay curves as a function of mixing time for a) PEG 4000 MW (137 mPa.s) and b) PEG 35000 MW (15489 mPa.s) at different tumbling regimes. Error bars represent standard errors (measured in triplicate).

131
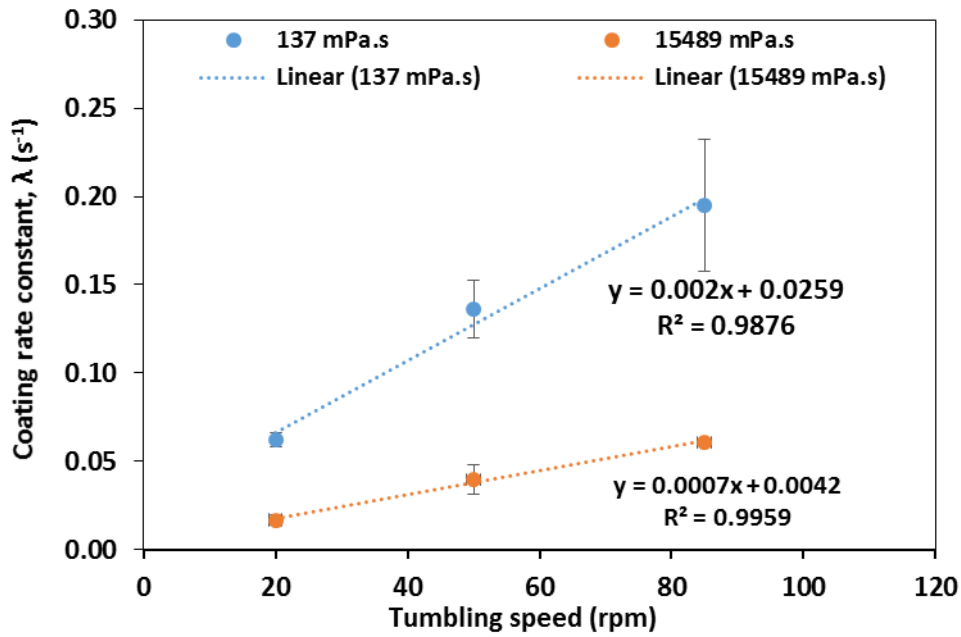
Figure 5.23. Fitting rate constants as a function of the tumbling speed. Error bars represent standard deviation

In addition, the tumbling speed also seems to influence the time for the coating process via contact spreading to reach an asymptotic value of CoV; the cataracting regime reaches the end point within the shortest time followed by the cascading and rolling regimes. For both viscosities, the t_c for the rolling regime reaches is almost triple that of the time of the cataracting regime. Figure 5.24 plots the t_c as a function of the tumbling regime. Both PEG viscosities show similar trends; the t_c was inversely proportional to the drum speed. This difference in coating behaviour at different speed might be related to the different particle motion behaviour in different flow regimes (mixing); in particular, the collision between particles and between the particles and the drum. Mixing in the drum can occur in two ways; axial mixing and radial-angular (cross-sectional) mixing. The former refers to the rate of mixing in a direction along the axis of rotation while the latter refers to that in a plane direction perpendicular to the axis of rotation (Dubey *et al.*, 2011).
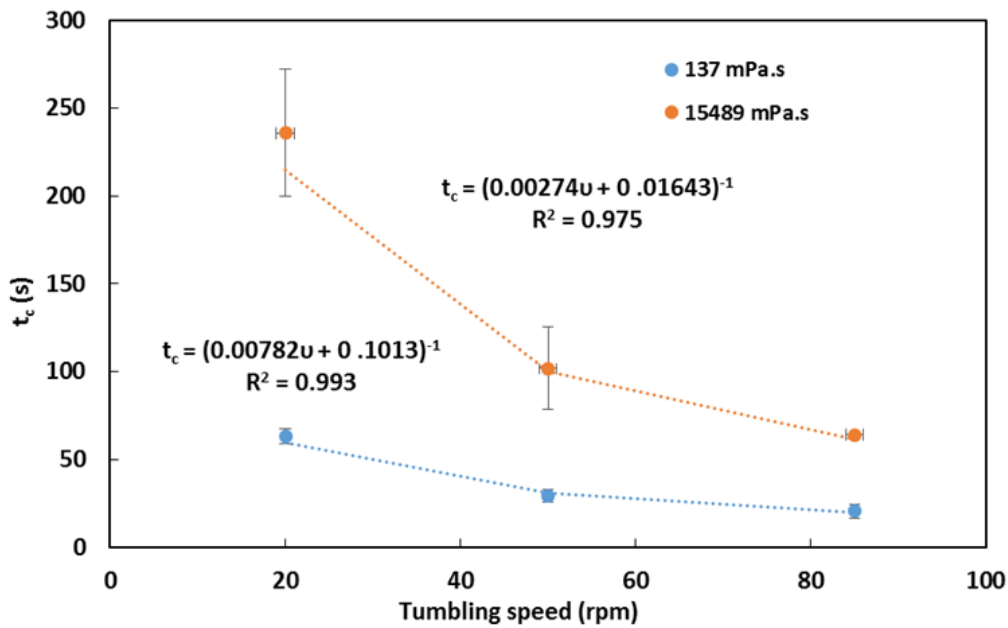
Figure 5.24. Time taken for coating completion, t_c, as a function of tumbling regime at different PEG viscosities. Error bars represent standard deviation

Figure 5.25 and 5.26 depict the contact spreading behaviour of alumina particles coated with PEG 35000 MW (15489 mPa.s) in cataracting and cascading flow regime. It can be observed that after 10 s tumbling time, most of the dyed particles were located at both ends of the drum walls, in the form of wet agglomerates and only a few dyed particles can be seen at the middle of the particle bed. It can be concluded that liquid spreading is faster at both end drum walls compared to the middle of the bed. As the tumbling time increased up to 40 s (cataracting), the wet agglomerates disappeared and it can be seen that the dyed particles have almost spread to the whole area of the particle bed. While for the cascading regime, as the tumbling time increased up to 60 s, it clearly can be seen that at both end walls more liquid is spread than in the middle area of the drum.
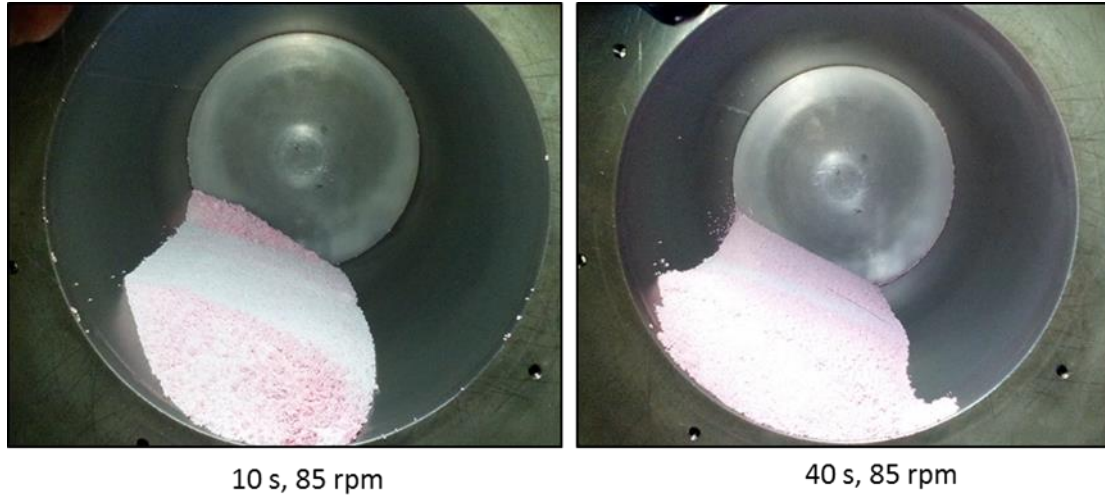
Figure 5.25. Contact spreading behaviour in the cataracting regime (85 rpm) of alumina coated with PEG 35000 MW (15489 mPa.s) at 10 s (left)) and 40 s (right) mixing time
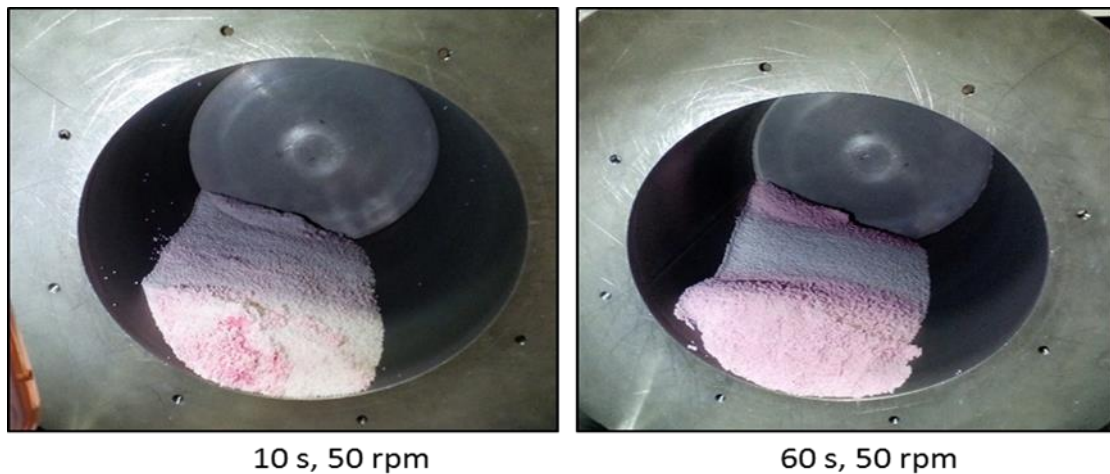
Figure 5.26. Contact spreading behaviour in the cascading regime (50 rpm) of alumina coated with PEG 35000 MW (15489 mPa.s) at 10 s (left) and 60 s (right) mixing time

In the case of the rolling regime, similar behaviour to the cataracting and cascading regimes can be observed, where liquid distribution happens faster at both ends of the drum walls compared to the middle of the particle bed (Figure 5.27). After 20 s mixing time, the dyed wet agglomerates (liquid bridges formed between wet particles) located at both end walls start to rupture and collide with other particles. However, at this time, the wet agglomerates in the middle only flow from the top surface downwards and

134

start to rupture as the time is increased. The wet particles then slowly start to spread the liquid to other particles in middle area of the particle bed.

20 s, 20 rpm   80 s, 20 rpm
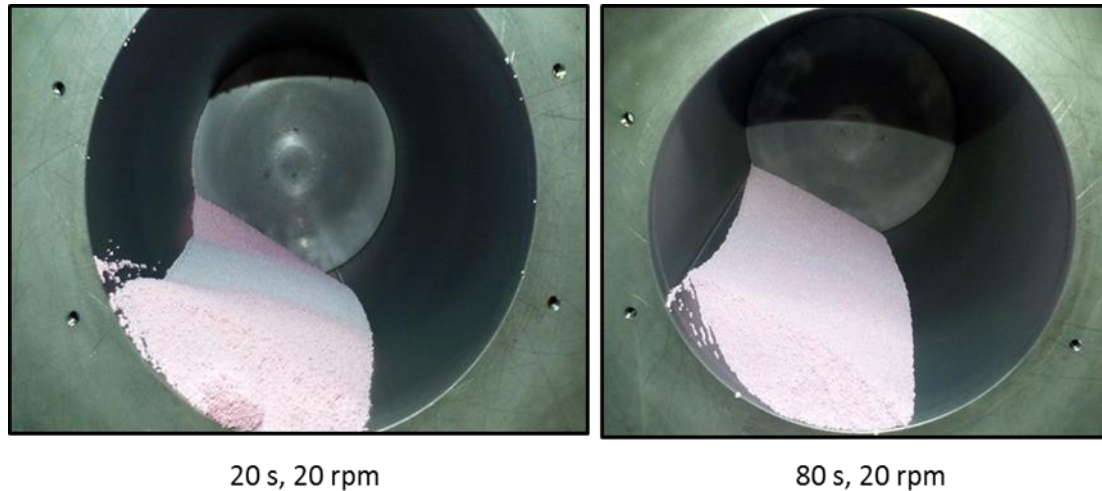
Figure 5.27. Contact spreading behaviour in the rolling regime (20 rpm) of alumina coated PEG 35000 MW (15489 mPa.s) at 20 s (left) and 80 s (right) mixing time

This observation was similar to a previous study by Mellmann (2001). They found that with a rolling regime, the particle bed was characterised by a uniform, static flow of particle layers at the top bed surface (active layer region) and a plug flow region that moves upward via solid body rotation with the rotational speed of the drum wall. In addition, the axial displacement of the particles in the plug flow region is mainly transported by solid body rotation around the drum axis with no or minimal axial displacement, and the rotational speed strongly influenced the axial particle velocity. In this rolling regime, as the speed was constant, the axial diffusion of wet particles mainly occurs in the active layer, similar to the finding reported by Delele *et al.*, (2016). The axial displacement was believed to happen once the wet agglomerates ruptured, thus taking a longer time to reach t_c (see Table 5.5) compared to other regimes for both viscosities. This observation is consistent with previous studies which found that axial mixing was better at the higher speed (Dubey *et al.*, 2011). Moreover, axial motion of wet particles behaved in a similar way to a diffusive process and could also be described by Fick's law (Liu *et al.*, 2013b). Fick's law of diffusion describes the migration a specified chemical species (A) at a location (x) in a material as proportional to the concentration gradient (dC ∕dx) of that same species (Cengel, 2006).

It seems possible that the difference in observations and results are due to the effect of speed or kinetic energy on rupture mechanisms of the liquid bridge formed after the collision. As rotation rate increases, the intensity of particle mixing is high and the turn over time significantly decreases (Denis *et al*., 2003). This means the collision energy between the particles is greater and there is enough energy to rupture the liquid bridge formed. Thus, wet particles will redistribute the liquid in the system and reach an end point of the coating process within a shorter time at higher drum speed. This assumption is supported by the findings of previous studies, where they concluded that an increase in rotation speed causes an increase in the shear layer (active region thickness), thus causing a higher rate exchange of mass, energy and momentum within the particle bed (Boateng and Barr, 1997; Delele *et al*., 2016). Also, the greater the fraction of bed occupied by the active layer, the more time particles will be exposed in the active layer (Henein *et al*., 1983). This will enhance the mixing. Thus a greater fraction of wet particles will collide and rebound. As a result, greater inter-particle coating uniformity within a shorter time is obtained using a cataracting regime compared to the other regimes due to more vigorous collisions between the wetted particles.

The rate of change of the CoV was also analysed as a function of the number of drum revolutions. Figure 5.28a-b shows the normalised CoV value and fitted decay curves as a function of a number of drum revolutions for both PEG viscosities. It was observed that the CoV value decreases with drum revolutions before leveling off at a final minimum CoV value for both viscosities. Surprisingly, there was no difference in coating rate when comparing different tumbling regimes as shown in Figure 5.29, and all data points collapse onto the same curve. For higher drum speed, the time to complete one revolution is faster than at lower speed. However, when considering the same number revolutions, a similar CoV values are obtained for all regimes (regardless of different speed used) as the same number of collisions occurs lead to similar rate of contact spreading in the system. The time to complete the coating process as a function of tumbling speed is also shown in Figure 5.30. Here, no difference in the t_c value was observed for all regimes at the same PEG viscosity used, as the coating rate influenced the t_c value obtained.
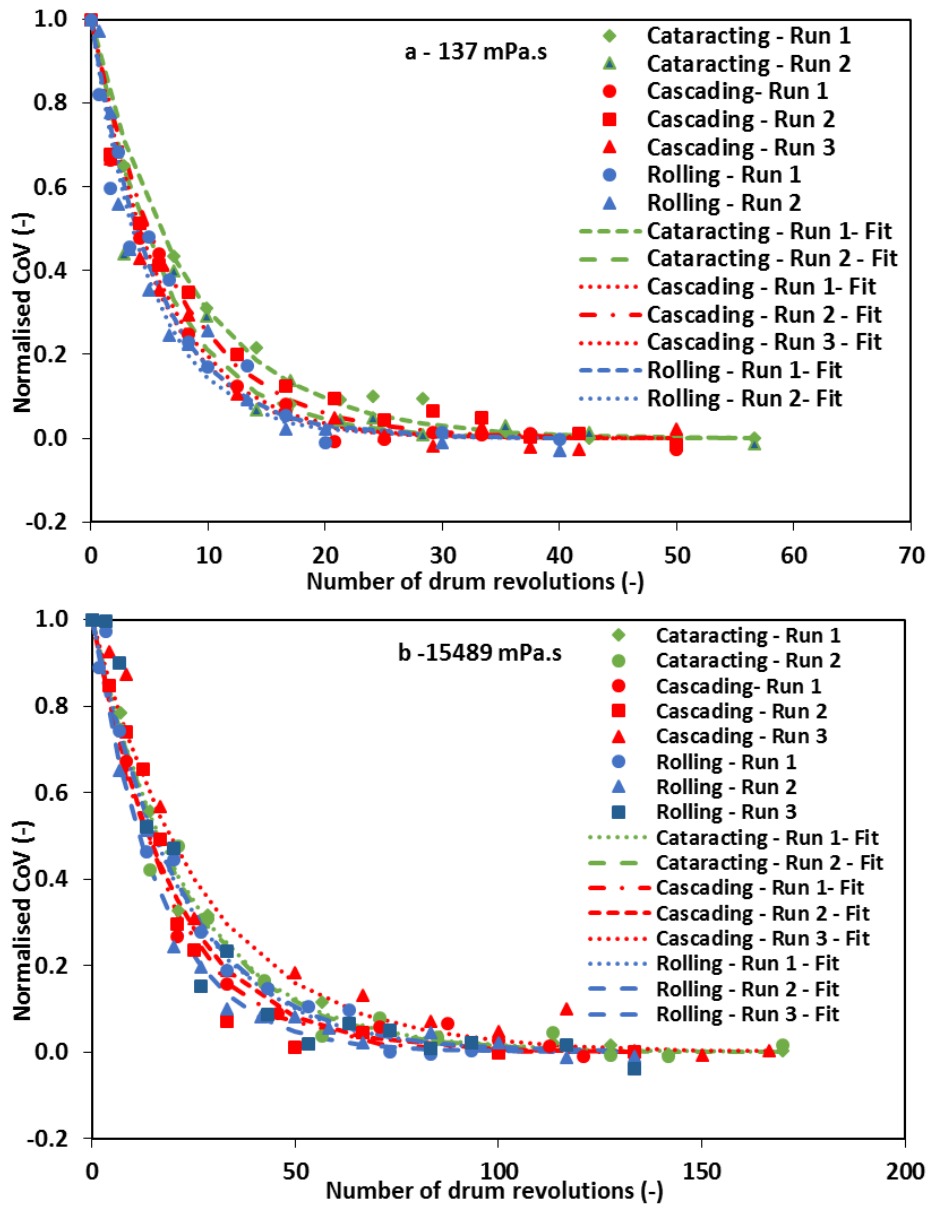
Figure 5.28 Normalised CoV (between CoV$_0$ and CoV$_\infty$) as a function of number of drum revolutions for a) PEG 4000 MW (137 mPa.s) and b) PEG 35000 MW (15489 mPa.s) at different tumbling regimes

These results might be due to particles of similar size and density mixing similarly after a certain number of revolutions. Thus, the same coating behaviour is observed for the different regimes when mixing is represented in terms of the number of drum revolutions. According to a previous study, at the same fill level and number of revolutions, the mixing index shows no difference, thus the liquid transfer between particles roughly occurs at a similar rate (Liu *et al*., 2013a).
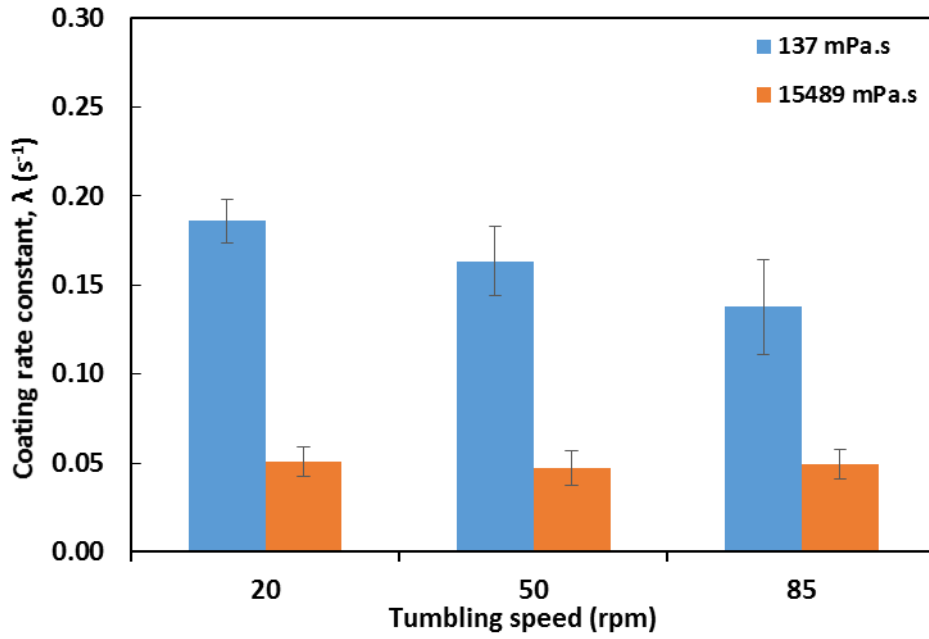
Figure 5.29. Coating rate as a function of tumbling speed at different PEG viscosity in terms of drum revolutions
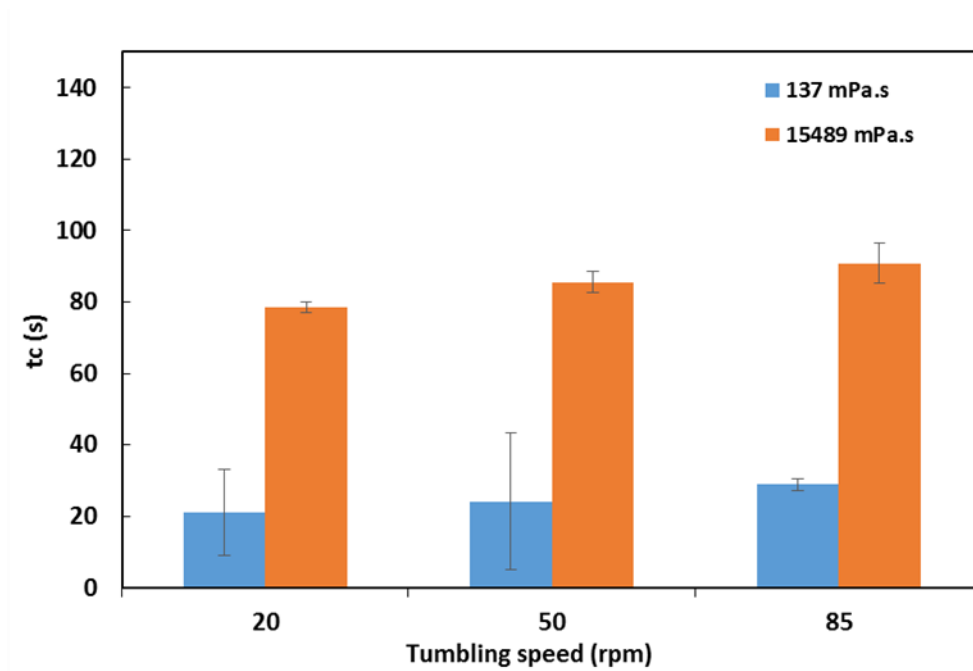
Figure 5.30. Time taken for coating completion, t_c as a function of tumbling regime at different PEG viscosity in terms of drum revolutions

5.4 Summary

This work is the first comprehensive experimental study to date of the batch contact spreading process in a tumbling drum coating system. The most obvious finding to emerge from this study is that even without the spray system, contact spreading occurs in this model system and could contribute significantly to the coating uniformity of the final coated particles. Contact spreading behaviour can be characterised by the extent of coating (asymptotic CoV), the coating rate constant, λ, and the time for the coating process to complete, t_c. It can be concluded that both parameters studied; viscosity and tumbling regime, significantly affected the contact spreading process. The results indicated that decreasing the viscosity and increasing drum speed both increased λ and reduced the t_c value, meaning a faster contact spreading process. These results are attributed to the differences in the formation and stability of liquid bridges between particles which influence the extent of liquid transfer via contact spreading in this system.

In the range of viscosity used, the Ca number is greater than 1, hence, the liquid bridge formed was assumed to be dominated by the viscous force. It explains that when a liquid bridge is formed, a higher viscosity will absorb more kinetic energy to the coating layer and thus decrease the possibility of the colliding particles to rebound. This chapter only discussed the liquid transfer via contact spreading in a tumbling drum system, but it is anticipated that contact spreading could also be an impact factor in other types of coating equipment. In the next chapter, contact spreading in a small-scale fluidised bed system is investigated.

CHAPTER 6

6 Investigation of the contact spreading mechanism for particle coating in small-scale fluidised bed

6.1 Introduction

In this chapter, a small-scale fluidised bed was designed and built[2] to study and understand the mechanism of the contact spreading in a different system from which was used in Chapter 5 (tumbling drum system). For these contact spreading experiments, to minimize the effect of the spray deposition on the particles, liquid was added to the system through a very short spray time (2 s). Following this, the spray was stopped, and the effect of liquid contact spreading was studied. The mixing time was considered after the initial spraying time finished. This method allows for the sole study of the contact spreading without influence from the spray deposition and spreading mechanism occurring simultaneously in the spray zone area.

These experiments used the same particles as in Chapter 5, i.e. alumina particles, but with different coating materials; hydroxypropyl methylcellulose (HPMC) solutions of different viscosities. This study is designed to:

◦ Identify the role of contact spreading in fluidised bed system

◦ Investigate the effect of mixing time, coating liquid spray rate and viscosity on contact spreading behaviour

◦ Investigate the effect of operating parameters (nozzle height, fluidisation velocity) on contact spreading behaviour

---

[2] *Designed and built with Layla Alhabeshi, University of Sheffield*

6.2 Experimental methods

This section summarises the experimental procedure and materials used. These are also explained in detail in Section 3.5.2. It will first described the determination of the minimum fluidisation velocity (U_{mf}), followed by calibration curve development for the coating solutions. Finally, an outline of the main experimental procedure will be described.

6.2.1 Minimum fluidisation velocity, U_{mf}

Alumina particles used in this study are classified in Group B in the Geldart classification (see Chapter 2, Section 2.2.2.5) based on their size and density ($0.85 - 1.0$ mm, 3.6 g/cm^3). Before operating the fluidised bed experiments, it is important to determine the minimum fluidisation velocity, U_{mf}, since the fluidisation velocity needs to be maintained above this value during the process. In this study, experimental and theoretical approaches were used to determine the U_{mf}. Based on the equipment available, firstly, the bed voidage method was used to measure the U_{mf}. This method measured the bed expansion by visually observing the fluidisation behaviour which was captured using a digital camera (14 megapixels) and an MPEG movie (1080 x 1920, 30 fps). For each fluidisation test, the volumetric air flow rate varied between 50 - 450 L/min, 10 cm static bed height (1.1, ratio of particle bed height to internal diameter of the tube), and the gas pressure varied between 2.0 - 3.5 bar. Different gas pressure was tested as it affected the maximum air flow rate needed to fluidise the alumina particles.

Figure 6.1 shows the fluidisation behaviour at different fluidisation flow rates ranging from 280-420 L/min. The difference in bed expansion of each condition was determined. At higher flow rates, due to the large bubbles in the powder bed, the bed is frequently swept from one side of the tube to the other side. Due to vigorous movement at higher flow rates, it is difficult to define the upper limit or surface of the bed clearly. Thus, the bed height was determined consistently based on the flat level of the particle bed as shown in Figure 6.1. The 'flat level' is defined at lower limit, as the bed height of fluidised particles over the cross-sectional area of the tube is flat. The measured bed

expansion was then plotted as a function of air flow rate at different gas pressure and is shown in Figure 6.2. It indicates that at different gas pressure, a similar trend was observed, where the bed expansion was constant at air flow rates from 50-220 L/min. The bed then started to expand from 220 L/min up to 450 L/min except for the lowest gas pressure, 2.0 bar, which only can go up to 350 L/min. The results confirmed previous findings that the U_{mf} was dependent on the size and density of the particles, and independent of the gas pressure (Escudero, 2010). Thus, for the fluidised bed experiments, a gas pressure of 2.5 bar was selected so that the flow rate could be set up to 400 L/min. Based on the observations of the videos and the recorded data, the U_{mf} for the alumina particles was determined to be 0.576 m/s (220 L/min). The superficial velocity was measured by dividing the flow rate with the cross-sectional area of the fluidised bed tube (Appendix D1).

Minimum fluidisation velocity based on the bed pressure drop was also determined to compare with the visual method, and the experimental set-up is shown in Figure 6.3. Two pressure taps, one just above the distributor plate and the other above the bed, were linked to a digital differential manometer (Testo 512, United Kingdom) to record the pressure drop. First, the particles (1313.26 g) were poured into the fluidised bed tube, and air passed through it for approximately 5 min until the system was stable. The initial static bed height was recorded. The fluidisation velocity was increased incrementally, allowing sufficient time to reach a steady state. The manometer readings were noted for each increment in flow rate (50 - 400 L/min) and the superficial velocity calculated. The U_{mf} was then determined by plotting the pressure drop (ΔP) as a function of air flow rate and shown in Figure 6.4. From Figure 6.4, the pressure drops increase with flow rate (A-B) until the bed expands and the bed porosity increases. At point B, the transition from a static bed to a partially fluidised bed was observed. From point B to point C, the pressure drop remained constant with flow rate, and here, the bed was observed to transition from partially to fully fluidised. The velocity at which the pressure drop was at a maximum was taken as the U_{mf} and the value obtained, approximately 220-230 L/min, was close to the value from the visual method.

Air Flowrate [L/min]	280	300	320	350	380	400	420
Images							
Bed height [cm]	11.8	13.2	15	16	17.8	20	21.5
Ratio particle bed height to inner diameter of the tube	1.31	1.47	1.67	1.78	1.98	2.22	2.39

Figure 6.1. Different bed voidage for a 10 cm static bed height (1.1, ratio particle bed height to the inner diameter of the tube) undergoing fluidisation from 280 - 420 L/min air flow rates at 2.5 bar gas pressure
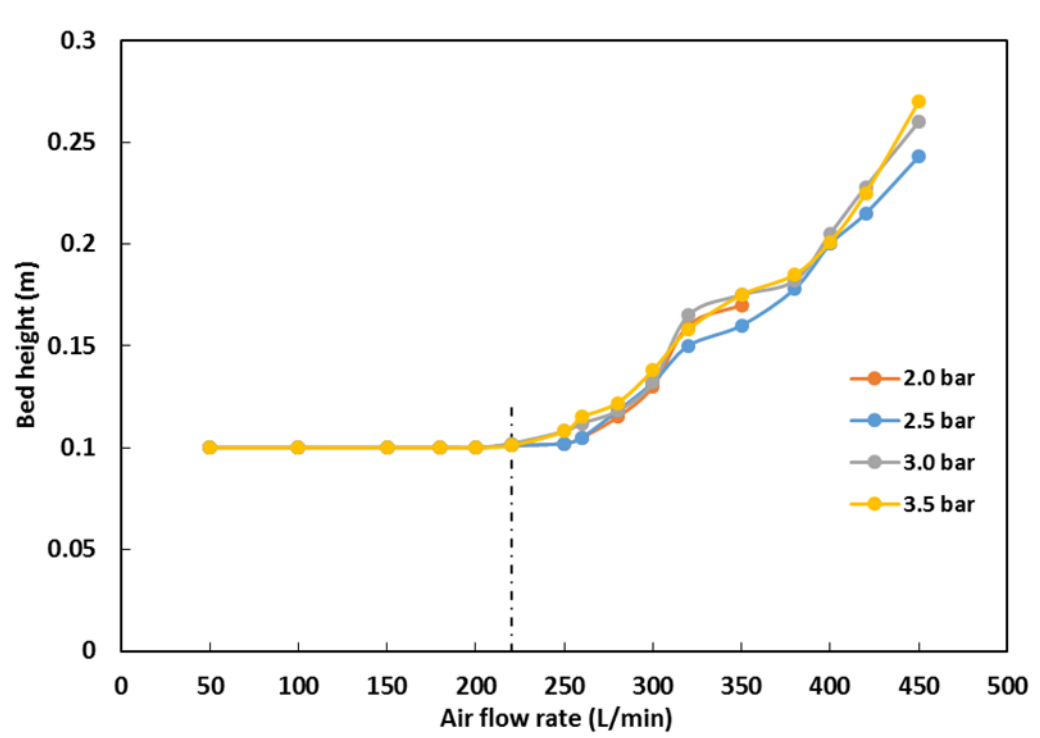
Figure 6.2. Bed expansion of the alumina particles fluidised at 10 cm static bed height, gas pressure from 2.0 – 3.5 bar and air flow rate of 50 – 450 L/min
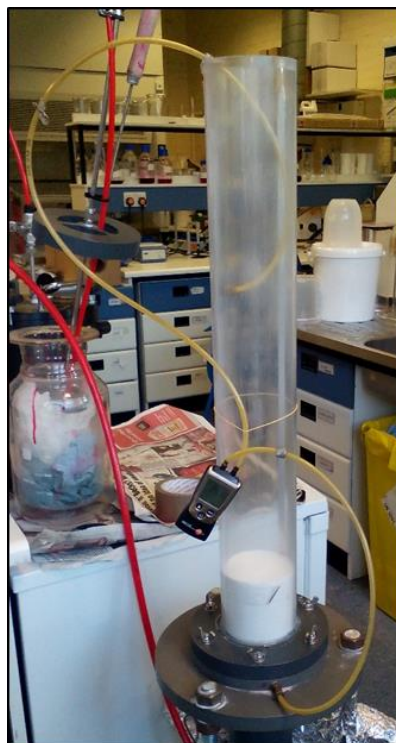
Figure 6.3. Bed pressure drop set-up equipment
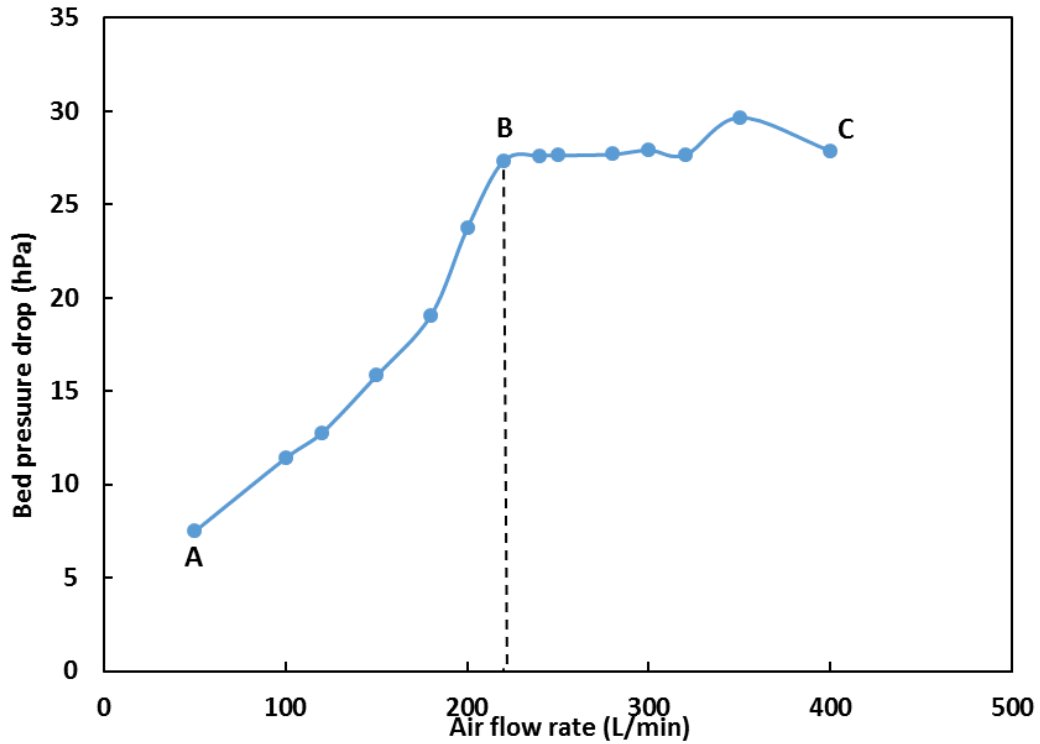
Figure 6.4. Bed pressure drop as a function of air flow rate (10 cm static bed height, ratio bed height to inner diameter: 1.1)

The U_{mf} values obtained from both experimental methods then were compared with the theoretical correlation from the Ergun equation (0.448 m/s) (Dixit and Puthli, 2009) (see Chapter 2, Section 2.2.2.4). Table 6.1 shows the values used for the theoretical measurement (Appendix D2). The results indicate that both values obtained were slightly different. This might be due to the values for velocity estimated based on Ergun equation are mostly reliable for spherical and small particles (Senadeera *et al.*, 2006). In this case, size of alumina particles used in range from 800 - 1200 µm which might not fit with the Ergun equation. Therefore, for the contact spreading experiments, the value obtained from the visual method, 220 L/min (0.576 m/s), was used

Table 6.1. Values used in the Ergun equation

Particle size, d_p [m]	Air density, ρ_g [kg/m^3]	Bulk density, ρ_p [kg/m^3]	Gravity acceleration, g [kg.m/s^2]	Air viscosity, µ [kg/m.s]	U_{mf} theory. [m/s]
0.00101	1.2	2064	9.81	0.00001983	0.448

6.2.2 Calibration curve

Before starting the fluidized bed experiments, a calibration curve was developed for the hydroxypropyl methylcellulose (HPMC) solutions used in this system. The viscosity was varied by using the same concentration (5% w/w) and different grades of HPMC: 603 (11 mPa.s), 606 (44 mPa.s) and 615 (177 mPa.s). To develop the calibration curve, the spray rate for each of the HPMC solutions was determined by collecting and weighing the amount of sprayed liquid for 30s spraying time (Figure 6.5). The coating liquid was sprayed using a top to bottom spraying system built in-house (see Section 3.4.2, Figure 3.17) and the liquid pressure was changed at a constant atomization pressure (1 bar) (Table 6.2). Here, the atomizing pressure was set at 1 bar to reduce any disturbance to the fluidising behaviour during spraying. The two-fluid internal mixing nozzle (Spray System, PA64, PF1650) was used for this study as described in Section 3.4.2, Figure 3.16. This measurement was repeated three times for each spray rate.

Figure 6.5. Set-up for spray rate measurement

Figure 6.6 shows the calibration curve for three different viscosities of HPMC solutions at different atomizing conditions. It shows that the spray rate increased with increasing liquid pressure. In addition, increasing viscosity required an increase in pumping pressure to keep the same spray rate as that of the lower viscosity. This calibration curve was then used to define the setting for the liquid pressure based on the spray rate of the sprayed liquid needed for each condition.
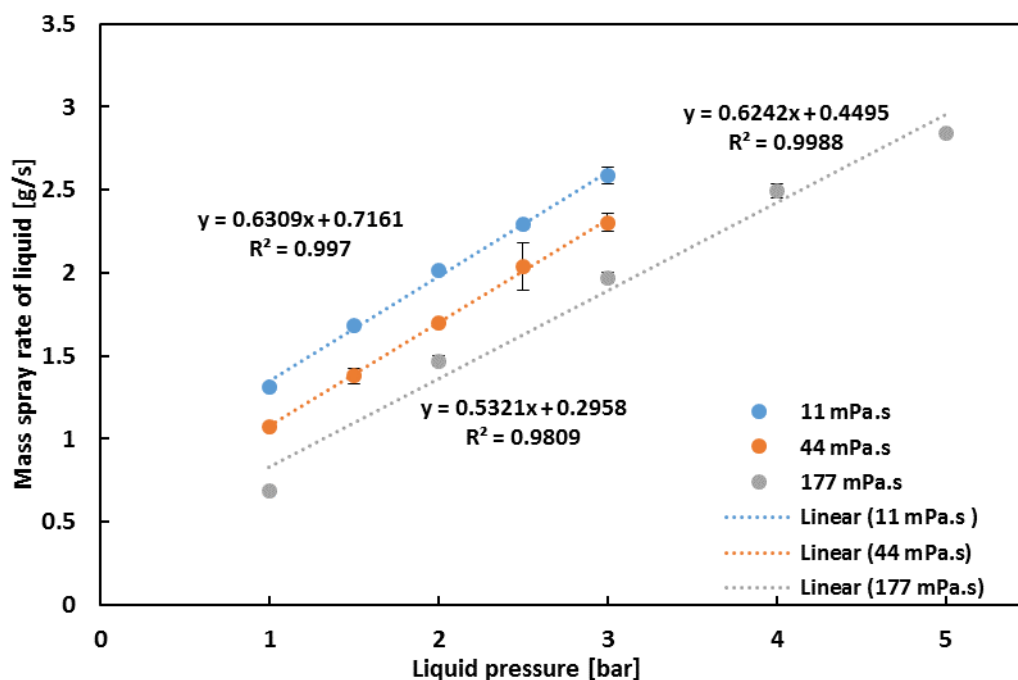
Figure 6.6. Calibration curve of HPMC solutions of different viscosities at different atomization conditions

6.2.3 Spray Distribution

An even liquid spray distribution is considered important to obtain a more uniform coating. Spray distribution (SD) is area distribution of the spray and this can be controlled by nozzle parameters; mainly the nozzle height and pressure. In addition, liquid properties such as viscosity also influence the SD. Thus, to study the effect of nozzle height and liquid viscosity on contact spreading, the SD of the different HPMC solutions needs to be investigated before conducting the coating experiments in the fluidised bed. The spray volumetric distribution of the nozzle was determined by setting up an experiment as shown in Figure 6.7. The set-up consisted of small cuvettes as spray collectors, a high-pressure pot to pump the liquid, a fluidised bed tube and a spray nozzle.

To evaluate the distribution of the liquid sprayed, the pneumatic nozzle was mounted at heights of a range of 16-22 cm and above the centre of the spray collector. An array of 5 x 5 cuvettes (4.5 mL) was used to collect the liquid from the sprayed nozzle across the spray centre line and it was assumed as an axisymmetric spray pattern. The

inner cuvette dimensions were 1 cm x 1cm x 4.5 cm (length x wide x height) and the outer thickness of the cuvette was 0.1 cm. The weighting method was used to determine the mass transversal volumetric distributions collected within 3 s by using a precision balance. Any of the sprayed liquid deposited in the space between cuvettes was wiped with a tissue prior to weighing and, therefore, the measurement only considers the liquid inside the cuvette. Results of volumetric spray distribution experiments are presented in Figures 6.8 - 6.10 for different nozzle heights and viscosities.
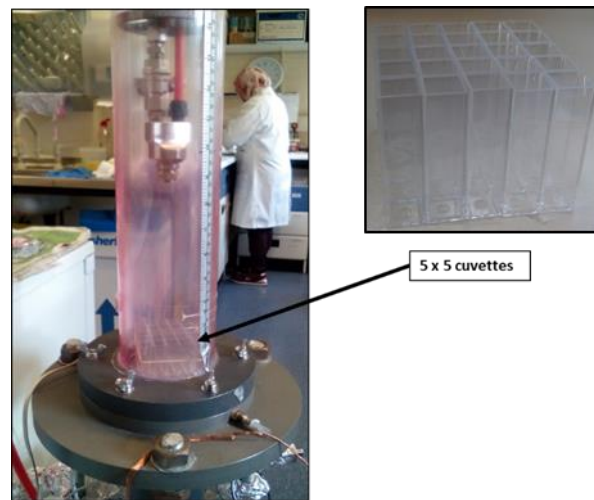
Figure 6.7. Set-up of the spray pattern measurement

At a constant atomization pressure, nozzle height and spray rate, the cross-sectional area of a spray nozzle for different viscosities shows a similar pattern (Figure 6.8). However, it indicates that the SD curves become sharper with an increase in viscosity. When viscosity increases, the liquid needs more energy to spread further from the centre of the nozzle. Thus, more liquid volume is collected directly below nozzle compared to a lower viscosity which shows a more uniform spreading of droplets radially across the cuvettes.
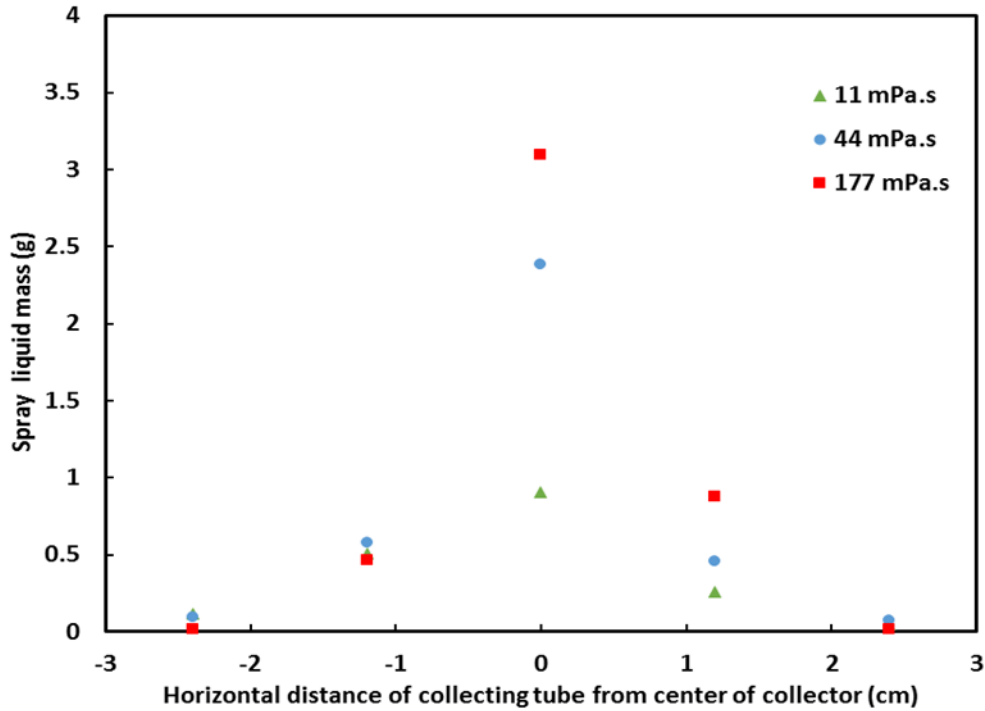
Figure 6.8. Spray pattern of different viscosity HPMC solutions at 22 cm nozzle height and 1 bar atomization pressure

In the fluidised bed system, the adjustment of height of the nozzle is important based on the bed diameter and the cross-sectional diameter used. The distribution area of the spray should be within diameter of the fluidised bed tube. This should avoid the droplets from adhering on the tube wall. The SD for different nozzle heights used in this work (16 cm and 22 cm nozzle height from the distributor plate) is shown in Figure 6.9. It indicates that the different nozzle heights give a similar cross-sectional area; roughly 5 cm in diameter. However, as expected, for the lower height, the liquid collected was concentrated to the centre as compared to a higher height which shows more uniform spreading of droplets radially. At a higher heights, there might be some loss of droplets due to evaporation occuring simultaneously in the fluid bed tube before colliding with particle surfaces as reported by (Hemati *et al.*, 2003; Sanaei-Moghadam *et al.*, 2017). This is observed here with a substantially lower spray volume at higher nozzle height. In this study, it shows that selected nozzle heights gave the spray distribution ~5cm not 9 cm as the inner diameter of the tube. This was to prevent the droplets attached to the tube wall which could influences the fluidisation behaviour of the wet particles.
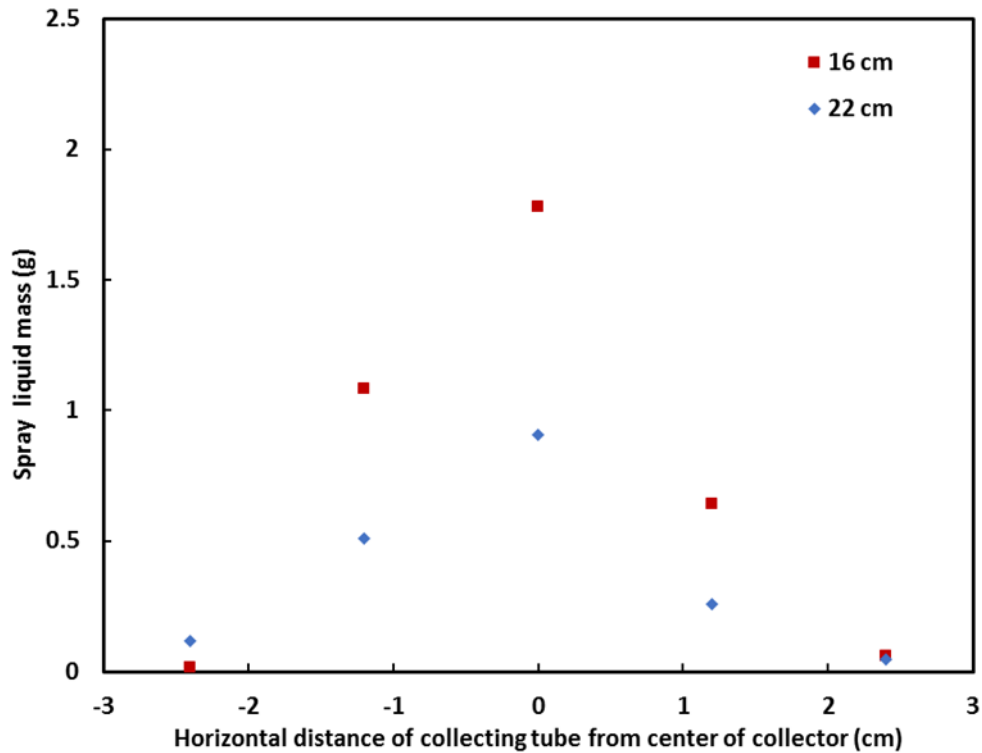
Figure 6.9. Spray pattern of HPMC solution (11 mPa.s) at different nozzle heights

Figure 6.10 shows the SD of the 11 mPa.s solution at different spray rates ranging from 1.3 to 2.9 g/s. The SD for different spray rates seem to have a similar pattern, but the 1.3 g/s spray rate shows that the liquid collected was greater towards the centre as compared to a higher spray rate which shows a more uniform spreading of droplets. This observation can be related to the different of air to liquid ratios (ALR) used, as spray characteristics strongly depend on the type of flow regimes developed inside the nozzle. Previous work had reported that at higher ALR, slug flow dominated and produced poor atomisation, while at lower ALR, dispersed bubble flow dominated and produced a greater spray coverage area (Tafreshi *et al*., 2002). In this case, the medium (2.0 g/s) and lower (2.9 g/s) ALR (see Table 6.2) gave a better spray coverage area (Figure 6.10) compared to highest ALR (1.3 g/s).
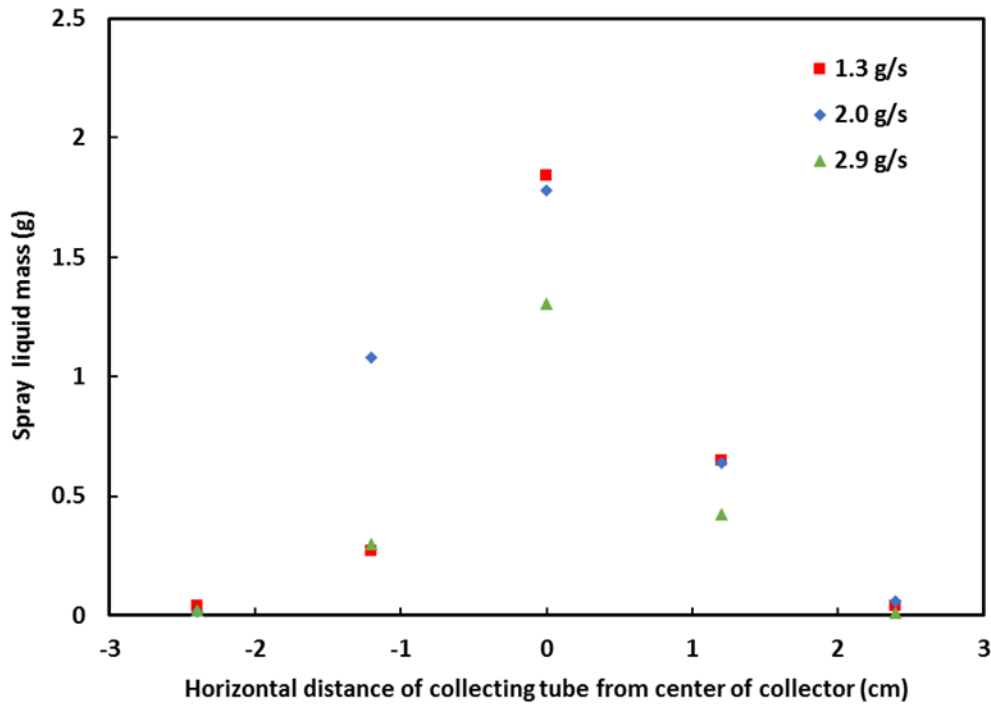
Figure 6.10. Spray pattern of the 11 mPa.s HPMC solution at different spray rates

6.2.4 Contact spreading experimental procedure

This section describes the general procedure for the contact spreading experiments in a fluidised bed system. For each condition, a series of experimental runs at increasing mixing times (typically 8-10) was conducted to give one dataset. For each run, a batch of alumina particles was weighed (1313.23 g). The amount calculated was based on 10 cm static bed height of the fluidised bed used. The alumina particles were poured into the fluidised bed using a funnel to avoid any spillage.

The coating solution was supplied to the system using a high-pressure pot as described in Chapter 3, Section 3.4.2. The height of the nozzle was set first at 16 cm height from the distributor plate. Once the height was set, the air supply for the fluidising particles and atomisation liquid was switched on before starting the experiments. The coating liquid was then sprayed for 2 seconds to the fluidised particles. Here, only a short spray time was used in order to follow contact spreading behaviour during the mixing

time subsequent to the spray. Once the liquid spray was stopped, the nozzle set-up was removed immediately from the bed to prevent dripping. After the mixing time (without spray time) was finished, the fluidising air was switched off immediately, the fluidisation chamber was removed, and the coated particles were collected in a tray and left to dry overnight.

The fluidised bed tube and the nozzle were cleaned before repeating the same experimental procedure for the other batches. This prevents any additional coating liquid being transferred to the next batch and the blockage of the nozzle due to possible solution build up. A total of 16 datasets comprising 198 individual experiments were performed to understand the effects of different operating variables on the coating uniformity of coated particles via contact spreading. The experimental conditions are summarised in Table 6.2.

Table 6.2 Experimental process variables and constants (1 bar atomization pressure)

Exp. Run	HPMC viscosity (mPa.s)	Fluidisation velocity (m/s)	Liquid pressure (bar)	Liquid spray rate (g/s)	Air to liquid ratio (ALR)	Nozzle height∗ (cm)
1 (2 runs)	11 mPa.s	1.5 U_{mf} (0.84)	1	1.3	1	16
2 (4 runs)	11 mPa.s	1.5 U_{mf} (0.84)	2	2.0	0.5	16
3 (2 runs)	11 mPa.s	1.5 U_{mf} (0.84)	3.5	2.9	0.29	16
4 (2 runs)	11 mPa.s	1.8 U_{mf} (1.05)	2	2.0	0.5	22
5 (2 runs)	11 mPa.s	1.3 U_{mf} (0.73)	2	2.0	0.5	22
6 (2 runs)	11 mPa.s	1.8 U_{mf} (1.05)	2	2.0	0.5	16
7 (2 runs)	44 mPa.s	1.8 U_{mf} (1.05)	2.5	2.0	0.4	22
8 (2 runs)	177 mPa.s	1.8 U_{mf} (1.05)	3.2	2.0	0.31	22

Note: ∗ the nozzle height is considered to be the distance from the distributor plate to the nozzle

6.2.5 Image analysis

Samples for image analysis were prepared and analysed as described in Section 4.1. The coated particles were visualized using the imaging system explained in Section 4.1. The LabVIEW software was used (see Section 4.1.4) for analysing the inter-particle coating to give a quantitative determination of coating behaviour, i.e., the coefficient of variation (CoV).

6.3 Results and discussion

This section covers the results and findings from four sets of experimental conditions carried out for this chapter. Section 6.4.1 discusses the results for the effect of spray rate on contact spreading, followed by the effect of fluidisation velocity in Section 6.4.2. Then, Section 6.4.3 will discuss the effect of viscosity, and finally, the effect of nozzle height will be discussed in Section 6.4.4.

6.3.1 Effect of spray rate

Figure 6.11 (a-c) shows a typical data set of coating evolution for alumina particles coated with HPMC solution (11 mPa.s) at different spray rates: 1.3, 2.0 and 2.9 g/s. A similar pattern was observed for each spray rate, where with an increase in mixing time, the curve shifted to higher % red and the distribution became narrower. This pattern is similar to previous results from Chapter 5, Section 5.3.1 when using a tumbling drum, and it can be concluded that contact spreading is occurring within the particle bed in the fluidised bed system. Note that for each data series, not all data points for that series are shown for visualisation purposes. The full data series are given in Appendix D3.

Figure 6.12a-c shows the coefficient of variation, CoV plotted as a function of time for each HPMC 603 (11 mPa.s) solution spray rate. The CoV was determined to investigate the variability of the coating layer between particles in the same batch and determined as explained in Chapter 4 (Eq. 4.1). The results show that as mixing time

increases, the coating variability decreases for all data series. This indicates that the coating becomes more uniform with time and gives proof that there is contact spreading occurring in the fluidised bed system. The CoV values for all data series also show that the CoV reaches an asymptotic value after a certain mixing time. Furthermore, the performance of the instrument and method was also carried out, and the results show good repeatability (Figure 6.12).

All the data series in Figure 6.12 are plotted together in Figure 6.13. From the graphs, the asymptotic CoV value appears to be similar for all spray rates used. However, the initial CoV values for each data series are slightly different. This might be due to the different ratio of liquid to particles used, which contributes to the difference in mean percentage red. The mean % red slightly increases with the spray rate (see Appendix D4). Therefore, the data are normalised based on Eq. 5.1 for better comparison of the coating rates. This type of normalisation is referred to as the relative CoV and is shown in Figure 6.14.
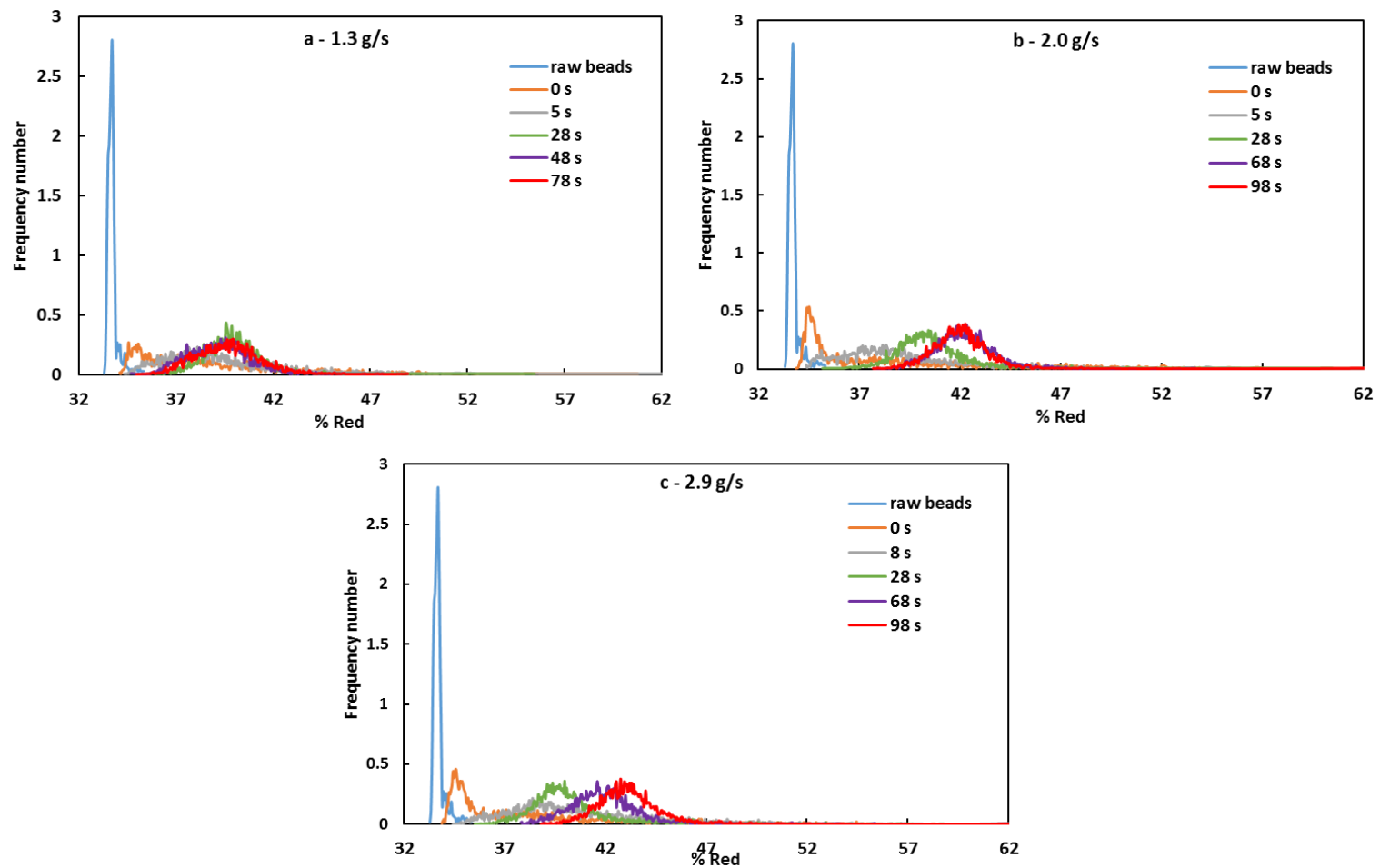
Figure 6.11. Coating evolution; frequency number plotted as a function of % red of alumina particles coated with HPMC 603 solution (11 mPa.s) at different spray rates, a: 1.3 g/s;b: 2.0 g/s and c: 2.9 g/s.
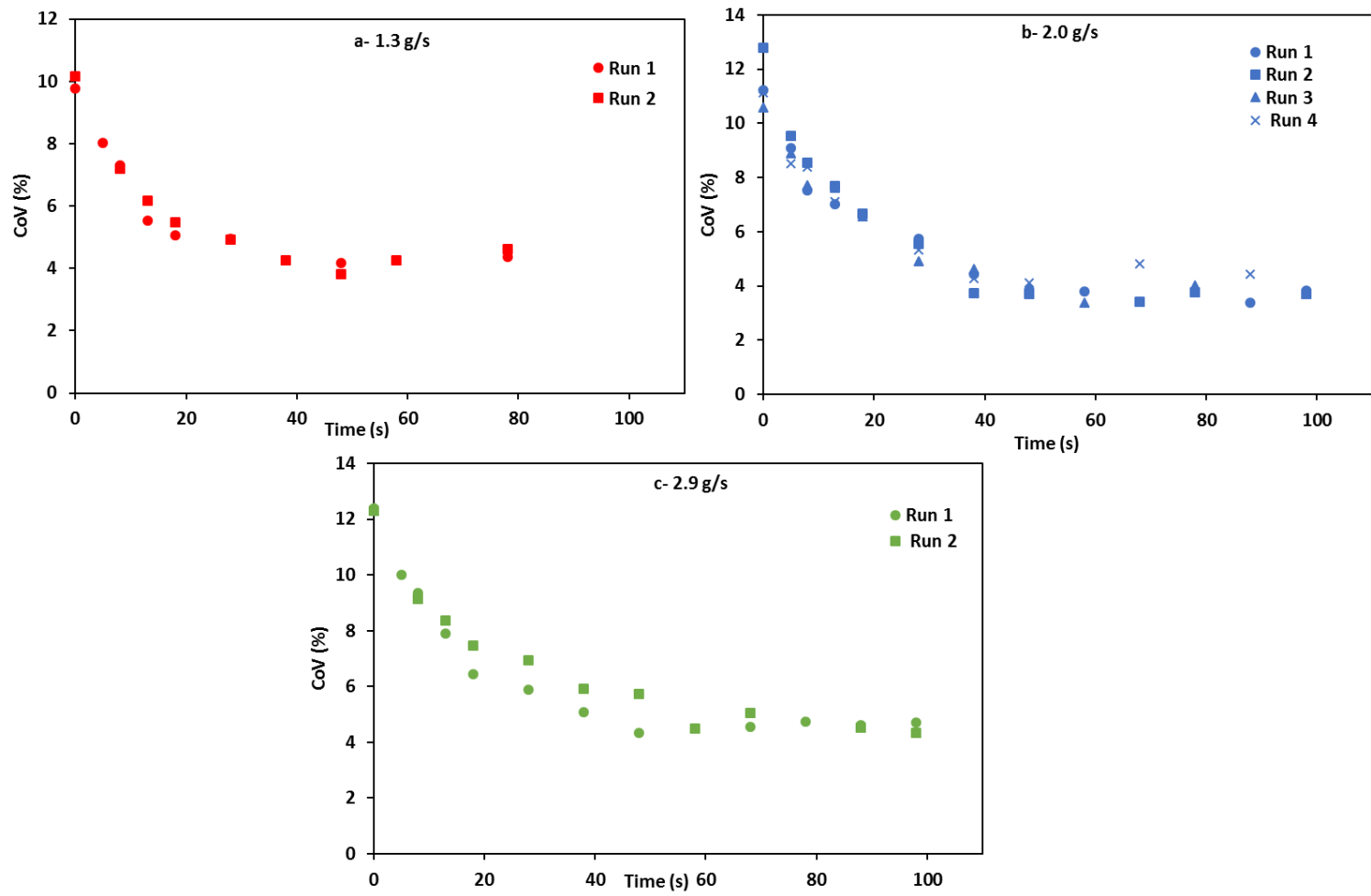
Figure 6.12. Coefficient of variation as a function of mixing time for alumina particles coated at different HPMC 603 (11 mPa.s) spray rates for all data series, a: 1.3 g/s;b: 2.0 g/s and c: 2.9 g/s.
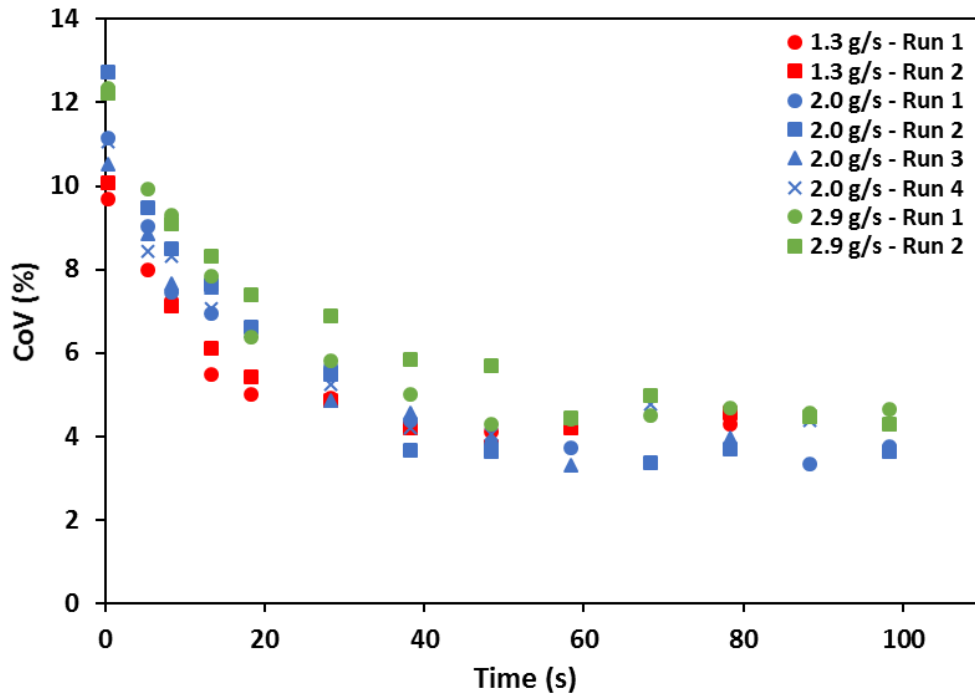
Figure 6.13. Coefficient of variation as a function of mixing time for alumina particles coated at different HPMC 603 (11 mPa.s) spray rates
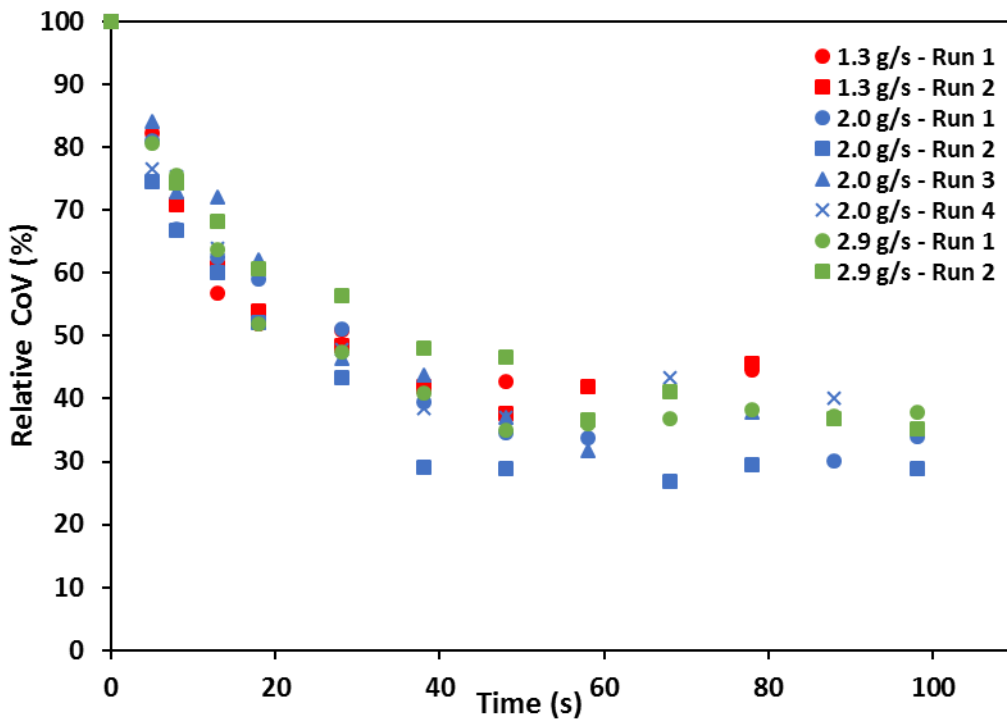
Figure 6.14. Relative coefficient of variation as a function of mixing time for alumina particles coated at different HPMC 603 (11 mPa.s) spray rates

157

Figure 6.14 indicates that regardless of the spray rate used, all the data series reach similar asymptotic CoV values. To determine the time to reach an asymptotic value, t_c, and the coating rate, λ, an exponential decay curve was fitted to each data set, normalised between CoV_o and the average CoV_∞ (Eq. 4.7) as described in Chapters 4 and 5. From Figure 6.15, all data series appeared to fit well with the fitting curve ($R^2 > 0.9$) and all the measured parameters are summarised in Table 6.3. However, surprisingly, the data series for the higher spray rates; 2.9 and 2.0 g/s, appear to fall nearly onto similar curves and appear to coat slower compared to the lowest spray rate, 1.3 g/s. For better comparison, averaged normalised CoV values for each spray rate were then plotted as a function of time and illustrated in Figure 6.16.
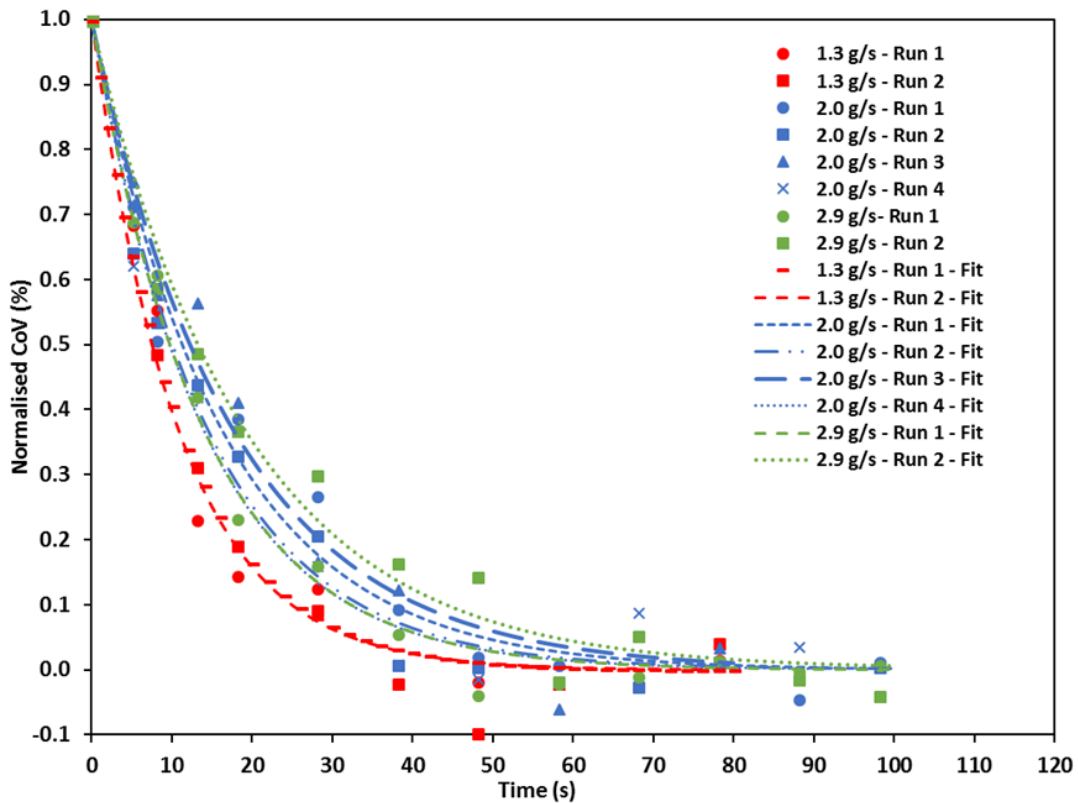
Figure 6.15. All data series of the normalised (between CoV_o and average CoV_∞) coefficient of variation and fitted decay curves as a function of mixing time for different HPMC 603 (11 mPa.s) spray rates

Table 6.3. Fitting constants and time taken for coating completion for all data series for the effect of spray rate

Spray rate (g/s)	Run	Liquid loading (mass of solution/mass of particles)	Coating rate constant, λ (s^{-1})	R^2	Time for 98% coating completion, t_c	CoV asymptote (%)
1.3	1	1.98×10^{-3}	0.0899	0.979	43.53	4.27
	2		0.0922	0.982	42.39	4.37
	Mean	-	**0.0911**	-	**42.96**	**4.32**
2.0	1		0.0615	0.977	63.63	3.72
	2		0.0691	0.983	56.65	3.64
	3	3.04×10^{-3}	0.0563	0.977	69.52	3.76
	4		0.0715	0.978	54.72	4.19
	Mean	-	**0.0646**	-	**61.13**	**3.83**
2.9	1	4.42×10^{-3}	0.0712	0.991	54.98	4.63
	2		0.0522	0.979	75.009	4.64
	Mean	-	**0.0617**	-	**64.99**	**4.63**

Note: The asymptotic CoV value is taken as an average of the CoV values at the final time points, where there is no clear decrease in CoV values

As can be observed in Figure 6.16, the lowest spray rate shows a steeper curve compared to other spray rates (2.9 and 2.0 g/s) which fall onto the same curve. This result was consistent with the measured value of the coating rate, λ, and the time taken for 98% of the coating to complete, t_c, as shown in Table 6.3. When the coating rate constant, λ, is plotted as a function of flow rate in Figure 6.17, the results indicate that the coating rate is slightly higher for 1.3 g/s spray rate compared to the 2.9 and 2.0 g/s spray rates. Furthermore, the coating rate also influences the t_c value, where with an increase in the coating rate, the t_c decreases as illustrated in Figure 6.18.
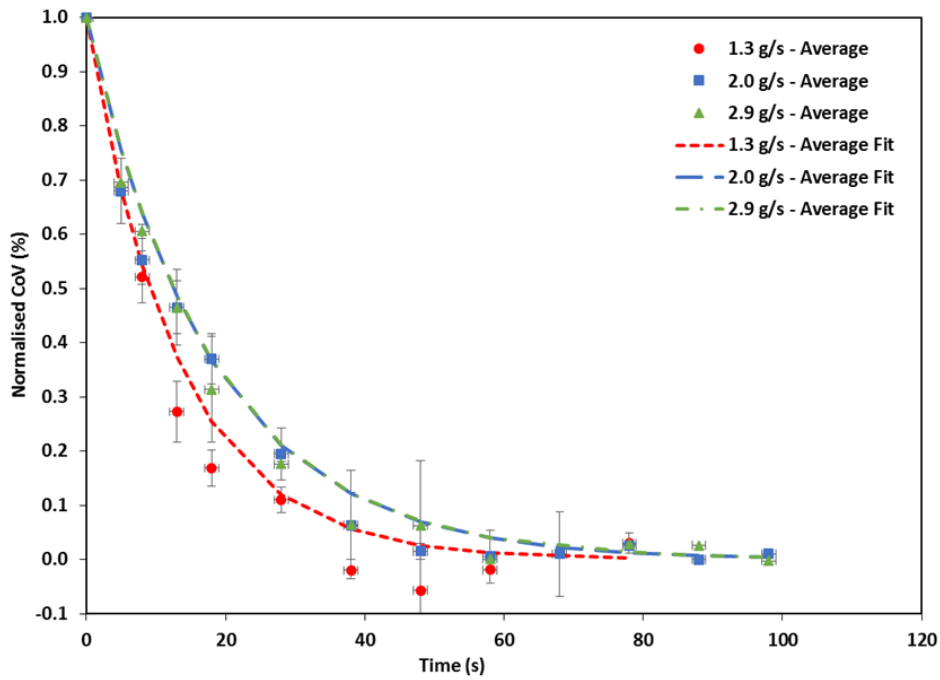
Figure 6.16. Average normalised (between CoV_0 and average CoV_∞) coefficient of variation and fitted decay curves as a function of mixing time for HPMC 603 solution (11 mPa.s) at different spray rates. Error bars represent standard error
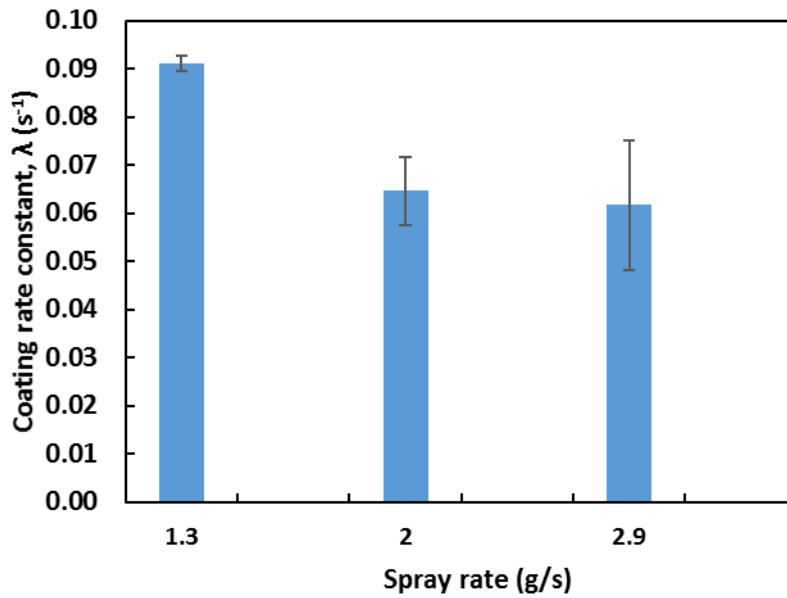
Figure 6.17. Coating rate constants as a function of the HPMC 603 solution (11 mPa.s) spray rates. Error bars represent standard error
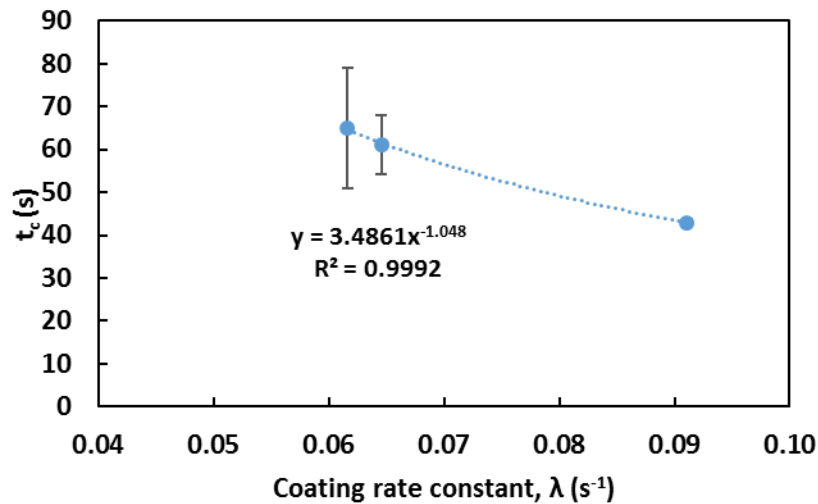
Figure 6.18. Time taken for coating completion, t_c as a function of coating rate constant, λ

This result might be due to differences in liquid content, which change the mixing behaviour in the fluidised bed. An increase in the spray rate means that the liquid content also increases with the same particle mass used (see Table 6.3). At 2.9 g/s spray rate, during the operation, a decrease in bed fluidity due to individual particles being gathered by agglomerates were observed. This contributed to nearly de-fluidisation behaviour, where the agglomerates formed find it difficult to move tangentially. But, as the time progressed, and the agglomerates broke up, the fluidisation became stable again. However, no more contact spreading occurred due to drying. This might be a possible reason for the red spots on a few of the coated particles at the asymptotic CoV value for 2.9 and 2.0 g/s spray rates as shown in Figure 6.19. This finding is supported by previous DEM-CFD simulations studied by He *et al.*, (2014). They found that due to strong viscous effects and enhanced sliding friction arising from liquid bridges, particles are not easily moved tangentially, and the bubble boundary becomes rough, and contributes to the irregular characteristic of the bubble behaviour.
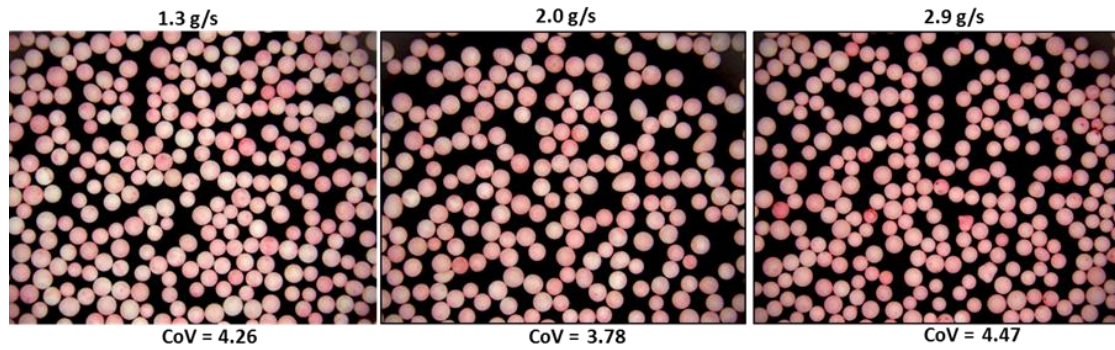
Figure 6.19. Image comparison of alumina coated with HPMC 603 solution (11 mPa.s) at different spray rates at asymptotic CoV value, 1.5 U_{mf} and 16 cm nozzle height from the distributor plate

Furthermore, higher liquid loading also tends to increase the time to complete the coating process, t_c. This might be due to the fact that agglomerates formed in the fluidised bed system need more time for rupture of the liquid bridges for higher liquid content as the mixing became slower and needed more time to be completed (He *et al*., 2014). Although the lower spray rate, 1.3 g/s, reached an asymptotic CoV value earlier compared to other spray rates, the particles still did not achieve good inter-particle coating uniformity (see Figure 6.19). This meant that even though the agglomerates break, no contact spreading occurs from the collision of the particles because the coating layer has already dried at the longer mixing time. The asymptotic CoV values observed here were different to the tumbling drum system as discussed in Chapter 5, Section 5.3. This might be due to no drying observed in the tumbling drum system. An increase in inter-particle forces also other possible effects caused by higher liquid loading which influences the fluidisation behaviour to move from B (sand like particles and the fluidisation is highly affected by the formation of gas bubbles in bed) to C group particles (cohesive particles), which are often very difficult to fluidise. In this case, a higher minimum fluidisation velocity needs to overcome the friction forces between the particles.

It can be concluded from this section that the liquid bridge rupture mechanism is important for contact spreading to occur in the fluidised bed system. It is believed that the higher liquid content effect on contact spreading might be improved if using a higher fluidisation velocity which could contribute to a larger bubble size and higher rising velocity. Thus, the faster the agglomerates will rupture, due to the high collision energy,

and distribute the liquid within the system via contact spreading. In the following section, the effect of fluidisation velocity on contact spreading is discussed.

6.3.2 Effect of fluidisation velocity

In this section, results for the effect of fluidisation velocity on contact spreading in the fluidised bed are discussed. Here, for HPMC 603 solution, a viscosity of 11 mPa.s and 2.0 g/s spray rate were selected from the previous study. This spray rate was selected as a middle value of the spray rate range. However, instead of a 16 cm height, a 22 cm nozzle height from the distributor plate was used. This height was selected since the range of superficial velocity, U_s, used from 1.3 to 1.8 U_{mf} will fluidise the particles up to 25 cm height from the distributor plate. This selection of fluidisation velocities is based on consideration of particle elutriation and adjustment of air spray rate so that particles are fluidized at different mixing behaviour. The bed behaviour observed at the different fluidisation velocities used resembled different regions of fluidisation: 1.8 U_{mf}, slugging phase; 1.5 U_{mf}, bubbling phase, and 1.3 U_{mf} was at a phase similar to slightly higher than minimum fluidisation.

Figure 6.20a-c shows a typical data series for the coating evolution of alumina particles coated with HPMC 603 solution (11 mPa.s) at different fluidisation velocities in the range from 1.3 to 1.8 U_{mf}. From this graph, the peak for 0 s is attributed to the coating evolution when the liquid is sprayed within the first 2 s. It is seen that at 0 s for 1.8 U_{mf}, the coating evolution has a wider distribution and higher % red intensity compared to others. Moreover, as time progresses, a similar pattern can be seen for 1.8 and 1.5 U_{mf}, where the coating evolution shifts to higher % red and led to narrower distributions. This indicates that for both velocities, a more uniform coating was obtained.

On the other hand, 1.3 U_{mf} fluidisation velocity appears to have a significantly different distribution compared to the others. At this velocity, after 2 s spray (0 s), there was virtually no shift in the % red to higher values even though the distribution seems to have a slightly wider distribution. This means that even as the time increases, the coated

particles did not reach uniform coating. When the percentage mean red is plotted as a function of mixing time (Figure 6.21), it shows that the % mean red was dependent on the fluidisation velocity used. This result was unexpected since the same solution and spray rate was used. The probable reason is that at lower velocity, the fluidised bed height is lower in comparison to higher velocities and hence the probability of droplets captured by the particles is reduced. Further, more droplets will adhere to the wall and hence increase the particle-wall effect. This phenomenon was observed for 1.3 and 1.5 U_{mf} as illustrated in Figure 6.22, where more particles adhered to the wall. In addition, this also explains the fluctuation in data points observed for lower velocity at lower mixing time (Figure 6.21).

The influence of fluidisation velocity on inter-particle coating variability is shown in Figure 6.23 by plotting the CoV values as a function of mixing time. The increase of the fluidisation velocity significantly decreased the coating variability and eventually levelled off (1.5 and 1.8 U_{mf}). However, for 1.3 U_{mf} velocity, as time progressed, the CoV values were nearly constant, and this result was consistent with the coating evolution and visual images observed in Figure 6.20 and 6.22. The evidence from these results suggests that little contact spreading occurs at 1.3 U_{mf} velocity. This is because at the time of spraying in 2 s, the particles in the spray zone initially exhibited capillary behaviour, forming agglomerates which gradually sank to the bottom part of the tube (see Figure 6.22), and the rising velocity was not enough to overcome the cohesive force by the inter-particle liquid bridges. As time progressed, these wet agglomerates ruptured, but there was no liquid spreading due to drying occurring simultaneously in the system. Since this velocity did not show any changes in CoV values, the following analysis was carried out only on the other two velocities; 1.5 and 1.8 U_{mf}.
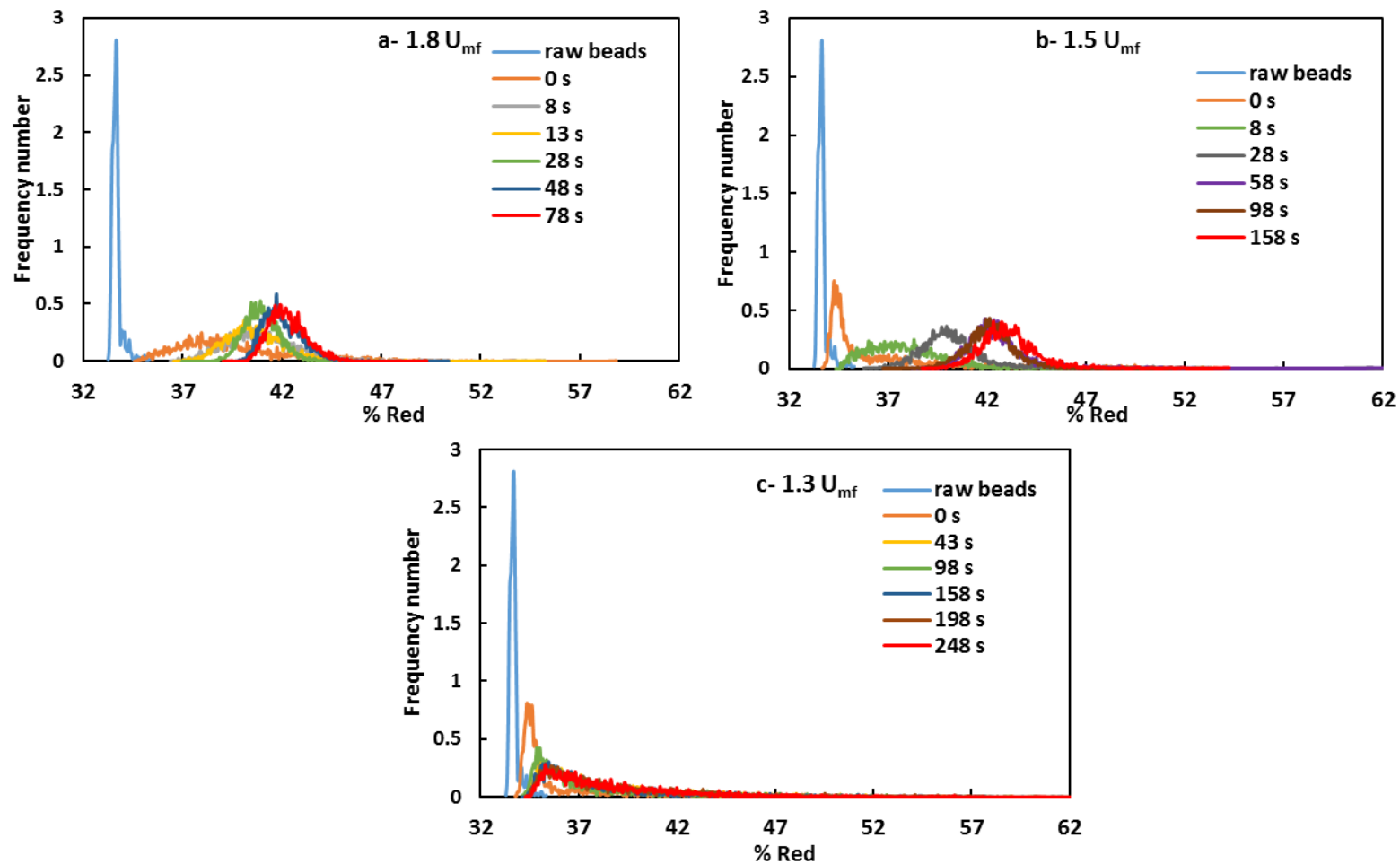
Figure 6.20. Coating evolution of alumina coated with HPMC 603 solution (11 mPa.s) at different fluidisation velocities, a: 1.8 U_{mf}; b: 1.5 U_{mf} and c: 1.3 U_{mf} (note that not all time points for each data series are shown for visualisation purposes)
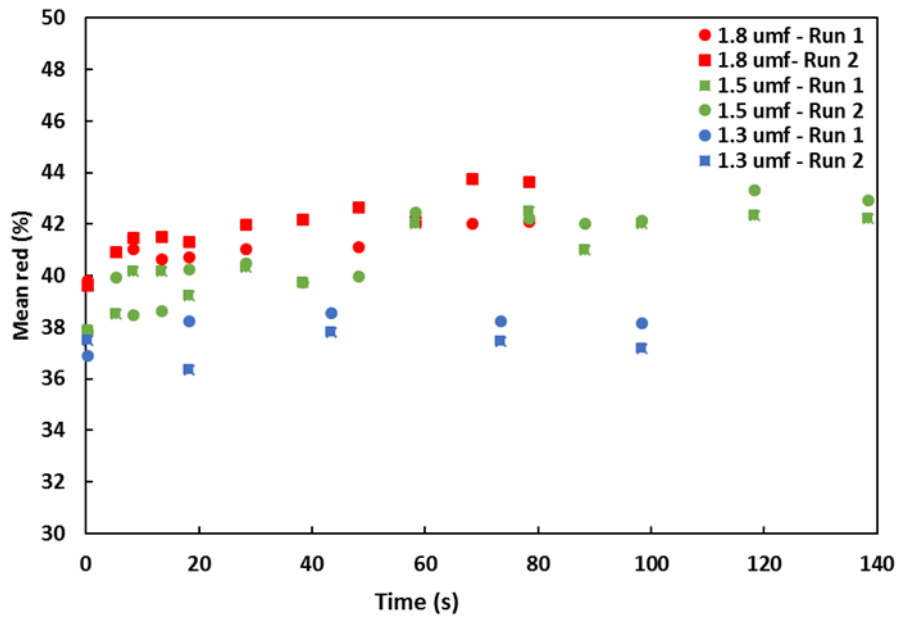
Figure 6.21. Mean % red as a function of mixing time for different fluidisation velocities
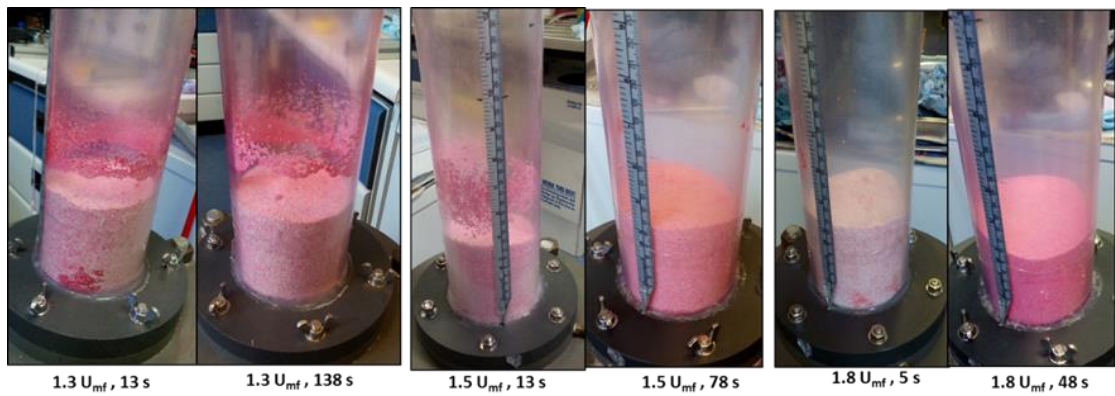
Figure 6.22. Visual images of alumina coated with HPMC 603 solution (11 mPa.s) at different fluidisation velocities in the fluidised bed tube
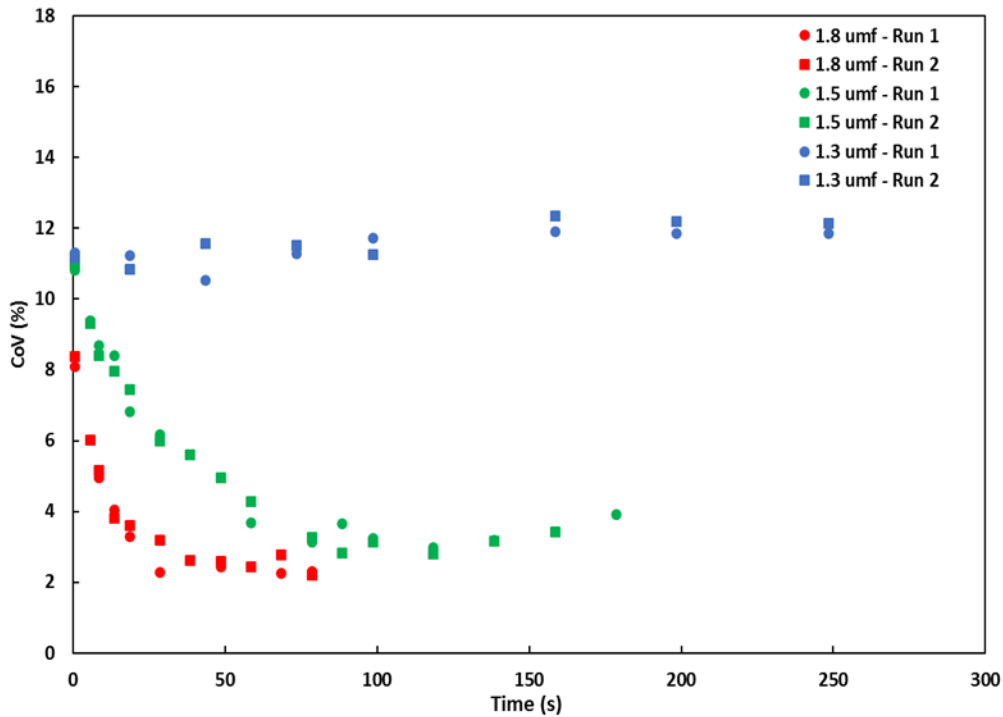
Figure 6.23. Coefficient of variation as a function of mixing time for alumina particles coated with HPMC 603 solution (11 mPa.s) at different fluidisation velocities

In Figure 6.24, the relative CoV as a function of time is shown for 1.5 and 1.8 U_{mf}. It is seen that all the normalised data series reach a similar asymptotic CoV value at certain mixing time even though a higher velocity showed a faster decrease in CoV value. Moreover, coating rate, λ, and time for coating completion, t_c, were determined as described in the previous section (Section 4.2.2), where the exponential decay curve fitting was used. The curves fit well to the whole data series as shown in Figure 6.25 and the fitting parameters measured are summarised in Table 6.4.
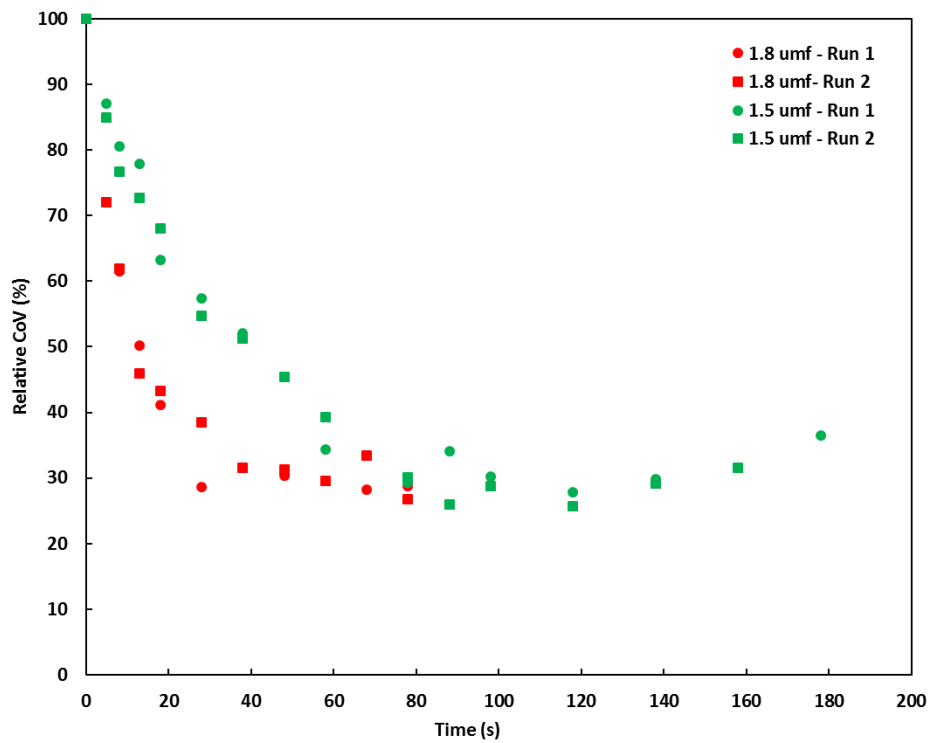
Figure 6.24. Relative coefficient of variation as a function of mixing time for alumina particles coated with HPMC 603 solution (11 mPa.s) at different fluidisation velocities
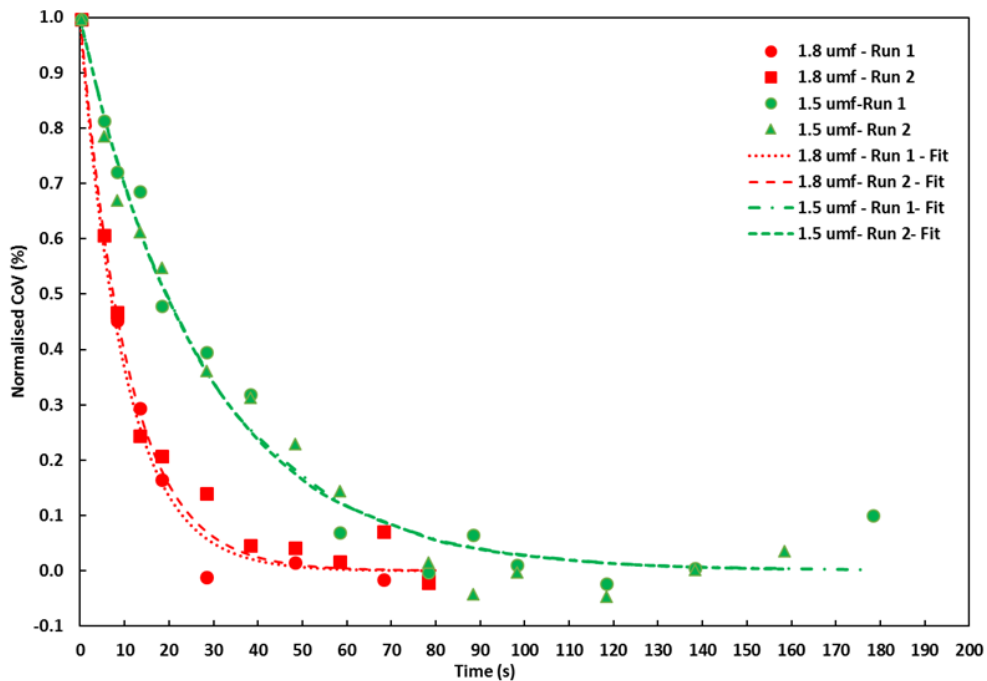
Figure 6.25. Normalised (between CoV_0 and average CoV_∞) coefficient of variation and fitted decay curves as a function of mixing time at different fluidisation velocities

168
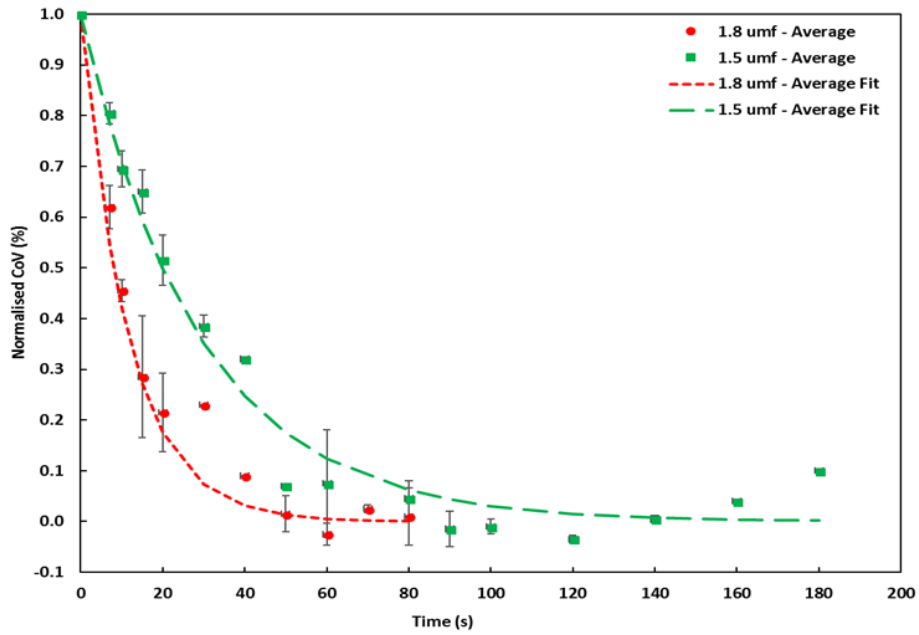
Figure 6.26. Average normalised (between CoV$_0$ and CoV$_\infty$) coefficient of variation and fitted decay curves as a function of mixing time. Error bars represent standard error

Average normalised CoV values (between CoV$_0$ and average CoV$_\infty$) were also plotted as a function of mixing time and fitted with the decay curves for both velocities (Figure 6.26). Here, note that not all data points were repeated (no error bars) due to the reason as explained in previous sections; rather than carrying out repeats for every time point, further time points were selected to ensure that data was obtained over the course of the whole coating process, until and after coating completion. As expected, Table 6.4 shows the coating rate constant, λ, of the higher fluidisation velocity significantly increased to nearly three times to that of the lower fluidisation velocity (see Figure 6.27).

Table 6.4. Fitting constants and time taken for coating completion for all data series at different fluidisation velocities

Fluidisation velocity (m/s)	Run	Coating rate constant, λ (s^{-1})	R^2	Time for 98% coating completion, t_c	CoV asymptote (%)
1.5 *Umf* (0.838)	1	0.0356	0.986	109.84	3.18
	2	0.0359	0.982	108.99	3.18
	Mean	**0.036**	-	**109.41**	**3.18**
1.8 *Umf* (1.048)	1	0.0932	0.984	41.98	2.37
	2	0.0999	0.993	39.17	2.37
	Mean	**0.097**	-	**40.57**	**2.37**

Note: The asymptotic CoV value is taken as an average of the CoV values at the final time points, where there is no clear decrease in CoV values
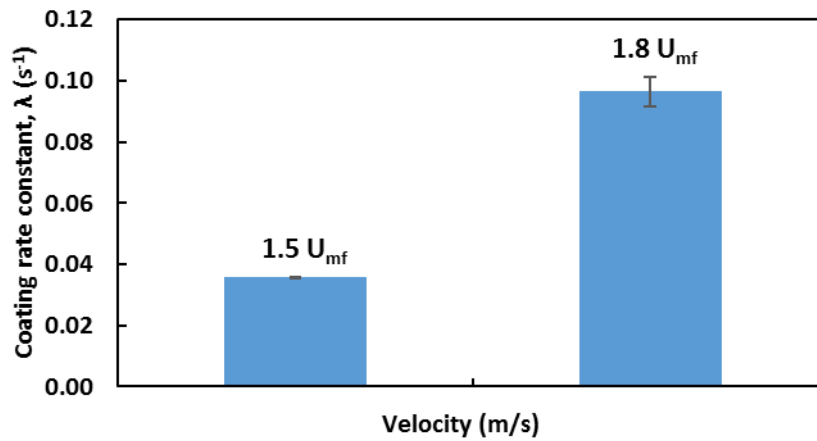
Figure 6.27. Coating rate constant, λ, as a function of fluidisation velocity

Furthermore, when the time for completion of coating, t_c, is plotted as a function of coating rate, λ, in Figure 6.28, it shows that λ significantly influences the time to complete the coating process; a higher λ value gave a shorter t_c value. This result matched the visual images of coated particles observed using image analysis at different fluidisation velocities, which are given in Appendix D6.
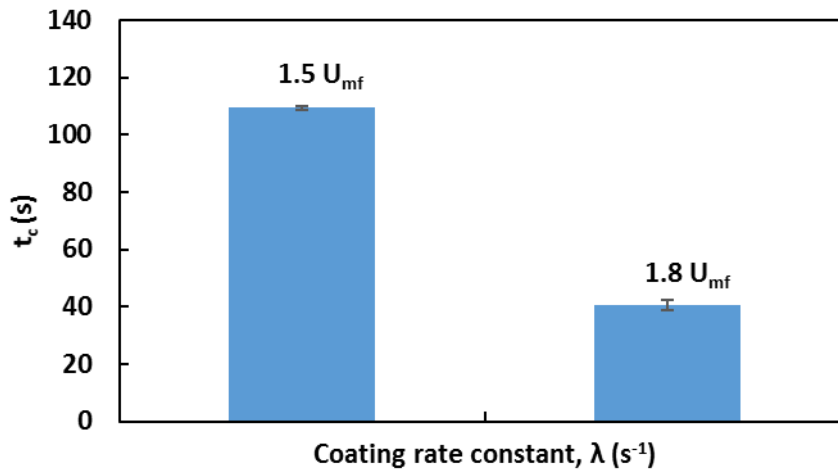
Figure 6.28. Time taken for coating completion, t_c, as a function of coating rate constant, λ, at different fluidisation velocities

There are several possible explanations for the difference in coating behaviour observed at different fluidisation velocities. One probable reason is related to the different particle motion behaviour at different fluidisation velocities; in particular, the collision between particles and between the particles and the tube wall. Mixing in fluidised beds is driven by the particle-free voids or bubbles that form from the excess gas velocity (U- U_{mf}) (Lim *et al.*, 2007). A higher fluidisation velocity for group B particles enhanced solid mixing. In this case, it was observed that the rising bubble size was larger at higher fluidisation velocity. Thus, a higher number of collisions between the particles occur, and the liquid tends to spread faster within the system. This mixing behaviour at higher fluidisation velocity is further supported by a study by Askarishahi *et al.*, (2015) who reported that higher fluidization velocity improved solid dispersion and the diffusion coefficients. According to Smith and Nienow, (1983), for coating over granulation to be the main phenomena occurring in a fluidised bed system, the excess velocity (U- U_{mf}) needs to be exceeded by at least 0.2 m/s. In this study, only the lowest velocity used, 1.3 U_{mf} (0.73 m/s) did not meet this criterion (U - U_{mf} = 0.157 m/s) (see Appendix D1) and hence, previous findings were in reasonable agreement with the experimental observations.

Moreover, a lower fluidisation velocity contributes to a lower fluidised bed height as seen in Figure 6.1. This will cause a decrease in particle flux through the spray zone (Vengateson and Mohan, 2016). At the time of spraying for 2 s, fewer droplets will impinge on the particles and more of the droplets adhere to the wall as seen in Figure 6.22 at 1.3 and 1.5 U_{mf}. On the other hand, as fluidisation velocity increases, particle circulation becomes faster, leading to more successful droplet-particle collisions, which will subsequently lead to more wet collisions occurring and hence improving liquid spreading within the particle bed.

Another possible reason is due to the difference in the fraction of agglomerates formed during the process at different fluidisation velocities. The fraction of agglomerates formed at both of the higher fluidisation velocities (1.5 and 1.8 U_{mf}) as a function of mixing time is shown in Figure 6.29. Here, the fraction of agglomerates represents the mass fraction of agglomerated particles of the total mass of a particle batch. After the coating process, prior to sampling for image analysis, the mass of dyed coated particle batches was recorded. Then, the coated particles were poured into the stacked sieves in order from largest (top) to smallest (bottom) aperture sieve size. The sieves were manually shake to avoid breakage of the agglomerates.The mass of agglomerates on each sieve size were weighed and the fraction of agglomerates for each particle batch was obtained by divided the total mass of agglomerates to the mass of a particle batch.

The results show that increasing the fluidisation velocity produced a smaller fraction of agglomerates. This means that a higher velocity of fluidised particles increases the relative collision rate between the particles and hence the rupture of the liquid bridges will be faster compared to a lower velocity. Subsequently, wet particles will redistribute the liquid in the system and complete the coating process in a shorter time at a higher velocity. This finding is consistent with previous studies which have reported that the higher the particle velocity to spray zone, the better droplets distribute onto particle surfaces, and hence lower the probability of large agglomerates forming (Vengateson and Mohan, 2016; Villa *et al*., 2016). The images of agglomerates formed at different fluidisation velocities are shown in Appendix D7.
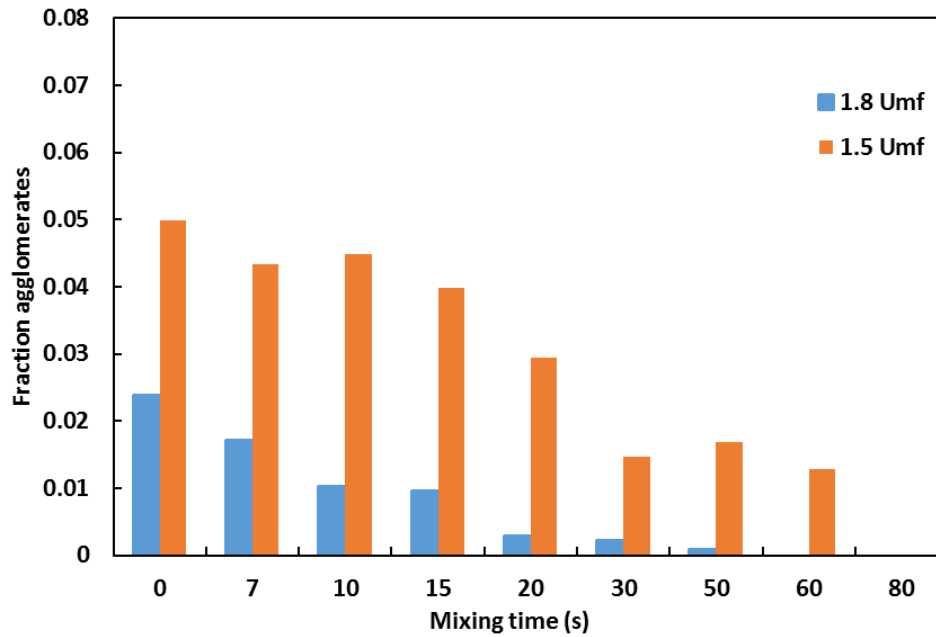
Figure 6.29. Agglomerate fraction as a function of mixing time at different fluidisation velocities

Previous studies reported that when a different size or density of particles is used, the fluidisation may be difficult due to the different sets of particles having different values for U_{mf}. When attempting to fluidize such a system, one set of particles will float above the other, where the top layer is known as the flotsam and the bottom layer is termed the jetsam (Niranjan, 1993). As reported by (Chiba *et al.*,1980), a high velocity is needed to ensure these two sets of particles become completely mixed as the jetsam will have a higher U_{mf} than the flotsam. In this study, the particle density of agglomerates formed was assumed to change, especially at a lower mixing time of the operation, e.g. agglomerates formed hold the liquid and the density of agglomerates may be different from that of the feed particles. This assumption is consistent with the observation in this study, where after the time of spraying, the wet agglomerates formed gradually pushed down onto the bottom part of the tube. The mixing behaviour became stable again (i.e. mixing as before agglomerates formed) as the time increased or when the velocity increased. This was due to a higher velocity fluidising the agglomerates to the top and the higher energy collisions ruptured the liquid bridges and the liquid freely spread in the system.

As a summary for this section, fluidizing air velocity is one of the important parameters which determines the success of contact spreading in the fluidised bed system. It is observed to have a significant effect on the coating behaviour via contact spreading; the higher the velocity, the faster the contact spreading process with a shorter time required to reach an asymptotic value of the CoV. This is due to the bubble-induced particle motion which occurs at a higher velocity, rupturing the liquid bridges formed between wetted particles which influences the mechanism of liquid transfer via contact spreading. In this section, only one viscosity of coating liquid was used. When using a higher velocity but with different coating liquid viscosity, the contact spreading mechanism might change, and this is discussed in the following section.

6.3.3 Effect of coating liquid viscosity

In this section, results for the effect of coating liquid viscosity on contact spreading in the fluidised bed are discussed. Here, three different molecular weight (MW) 5% HPMC solutions were used; HPMC 603, HPMC 606 and HPMC 615 corresponding to viscosities of 11 mPa.s, 44 mPa.s and 177 mPa.s respectively. The liquid spray rate used was 2.0 g/s by setting the liquid pressure for each solution based on the calibration curve in Figure 6.6. The nozzle height was set at 22 cm from the distributor plate and 1.8 U_{mf} was set for the fluidisation velocity. These settings were used so to be the same as previous fluidisation velocity parameters to allow for comparison of coating solution viscosity only.

A typical data series for coating evolution of alumina coated with three different viscosities of HPMC solutions are shown in Figure 6.30a-c. It is observed that when the frequency is plotted as a function of percentage red, the distributions show a similar pattern for all viscosities used, where they all become narrower with an increase in mixing time. This observation indicates that a lower degree of coating variability with time is achieved, and this is supported by Figure 6.31 where the CoV value is plotted as a function of time. The experiments were performed in duplicate to confirm good reproducibility for each experimental run.

174
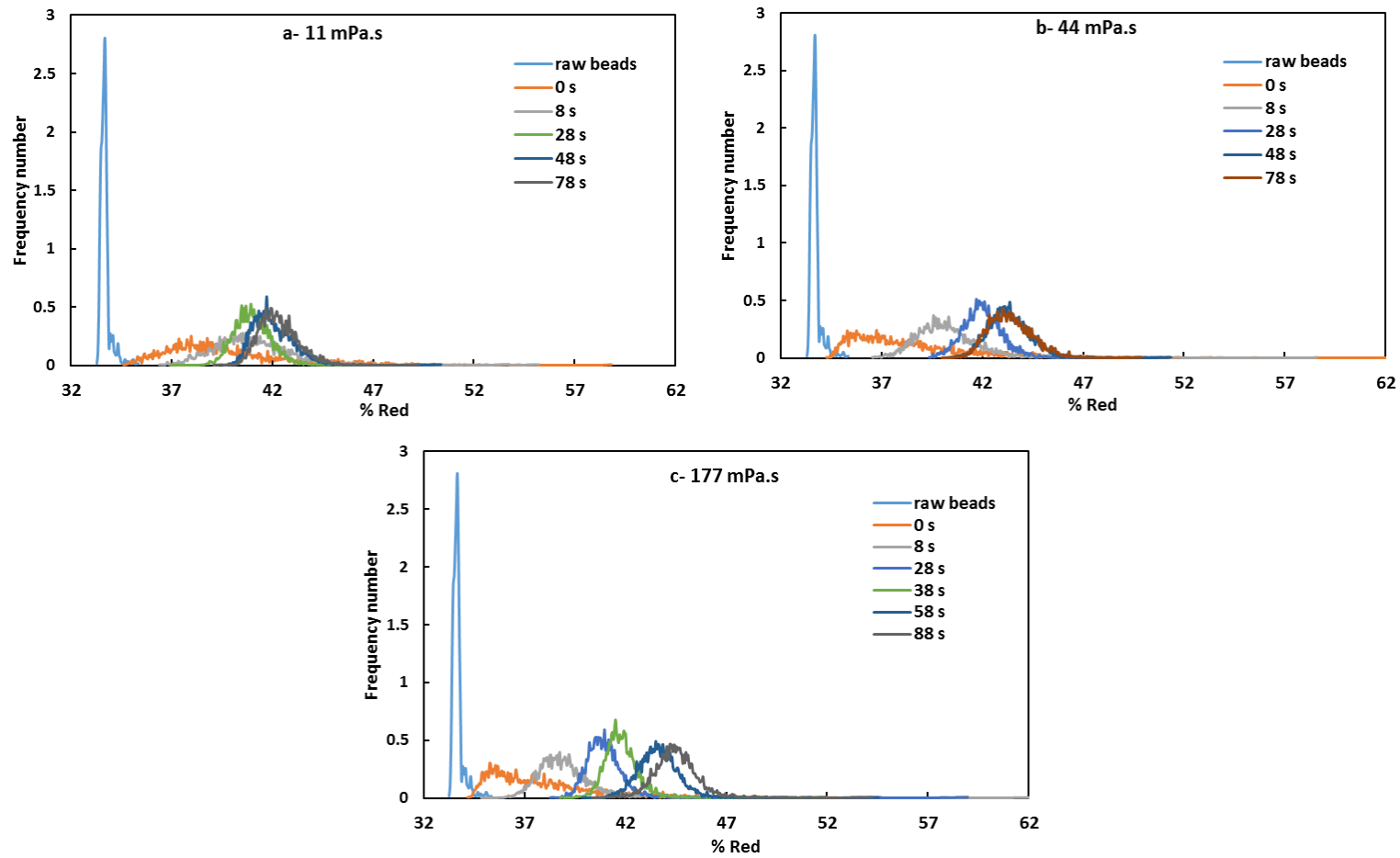
Figure 6.30. Coating evolution of alumina coated with HPMC solutions of different viscosities; a: 11 mPa.s, b: 44 mPa.s and c: 177 mPa.s (note that not all time points for each data series are shown for visualisation purposes)

Further, the CoV values are normalised (referred to as relative CoV data) as shown in Figure 6.32. Here, a similar pattern to previous parameters is observed where the CoV values eventually level off as time progresses and reach a similar asymptotic CoV value with all different viscosities used. However, surprisingly, despite the difference in viscosity, all the data series are observed to fall onto similar curves. This unexpected result was in complete contrast to the findings for effect of viscosity in tumbling drum system discussed in Chapter 5, Section 5.3. The difference in these findings might be due to the different coating system and range of viscosity, where the viscosity range used here in this system was lower and narrower (see Chapter 3, Section 3.2.1). Furthermore, the PEG solutions used in the tumbling drum could not be applied in fluidised bed system because these solutions dry too quickly, and no contact spreading can be observed when using the lowest PEG viscosity solution (137 mPa.s) (see Section 3.2, Figure 3.7).
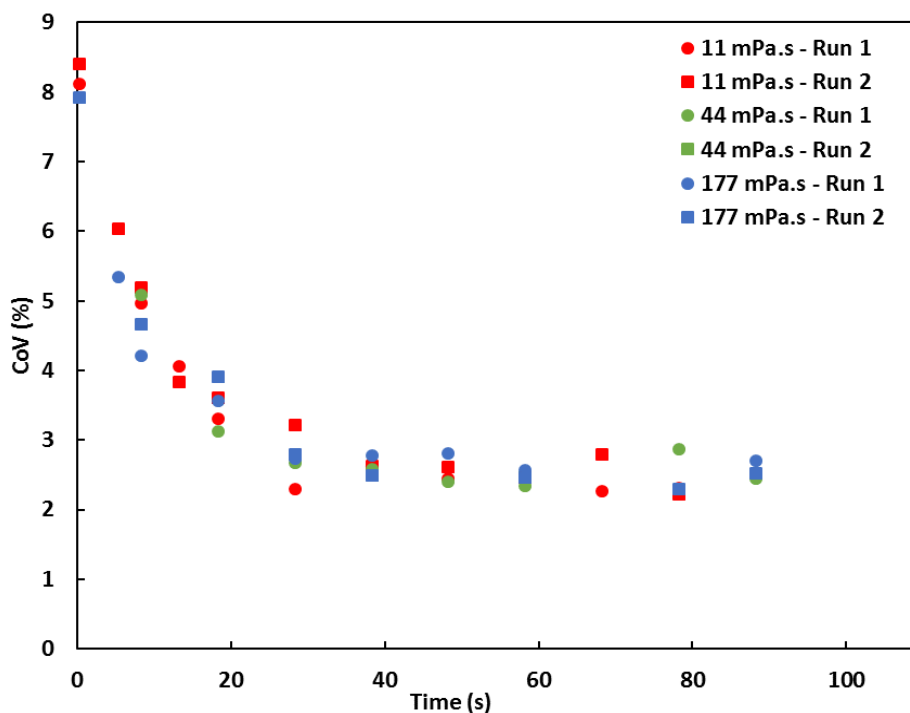
Figure 6.31. Coefficient of variation as a function of mixing time for alumina particles coated with HPMC solutions of different viscosities
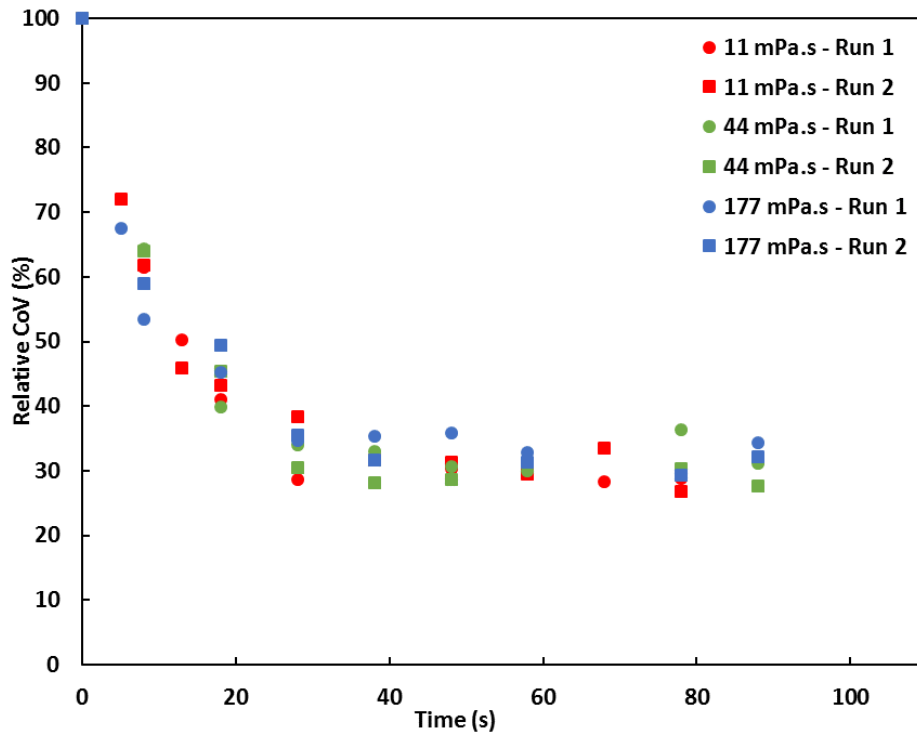
Figure 6.32. Relative coefficient of variation as a function of mixing time for alumina particles coated with HPMC solutions of different viscosities

Moreover, the coating rate, λ, and the time to complete 98% of the coating process, t_c, are also calculated for each viscosity based on the exponential decay curve fitting method. This was carried out using the method explained in Chapter 4, Section 4.2.2. Figure 6.33 shows that the decay curves fitted well ($R^2 > 0.9$) to the normalised data series and the values of the fitting constants are summarised in Table 6.5. Figure 6.34 shows a plot of an average normalised (between CoV_o and average CoV_∞) coefficient of variation and fitted decay curves, as a function of mixing time for alumina coated with different viscosity solutions. It is seen that the normalised CoV data series are not significantly different at the different viscosities used.
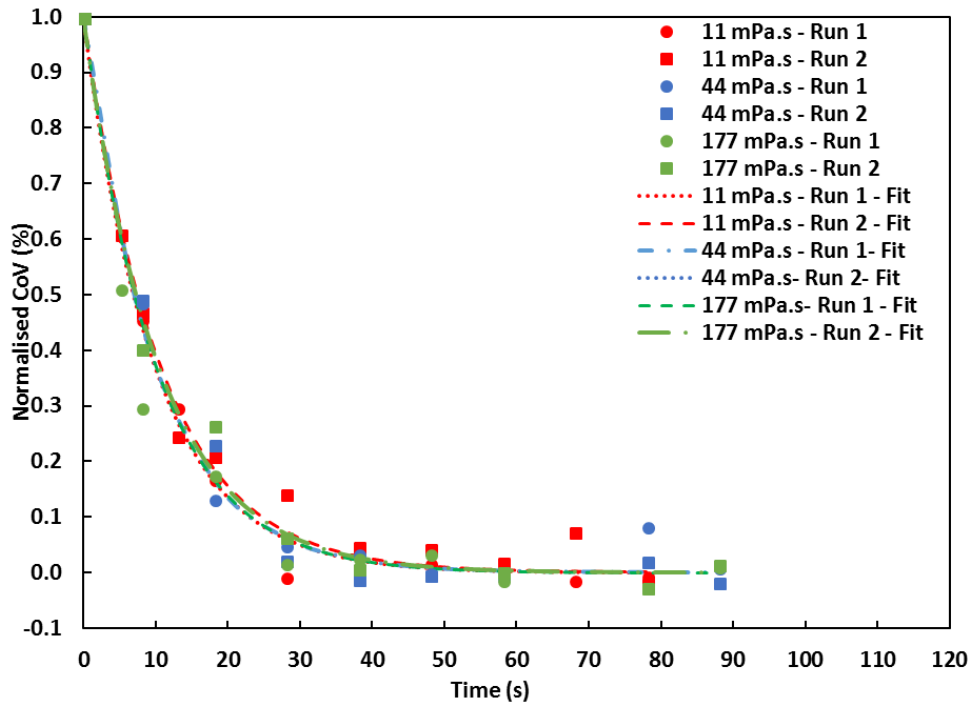
Figure 6.33. Normalised (between CoV$_0$ and average CoV$_\infty$) coefficient of variation and fitted decay curves as a function of mixing time for alumina coated with HPMC solution of different viscosities
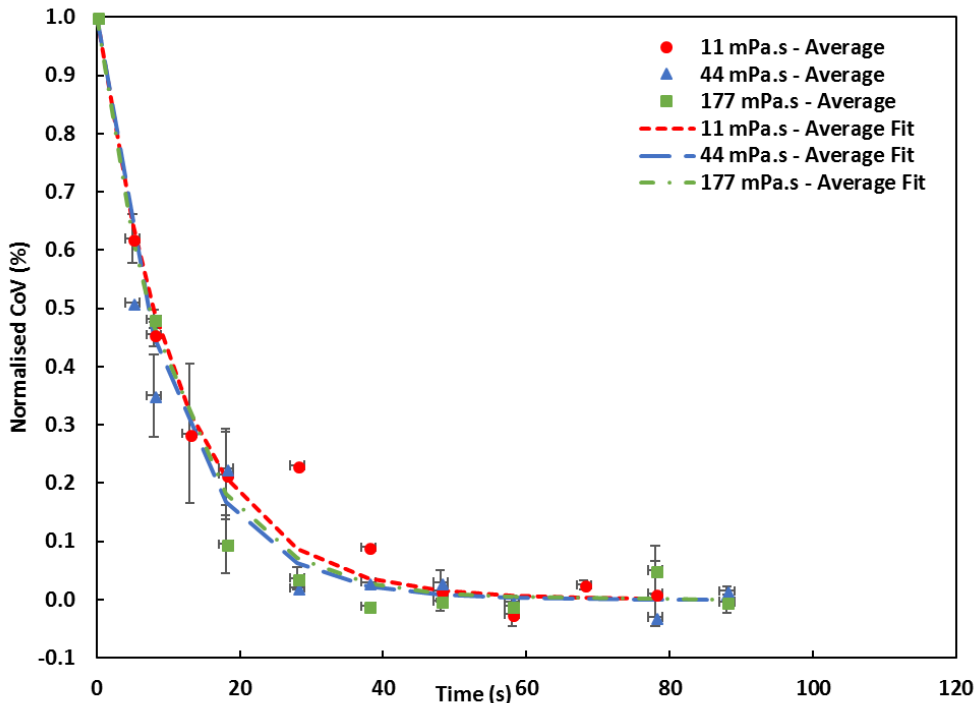
Figure 6.34. Average normalised (between CoV$_0$ and average CoV$_\infty$) coefficient of variation and fitted decay curves as a function of mixing time for alumina coated with HPMC solution of different viscosities. Error bars represent standard error

According to Table 6.5, the measured coating rate constant, λ, time for coating completion, t_c, and asymptote CoV values obtained are not significantly different at the different viscosities used. Moreover, when the λ and t_c are plotted as a function of viscosity (Figure 6.35), it clearly seen that the range of viscosity used did not influence the coating rate and the time taken to reach 98% of the coating process via contact spreading.

Table 6.5. Fitting constants and time taken for completion for the effect of viscosity

Viscosity (mPa.s)	Run	Coating rate constant, λ (s^{-1})	R^2	Time for 98% coating completion, t_c	CoV asymptote (%)
11	1	0.099	0.993	39.17	2.37
	2	0.093	0.984	41.98	2.37
	Mean	**0.097**	-	**40.57**	**2.37**
44	1	0.098	0.989	39.54	2.43
	2	0.093	0.992	41.97	2.38
	Mean	**0.096**	-	**40.76**	**2.41**
177	1	0.110	0.977	35.50	2.67
	2	0.095	0.985	41.27	2.47
	Mean	**0.103**	-	**38.39**	**2.57**

Note: The asymptotic CoV value is taken as an average of the CoV values at the final time points, where there is no clear decrease in CoV values
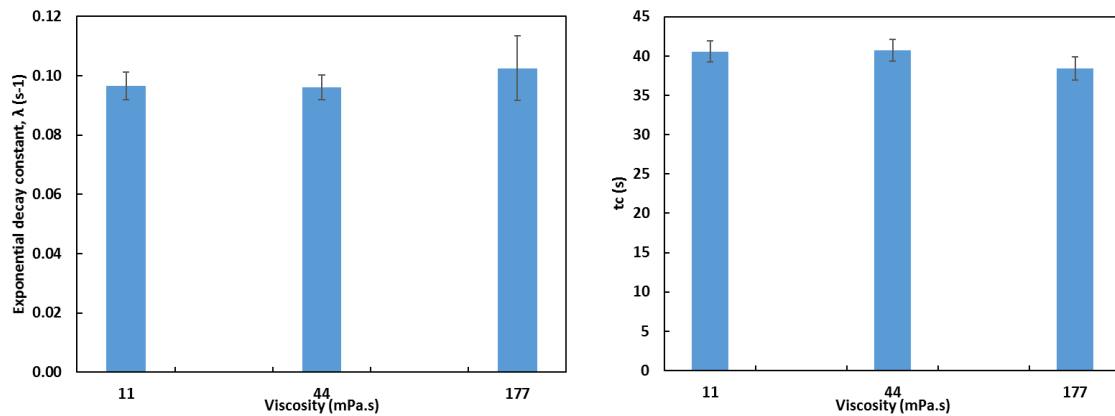
Figure 6.35. Coating rate constants (left) and time taken for coating completion, t_c (right) as a function of viscosity

Figure 6.36 shows the fraction of agglomerates formed in the fluidised bed system as the time increases when different viscosities of HPMC solutions are used. As expected, it indicates that the agglomerate fraction increases with viscosity. This probably occurs due to lower wettability (see Table 3.6, Section 3.3.1) and higher drying rate for higher viscosity solutions at the same excess velocity used. When wet collisions occur, the liquid bridges formed subsequently break and distribute the liquid in the system. Breakage of the agglomerates formed may be observed when the liquid or solid bridges break apart due to collision forces. Simons *et al.*, (1994) reported that the energy needed to rupture a liquid bridge increases when the surface tension increases or contact angle is decreased. In this case, the surface tension for each solution is similar and can be neglected. Thus, the breakage mechanism of the liquid bridge can be considered to be affected by the viscosity and contact angle of the liquid used; higher viscosity leads to higher contact angle and increased drying rate, hence, a greater fraction of agglomerates are formed. Moreover, higher viscosity solutions do not wet effectively as lower viscosity solutions as the base width of the droplet decreases while the drop height increases on the fine particle surface as shown in Figure 5.16, Section 5.3.1. This meant that when liquid bridges are formed, higher viscosity not uniformly spread on the particle surface compared to lower viscosity. Thus, upon rupturing, if this is followed by rapid drying, more coating liquid will be trapped within the agglomerates mainly for higher viscosity solutions, lead to less uniformity of final coated particles obtained.
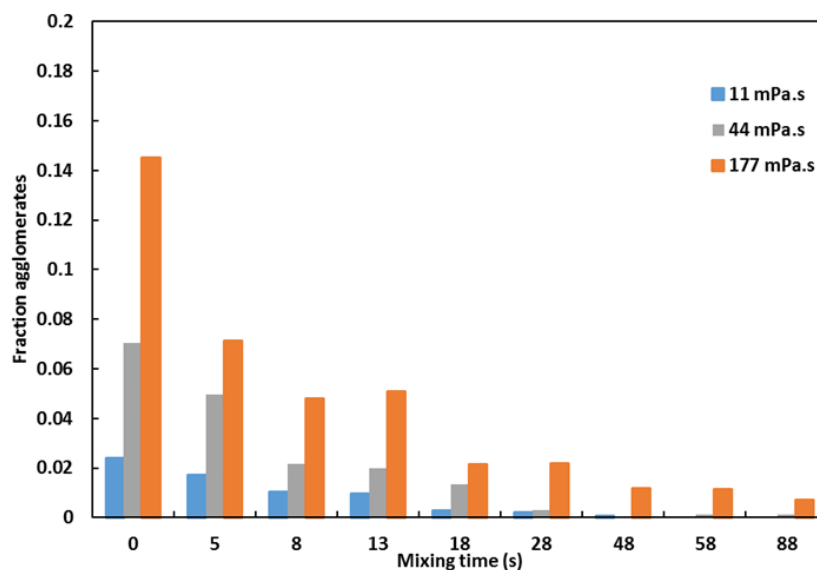
Figure 6.36. Fraction of agglomerates as a function of mixing time at different viscosities

However, surprisingly, this trend in the fraction of agglomerates is not consistent with the coating rate via contact spreading (Table 6.5 and Figure 6.36). It seems that even though the higher viscosity leads to a higher fraction of agglomerates formed, the coating rate was similar. The probable reason for this may be due to the behaviour of liquid bridge forces formed during wet collisions. Liquid bridge forces between particles consist of static and dynamic forces; the former depends on liquid surface tension and liquid bridge shape, while the latter depends on liquid viscosity and relative particle motion *(Zhou et al.*, 2017). The ratio between dynamic and static liquid bridge forces are measured by capillary number, *Ca,* (Eq. 6.1) while the ratio of surface tension forces to gravitational forces, is given by granular *Bo* number (Bo_g) in Eq. 6.2 (Boyce *et al.*, 2017b; McCarthy, 2003). Both values are measured and shown in Table 6.6.

$$Ca = \frac{\mu v_c}{\gamma} \qquad\qquad \textbf{Equation 6.1}$$

$$Bo_g = \frac{6\gamma}{\rho_p g d_p{}^2} \qquad\qquad \textbf{Equation 6.2}$$

where g is the acceleration due to gravity, ρ_p is the particle density, d_p is the particle diameter, v_c is the characteristic collision velocity, μ is the viscosity and γ is surface tension.

Table 6.6. Capillary and Bond number for each HPMC solution at different viscosity

5% HPMC solution	Viscosity, μ (mPa.s)	Capillary number (-)	Bo$_g$ number (-)
603	11	0.106	7.99
606	44	0.443	7.62
615	177	1.733	7.84

For each different viscosity of HPMC solution, it shows that the capillary numbers, *Ca* are lower than 1 except for the 177 mPa.s solution, which shows a capillary number slightly greater than 1. Ennis *et al.*, (1990) proposed that if *Ca* is greater than 1, the dynamic or liquid viscous effects dominate the liquid bridge force. In this experimental system, due to the lower *Ca* number for both 11 and 44 mPa.s, the static liquid bridge plays a dominant role compared to the viscous effects. For 177 mPa.s, both viscous and capillary are both important as the *Ca* value, 1.733, is more than 1. In this case, the viscous force could not necessarily be ignored. Here, as the surface tension is similar, when wet collisions occur, the liquid bridge strength formed is assumed similar (Bo$_g$ number in Table 6.6), thus the bridge will rupture and spread the liquid in the system at similar rate. Due to this, regardless of viscosity used, coating rate happens at similar rate.

Another probable reason for no effect of viscosity is the difference in the method of liquid additon to the system compared to tumbling drum system. In this case (fluidised bed), the liquid is sprayed for 2 s to the fluidised particles and the mixing time started once the spray stops. Here, the initial wetting is based on the droplets produced in 2 s spraying time. Further, the fraction of the particles in this spray zone can be divided into three groups; completely wet, partly wet based on the drop surface area and, finally, no wet particles. Subsequently, when these particles return to the particle bed, not all collisions of the particles will successfully form liquid bridges via contact spreading. Even if the liquid bridge is formed successfully, the bridge is weak, where the formation occurs only at the wet surface of the particle. This depends on the spreading area of the droplet on particle surface. In contrast, in tumbling drum system, the 10% of particle batch was initially coated before being mixed into the remaining 90% agitating particles in the drum. Here, the initial wetting is based on this 10 % wet particles, where the particle is completely wet at the initial point when introduced into the system. Also, due to this, whenever collisions between the particles happen, liquid bridges will form; thus, in the tumbling drum system, different viscosities showed a significant effect on the contact spreading mechanism.

6.3.4 Effect of nozzle height

In this section, results for the effect of two nozzle heights from the distributor plate on contact spreading in the fluidised bed are discussed. Here, 5% HPMC 603 solution, viscosity of 11 mPa.s was used. The spray rate used was 2.0 g/s and the nozzle was set at different heights; 16 cm and 22 cm from the distributor plate. The spray distribution at different nozzle height is shown in Figure 6.9, Section 6.2.3. As explained in Section 6.2.3, the spray distribution of different nozzle heights gives a similar cross-sectional area; roughly 5 cm in diameter. However, a higher height shows more uniform spreading of droplets but lower spray volume due to some loss of droplets due to evaporation.

Figure 6.37 shows the results of a typical data series for the coating evolution of alumina coated with HPMC 603 solution at different nozzle heights; 16 cm and 22 cm. In this figure, not all time points are shown for each data series for visualisation purposes. The full data series are given in Appendix D9. The coating evolution for both nozzle heights show a similar distribution trend; as the time increases from 0 s to 5 s, there was a shift in the % red dye to slightly higher values. Further, with an increase in mixing time, the distribution became narrower, which indicates a higher inter-particle coating uniformity.
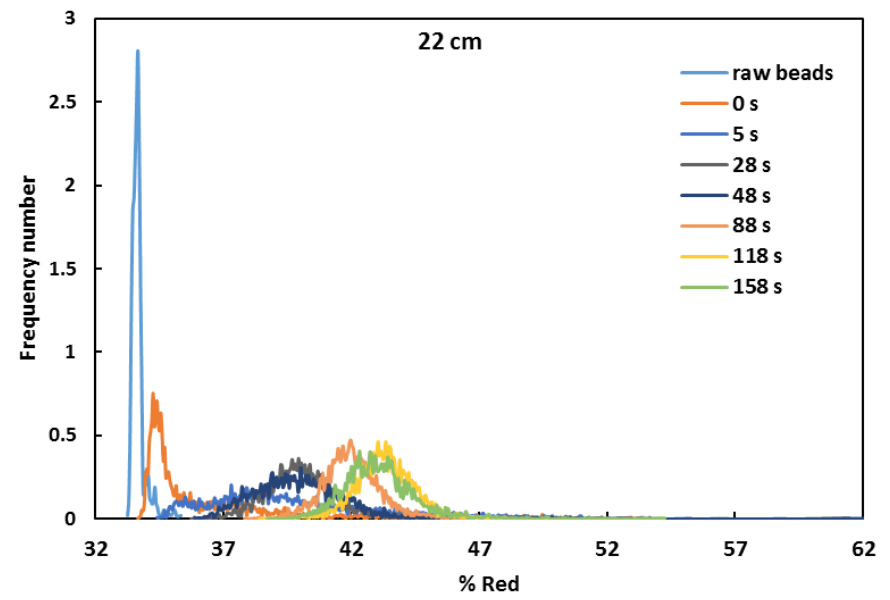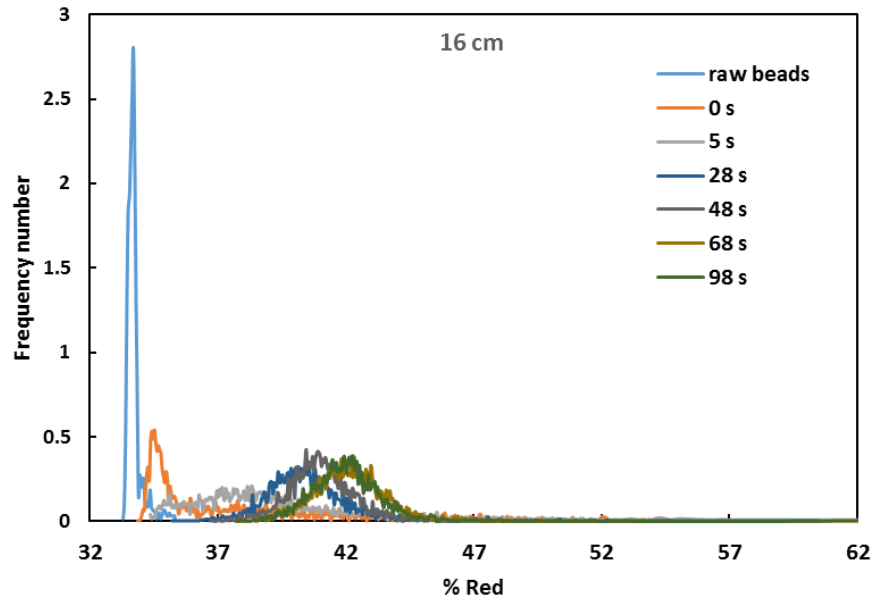
Figure 6.37. Coating evolution of alumina particles coated with HPMC 603 (11 mPa.s) at different nozzle height

Figure 6.38 plots CoV as a function of mixing time for different nozzle heights. The experiments were duplicates at both nozzle heights. It shows that all data series for each condition were repeatable. It was observed that a similar trend occurred as previous parameters studied; CoV values decrease with time and reach a constant value after a certain mixing time. When the CoV values are normalised (relative CoV) and plotted as function of mixing time in Figure 6.39, it appears that both nozzle heights reach a similar asymptotic CoV value at different mixing time. From both Figure 6.38 and Figure 6.39, a slightly faster coating rate for the lower height (16 cm) was observed.
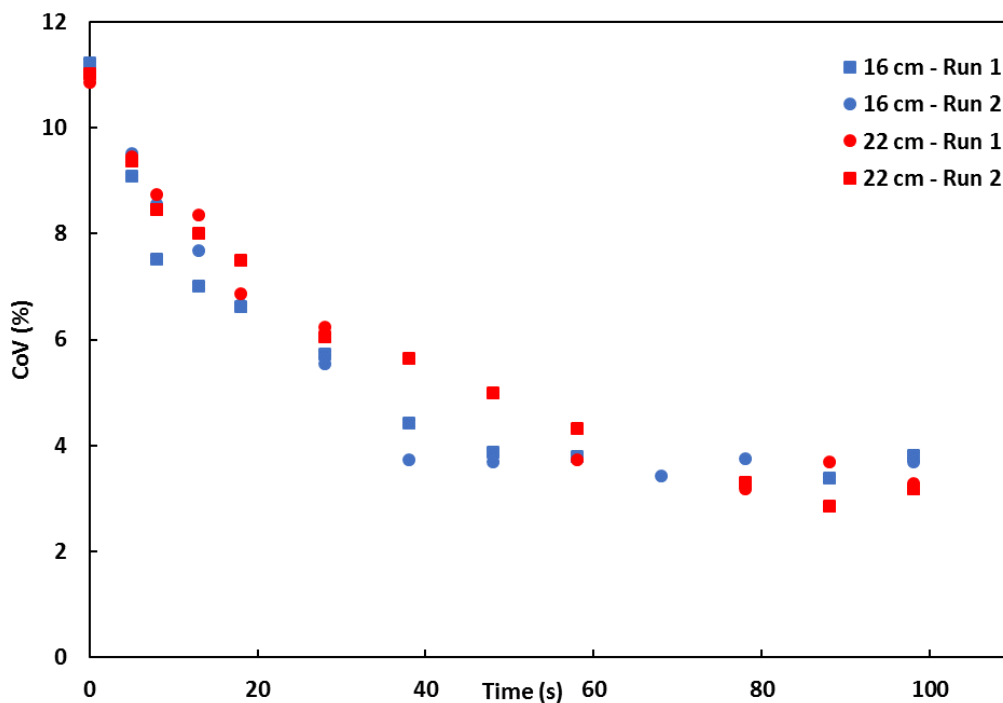
Figure 6.38. Coefficient of variation as a function of mixing time for alumina particles coated with HPMC 603 solution (11 mPa.s) at different nozzle heights
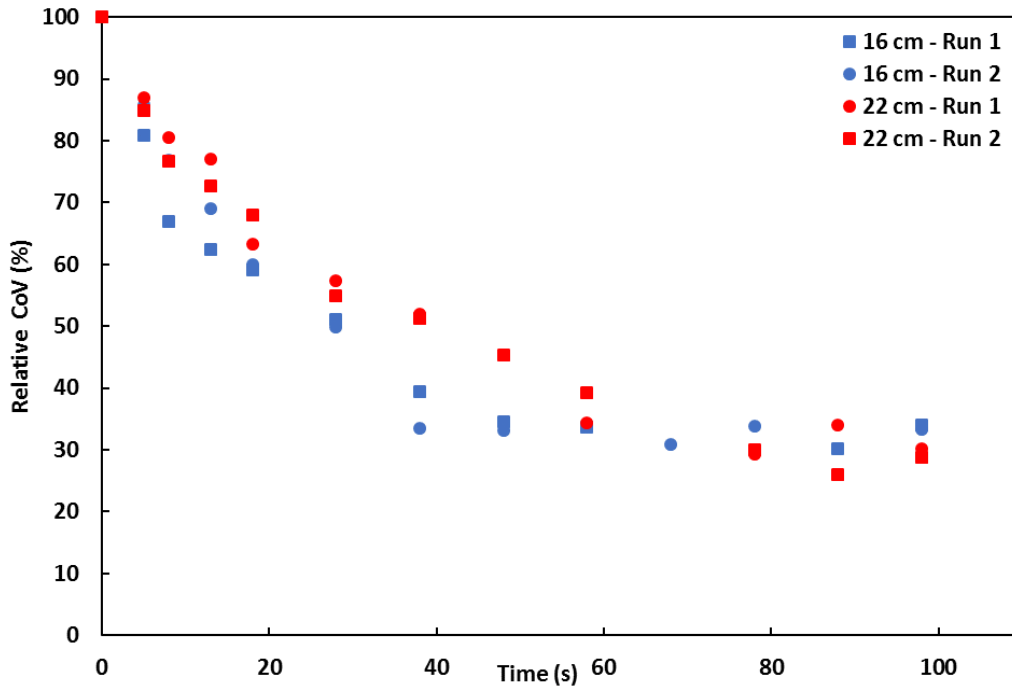
Figure 6.39. Relative coefficient of variation as a function of mixing time for alumina particles coated with HPMC 603 (11 mPa.s) at different nozzle heights

Moreover, to compare the coating rate, λ, and the time to reach an asymptotic CoV value, t_c, for each curve, an exponential decay curve was fitted to each data set. Here, normalisation was carried out between the CoV_o and the average CoV_∞ and this fitting method good for comparison of coating rate since the asymptotic CoV value reaches a similar value for all nozzle heights used. Figure 6.40 shows that all the curves fitted well to all the normalised CoV values data series and this is supported by the fact that the R^2 values obtained are more than 0.9 (Table 6.7).

It more clearly been seen in Figure 6.41 that the average normalised CoV values observed with time depended on the nozzle height set up; a lower nozzle height indicated a quicker decrease in CoV value, and the curves are steeper compared to the 22 cm nozzle height. All the measured fitting parameters are summarised in Table 6.7.
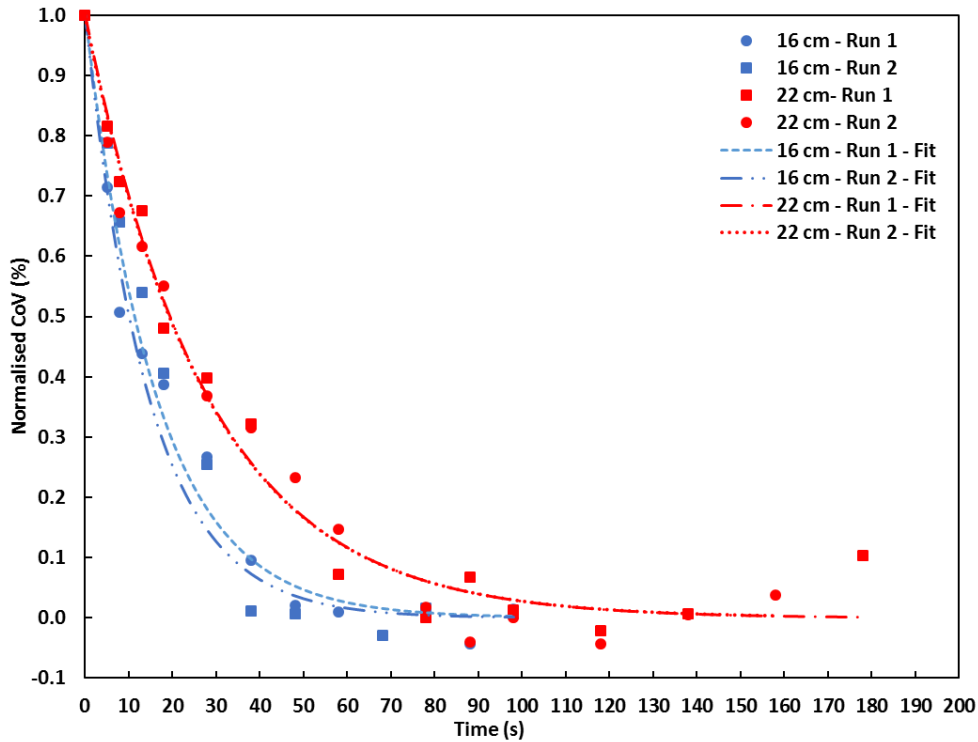
**Figure 6.40. All data series of the normalised (between CoV₀ and average CoV∞)
coefficient of variation and fitted decay curves as a function of mixing time for
different nozzle heights**
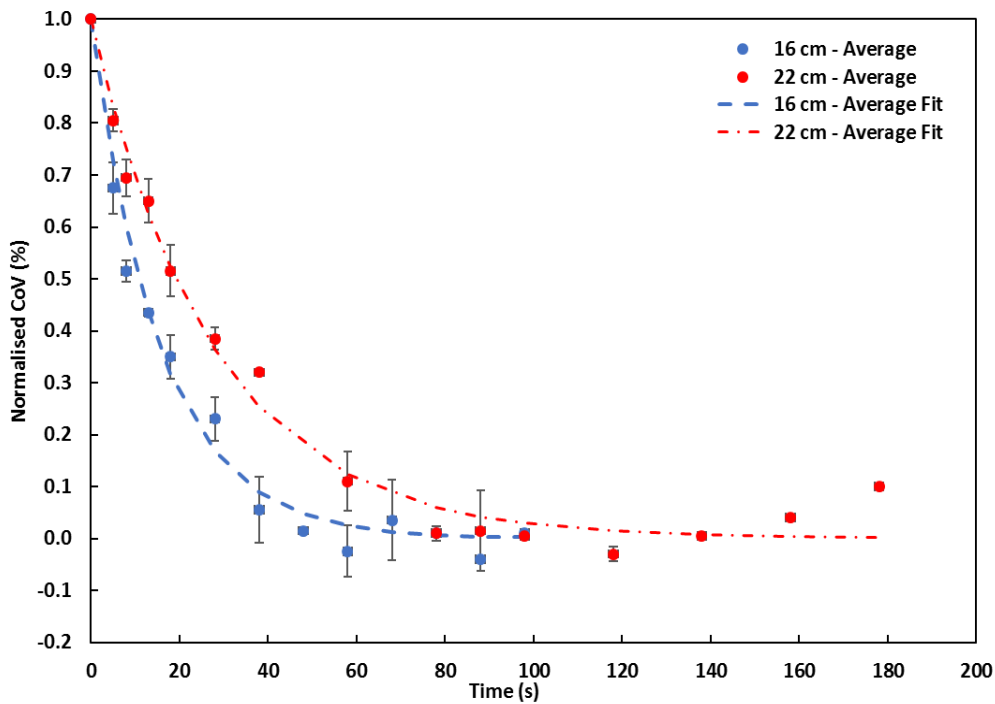
**Figure 6.41. Average normalised (between CoV₀ and average CoV∞) coefficient of
variation and fitted decay curves as a function of mixing time for different nozzle
heights. Error bars represented standard error**

Table 6.7. Fitting constants and time taken for coating completion for all data series experiments for the effect of nozzle height (1.5 U_{mf})

Nozzle height from distributor plate (cm)	Run	Coating rate constant, λ (s^{-1})	R^2	Time for 98% coating completion, t_c	CoV asymptote (%)
16	1	0.0615	0.977	63.63	3.72
	2	0.0544	0.981	71.86	3.64
	Mean	**0.0580**	-	**67.75**	**3.68**
22	1	0.0358	0.982	109.4	3.18
	2	0.0358	0.981	109.2	3.18
	Mean	**0.0358**	-	**109.3**	**3.18**

Note: The asymptotic CoV value is taken as an average of the CoV values at the final time points, where there is no clear decrease in CoV values

According to Table 6.7, the coating rate values were significantly different at different nozzle heights used, where the higher nozzle height shows a decrease in λ value from 0.058/s to 0.036/s compared to the lower nozzle height. This indicates that the contact spreading is slower at higher nozzle height. Furthermore, to point out the effect of coating rate on t_c at different nozzle height, the mean of t_c values is plotted as a function of λ and shown in Figure 6.42. It clearly can be seen that the t_c decreases with an increase of λ value and decrease in nozzle height.
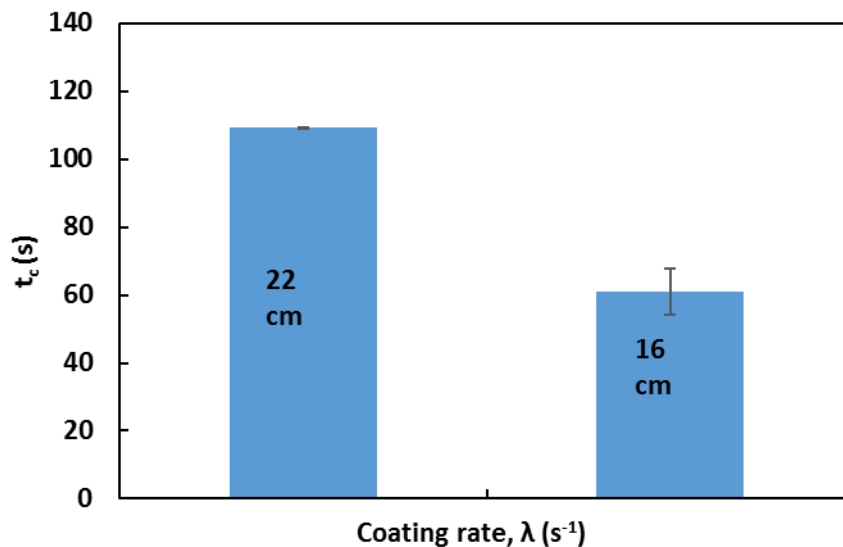
Figure 6.42. Coating rate constants plotted as a function of t_c at different nozzle heights. Error bars represent standard error.

The findings observed for this parameter were unexpected as some authors have speculated that an increase in nozzle height will distribute the liquid better on fluidised particles in the spray zone area (Börner *et al.*, 2014; Sanaei-Moghadam *et al*., 2017) and this was consistent with the spray distribution observed at higher nozzle height in Figure 6.9. However, lower nozzle height contributes to higher rate of contact spreading. The probable reason for this might be the particle flux at 1.5 U_{mf} used is higher at lower nozzle height. As can be seen in Figure 6.22, at lower mixing time, more particles and droplets adhere at the tube wall and so there will be not as many particle collisions occurring in the particle bed. This may likely happen when using the 22cm nozzle height. In contrast, with the 16 cm nozzle height, even though the spray does not distribute well as the 22 cm nozzle height, at the time of 2 s spraying, there is higher particle flux in the spray zone, hence no particles were observed to adhere at tube wall. Here, it is assumed that all the droplets successfully collide to the fluidised particles. As the mixing time increases, more collisions of wet particles occur in the particle bed, thus more liquid will distribute in the system via the contact spreading mechanism.

6.4 Summary

This work has demonstrated the first comprehensive experimental study to date of a batch contact spreading process in a small-scale fluidised bed coating system. Results show that contact spreading occurs in this model system and contributes to the coating uniformity obtained for final coated particles without a spray zone effect. A similar observation has been seen in the tumbling drum system (Chapter 5, Section 5.3). However, the extent of the coating is different; the final coated particles obtained from the fluidised bed system do not really achieve final uniformity due to drying also occurring simultaneously. In fluidised bed system, contact spreading behaviour can also be characterised by the coating rate, λ, and the time to complete 98% of the coating process, t_c. It can be concluded that fluidisation velocity and nozzle height significantly affected the contact spreading process. The results indicated that an increase in fluidisation velocity and decrease in nozzle height increased the coating rate, *λ,* and reduced the time for completion of coating. This meant that the contact spreading process occurs faster under both these conditions.

However, for liquid spray rate, the rate of coating was slightly higher for 1.3 g/s spray rate and nearly constant at 2.9 and 2.0 g/s spray rate. Here, the time for coating completion is influenced by the coating rate where an increase in the coating rate reduces the time for completion. Moreover, for the effect of viscosity, the results show no significant effect of this parameter on contact spreading behaviour, where similar values were obtained for the coating rate, λ, and time for coating completion. This unexpected result might be due to the lower capillary number and the viscous effects may be assumed to be minimal, thus the static liquid bridge plays a dominant role. When wet collision occurs, the liquid bridge strength formed is assumed similar (Bond number is similar as surface tension is similar), thus the bridge will rupture and spread the liquid in the system at a similar rate.

Another probable reason for the non-effect of liquid viscosity on contact spreading behaviour in this system is the method used to supply the liquid in the coating system. In the fluidised bed, a spray system was used, while the tumbling drum system, 10% of the batch was initially coated before being placed in the system. In the next chapter, a similar method of the introduction of coating liquid as that used in the tumbling drum will be used to investigate the effect of viscosity on contact spreading behaviour in the same fluidised bed system used here.

CHAPTER 7

7 Contact spreading in a fluidised bed: Isolating the contact spreading mechanism

7.1 Introduction

In this chapter, contact spreading experiments were carried out in the same fluidised bed described in Chapter 6, but with some additional modifications. These modifications allowed for the study and understanding of the mechanism of contact spreading using a different method to that used in Chapter 6. Here, instead of using a spray to supply the liquid into the system at the initial stage of each experiment, a similar method to the tumbling drum experiments (Chapter 5) was used. Here, 10% of the entire particle batch was pre-coated before adding to the remaining 90% to be fluidised. This method was used to investigate the liquid transfer in the fluidised bed and results will be compared to those obtained from using the spray system in Chapter 6.

These experiments used the same particles and coating materials as in Chapter 6, i.e., alumina particles and dyed 5% hydroxypropyl methylcellulose (HPMC) aqueous solutions. This study is designed to:

◦ Investigate the effect of mixing time, viscosity and fluidisation velocity on contact spreading behaviour

◦ Investigate the effect of two different methods of liquid supply (spray method and pre-coated particles method) to the system on contact spreading behaviour

◦ Provide insight into the importance of the contact spreading mechanism in a fluidised bed coating system

7.2 Experimental methods

7.2.1 Contact spreading experimental procedure

This section describes the general experimental procedure carried out for contact spreading experiments in a fluidised bed system using the pre-coated particles method. A more detailed description is given in Section 3.4.3. For each experiment, 10% of a batch of alumina particles (131.32 g) was coated with HPMC solution of a certain viscosity and placed in a fluidised bed containing the remaining 90% of the particles (see Figure 3.19). The fluidised bed tube dimensions used for these experiments were 69.8 cm x 10 cm (see Figure 3.18). Fluidisation time was varied from 0 s – 80 s. Experimental conditions for all data sets are summarised in Table 7.1. After the mixing time was finished, the fluidising air was immediately switched off and the tube was then removed, and the coated particles were collected in a tray and left to dry overnight. The fluidised bed tube was cleaned before the same experimental procedure was repeated for the other batches. This prevented any additional coating liquid being transferred to the next batch. Table 7.1 lists the 10 sets of experimental conditions used, comprising 69 individual experiments at different time points.

Table 7.1 Experimental process variables for the pre-coated particles method

Exp. Run	HPMC viscosity (mPa.s)	Fluidisation velocity (m/s)
1 (3 runs)	11	1.8 U_{mf} (1.05)
2 (3 runs)	44	1.8 U_{mf} (1.05)
3 (2 runs)	177	1.8 U_{mf} (1.05)
4 (2 runs)	11	1.5 U_{mf} (0.84)

7.2.2 Image analysis

Samples for image analysis were prepared and analysed as described in Section 4.1. The coated particles were visualized using the imaging system explained in Section 4.1. LabVIEW software was used (see Section 4.1.4) for analysing the inter-particle coating to give a quantitative determination of coating behaviour, i.e., the coefficient of variation (CoV) (see Eq. 4.1).

7.3 Results and discussion

Section 7.3.1 discusses the results for the effect of viscosity on contact spreading using the pre-coated particles method. Section 7.3.2 compares these results to the results from the spray method described in Chapter 6, Section 6.3.3. Section 7.3.3 will discuss the effect of fluidisation velocity on contact spreading using the pre-coated particles method, and finally, Section 7.3.4 will compare these results to those obtained from the spray method described in Chapter 6, Section 6.3.2.

7.3.1 Effect of viscosity on contact spreading by the pre-coated particles method

Typical data sets of coating evolution for alumina particles coated with three different viscosities of HPMC solutions; 11 mPa.s, 44 mPa.s, and 177 mPa.s, are shown in Figure 7.1 (a-c). A coating evolution graph refers to the frequency distribution of the dyed particles as a function of % red. Note that for each graph, not all-time series are shown for visualisation purposes. The full data series results can be found in Appendix E1. In Figure 7.1 (a-c), 0 s is the initial frequency distribution from when the pre-coated particles are added to the static particle bed. The curve shows a uniform peak at low percentage red value, indicating a large number of relatively white particles, with a long tail which indicates a number of particles coated to different degrees of redness. From Figure 7.1 (a-b), both 11 and 44 mPa.s coating liquid viscosities show a similar distribution; with an increase in a mixing time from 0 s to 20 s, there was a shift in the

frequency of the dyed particles towards higher percentage red values. For both viscosities, the distributions become narrower with increasing mixing time. This reveals that a more uniform coating is produced. However, Figure 7.1c (177 mPa.s) appears to show a different trend; there is virtually no shift in the % red dye to a higher value even with an increase in time. This means that even as the time increases, the particles coated with the highest viscosity solution exhibit a highly non-uniform coating compared to the lower viscosity solutions.

Figure 7.2a plots the % mean red of the pre-coated particles as a function of viscosity while Figure 7.2b plots the % mean red against mixing time. This indicates that the viscosity contributes to the decrease in % mean red value. This trend was not unexpected as even though the same concentrations of HPMC and red dye were used, a similar trend was observed in Chapters 5 and 6. This slight change in the red intensity of the solutions is thought to be due to the difference in the molecular weight of the HPMC used.

To quantitatively determine the inter-particle coating variability, the CoV values for each of the data sets were calculated based on Eq. 4.1 as explained in Chapter 4, Section 4.2.1.1. The CoV values were then plotted as a function of time for each viscosity and are shown in Figure 7.3 (a-c). This graph reflects the observations from the images (Appendix E2), where the coating uniformity increases with time for the lowest viscosity (11 mPa.s) solution and levels off at certain mixing time. A similar pattern was observed for the 44 mPa.s solution, but the CoV did not decrease to the same extent before starting to level off. For the highest viscosity (177 mPa.s), the CoV was almost constant, showing none of the initial decrease in CoV as seen with the two lower viscosity solutions. This corresponds with the coating evolution graph seen in Figure 7.1c. This means that there is little to no contact spreading happening in the fluidised bed when the highest viscosity solution is used.
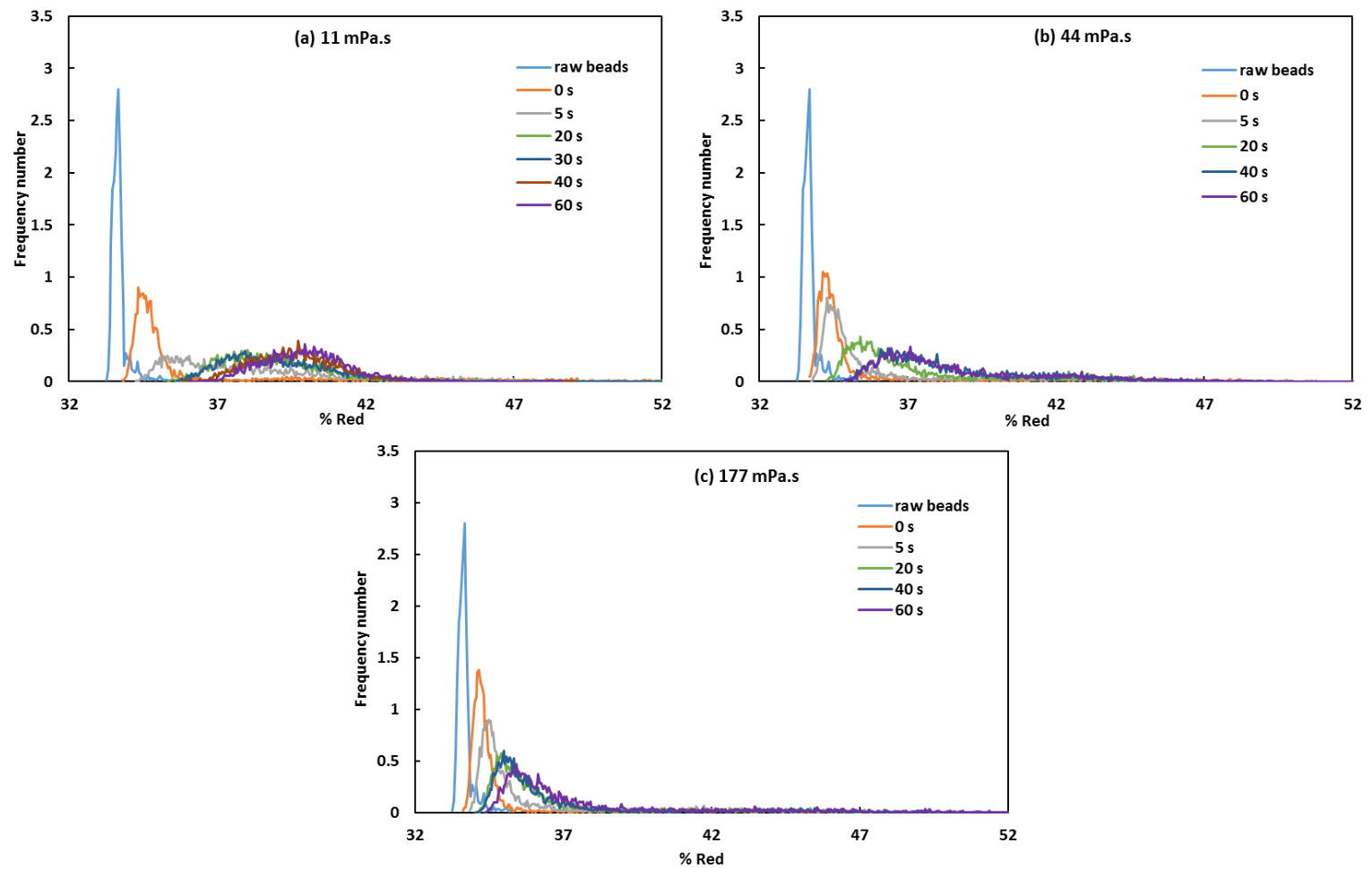
Figure 7.1. Coating evolution; frequency number as a function of % red for alumina coated with different viscosity HPMC solutions; (a) 11 mPa.s, (b) 44 mPa.s and (c) 177 mPa.s
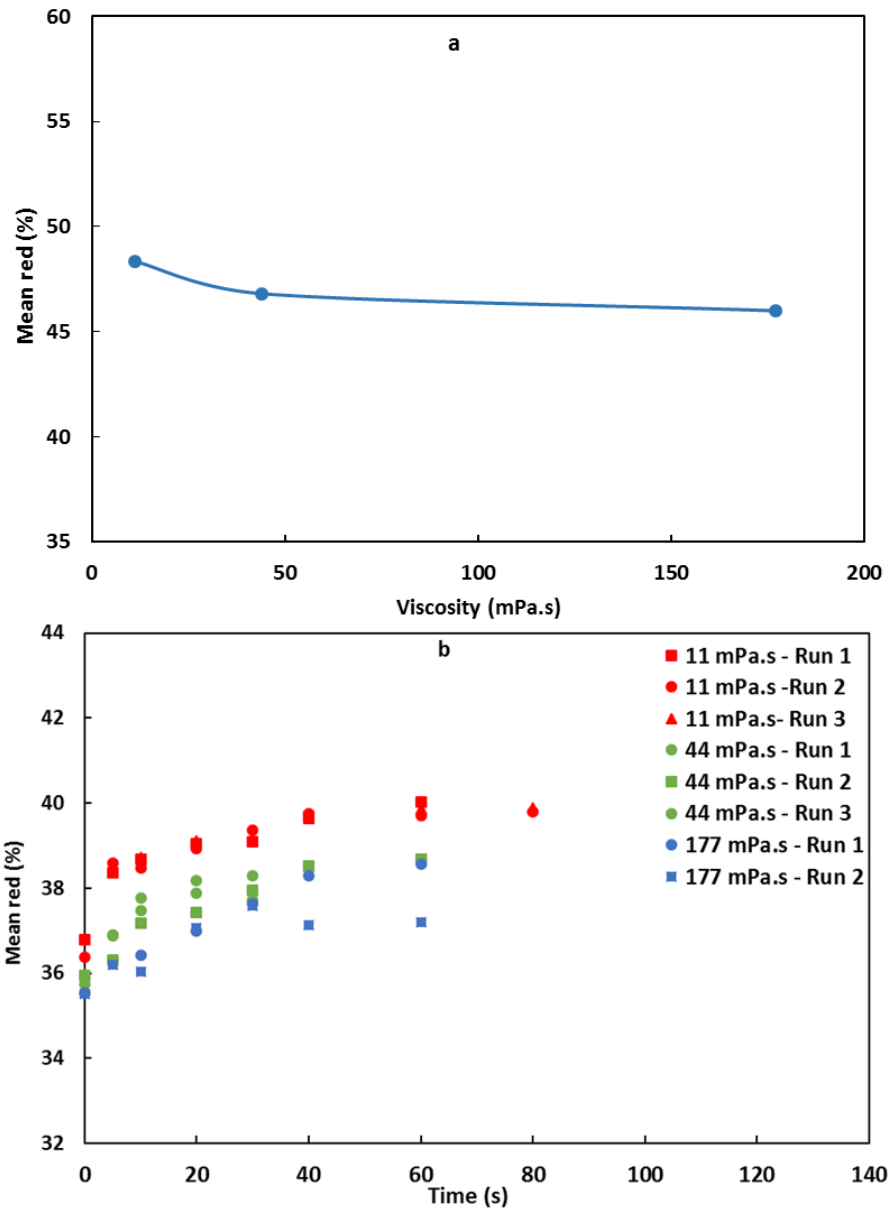
Figure 7.2. Mean % red plotted as a function of a) viscosity, for the pre-coated particles, and b) mixing time
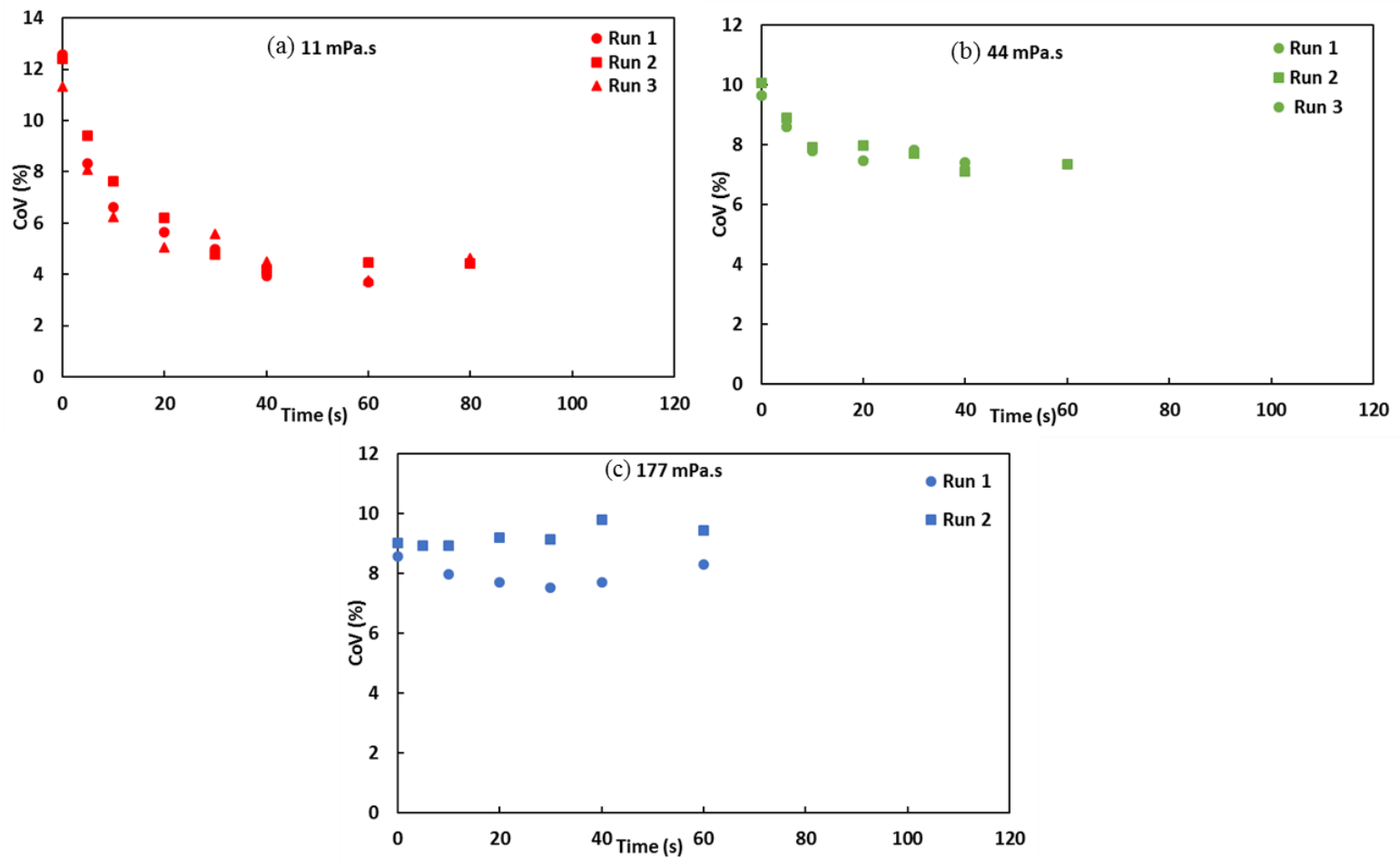
Figure 7.3. Coefficient of variation as a function of mixing time for alumina particles coated with different viscosity HPMC solutions for all data series; (a) 11 mPa.s, (b) 44 mPa.s and (c) 177 mPa.s.

To compare the curves between the different viscosities, all the data sets were plotted together and are shown in Figure 7.4. Here, as the initial point of 0 s for each viscosity was different (due to the different red intensities of the different molecular weight HPMC solutions), the data sets were normalised based on Eq. 5.1 and are shown in Figure 7.5. The term used for this normalisation is referred to as the relative CoV. From this figure, it is clear that the viscosity significantly affects the contact spreading behaviour when using the pre-coated particles method. The relative CoV values increase with an increase in viscosity and are virtually constant for highest viscosity. Since 177 mPa.s HPMC did not show any change in CoV values, the following analysis was carried out only on the other two viscosities; 11 and 44 mPa.s. Both these viscosities appeared to reach a different asymptotic value after a certain mixing time.
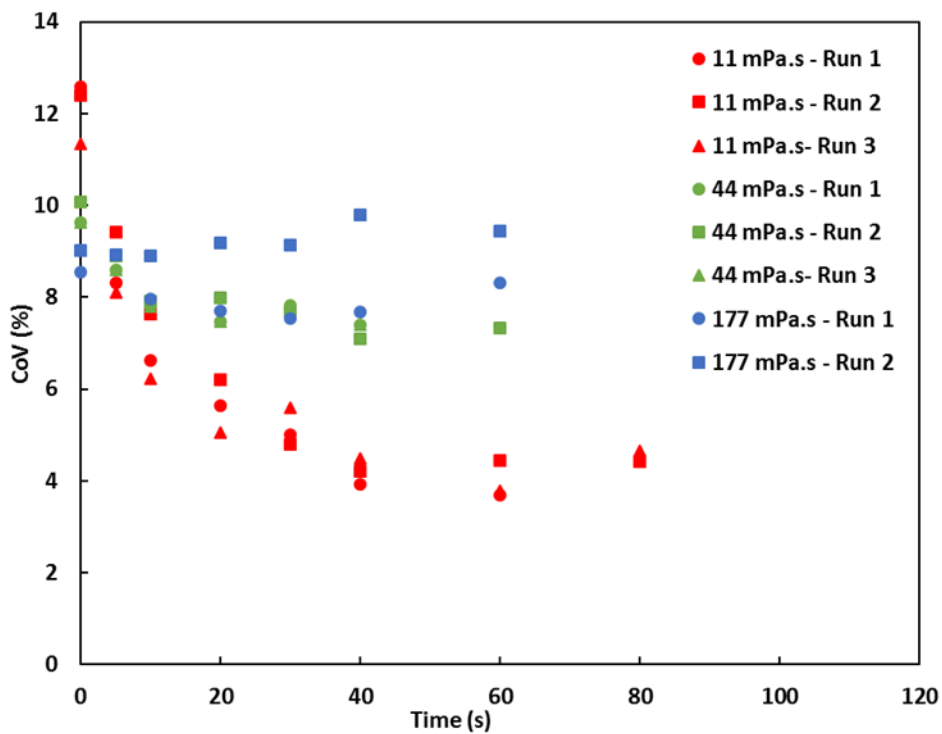
Figure 7.4. Coefficient of variation as a function of mixing time for alumina particles coated with different HPMC viscosities.
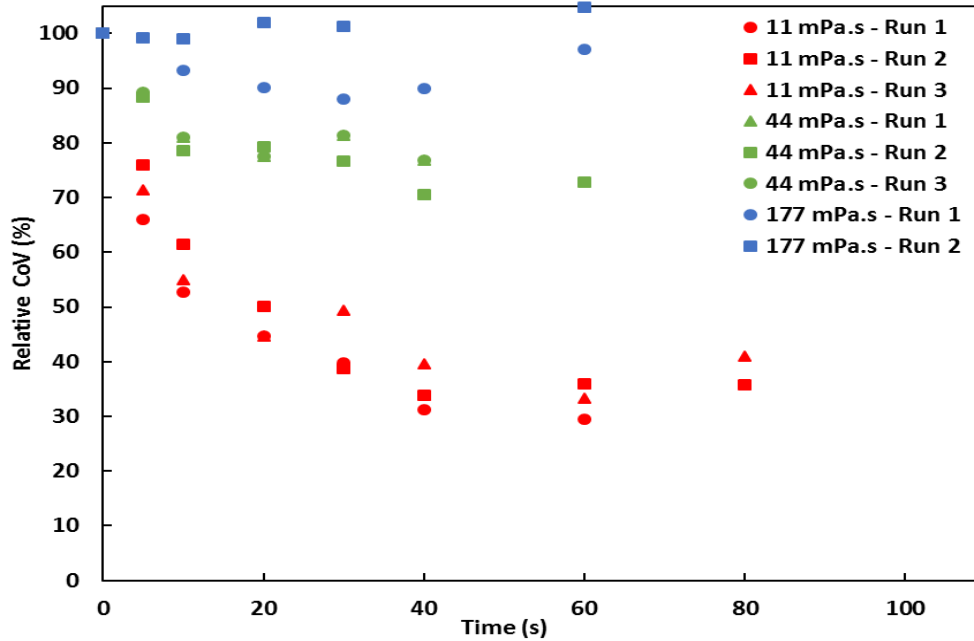
Figure 7.5. Relative coefficient of variation as a function of mixing time for alumina particles coated with different HPMC viscosities.

To determine the coating rate, λ, and the time to reach an asymptotic value, t_c, for 11 mPa.s and 44 mPa.s coating liquid viscosities, an exponential decay curve was fitted to each data set, normalised between CoV_o and the average CoV_∞ (Eq. 4.7) as described in Chapter 4, Section 4.2.2. According to Figure 7.6, all data series appear to be accurately represented by the fitting curve ($R^2 > 0.9$) and all the measured parameters are summarised in Table 7.2. Surprisingly, the data series for both viscosities appear to fall onto similar curves, and the higher viscosity solution appears to coat slightly faster compared to the lower viscosity solution. The averaged normalised CoV values for each viscosity are also plotted as a function of time and shown in Figure 7.7.
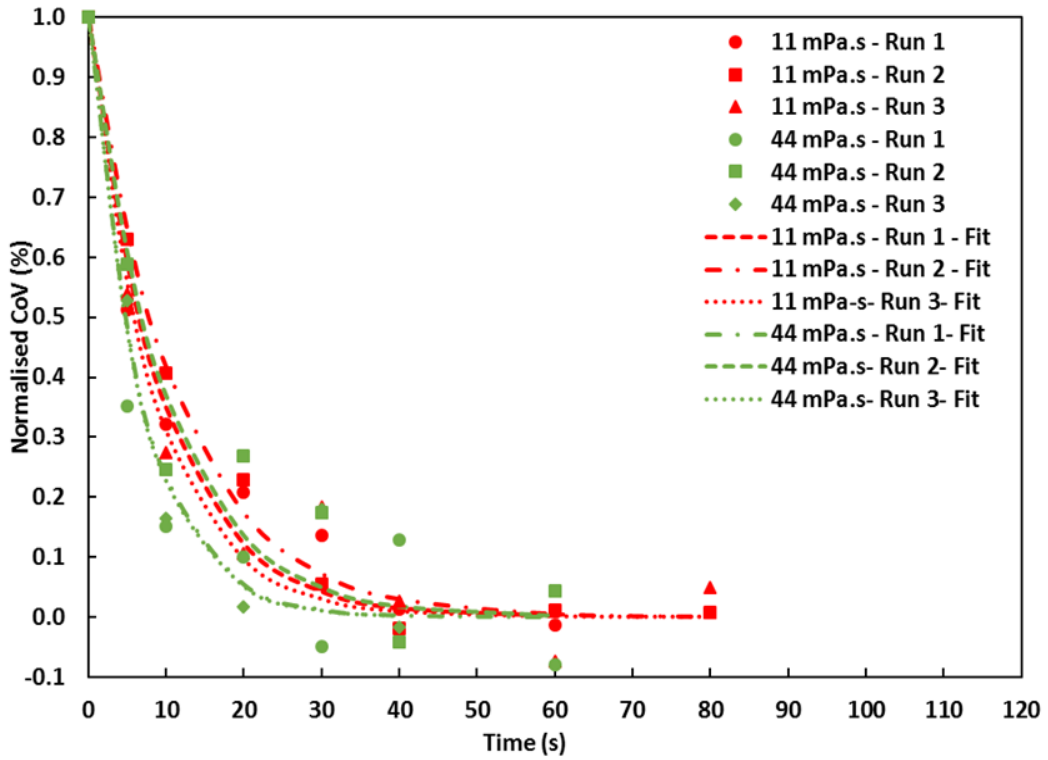
Figure 7.6. Normalised (between CoV$_o$ and average CoV$_\infty$) coefficient of variation and fitted decay curves as a function of mixing time using different HPMC viscosities.
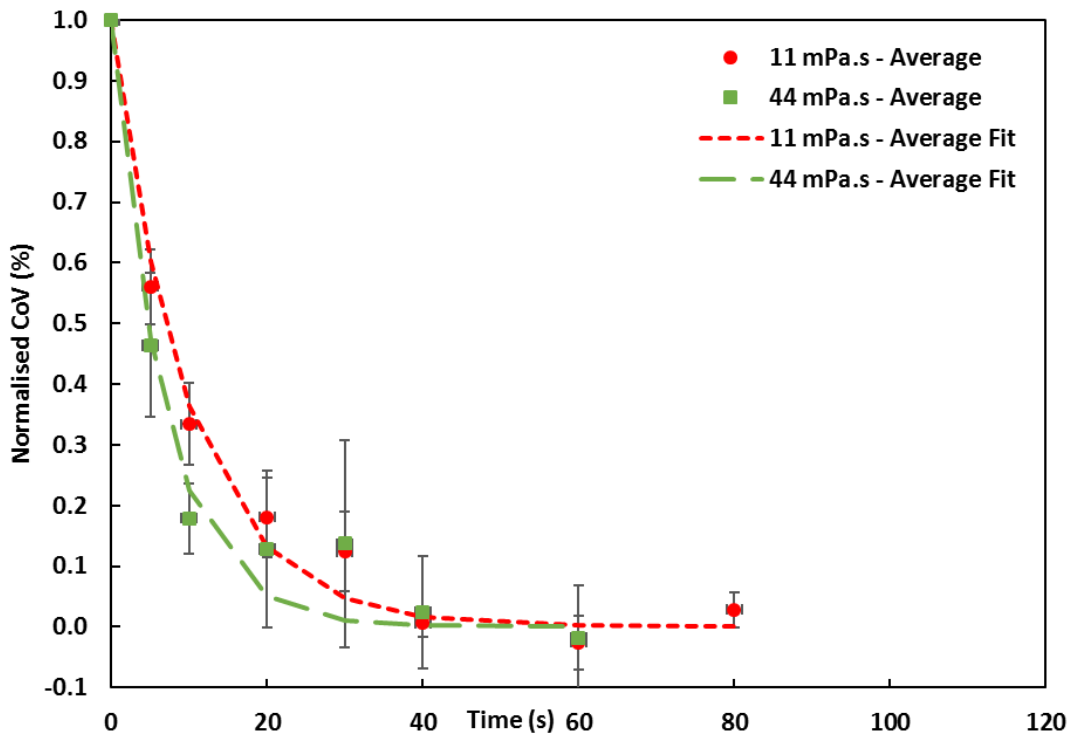
Figure 7.7. Average normalised (between CoV$_o$ and CoV$_\infty$) coefficient of variation and fitted decay curves as a function of mixing time for different HPMC viscosities. Error bars represent standard errors

200

Table 7.2. Fitting constants and time taken for coating completion for different viscosity solutions (11 and 44 mPa.s)

Coating liquid viscosity (mPa.s)	Run	Coating rate constant, λ (s^{-1})	R^2	Time for 98% coating completion, t_c	CoV asymptote (%)
11	1	0.105	0.969	37.11	3.82
	2	0.087	0.993	44.74	4.36
	3	0.117	0.961	33.37	4.30
	Mean	**0.103**	-	**38.41**	**4.16**
44	1	0.145	0.937	26.81	7.21
	2	0.100	0.930	39.20	7.21
	3	0.148	0.952	26.41	7.43
	Mean	**0.131**	-	**30.81**	**7.28**

Note: The asymptotic CoV value is taken as an average of the CoV values at the final time points, where there is no clear decrease in CoV values

In Table 7.2, it is clear that the coating rate, λ, is slightly higher for the 44 mPa.s solution and the time to reach 98 % coating completion is also approximately 8 s faster compared to the 11 mPa.s solution. However, this result was inconsistent with the observation in Figure 7.8. Here, when the asymptotic CoV values are plotted as a function of viscosity, the higher viscosity gives a higher value of the CoV$_\infty$ showing that the lower viscosity gives a more uniform coating. But, when considering the large error bars, it is difficult to draw a conclusion.

The images of particles coated with the solutions are plotted as a function of time as seen in Figure 7.9. The images in Figure 7.9 appear to show a similar observation as Figure 7.8; the lower viscosity solutions appear to be more evenly coated than the higher viscosity solution. This observation contrasts with the results obtained in Table 7.2. This is because the quantitative information from these types of normalised curve only gives the rate of coating until no further contact spreading occurs. It gives no determination of how uniform the final coating is.
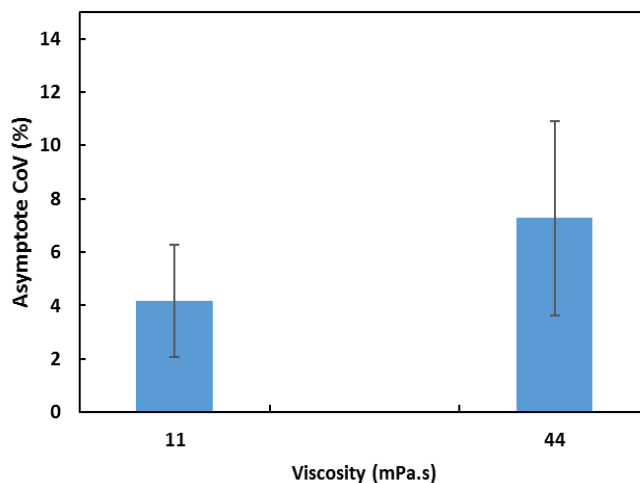
Figure 7.8. Asymptotic CoV as a function of viscosity
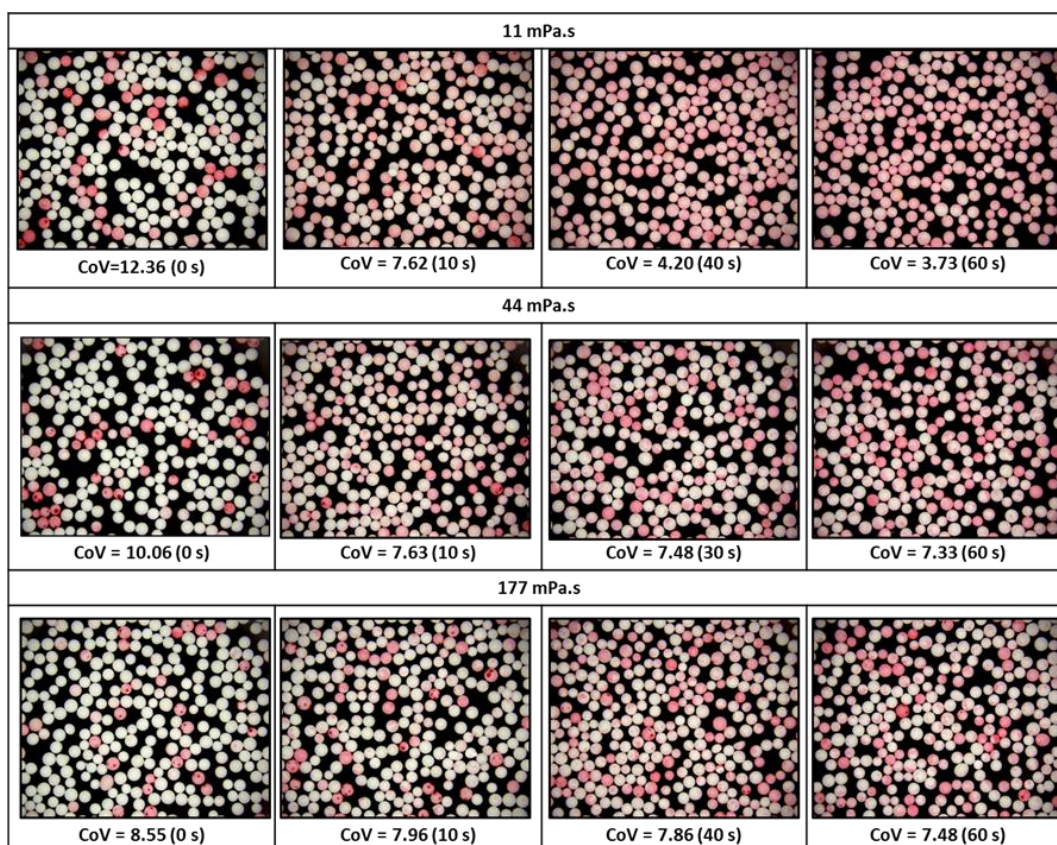
Figure 7.9. Images of alumina particles coated with different viscosity coating solutions as a function of time

A possible explanation for the different results obtained at different viscosities may be due to the amount of agglomerates obtained during the coating process being different for different viscosities. Figure 7.10 plots the fraction of agglomerates as a

function of mixing time for each viscosity used. Here, the fraction of agglomerates represents the mass of agglomerated particles to the total mass of a particle batch. It can be observed that the fraction of agglomerates increases with an increase in viscosity of the HPMC solutions. This probably occurs due to stronger liquid bridges being formed and a decrease in bed fluidity for higher viscosities at the same excess velocity used.
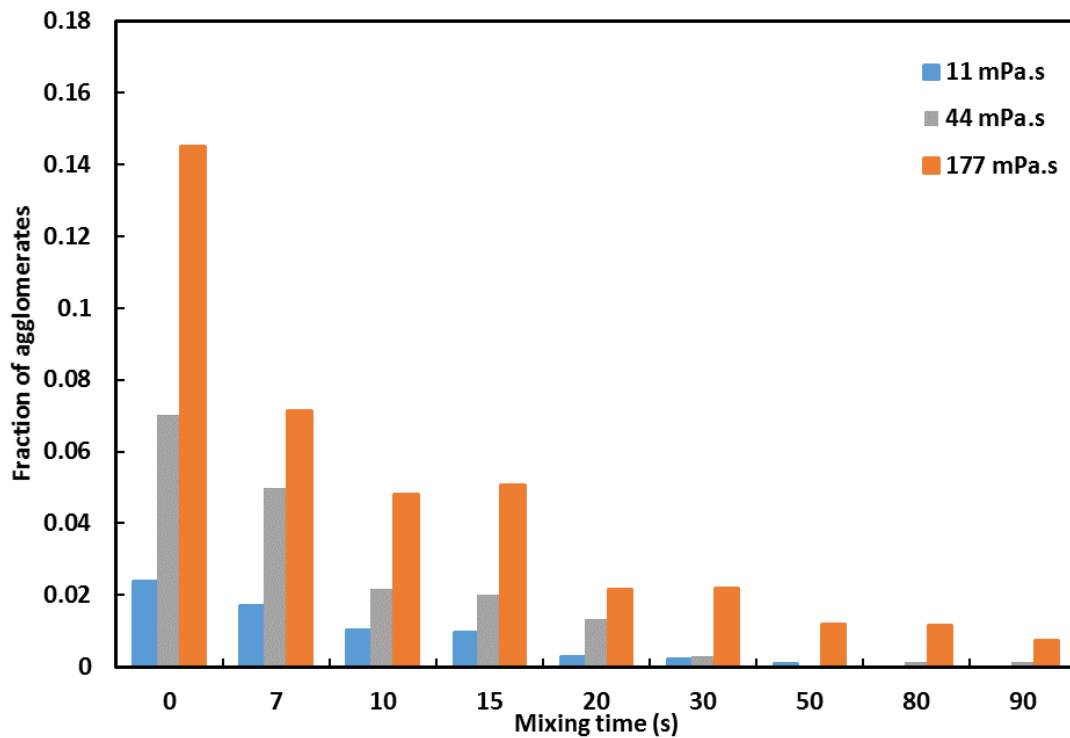
Figure 7.10. Agglomerate fraction as a function of mixing time at different viscosities

When wet collisions occur, the viscous force reduces the particle motion, thus the bridge formed is less likely to break. Because the bridge is less likely to rupture, the liquid in the system is also less likely to re-distribute. This finding is supported by the image comparison of the wet agglomerates formed at different viscosities, shown in Figure 7.11. Figure 7.11 indicates that the number of agglomerates formed in the range > 5.6 mm sieve size increases with viscosity. In addition, the size of the agglomerates also increases with an increase in viscosity but decreases as the mixing time increases. This might be due to the contact angle increases with the viscosity which leads to lower liquid spreading upon collision between the particles.
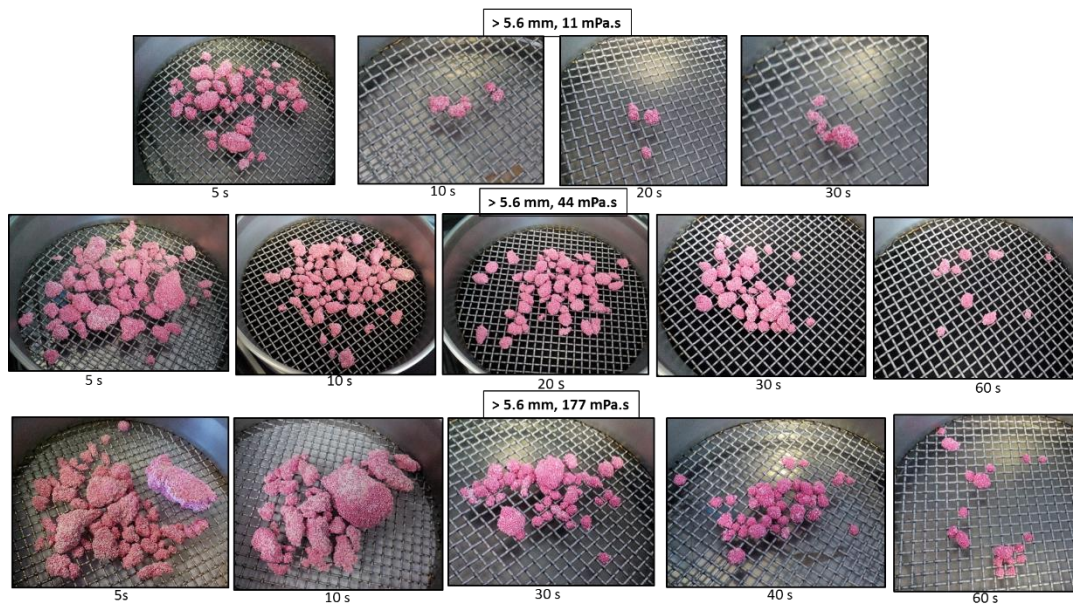
Figure 7.11. Image comparison of agglomerates formed at different viscosities

Simons and Fairbrother (2000) found that the formation of liquid bridges and their ability to join particles together depends also on the wetting behaviour of the liquid on the particles. For the combination of materials used in this thesis, an increase in viscosity results in an increase in the contact angle (see Section 3.3, Table 3.6) meaning that the wettability of the liquid on the particle surface decreases, thus a higher viscosity leads to lower liquid spreading and produces stronger adhesion between wet particles.

However, these findings are in contrast to the previous results obtained on the effect of viscosity using the spray method in Chapter 6, where there was no significant effect observed on the contact spreading regardless of the viscosity used. In the following section, the results for the effect of viscosity on contact spreading using both the spray method and the pre-coated particles method in the fluidised bed system are compared and discussed in detail.

7.3.2 Comparison of the effect of viscosity on contact spreading using the spray and the pre-coated particles method

In this section, the results for the effect of viscosity on contact spreading using the pre-coated particles method are compared to the findings of previous work in Chapter 6 which used a spray method of liquid addition. Figure 7.12 (a-c) shows the CoV for each viscosity plotted as a function of time for all data series obtained for both methods. It can be observed from these figures that the change in CoV with time for the pre-coated particles method is significantly different compared to the spray method results obtained in Chapter 6. A similar trend can be observed for lower viscosities (11 and 44 mPa.s), where the CoV values for the spray method are lower and decrease with time before levelling out at an asymptotic CoV value. The greatest difference between the two methods is seen when using the highest viscosity solution, 177 mPa.s. At this viscosity, the CoV for the spray method decreases with time and then starts to level off after a certain time, while nearly no changes in the CoV were observed for the pre-coated particles method.

In Figure 7.13 (a-c), relative CoV values are plotted as a function of the mixing time for all data series for both methods for a better comparison since the initial values of the CoV were different. The relative CoV values at 11 mPa.s for both methods used fall onto similar curves and reach similar asymptotic CoV values. For the higher viscosities, 44 and 177 mPa.s, the greatest difference between the two methods is observed. The curves for the spray method are steeper than the curves for the pre-coated particles method. Moreover, the highest viscosity solution (177 mPa.s) for the pre-coated particles method shows virtually no change in the CoV with time. Since there were no changes in the CoV values observed for 177 mPa.s using the pre-coated particles method, the following analysis for comparison was carried out only for the other two lower viscosities; 11 and 44 mPa.s.
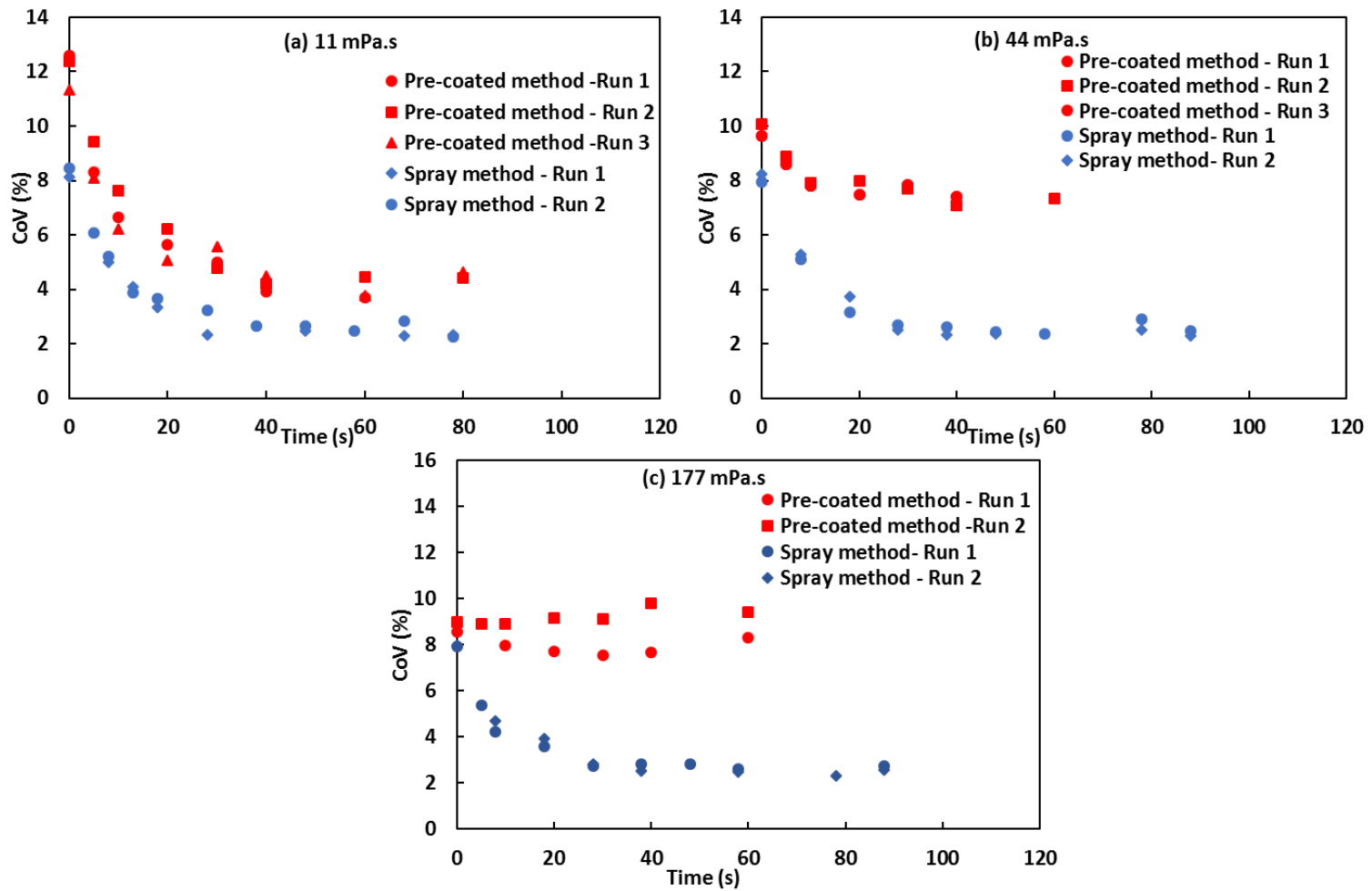
Figure 7.12. Coefficient of variation as a function of mixing time for alumina particles coated with different viscosity solutions for all data series using the spray and the pre-coated particles method: (a) 11 mPa.s, (b) 44 mPa.s and (c) 177 mPa.s.
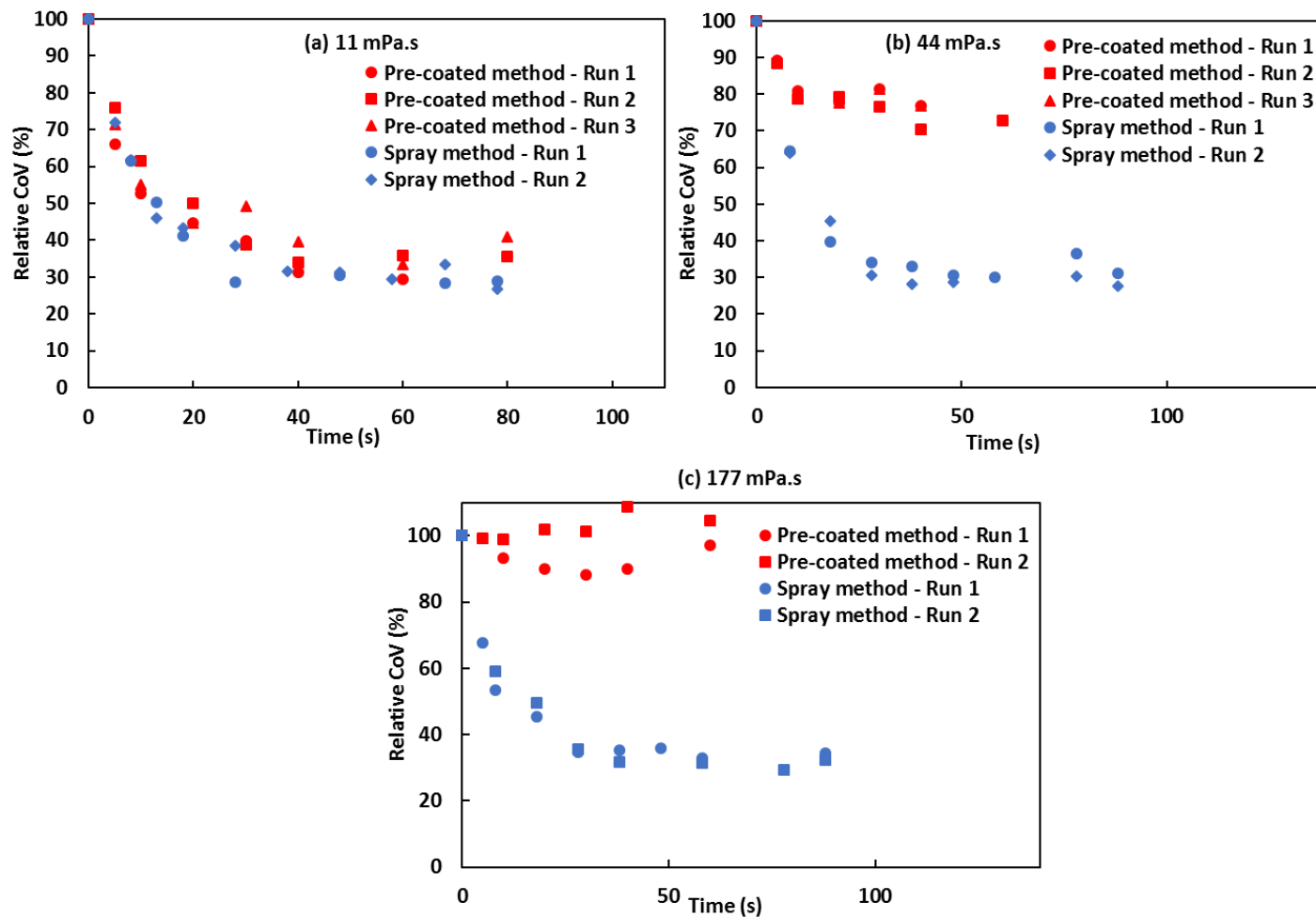
Figure 7.13. Relative coefficient of variation as a function of mixing time for alumina particles coated with different viscosity solutions for all data series using the spray and the pre-coated particles method; (a) 11 mPas, (b) 44 mPa.s and (c) 177 mPa.s.

207

Figure 7.14 shows the normalised (between CoV$_o$ and average CoV$_\infty$) coefficient of variation and fitted decay curves as a function of mixing time for 11 and 44 mPa.s coating solutions using the pre-coated particles and the spray method. It can be clearly seen that at 11 mPa.s, the coating rate was similar for both methods. For the 44 mPa.s solution, there was a small difference in the rate of coating; a slightly quicker rate for the pre-coated particles method. Table 7.3 summarises all the coating rates, λ, the times taken to complete the coating process, t_c, and the asymptotic CoV values for both methods at the two different viscosities.
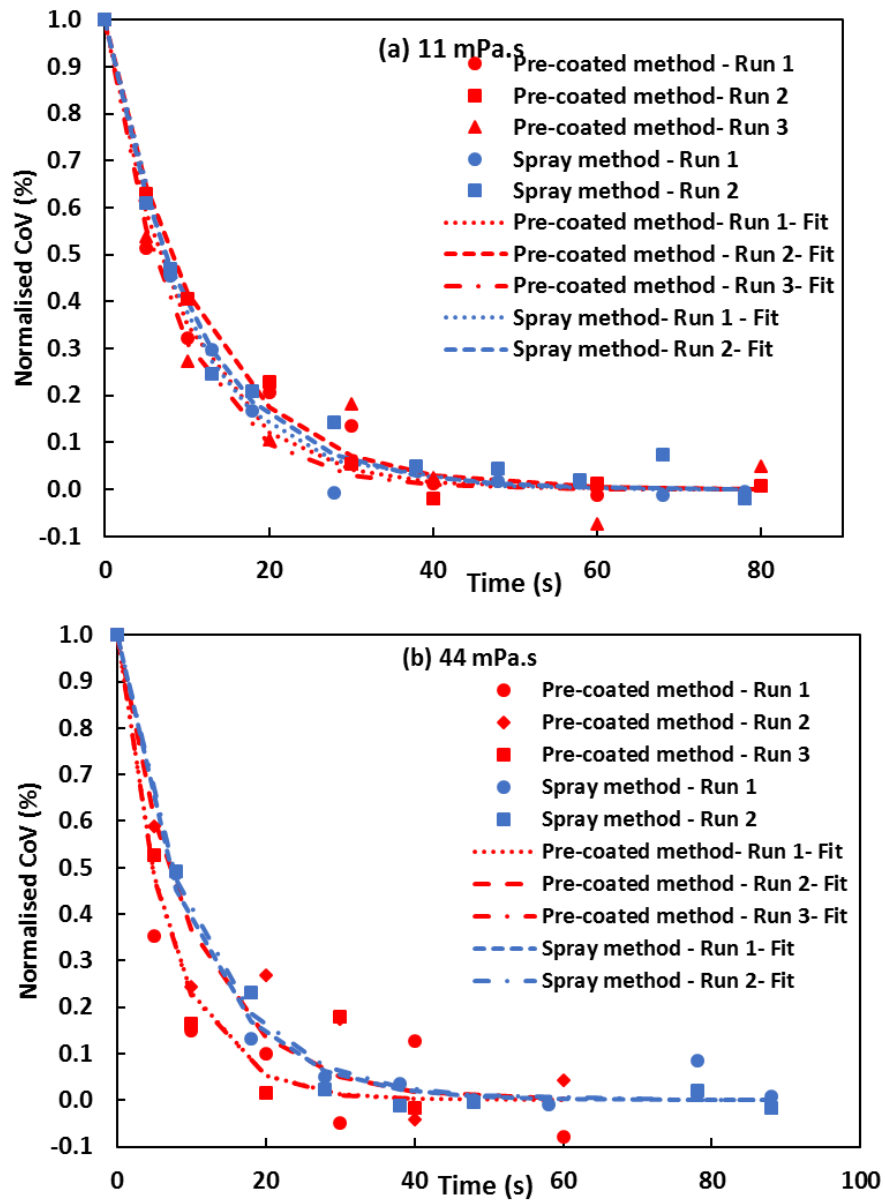
Figure 7.14. All data series of the normalised (between CoV$_o$ and average CoV$_\infty$) coefficient of variation and fitted decay curves as a function of mixing time for different viscosities using the pre-coated particles and the spray method;(a) 11 mPas and (b) 44 mPas

Table 7.3. Fitting constants and time taken for coating completion for all data series at different viscosities using the pre-coated particles (PCP) and the spray methods

Run	Coating rate constant, λ (s^{-1})		R^2		Time for 98% coating completion, t_c		CoV asymptote (%)	
	Spray	PCP	Spray	PCP	Spray	PCP	Spray	PCP
11 mPa.s								
1	0.099	0.105	0.993	0.969	39.17	37.11	2.37	3.82
2	0.093	0.087	0.984	0.993	41.98	44.74	2.37	4.36
3	-	0.117	-	0.961	-	33.37	-	4.30
Mean	**0.097**	**0.103**	-	-	**40.57**	**38.41**	**2.37**	**4.16**
44 mPa.s								
1	0.098	0.145	0.989	0.937	39.54	26.81	2.43	7.21
2	0.093	0.100	0.992	0.930	41.97	39.20	2.38	7.21
3	-	0.148	-	0.952	-	26.41	-	7.43
Mean	**0.096**	**0.131**	-	-	**40.76**	**30.81**	**2.41**	**7.28**

Note: The asymptotic CoV value is taken as an average of the CoV values at the final time points, where there is no clear decrease in CoV values

Table 7.3 shows that there is no significant difference between the coating rate constant and the time for coating completion for the two methods at 11 mPa.s. However, even though λ was similar, the asymptotic CoV value was different. The final CoV value is of extreme importance for 'real' coating systems; not only the coating rate, but the extent of coating uniformity of the final product is critical. For instance, in the food industry, a highly uniform coating of final product is desired to provide the same amount of nutrients required.

Figure 7.15 shows images of particles coated using the spray method and the pre-coated particles method. The former appears to reach a more uniform coating than the latter. For 44 mPa.s, the λ obtained using both methods were slightly different and gave different t_c values. However, more significantly, the value of the asymptotic CoV between the two methods was considerably different; it is much higher for the pre-coated particles method. Here, the CoV started to level off earlier (Figure 7.12b), but the particles were not as uniformly coated compared with the spray method (Figure 7.15). The drying that occurs in the system enhances the solidification of the liquid bridge, preventing the bridge rupturing and liquid transferring. In real systems, the formulation and operational conditions affecting the drying rate will, therefore, be expected to be critical regarding the extent of liquid transfer between particles.
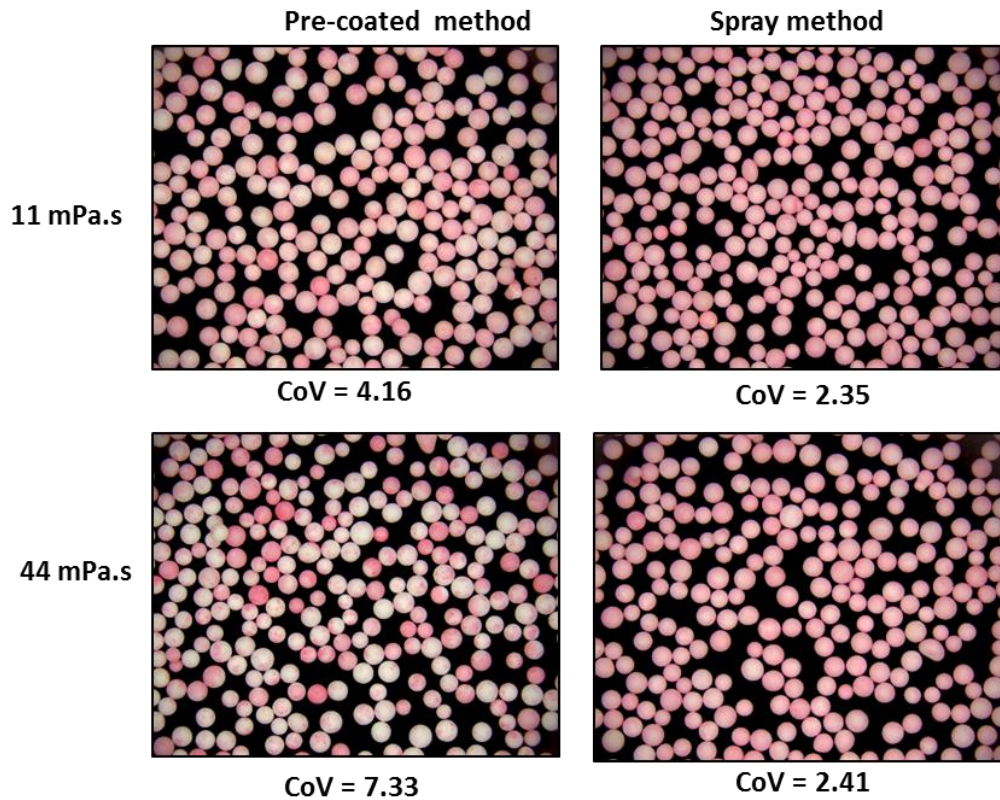
Figure 7.15. Image comparison at the asymptotic CoV value using the spray and the pre-coated particles method at different solution viscosities.

When the coating rate constant, λ, and the asymptotic CoV values were plotted as a function of viscosity for both methods in Figure 7.16 (a-b), it can be seen that viscosity influences the coating rate and the asymptotic CoV values for the pre-coated particles method, but not for the spray method. Moreover, it can be concluded that when the pre-coated particles method is used, the coating rate constant can predict the time to asymptote, t_c, but not the asymptotic CoV value, i.e. the extent of coating.
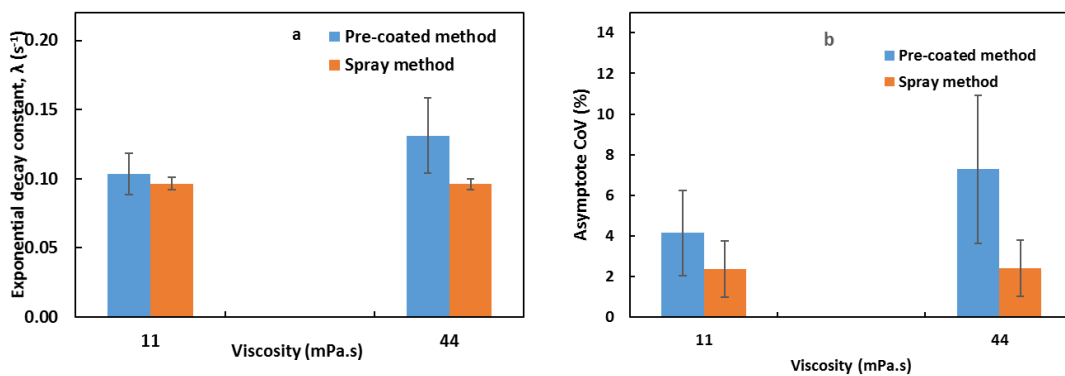
Figure 7.16 a) Coating rate constant, λ, and b) asymptotic CoV as a function of viscosity

There are several possible explanations for the different results obtained when using the different methods of liquid addition to the fluidised bed system at different solution viscosities. One of the reasons might be the different states of wet particles formed at the initial stage of the coating process by the different methods. Different states of wet particles formed using the pre-coated particles and the spray method at the initial process are proposed and illustrated in Figure 7.17. For both methods, the build-up of agglomerates is the dominant mechanism during the initial phase of the contact spreading process. The strength, size and amount of wet agglomerates formed during this initial process influence the uniformity of the final coated particles via contact spreading. With the pre-coated particles method, relatively more stronger bonds are formed resulting in larger and a higher fraction of wet agglomerates during the coating process; this contributing to lower inter-particle coating uniformity. With the spray method, on the other hand, a smaller proportion of strong bonds are formed together with weaker bonds, resulting in smaller and a lower fraction of wet agglomerates, leading to higher inter-particle coating uniformity. A lower fraction of agglomerates is shown in Figure 7.18 for the spray method and at longer mixing times.
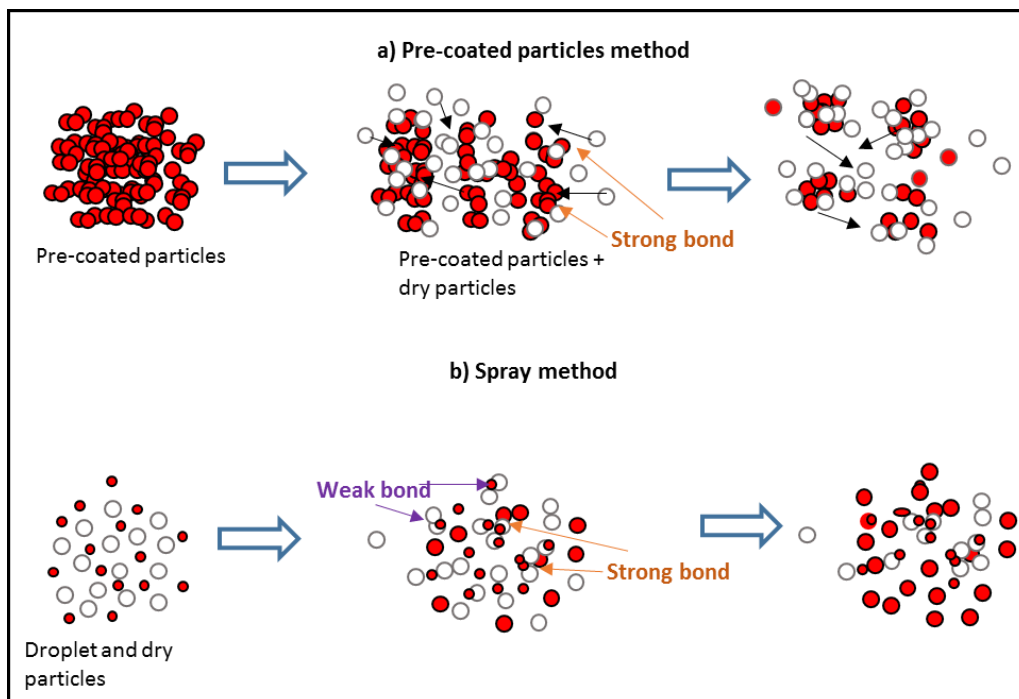
Figure 7.17. Proposed different states of wet particle mechanisms within a fluidised bed via contact spreading using the spray and the pre-coated particles methods.
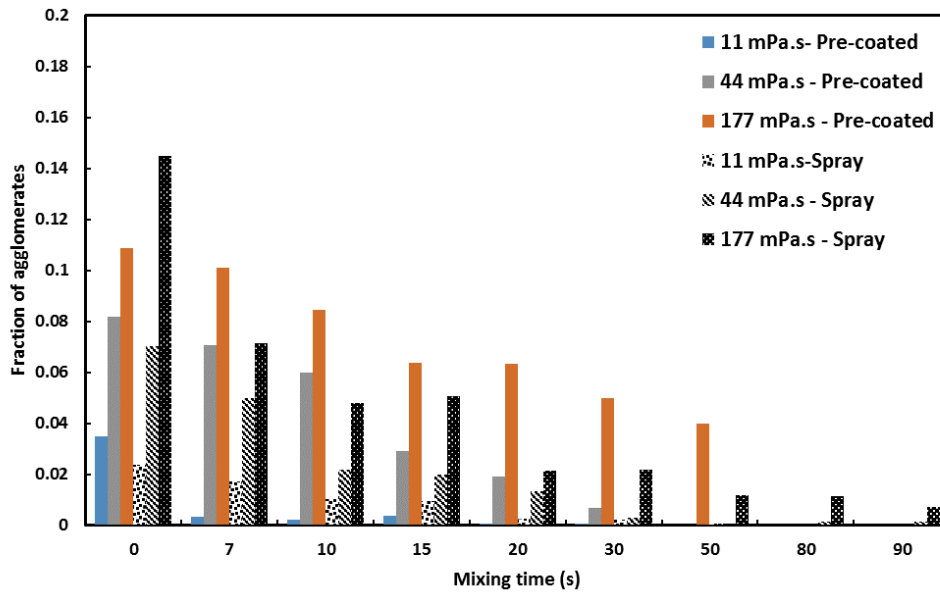
Figure 7.18. Agglomerates fraction as a function of mixing time at different viscosities for spray and pre-coated particles method

It can be concluded from this section that the liquid bridge rupture mechanism is important for contact spreading to occur in the fluidised bed system. The formation and rupture mechanism of the agglomerates affected by the viscosity solutions and the liquid loading methods. A higher viscosity produced larger and a higher fraction of wet agglomerates during the coating process leads to higher inter-particle coating variability mainly using pre-coated method. It is believed that lower fluidisation velocity will also significantly affect the contact spreading when using the pre-coated particles method. Thus, in the following section, the effect of fluidisation velocity on contact spreading when using the pre-coated particles method is discussed.

7.3.3 Effect of fluidisation velocity on contact spreading when using the pre-coated particles method

In this section, results for the effect of fluidisation velocity on contact spreading when using the pre-coated particles method in the fluidised bed are discussed. Here, HPMC 603 solution with a viscosity of 11 mPa.s was selected from the previous study. This solution was used as it gave better coating at 1.8 U_{mf} fluidisation velocity. The bed behaviour observed at the different fluidisation velocities used here resembled different

regions of fluidisation, e.g. at 1.8 U_{mf}, slugging fluidisation was observed and at 1.5 U_{mf}, bubbling fluidisation occurred.

A typical data series of coating evolution for alumina particles coated with 11 mPa.s viscosity solution at different fluidisation velocities is shown in Figure 7.19. Note that for each graph, not all-time series are shown for visualisation purposes. The full data series results can be found in Appendix E3. It can be observed in Figure 7.19 that different fluidisation velocities gave a different pattern of coating distribution, where the distribution at 1.8 U_{mf} shifted to higher % red as the time progressed and the distribution became narrower. This indicated that a more uniform coating was obtained with time. However, this pattern was different when the particles were fluidised at 1.5 U_{mf}. Here, the distribution took more time to shift to a slightly higher % red and did not lead to a narrower distribution. This meant that even as the time increased, the coated particles did not reach a highly uniform coating. Here, 0 s corresponds to the coating distribution when the pre-coated particles were added to the static particle bed.

In addition, this coating evolution pattern was consistent with the images of alumina coated with 11 mPa.s HPMC solution at different fluidisation velocities in the fluidised bed tube, illustrated in Figure 7.20. The influence of fluidisation velocity on inter-particle coating variability is then quantitatively expressed in Figure 7.21 by plotting the CoV as a function of mixing time at the two velocities; 1.8 and 1.5 U_{mf}. A similar pattern is obtained for both velocities, where the CoV decreases with an increase in mixing time before starting to level off after a certain time. However, both velocities clearly reach different asymptotic CoV values.
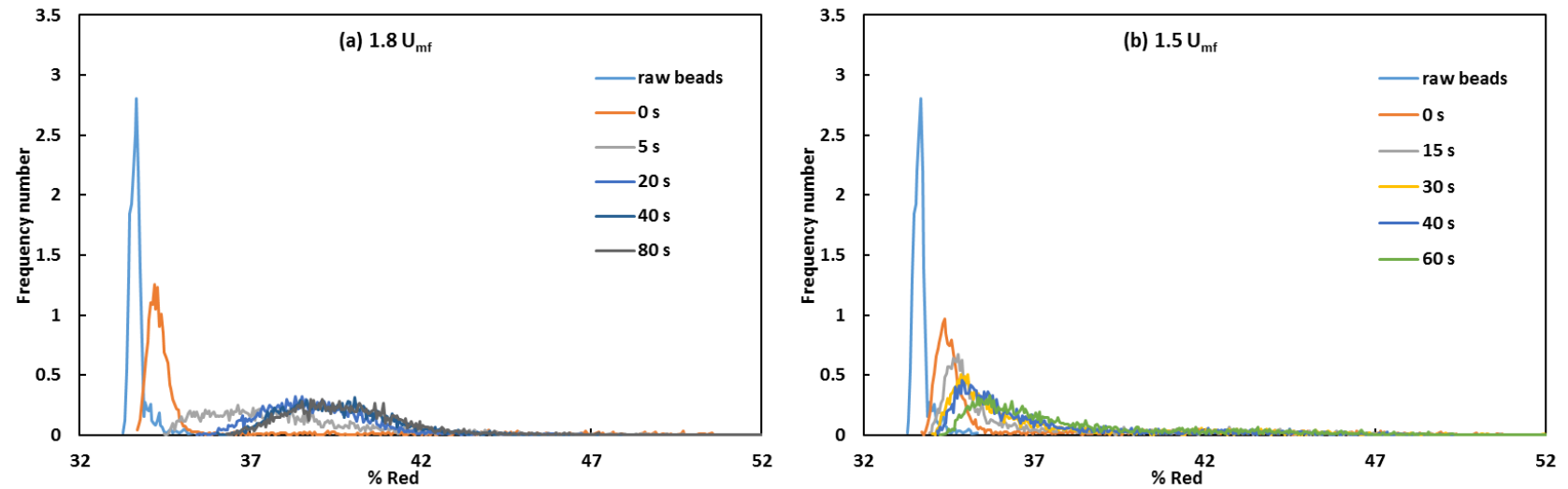
Figure 7.19. Coating evolution; frequency number as a function of % red for alumina coated at different velocities with 11 mPa.s HPMC solution, (a) 1.8 U_{mf} and (b) 1.5 U_{mf} (note that not all time points for each data series are shown for visualisation purposes)
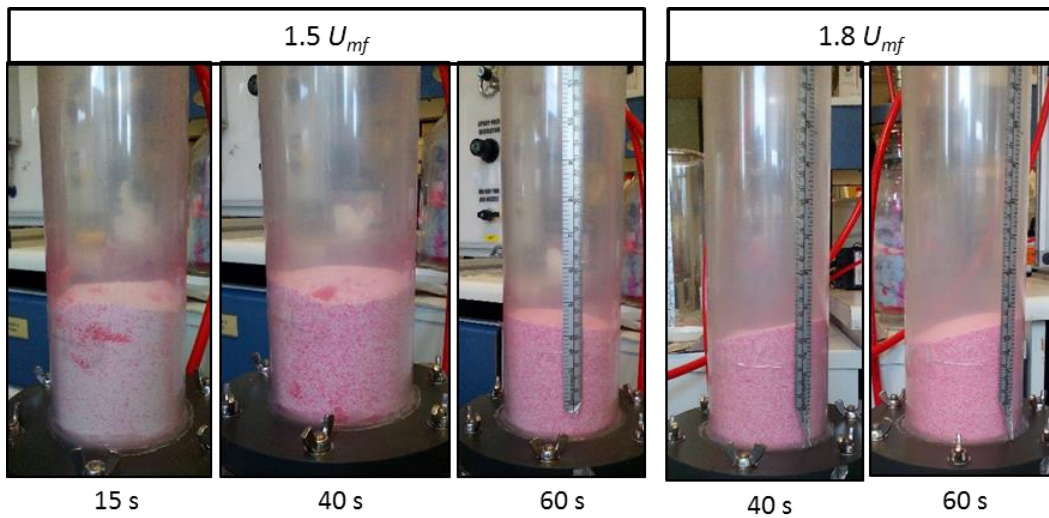
Figure 7.20. Images of alumina particles coated with 11 mPa.s HPMC solution at different fluidisation velocities and mixing times in the fluidised bed tube using the pre-coated particles method.
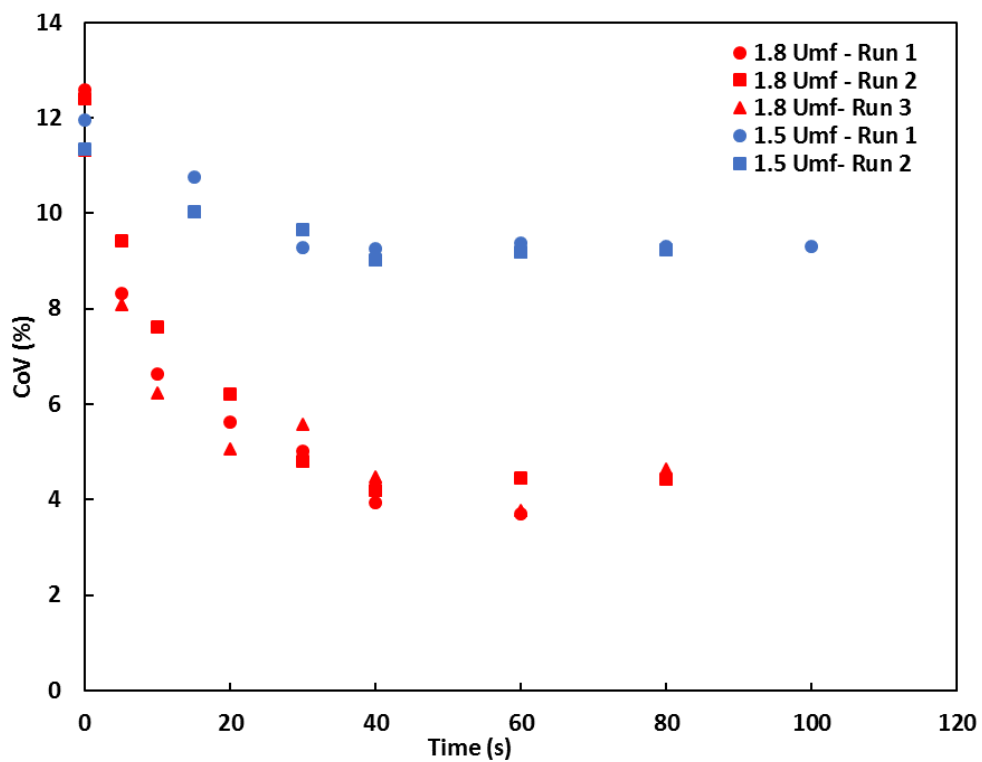
Figure 7.21. Coefficient of variation as a function of mixing time for alumina particles coated with 11 mPa.s HPMC solution at different fluidisation velocities.

In Figure 7.22, the data from Figure 7.21 were normalised (Eq. 5.1), referred to as the relative CoV, and plotted as a function of mixing time. Here, the relative CoV clearly indicates that the different fluidisation velocities significantly affect the contact spreading mechanism in the fluidised bed system when using the pre-coated particles method. Also, different asymptotic CoV values are reached. To determine the coating rate and the time taken to complete the coating process, t_c, the exponential decay curve fitting was used as described in the Chapter 4, Section 4.2.2 and illustrated in Figure 7.23. As explained in Section 7.3.1 and 7.3.2, when the relative CoV data series for different velocities used did not reach similar asymptotic CoV values, the coating rate constant, λ, cannot be related to the t_c and the asymptotic CoV value obtained. Thus, in this case, the contact spreading occurring in the coating system can only be explained based on the results shown in Figure 7.22. However, the coating rate, λ, time for completion, t_c, and the asymptotic CoV values were still determined and explained.
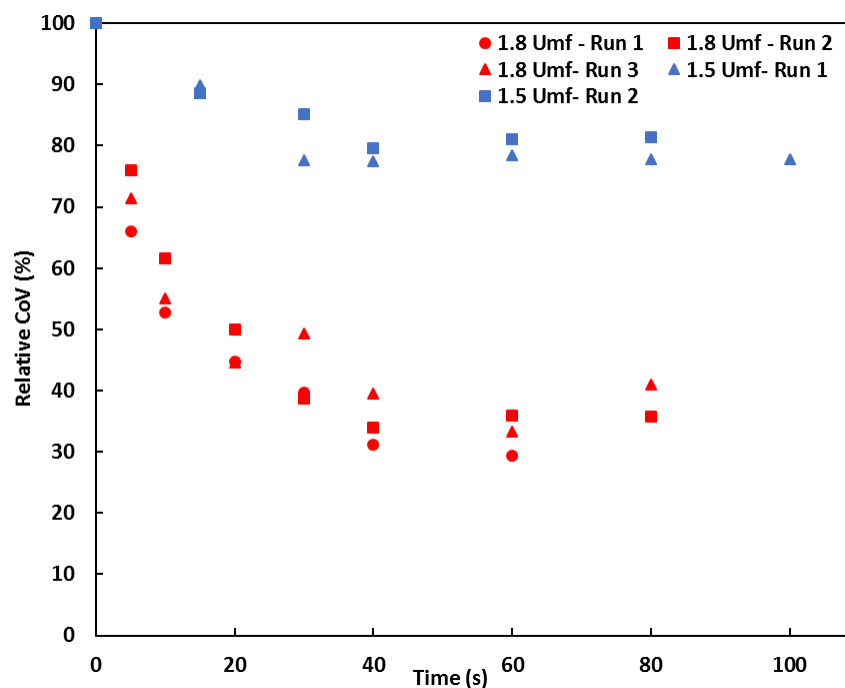
Figure 7.22. Relative coefficient of variation as a function of mixing time for alumina particles coated with HPMC 603 solution at different fluidisation velocities

216
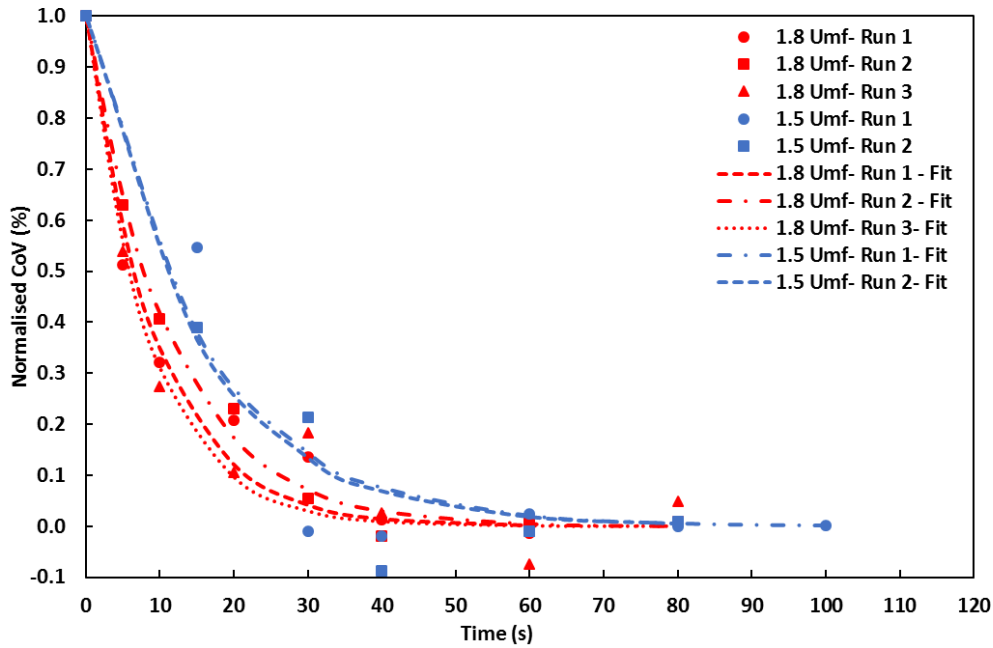
Figure 7.23. Normalised (between CoV_o and average CoV_∞) coefficient of variation and fitted decay curves as a function of mixing time at different fluidisation velocities.

From Figure 7.23, it can be seen that the curves fit well to the whole data series. The fitting parameters are summarised in Table 7.4. Figure 7.24 shows a plot of an average normalised (between CoV_o and average CoV_∞) coefficient of variation and fitted decay curves, as a function of mixing time for alumina coated at different fluidisation velocities. It can be clearly seen that the normalised CoV data series are clearly different at the different fluidisation velocities when using the pre-coated particles method.

Table 7.4. Fitting constants and time taken for completion for all data series for effect of fluidisation velocity (11 mPa.s HPMC solution)

Fluidisation velocity	Run	Coating rate constant, λ (s^{-1})	R^2	Time for 98% coating completion, t_c	CoV asymptote (%)
1.8 U_{mf}	1	0.105	0.969	37.11	3.82
	2	0.087	0.993	44.74	4.36
	3	0.117	0.961	33.37	4.30
	Mean	**0.103**	-	**38.41**	**4.16**
1.5 U_{mf}	1	0.064	0.937	60.66	9.31
	2	0.067	0.961	58.29	9.21
	Mean	**0.066**	-	**59.47**	**9.26**

Note: The asymptotic CoV value is taken as an average of the CoV values at the final time points, where there is no clear decrease in CoV values
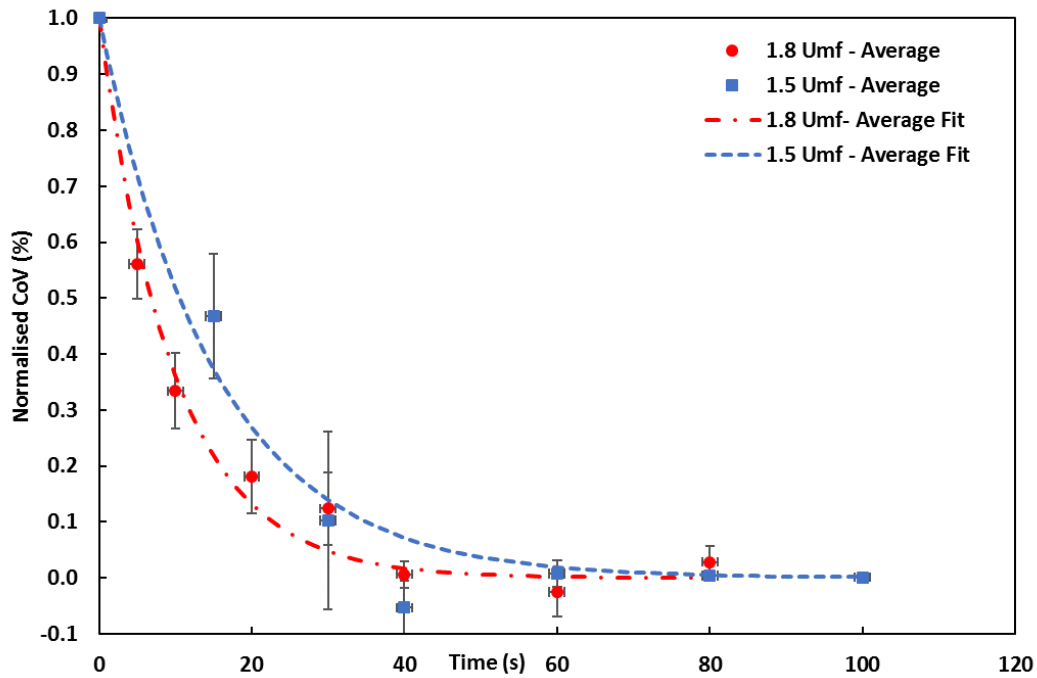
Figure 7.24. Average normalised (between CoV$_o$ and average CoV$_\infty$) coefficient of variation and fitted decay curves as a function of mixing time for alumina coated with 11 mPa.s HPMC solution at different fluidisation velocities. Error bars represent standard error.

As can be seen from Table 7.4, the coating rate constant when using the higher fluidisation velocity was nearly twice that of the coating rate constant at the lower fluidisation velocity. Moreover, the asymptotic CoV and the t_c for the higher fluidisation velocity were approximately half those of the lower fluidisation velocity. This observation is consistent with previous findings in Chapter 6 when using the spray method when different velocities were used. In this case, it can be concluded that the fluidisation velocity significantly affects the contact spreading mechanism in the fluidised bed system using the pre-coated particles method. The reason might be the difference in the agglomeration behaviour occurring in the systems; a similar reason to that given in the previous section (Section 7.3.2).

Figure 7.25 plots the fraction of agglomerates as a function of mixing time for each viscosity used. The fraction of agglomerates increases with a decrease in the fluidisation velocity. This result is consistent with the images seen in Figure 7.20, where wet agglomerates were observed at 1.5 U_{mf}, and especially at lower mixing times. This trend also further validates the fact that at higher air velocities, the agglomerates break up

218

quickly which allows the liquid to spread throughout the bed and reach a reasonable state of uniformity, as found by Zhou *et al.*, (2013). This previous study mentioned that agglomerates formed by liquid bridge forces were easily broken into discrete particles by strong gas shear forces (at higher fluidising velocities).
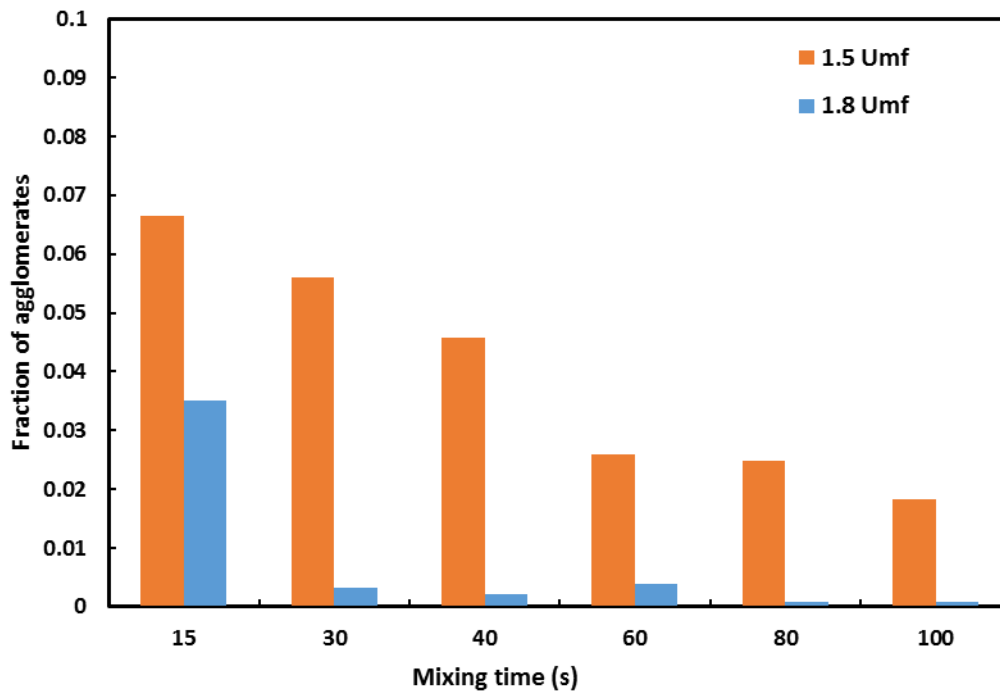
Figure 7.25. Agglomerate fraction as a function of mixing time at different fluidisation velocities

Even though the findings for the effect of fluidisation velocity on contact spreading obtained in this study are consistent with previous results obtained using the spray method in Chapter 6 (Section 6.3.2), at the asymptotic CoV value, the coated particles obtained using the pre-coated particles method were not as uniformly coated as those obtained from the spray method. This might be due to the different methods used to supply the liquid to the system; pre-coated method and spray method, as discussed in Section 7.3.2. In the following section, the results for the effect of velocity on contact spreading using both these methods in the fluidised bed system are compared and discussed.

7.3.4 Comparison of the effect of fluidisation velocity between both methods

In this section, the results for the effect of fluidisation velocity on contact spreading using the pre-coated particles method were compared to the findings of previous work in Chapter 6 where the liquid was introduced to the system using the spray method. Both methods use the same viscosity of HPMC solution (11 mPa.s) and ratio of liquid to particles (4 g liquid mass). Figure 7.26 (a-b) shows the CoV for each fluidisation velocity plotted as a function of time for all data series obtained for both methods. It can be observed from these figures that the CoV decreases with time for all data series and becomes constant after a certain time. Figure 7.27 (a-b) shows the relative CoV as a function of mixing time for different velocities using both methods. Figure 7.27b shows that at 1.5 U_{mf}, the pre-coated particles method showed significantly different results compared to the spray method. However, at 1.8 U_{mf}, both methods show a similar relative CoV pattern and reach similar asymptotic CoV values.

Moreover, to compare the coating rate constant, λ, time taken to complete the coating process, t_c, and the asymptotic CoV value for both methods, the normalised (between CoV_o and average CoV_∞) coefficient of variation and fitted decay curves as a function of mixing time are shown in Figure 7.28. It can be clearly seen that at 1.8 U_{mf}, all the data series for both methods fall onto similar curves, while at 1.5 U_{mf}, there is a significant difference in the rate of the coating change; a higher rate is seen for the pre-coated particles method. Table 7.5 summarises all the coating rate constants, λ, the times taken to complete the coating process, t_c, and the asymptotic CoV values for both methods at the two different fluidisation velocities.
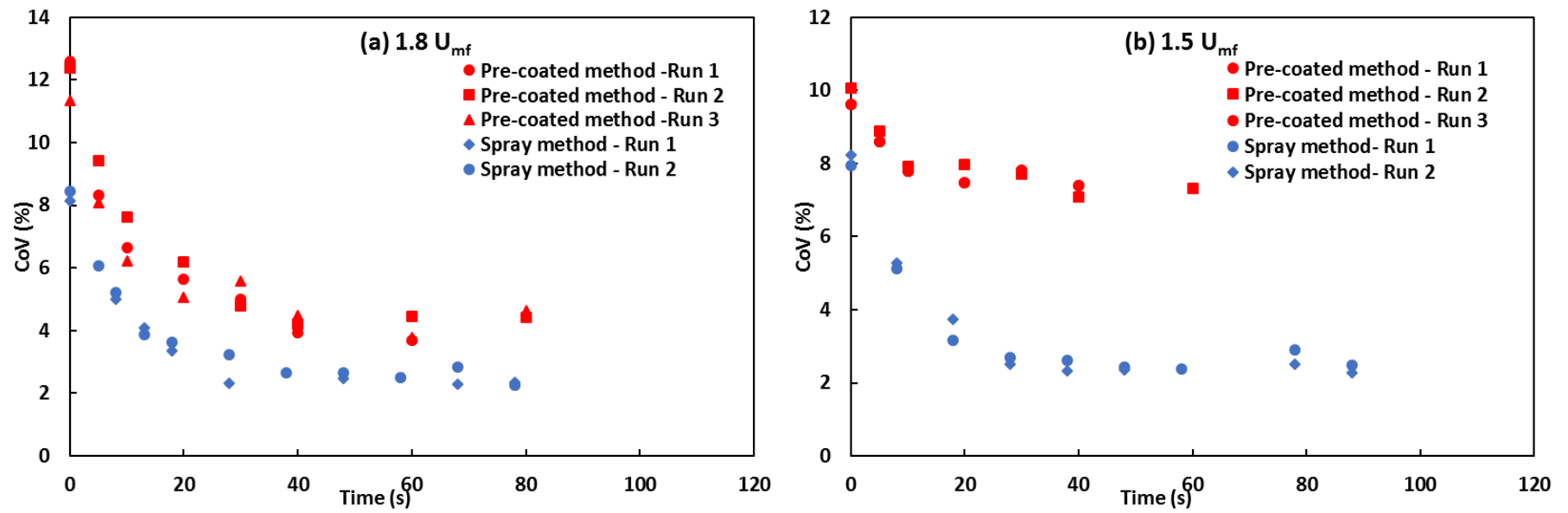
Figure 7.26. Coefficient of variation as a function of mixing time for alumina particles coated at different fluidisation velocities for all data series by the spray and pre-coated particles methods; (a) 1.8 U$_{mf}$ and (b) 1.5 U$_{mf}$
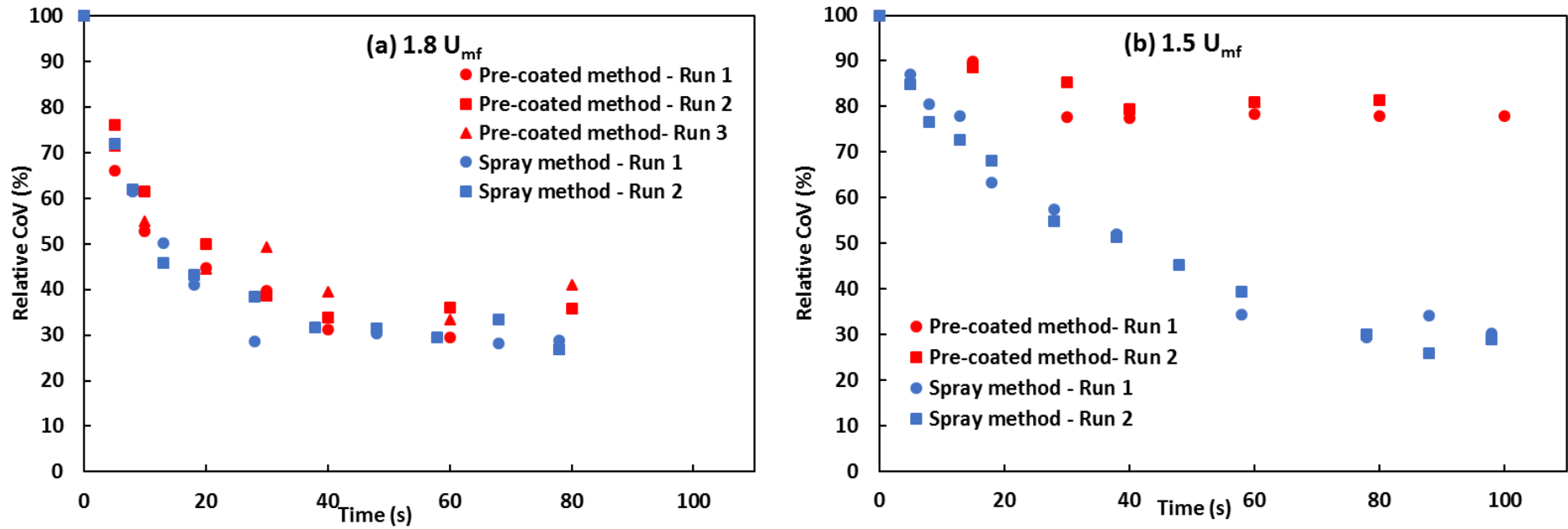
Figure 7.27. Relative coefficient of variation as a function of mixing time for alumina particles coated at different fluidisation velocities for all data series by the spray and pre-coated particles methods; (a) 1.8 U_{mf} and (b) 1.5 U_{mf}
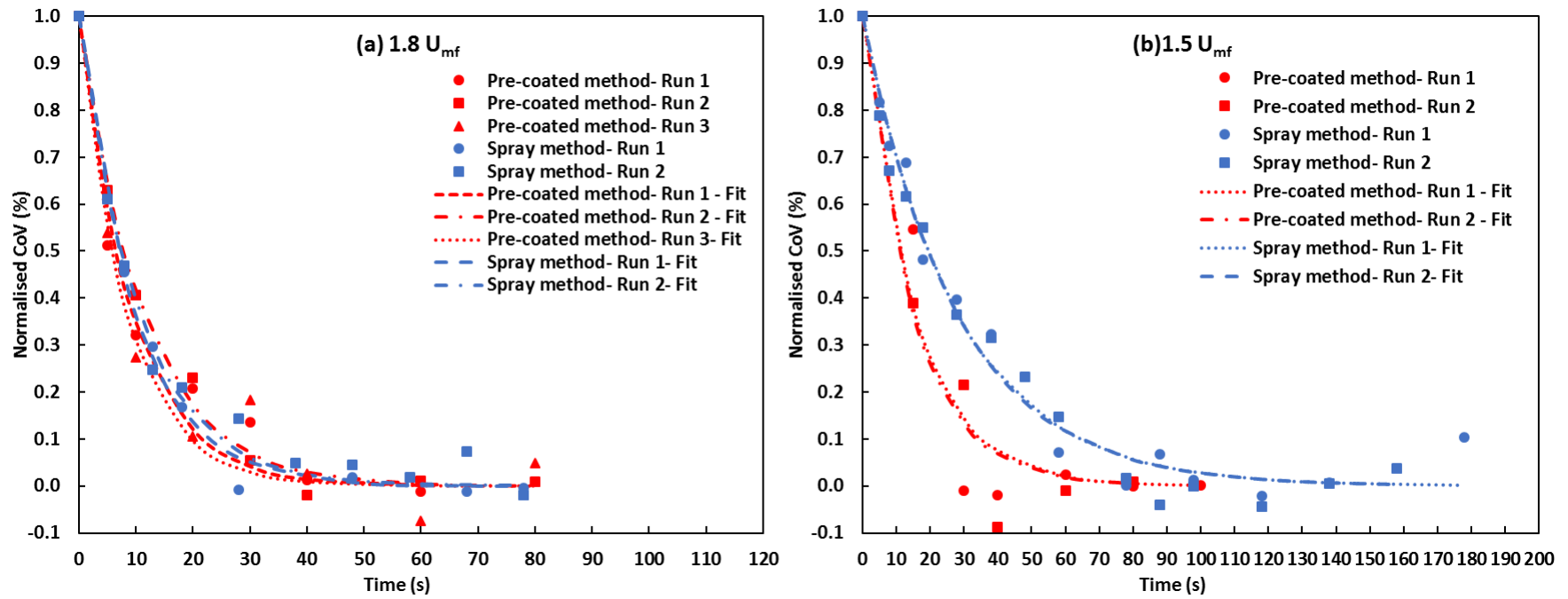
Figure 7.28. All data series of the normalised (between CoV$_o$ and average CoV$_\infty$) coefficient of variation and fitted decay curves as a function of mixing time for different fluidisation velocities by the pre-coated particles and spray methods; (a) 1.8 U_{mf} and (b) 1.5 U_{mf}

Table 7.5. Fitting constants and time taken for coating completion for all data series at different fluidisation velocities using the pre-coated particles (PCP) and the spray method.

Run	Coating rate constant, λ (s^{-1})		R^2		Time for 98% coating completion, t_c		CoV asymptote (%)	
	Spray	PCP	Spray	PCP	Spray	PCP	Spray	PCP
1.8 U_{mf}								
1	0.099	0.105	0.993	0.969	39.17	37.11	2.37	3.82
2	0.093	0.087	0.984	0.993	41.98	44.74	2.37	4.36
3	-	0.117	-	0.961	-	33.37	-	4.30
Mean	**0.097**	**0.103**	-	-	**40.57**	**38.41**	**2.37**	**4.16**
1.5 U_{mf}								
1	0.036	0.064	0.985	0.937	109.8	60.66	3.17	9.31
2	0.036	0.067	0.981	0.961	109.0	58.29	3.17	9.20
Mean	**0.036**	**0.066**	-	-	**109.4**	**59.47**	**3.17**	**9.26**

Note: The asymptotic CoV value is taken as an average of the CoV values at the final time points, where there is no clear decrease in CoV values

According to Table 7.5, at 1.8 U_{mf} the coating rate for both methods was similar and the time taken to reach the end point of the coating process was approximately the same. However, a higher asymptotic CoV value for the pre-coated particles method was obtained and as shown in Figure 7.29, the coated particles at this time were not as uniformly coated as the particles from the spray method. In addition, at 1.5 U_{mf}, the coating rates for both methods were significantly different; the pre-coated particles method had a coating rate nearly twice that of the spray method. The time taken to complete the coating process was also less for the pre-coated particles method and this can be related to the coating rate constant obtained. However, as observed when using a higher velocity (1.8 U_{mf}), the asymptotic CoV value for the pre-coated particles method was higher even though the coating rate was higher compared to spray method. Also, the coated particles, as seen in Figure 7.29, did not reach a uniform coating. Although the CoV started to level off earlier, highly uniform coated particles were not achieved. The findings observed here are consistent with findings in the previous section (Section 7.3.2) where, when using the pre-coated particles method and different viscosities, the coating rate could predict the t_c values but not the asymptotic CoV values, i.e. the extent of coating.
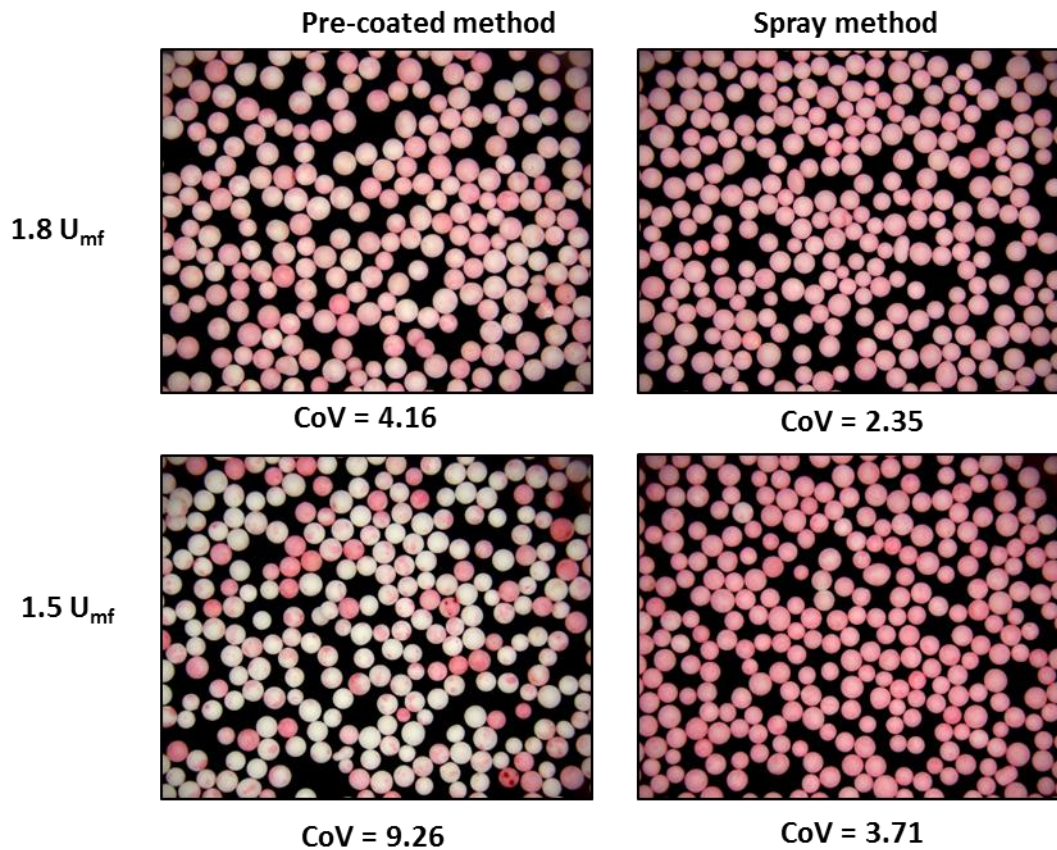
Figure 7.29. Image comparison at asymptotic CoV values for the spray and pre-coated particles methods at different fluidisation velocities.

The difference in the findings observed here for the pre-coated particles and the spray method can be explained in a similar way to that in Section 7.3.2. The images support the fact that different fluidisation velocities influence the liquid distribution via contact spreading and the uniformity of the final coated particles. A higher fluidisation velocity will break the liquid bridges faster due to the bubble induced motion which occurs at higher velocity regimes.

7.4 Summary

It was found that the liquid viscosity, mixing time and fluidisation velocity all influence the spreading of the liquid in the bed when using the pre-coated particles method. The results indicate that an increase in fluidisation velocity and decrease in viscosity contribute to a faster contact spreading process. It was not possible to eliminate the occurrence of agglomeration in the system. Agglomerates appeared mainly at lower mixing times which influenced subsequent liquid spreading and, therefore, the uniformity of the final coated particles. In this system, when using the pre-coated particles method, contact spreading behaviour can be characterised by the coating rate, λ, and the time taken to complete the coating process, t_c. However, the asymptotic CoV values, i.e. the extent of coating, cannot be related to the coating rate due to the fact that none of the final coated particles really achieve total uniformity due to drying occurring simultaneously in the system.

Furthermore, when the pre-coated particles method was compared to the spray method (Chapter 6), it was shown that the coating liquid addition method influenced the contact spreading process; mainly the final coating uniformity of the coated particles. The pre-coated particles method gave a different coating rate and non-uniform distribution of final coated particles at different viscosities and fluidisation velocities used. However, the extent of contact spreading seen when using the spray method was not significantly affected by the different solution viscosities. The difference in the results observed in both methods were likely due to the different states of wet agglomerates formed during the initial coating process which influenced the final coating uniformity of the coated particles produced via contact spreading.

CHAPTER 8

8 Theoretical contact spreading mechanisms from experimental observations

8.1 Introduction

This study has demonstrated for the first time that the contact spreading mechanism is an important contributor to the coating uniformity of the final coated particles. In a tumbling drum system, contact spreading is significantly affected by the coating liquid viscosity and the tumbling speed, while in a fluidised bed system the contact spreading is affected by the coating liquid viscosity, fluidisation velocity and nozzle height.

In the tumbling drum system, the results are attributed to the differences in the formation and stability of liquid bridges between particles, mainly at lower mixing times which influence the extent of liquid transfer via contact spreading in this system.

For the fluidised bed system, two different methods were used to supply the liquid into the system; the pre-coated particles method and the spray method. These methods gave similar results for contact spreading behaviour when investigating fluidisation velocity but different results when investigating solution viscosity. As discussed in Section 7.3.2 and 7.3.4, the reason for the results observed in both methods is likely due to the different states of the wet agglomerates formed during the initial coating process, and the fact that drying occurs simultaneously in the system. These factors are believed to influence the liquid transfer and final coating uniformity of the coated particles in this system.

From the results of both coating systems, it is clear that the build-up of wet-agglomerates is a significant mechanism during the initial phase of the contact spreading

process, which influences the liquid spreading and the uniformity of the final coated particles. This finding extends our knowledge of the importance of liquid bridge (wet agglomerates) formation and rupture behaviour on liquid transfer via contact spreading.

To quantify this effect, it is helpful to look at the mechanism of particle coalescence itself. Particle coalescence relies on the formation of liquid bridges between particles. The formation and breakage of these liquid bridges is related to the kinetic energy associated with the collision of wet particles. For both fluidised bed and tumbling drum systems, the collision behaviour will depend on the equipment design and the operating conditions.

The wet particles may rebound or coalesce when they collide depending on the impact energy; high energy collisions will utilise the energy in breaking the liquid bridges while low energy collisions may not have enough energy to cause liquid bridge breakage. Both conditions can influence the contact spreading behaviour. Therefore, a theoretical study on collision behaviour is discussed in this chapter.

8.2 Theory of Viscous Stokes Number

As discussed in Chapter 2, Section 2.3.2.3, a few models based on dimensionless numbers have been reported which predict the mechanisms of agglomerate formation, growth and rupture. For instance, by neglecting the capillary forces, Ennis *et al*. (1991) proposed the viscous Stokes number, St_v, (Eq. 8.1) to predict whether wet collisions between two particles will either stick or separate by comparing the viscous dissipation to the initial kinetic energy of the collision as illustrated in Figure 8.1. Coalescence occurs between wet particles which collide with insufficient relative kinetic energy to overcome the viscous dissipation force.

To map the agglomeration and coating regime, a critical Stokes number, St_c,(Eq. 8.2) was proposed which represents the ratio of the initial collision kinetic energy to the energy dissipated by viscous lubrication forces (Ennis *et al.*, 1991).
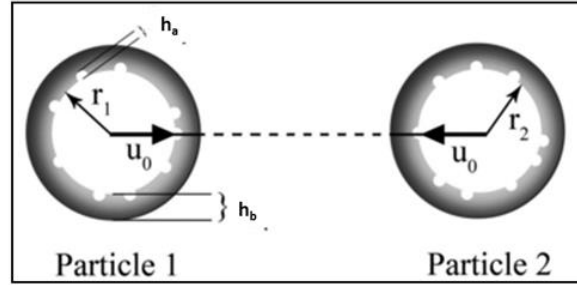
Figure 8.1. Schematic view of two colliding particles, each particle covered with a coating layer thickness, h_b. Adapted from Hede *et al.*, (2009).
(Note: r_1,r_2:particle radius, u_0:collision velocity and h_a: particle asperity)

$$St_v = \frac{4\rho_p d_p V_c}{9\mu}$$ **(Equation 8.1)**

$$St_c = \left(1 + \frac{1}{e_r}\right) ln\left(\frac{h_b}{h_a}\right)$$ **(Equation 8.2)**

Here, μ is the liquid viscosity, V_c is the characteristic particle collision velocity, d_p is the particle size, ρ_p is the particle density, e_r is the particle coefficient of restitution, h_b is the thickness of the coating layer and h_a is a measurement of the particle asperity height. According to this model, if $St_v < St_c$, the two particles will coalesce (collision success), while if $St_v > St_c$, the particles will rebound and the liquid will redistribute in the coating system. To relate the Stokes number with the process variables used in order to express the contact spreading behaviour, the Stokes number needs to be determined and this is explained in the following section.

8.2.1 Determination of the Viscous Stokes Number

Eq. 8.1 contains several material properties (particle density, particle size and viscosity), all of which have been measured experimentally in this work. The particle diameter used is the $d_{4,3}$ value (1020 µm). This is a representative particle size as the batch has a narrow size distribution, as described in Section 3.1.1. It also contains the particle collision velocity, V_c. Approximating V_c provides a challenge, as the velocities in a fluidised bed are not known. There will be a distribution of particle velocities, and these are likely be heavily influenced by the liquid content in the system.

In fluidised bed systems, V_c has been approximated as in the literature as the terminal velocity (V_t) of the particles (Eq. 8.3) or the bubble rise velocity, U_b (Ennis *et al.*, 1991; Boyce *et al.*, 2017b). However, since U_b is difficult to determine experimentally, in this case the excess air velocity, U_e, has been chosen to represent V_c shown in Eq. 8.4, a similar way used by Hede *et al.*, (2008) and Villa *et al.*, (2016).

In tumbling drum systems, the wall speed of a tumbling drum has been used as the characteristic velocity to approximate V_c. This method has been used previously in the literature, and the equation for calculation is given in Eq. 8.5 (Ennis *et al.*, 1991; Iveson and Litster, 1998).

$$v_t = \frac{6U_b d}{d_b \delta^2} \qquad \text{(Equation 8.3)}$$

$$U_e = U_s - U_{mf} \qquad \text{(Equation 8.4)}$$

$$v_w = \omega D \qquad \text{(Equation 8.5)}$$

Here, ω is the rotational speed, D is the drum diameter, U_s is the superficial velocity, U_{mf} is the minimum fluidisation velocity, U_b is the gas bubble rise velocity, d is the particle diameter, d_b is the average gas bubble diameter and δ is the dimensionless bubble space

defined as the axial fluidised bed bubble spacing divided by the fluidised bed gas bubble radius.

In both tumbling drums and fluidised bed systems the particle velocities will be distributed. This will result in a distribution of particle collision velocities. In order to consider the full range of Stokes numbers of the interparticle collisions, an approximation for the collision velocity distribution must be made. For the fluidised bed system, the collision velocity is assumed to be in the range from 0 m/s (i.e. stagnant) up to the maximum excess air velocity, U_e, while in the case of the tumbling drum system, the collision velocity is assumed to be from 0 m/s up to the wall velocity of the drum, V_w. Table 8.1 summarises the values for each parameter in Eq. 8.1 required to estimate the distribution of the viscous Stokes number in both the tumbling drum and fluidised bed.

Table 8.1 Values for each parameter used to estimate the distribution of Stokes number in both coating systems

Parameter	Coating Method				
	Spray - fluidised bed	Pre-coated - fluidised bed	References	Pre-coated - tumbling drum	References
Collision velocity (m/s)	0-1.05		• Based on excess velocity - Hede *et al.*, (2008) - Villa *et al.*, (2016	0-0.93	• Based on wall velocity -Ennis *et al*, 1991
Particle size, $d_{4,3}$ (μm)	1020		Exp.	1020	Exp.
Viscosity (Pa.s)	0.011-0.177		Exp.	0.137-15.489	Exp.
Particle envelope density, ρ_p (kg/m³)	3260		Exp.	3260	Exp.

Note: Exp. = Value measured from experimental work

8.2.2 Viscous Stokes Number Analysis

Figure 8.2 (a-b) illustrates the distribution of viscous Stokes number plotted as a function of the collision velocity for both coating systems in the fluidised bed and tumbling drum. As given in Eq. 8.1, St_v increases linearly with the collision velocity. It can be seen that broader distributions of St_v values are obtained for the lower viscosity systems. This result was expected and is supported by the theory of Ennis *et al*., (1990) who reported that a higher St_v value is obtained as the viscous dissipation becomes larger compared to the initial impact velocity during wet collisions. Note also the great difference in the range of St_v between the fluidised bed and tumbling drum systems, due in large part to the differences in coating liquid viscosities used between these systems.
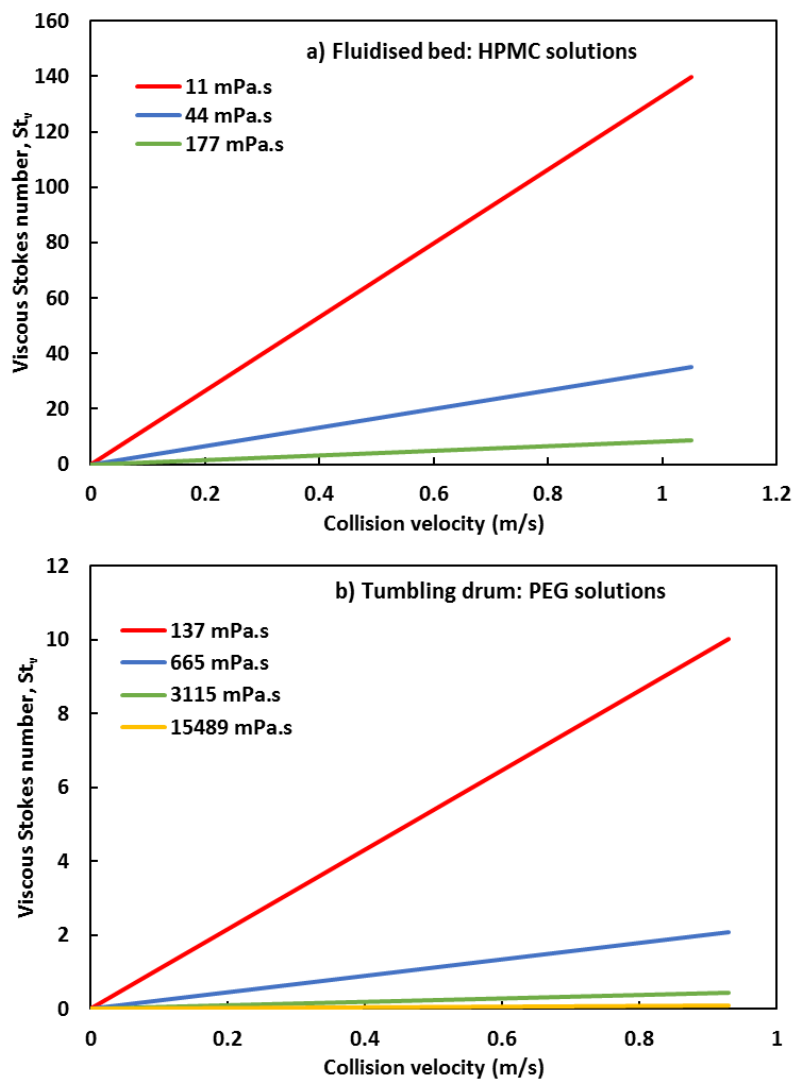
Figure 8.2. Viscous Stokes number as a function of collision velocity in a) fluidised bed (spray and pre-coated particles methods) and b) tumbling drum system.

To investigate the potential to use St_v to predict the agglomeration and coating regimes based on the relationship between the viscous Stokes number and the collision velocity, critical Stokes numbers were calculated based on Eq. 8.2. To calculate St_c, the coefficient of restitution, e_r, coating thickness, h_b and particle asperity height, h_a, are all required. These are difficult to determine, and due to time restrictions and equipment access issues, these were not measured experimentally. The coefficient of restitution ranges from 0 to 1 and has been estimated as 0.5 in this study. Particle asperity, h_a can be considered to be 2% of the particle diameter up to a maximum value of 3 μm (Chaudhury *et al.*, 2014). However, in this study, since 2% of the particle diameter is higher than the estimated coating layer thickness, h_b, the value for h_a is estimated as 1 μm. As the same particles were used for all experiments in this work, the choice of assumption for h_a is not critical. However, a more accurate estimate of this value would be required to compare these results against other materials. Table 8.2 summarises the estimated values for particle asperity, h_a and coefficient of restitution, e_r in Eq. 8.2 required to estimate the critical viscous Stokes number, St_c in both the tumbling drum and fluidised bed.

Table 8.2. Estimated values used for particle asperity, h_a and coefficient of restitution, e_r in different systems

Method	Coating liquid (mPa.s)	Particle asperity, ha (μm) / Reference	Coefficient of restitution, e_r / Reference
Fluidised bed (Spray- and Pre-coated method)	HPMC-11 mPa.s		0.5
	HPMC-44 mPa.s	1.0 • can be considered to be 2% of the particle diameter up 3 μm and $h_a \ll$ coating layer thickness (Chaudhury *et al.*, 2014)	• Alumina particles (dry e_r = 0.74), 1.75 mm (Antonyuk *et al.*, 2009)
	HPMC-177 mPa.s		• Glass beads (wet e_r = 0.61): 1.74 mm, coating thickness ~ 200-400 μm, viscosity (72.8-37.3 mNm^{-1}) (Cruger *et al.*, 2016)
Tumbling drum (Pre-coated method)	PEG-137 mPa.s		
	PEG-665 mPa.s		
	PEG-3115 mPa.s		-e_r for wet alumina particles estimate to be < 0.61 as higher viscosity used in this study
	PEG-15489 mPa.s		

When considering the coating layer thickness h_b, two extremes can be identified. Initially, for both tumbling drum and fluidised bed systems, the liquid can be assumed to be uniformly coated over 10% of the particle mass. Over time, as the liquid transfers due to contact spreading, the average amount of liquid on each wet particle will decline. The limit of this process is for each particle in the system to be evenly coated with liquid (i.e. the liquid is uniformly coated over 100% of the particle mass), which would provide a final CoV of zero. While this limit has not been reached for any system studied in this work, it provides a useful natural limit for discussion. According to these assumptions, the calculated h_b and St_c are summarised in Table 8.3, and these values are then applied to the graph of St_v as a function of velocity to map the agglomeration and coating regime as shown in Figure 8.3 (a-b).

Table 8.3. Estimated coating thickness, h_b using different systems

Method	Coating liquid (mPa.s)	Average Coating thickness, h_b (m)		St_c (-)	
		Upper limit	Lower limit	Upper limit	Lower limit
Fluidised bed **(Spray-and Pre-coated method)**	HPMC-11 mPa.s				
	HPMC-44 mPa.s	1.61×10^{-5}	1.65×10^{-6}	8.34	1.50
	HPMC-177 mPa.s				
Tumbling drum **(Pre-coated method)**	PEG-137 mPa.s				
	PEG-665 mPa.s	1.07×10^{-5}	1.08×10^{-6}	7.11	0.23
	PEG-3115 mPa.s				
	PEG-15489 mPa.s				

The details of the calculations are described in Appendix F1. Figure 8.3a-b shows the distribution of St_c and St_v as a function of velocity for each coating solution in both the tumbling drum and fluidised bed (spray and pre-coated particles methods) systems. In this graph, each system has the same starting point (when 10% of particles were

uniformly coated, corresponding to the St_c upper limit) and theoretical lower boundary (when 100% of particles were uniformly coated, corresponding to the St_c lower limit).

At the upper limit of St_c for both methods used in the fluidised bed systems (Fig. 8.3a), it can be observed that the fraction of $St_v > St_c$ increases as the viscosity of the solution decreases, roughly from 0 % to 95 %. This means that a decrease in viscosity contributes to a higher percentage of the collision velocities predicted to rebound. Thus, assuming the velocity distributions are similar in the fluidised bed for different viscosities, as the wet particles collide, a higher fraction of agglomerates are predicted to form for higher viscosities at the beginning of the coating process. However, as the time progresses, the St_c decreases to a certain limit and here, the vast majority of collision velocities have $St_v < St_c$, meaning that most collision velocities are predicted to rebound.

Figure 8.3a implies that as the viscosity of the coating liquid decreases, more collisions are expected to rebound, resulting in a faster coating rate. For the spray method (Chapter 6), no effect of viscosity was found for the coating rate. However, the fraction of agglomerates formed was larger for higher viscosity coating solutions than for the lower viscosity solutions. It is possible that the effect of drying in this system was dominant.

For the pre-coated particles method in the fluidised bed (Chapter 7), the extent of coating was much lower than for the spray method, and this make comparison difficult. However, the fraction of agglomerates produced using this method was much higher for high viscosity solutions than for low viscosity solutions, as predicted by Figure 8.3a.

Figure 8.3b shows that, in contrast to the fluidised bed systems, at the upper limit of St_c for the lowest PEG viscosity solution (137 mPa.s) only roughly 30% of $St_v > St_c$, while the fraction of $St_v > St_c$ for other PEG solutions (665-15489 mPa.s) was 0 %. Thus, all collision velocities for higher PEG solution viscosities are predicted to coalesce. At the lower limit of St_c, the fraction of $St_v > St_c$ for 137-3115 mPa.s PEG solutions increases but remains at 0% for the 15489 mPa.s solution.

The tumbling drum coating results in Chapter 5 do show an increase in coating rate with a decrease in liquid viscosity. Interestingly, however, the estimated values of St_c shown in Figure 8.3b predict that initially the vast majority of collisions will result in agglomeration. This is in contrast to the relatively rapid coating behaviour seen in Chapter 5, especially for lower viscosity coating solutions. This may be due to the assumptions behind the estimates for both St_v and St_c.

In order to further examine the impact of St_v on contact spreading, the relationship between St_v with the time to reach an asymptotic CoV, t_c, and the asymptotic CoV are shown in Figures 8.4 – 8.5. Figure 8.4a-c gives the average of the time to reach an asymptotic CoV value, t_c, as a function of viscous Stokes number. A similar trend can be seen for either of the methods used in the fluidised bed system, where there was no correlation between t_c and St_v. In contrast, the tumbling drum system appears to show a relationship between t_c and St_v. A straight line has been fitted to this data, however it is important to acknowledge that the R^2 value of 0.7781 is relatively poor, and while there is an increasing trend between t_c and St_v, the exact nature of the correlation is not clear.

Figure 8.4 shows that there are significant differences in the coating behaviour between the two systems studied here. There are several critical differences between fluidised beds and tumbling drums, which explain these findings. While the effect of characteristic velocities and liquid viscosities has been examined, it is also expected that there will be differences in the collision frequencies in each system, which will have a significant effect on the coating rate. As the fluidised bed is a dilute phase system compared to the tumbling drum, it could be expected that collisions occur relatively less frequently in the fluidised bed. There is also the effect of drying in the systems. Liquid in the tumbling drum will experience some drying, but this would be expected to be a much smaller influence than in the fluidise bed, where significant drying is occurring simultaneously with coating. The wet agglomerates that form in fluidised bed may dry completely prior to rupture, reducing the ability to transfer liquid in the system. The differences between the systems were demonstrated when the 137 mPa.s PEG solution used in the tumbling drum was applied in the fluidised bed system using the spray method;

no contact spreading was observed in the system. There is potential to strengthen the viscous Stokes number analysis in the future by incorporating a drying factor in the applied dimensionless number.
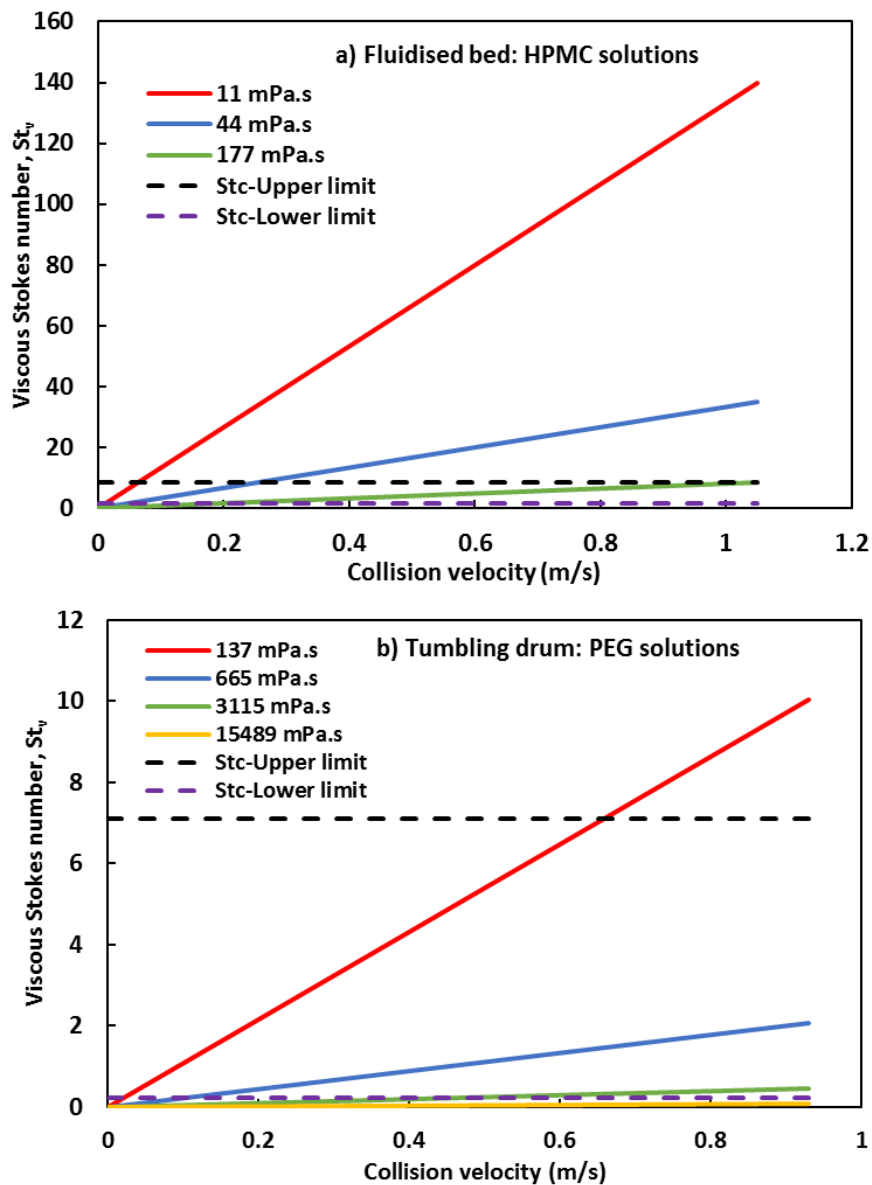
Figure 8.3. Viscous Stokes number and critical Stokes number distribution as a function of collision velocity for a) fluidised bed system (spray and pre-coated particles method) and b) tumbling drum system.
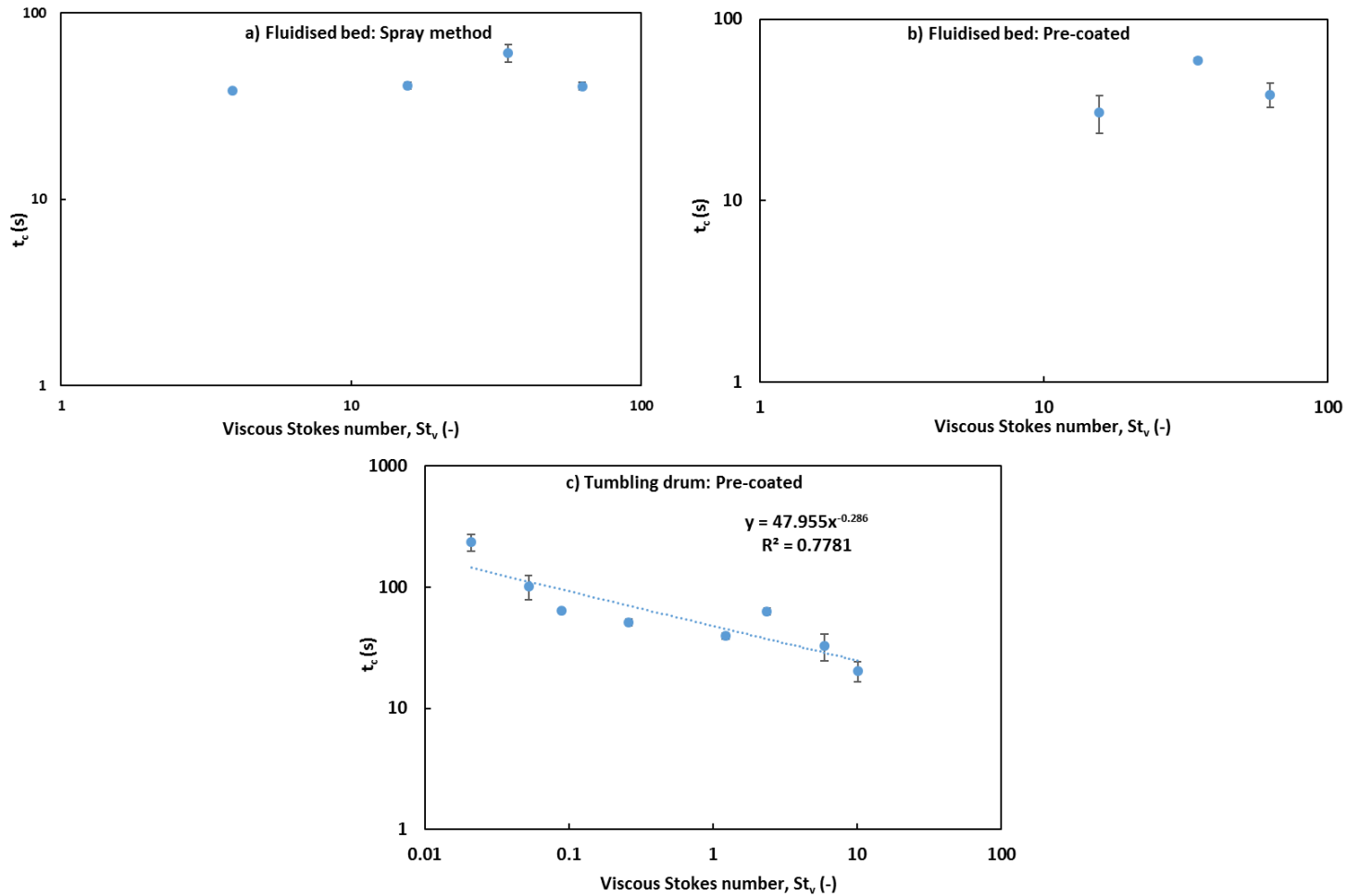
Figure 8.4. Average time taken for coating completion, t_c, as a function of viscous Stokes number for a) spray method in the fluidised bed (2.0 g/s spray rate), b) pre-coated particles method in the fluidised bed and c) pre-coated particles method in the tumbling drum. Error bars represent standard deviation

Figure 8.5 illustrates the average asymptotic CoV value as a function of viscous Stokes number for both systems. For the tumbling drum, the extent of coating (expressed through the value of the asymptotic CoV) is fairly consistent between roughly 1 and 2 % over almost 3 orders of magnitude of St_v, indicating that the extent of inter-particle coating was independent of St_v. None of the systems reach fully uniform coating. For the fluidised bed systems, the asymptotic CoV values are somewhat higher, likely due to the previously discussed effects of drying. For the pre-coated fluidised bed system in particular, there are large variations in the asymptotic CoV values, and on the whole, they are very high, indicating that there is very broad final coating distribution.

Overall, the correlation between St_v and t_c shows potential to be applied as a guide for selecting preliminary operating conditions in coating systems which have a small effect of drying, for example high shear mixers, tumbling drums and pans, and paddle mixers. However, the St_v and St_c measured in this work can only be regarded as approximate, and their validity only for the system studied. Also, for fluidised bed and tumbling drum system, it has been limited to free-flowing, large, high density spherical particles, and further work needs to be conducted to apply these findings to irregular, cohesive, and/or fine powder systems with broad size distributions.

8.3 Summary

In this work, the viscous Stokes number and the critical viscous Stokes number were used to give an analysis of the sticking criterion, which determines whether a collision leads to agglomeration or rebound of the involved particles. This method was applied to both coating systems: a fluidised bed and a tumbling drum system. The attempt to develop the theory of contact spreading using aforementioned dimensionless number are all based on estimation and this might only valid for the system studied. For the fluidised bed system, the predicted increase in coating rate with decreasing solution viscosity was not demonstrated. This is attributed to the large effect of drying in this system. For the tumbling drum, the predicted increase in coating rate with decreasing liquid viscosity matched the experimental coating behaviour shown in Chapter 5.

However, the estimated values of St_v and St_c predicted that most collisions would result in agglomeration, in contrast to the relatively rapid contact spreading behaviour demonstrated in the tumbling drum.

When the time to reach the end of the process, t_c, and asymptotic CoV values were compared with St_v, the results found no correlation between t_c and St_v in both methods used in the fluidised bed system but show a trend for the tumbling drum system; increases in St_v give a decrease in t_c. For asymptotic CoV values, there are no correlations with St_v observed for all the systems studied. The viscous Stokes number does not account for the drying rate of the solutions. Hence, in future, incorporating a drying factor in the dimensionless number could add more value in contact spreading studies, mainly in fluidised bed systems. The theory development of the contact spreading using the St_v could also be improved in the future by experimentally measured each parameter that have been estimated in Eq. 8.1 and Eq. 8.2 (e.g, collision velocity, coating thickness and particle asperity).
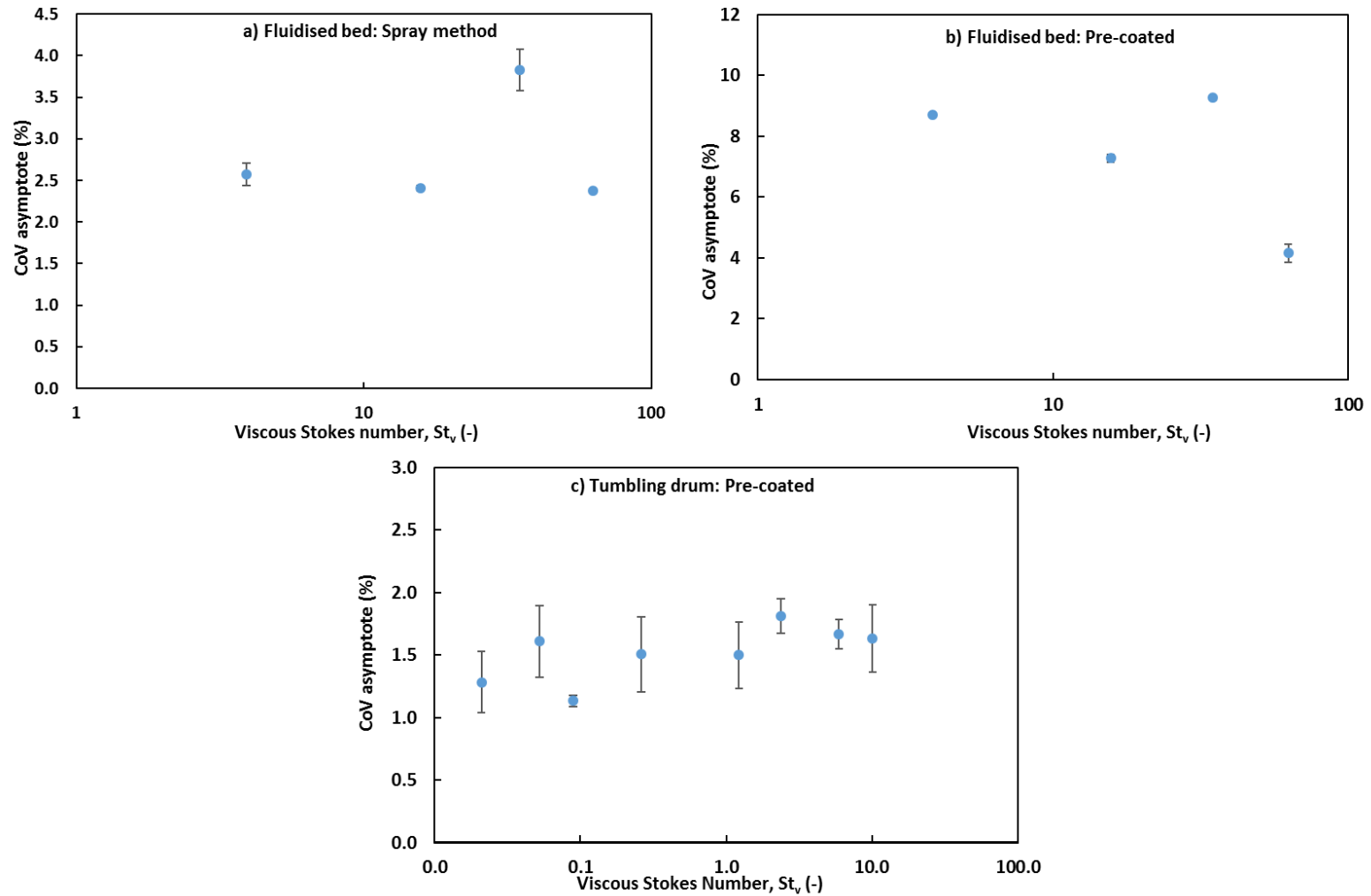
Figure 8.5. Average asymptotic CoV as a function of viscous Stokes number for a) spray method in the fluidised bed, b) pre-coated particles method in the fluidised bed and c) pre-coated particles method in the tumbling drum. Error bars represent standard deviation

CHAPTER 9

9 Conclusions and Recommendations

9.1 Introduction

The key research objectives of this study were to add new knowledge regarding the liquid distribution within particle batches via contact spreading mechanisms in different coating systems. A new image analysis technique was developed to characterise the coating layer uniformity between coated particles within a batch. Two coating systems; a tumbling drum and a fluidised bed with and without a spray system were designed and constructed to study the influence of operating conditions, properties of coating materials and initial liquid loading method on contact spreading behaviour. This chapter summarises the research findings and their contribution to knowledge and proposes some future works that can be further explored.

9.2 Research Conclusions

This research has successfully carried out the first comprehensive experimental study into contact spreading in different coating systems: tumbling drum and fluidised bed systems.

For this study, a new image analysis system was developed to qualitatively and quantitatively measure the liquid distribution of particle coating. This has resulted in improvements being made to characterise the inter-particle coating uniformity within a particle batch. This novel imaging system is very accurate, easy to use, and many particles (ca.2000-4000 per batch) can be measured and analysed in a short period of time compared to other existing methods.

The key experimental findings of this research are summarised below:

- Contact spreading occurs in both coating systems contributing to the coating uniformity obtained for final coated particles without a spray zone effect. This suggests that this mechanism should indeed be considered when studying the coating process and may be a significant factor.

- In the tumbling drum system, using the pre-coated particles method of liquid addition, the tumbling time, coating solution viscosity and tumbling regime (rolling, cascading and cataracting) significantly affected the liquid transfer through contact spreading. As mixing time increased, the value of the coefficient of variation (CoV) decreased until an asymptotic value of the CoV was obtained. This asymptotic value, which represents the extent of coating, was similar for all conditions investigated; and a relatively uniform coating was observed. With an increase in drum speed, the coating rate increased and the time to complete the coating process decreased. Regarding the effect of coating liquid viscosity, the lower viscosity, the faster the coating rate; resulting in a reduction in time to complete the coating process.

- In the fluidised bed studies using the spray method, fluidisation velocity and nozzle height significantly affected the contact spreading process. An increase in fluidisation velocity and a decrease in nozzle height increased the coating rate and reduced the time for the completion of coating. However, in the ranges of liquid spray rate studied, the only lowest spray rate had a small influence on contact spreading, and no differences were observed for the effect of viscosity on contact spreading behaviour.

- Further studies were carried out in the fluidised bed using the pre-coated particles method to supply the liquid, to investigate different methods of liquid introduction. In these studies, the liquid viscosity, mixing time and fluidisation velocity all influenced the contact spreading. An increase in fluidisation velocity and a decrease in viscosity contribute to a faster contact spreading process. In this system, even though the contact spreading behaviour can be characterised by the coating rate and the time taken to complete the coating process, the asymptotic CoV values cannot be related to the coating rate due to the fact that the final coated particles do not really achieve total uniformity

243

due to drying occurring simultaneously as compared to fluidised bed spray method.

- Different initial liquid loading methods in the fluidised bed system significantly affected the extent of contact spreading. The spray method of liquid supply gave a more uniform coating compared to pre-coated particles method.

- In both systems, a viscous Stokes number, St_v, and critical viscous Stokes number, St_c, as a function of collision velocity were applied to predict whether a collision either leads to agglomeration or rebound of the involved particles. It is demonstrated that the predicted increase in coating rate with decreasing liquid viscosity is consistent with the pre-coated method for tumbling drum system. However, this is not the case for the fluidised bed system due to the large effect of drying in this system.

- As the time to complete coating process, t_c, was compared with St_v, there was no correlation between t_c and St_v in both methods used in the fluidised bed system. However, there is a trend for the tumbling drum system; an increase in St_v results in a decrease in t_c.

- When the asymptotic CoV values were compared with St_v, there were no correlations observed for all the systems studied.

9.3 Future work

This study has provided evidence that contact spreading mechanism occurs in the coating systems used: tumbling drum and fluidised bed system and contributes to the coating uniformity of the final coated particles. This thesis provides an additional knowledge for industries which employ coating techniques. However, this first contact spreading experimental study has also opened up new research questions, and these can be further explored as detailed below:

- The initial liquid loading method is one of the main variables which shows a significant effect on contact spreading. However, so far, this variable has only

been investigated in the fluidised bed system. Thus, a spray coating method in the tumbling drum should be applied to compare the contact spreading behaviour with the pre-coated particles method.

- In this current study, similar but different model coating liquids were used for the two coating systems. Future work should aim to employ the same coating liquid in both systems to allow for better comparison.

- Material properties, for example, particle shape, porosity and roughness may also influence the contact spreading behaviour. Thus, the effect of these types of properties on contact spreading could greatly contribute to our understanding of liquid distribution in coating systems.

- In the fluidised bed system, drying of the coating was believed to play a role during contact spreading. Therefore, consideration of this factor during particle coating processes could assist in coating prediction. Moreover, the effect of temperature on contact spreading in both coating systems could also increase our knowledge of contact spreading.

10 References

Abe, E., Yamada, N., Hirosue, H., & Nakamura, H. (1998). Coating mass distributions of seed particles in a tumbling fluidized bed coater. *Powder Technology*, *97*(1), 85–90.

Alchikh-Sulaiman, B., Alian, M., Ein-Mozaffari, F., & Lohi, A. (2015). Using the discrete element method to assess the mixing of polydisperse solid particles in a rotary drum. *Particuology*, *0*, 1–10.

Alghunaim, A., Kirdponpattara, S., & Zhang, N. B. (2016). Technique for determining contact angle and wettability of powders. *Powder Technology*, *287*, 201–215.

Andrade, R. D., Skurtys, O., & Osorio, F. A. (2012a). Atomizing Spray Systems for Application of Edible Coatings. *Comprehensive Reviews in Food Science and Food Safety*, *11*(3), 323–337.

Andrade, R., Skurtys, O., & Osorio, F. (2012b). Experimental study of drop impacts and spreading on epicarps: Effect of fluid properties. *Journal of Food Engineering*, *109*(3), 430–437.

Andrade, R., Skurtys, O., & Osorio, F. (2013). Drop impact behavior on food using spray coating: Fundamentals and applications. *Food Research International*, *54*(1), 397–405.

Andrade, R., Skurtys, O., & Osorio, F. (2015). Drop impact of gelatin coating formulated with cellulose nanofibers on banana and eggplant epicarps. *LWT - Food Science and Technology*, *61*(2), 422–429.

Antonyuk, S., Heinrich, S., Deen, N., & Kuipers, H. (2009). Influence of liquid layers on energy absorption during particle impact. *Particuology*, *7*(4), 245–259.

Anwar, S. H., Weissbrodt, J., & Kunz, B. (2010). Microencapsulation of fish oil by spray granulation and fluid bed film coating. *Journal of Food Science*, *75*(6), E359-71.

Askarishahi, M., Salehi, M.-S., Godini, H. R., & Wozny, G. (2015). CFD study on solids flow pattern and solids mixing characteristics in bubbling fluidized bed: Effect of fluidization velocity and bed aspect ratio. *Powder Technology*, *274*, 379–392.

Atarés, L., Depypere, F., Pieters, J. G., & Dewettinck, K. (2012). Coating quality as

affected by core particle segregation in fluidized bed processing. *Journal of Food Engineering*, *113*(3), 415–421.

Bansode, S. S., Banarjee, S. K., Gaikwad, D. D., Jadhav, S. L., & Thorat, R. M. (2010). Microencapsulation : A review. *International Journal of Pharmaceutical Sciences Review and Research*, *1*(2), 38–43.

BETE Fog Nozzle, Inc. (2017). BETE. Retrieved September 1, 2018, from http://www.bete.com.spraypatterns/fan_nf4015.html

Boateng, A. A., & Barr, P. V. (1997). Granular flow behaviour in the transverse plane of a partially filled rotating cylinder. *Journal of Fluid Mechanics*, *330*, S0022112096003680.

Boerefijn, R., Juvin, P.-Y., & Garzon, P. (2009). A narrow size distribution on a high shear mixer by applying a flux number approach. *Powder Technology*, *189*(2), 172–176.

Bolleddula, D. A., Berchielli, A., & Aliseda, A. (2010). Impact of a heterogeneous liquid droplet on a dry surface: application to the pharmaceutical industry. *Advances in Colloid and Interface Science*, *159*(2), 144–59.

Börner, M., Hagemeier, T., Ganzer, G., Peglow, M., & Tsotsas, E. (2014). Experimental spray zone characterization in top-spray fluidized bed granulation. *Chemical Engineering Science*, *116*, 317–330.

Boyce, C. M. (2018). Gas-solid fluidization with liquid bridging: A review from a modeling perspective. *Powder Technology*, *336*, 12–29.

Boyce, C. M., Kolehmainen, J., & Sundaresan, S. (2017a). Growth and break up of a wet agglomerate in a dry gas-solid fluidized bed. *AIChE Journal*, *63*(7), 2520–2527.

Boyce, C. M., Ozel, A., Kolehmainen, J., & Sundaresan, S. (2017b). Analysis of the effect of small amounts of liquid on gas–solid fluidization using CFD-DEM simulations. *AIChE Journal*, *63*(12), 5290–5302.

Brock, D., Zeitler, J. A., Funke, A., Knop, K., & Kleinebudde, P. (2014). Evaluation of critical process parameters for inter-tablet coating uniformity of active-coated GITS using Terahertz Pulsed Imaging. *European Journal of Pharmaceutics and*

Biopharmaceutics : Official Journal of Arbeitsgemeinschaft Für Pharmazeutische Verfahrenstechnik e.V, *88*(2), 434–42.

Capece, M., & Dave, R. (2011). Application of fluidized bed film coating for membrane encapsulation of catalysts. *Powder Technology*, *211*(2), 199–206.

Cengel, Y.A. (2006). Heat and Mass Transfer: a practical approach 3rd ed., McGraw-Hill.

Chan, L. W., Tang, E. S. K., & Heng, P. W. S. (2006). Comparative study of the fluid dynamics of bottom spray fluid bed coaters. *AAPS PharmSciTech*, *7*(2), E37.

Chang, R., & Leonzio, M. (1995). The effect of run time on the inter-unit Uniformity of Aqueous Film Coating Applied To Glass beads in a hi-coater. *Drug Development and Industrial Pharmacy*, *21*(16), 1895–1899.

Chaudhury, A., Wu, H., Khan, M., & Ramachandran, R. (2014). A mechanistic population balance model for granulation processes: Effect of process and formulation parameters. *Chemical Engineering Science*, *107*, 76–92.

Chen, W., Chang, S. Y., Kiang, S., Early, W., Paruchuri, S., & Desai, D. (2008). The measurement of spray quality for pan coating processes. *Journal of Pharmaceutical Innovation*, *3*(1), 3–14.

Cheng, X. X., & Turton, R. (2000). The prediction of variability occurring in fluidized bed coating equipment. II. The role of nonuniform particle coverage as particles pass through the spray zone. *Pharmaceutical Development and Technology*, *5*(3), 323–332.

Chiba, S., Nienow, a W., & Chiba, T. (1980). Fluidised binary mixtures in which the denser component maybe flotsam. *Powder Technology*, *26*, 1–10.

Chou, S. H., Liao, C. C., & Hsiau, S. S. (2010). An experimental study on the effect of liquid content and viscosity on particle segregation in a rotating drum. *Powder Technology*, *201*(3), 266–272.

Christoph Link, K., & Schlünder, E.-U. (1997). Fluidized bed spray granulation. *Chemical Engineering and Processing: Process Intensification*, *36*(6), 443–457. https://doi.org/10.1016/S0255-2701(97)00022-6

Chua, K. W., Makkawi, Y. T., Hewakandamby, B. N., & Hounslow, M. J. (2011). Time

scale analysis for fluidized bed melt granulation-II: Binder spreading rate. *Chemical Engineering Science*, *66*(3), 327–335.

Co., S. S. (2000). Guidelines for Spray Nozzle Selection Start By Understanding Nozzle Types : Hydraulic Atomizing vs . Air Atomizing, 4. Retrieved from www.spray.com

Cocco, R., Karri, S. B. R., & Knowlton, T. (2014). Introduction to fluidization. *Chemical Engineering Progress*, *110*(11), 21–29.

Cooper-White, J. ., Crooks, R. ., & Boger, D. . (2002). A drop impact study of worm-like viscoelastic surfactant solutions. *Colloids and Surfaces A: Physicochemical and Engineering Aspects*, *210*(1), 105–123.

Crocker, J. C., & Grier, D. G. (1996). Methods of digital video microscopy for colloidal studies. *Journal of Colloid and Interface Science*, *179*(1), 298–310.

Cruger, B., Heinrich, S., Antonyuk, S., Deen, N. G., & Kuipers, J. A. M. (2016). Experimental study of oblique impact of particles on wet surfaces. *Chemical Engineering Research and Design*, *111*(1), 449–460.

Darabi, P., Li, T., Pougatch, K., Salcudean, M., & Grecov, D. (2010). Modeling the evolution and rupture of stretching pendular liquid bridges. *Chemical Engineering Science*, *65*(15), 4472–4483.

Darabi, P., Pougatch, K., Salcudean, M., & Grecov, D. (2009). A novel coalescence model for binary collision of identical wet particles. *Chemical Engineering Science*, *64*(8), 1868–1876.

Darabi, P., Pougatch, K., Salcudean, M., & Grecov, D. (2011). DEM investigations of fluidized beds in the presence of liquid coating. *Powder Technology*, *214*(3), 365–374.

Delele, M. A., Weigler, F., Franke, G., & Mellmann, J. (2016). Studying the solids and fluid flow behavior in rotary drums based on a multiphase CFD model. *Powder Technology*, *292*, 260–271.

Denis, C., Hemati, M., Chulia, D., Lanne, J. Y., Buisson, B., Daste, G., & Elbaz, F. (2003). A model of surface renewal with application to the coating of pharmaceutical tablets in rotary drums. *Powder Technology*, *130*(1–3), 174–180.

Depypere, F., Van Oostveldt, P., Pieters, J. G., & Dewettinck, K. (2009). Quantification of microparticle coating quality by confocal laser scanning microscopy (CLSM). *European Journal of Pharmaceutics and Biopharmaceutics*, *73*(1), 179–186.

Ding, Y. L., Forster, R. N., Seville, J. P. K., & Parker, D. J. (2001). Some aspects of heat transfer in rolling mode rotating drums operated at low to medium temperatures. *Powder Technology*, (121), 168–181.

Dixit, R., & Puthli, S. (2009). Fluidization technologies: Aerodynamic principles and process engineering. *Journal of Pharmaceutical Sciences*, *98*(11), 3933–3960.

Donahue, C. M., Davis, R. H., Kantak, A. A., & Hrenya, C. M. (2012). Mechanisms for agglomeration and deagglomeration following oblique collisions of wet particles. *Physical Review E - Statistical, Nonlinear, and Soft Matter Physics*, *86*(2), 1–5.

Donahue, C. M., Hrenya, C. M., & Davis, R. H. (2010). Stokes's Cradle: Newton's Cradle with Liquid Coating. *Physical Review Letters*, *105*(3), 34501.

Donida, M., Rocha, S. C. S., & Bartholomeu, F. (2005). Influence of Polymeric Suspension Characteristics on the Particle Coating in a Spouted Bed. *Drying Technology*, *23*(9–11), 1811–1823.

Dreu, R., Luštrik, M., Perpar, M., Žun, I., & Srčič, S. (2012). Fluid-bed coater modifications and study of their influence on the coating process of pellets. *Drug Development and Industrial Pharmacy*, *38*(4), 501–511.

Dubé, O., Alizadeh, E., Chaouki, J., & Bertrand, F. (2013). Dynamics of non-spherical particles in a rotating drum. *Chemical Engineering Science*, *101*, 486–502.

Dubey, A., Hsia, R., Saranteas, K., Brone, D., Misra, T., & Muzzio, F. J. (2011). Effect of speed, loading and spray pattern on coating variability in a pan coater. *Chemical Engineering Science*, *66*(21), 5107–5115.

Easo, L.A. (2017). Liquid dispersion in sheared particulate material, PhD thesis, Purdue University, US.

Ennis, B. J., Li, J., Gabriel I., T., & Robert, P. (1990). The influence of viscosity on the strength of an axially strained pendular liquid bridge. *Chemical Engineering Science*, *45*(10), 3071–3088.

Ennis, B. J., Tardos, G., & Pfeffer, R. (1991). A microlevel-based characterization of granulation phenomena. *Powder Technology*, *65*(1–3), 257–272.

Escudero, D. R. (2010). *Bed height and material density effects on fluidized bed hydrodynamics*. Iowa State University.

Fang, Z., & Bhandari, B. (2010). Encapsulation of polyphenols – a review. *Trends in Food Science & Technology*, *21*(10), 510–523.

Félix, G., Falk, V., & D'Ortona, U. (2002). Segregation of dry granular material in rotating drum: Experimental study of the flowing zone thickness. *Powder Technology*, *128*(2–3), 314–319.

Finnie, G. J., Kruyt, N. P., Ye, M., Zeilstra, C., & Kuipers, J. A. M. (2005). Longitudinal and transverse mixing in rotary kilns: A discrete element method approach. *Chemical Engineering Science*, *60*(15), 4083–4091.

Fisher, R. A. (1926). On the capillary forces in an ideal soil; correction of formulae given by W. B. Haines. *The Journal of Agricultural Science*, *16*(3), 492.

Freireich, B., Kumar, R., Ketterhagen, W., Su, K., Wassgren, C., & Zeitler, J. A. (2015). Comparisons of intra-tablet coating variability using DEM simulations, asymptotic limit models, and experiments. *Chemical Engineering Science*, *131*, 197–212.

Freireich, B., & Li, J. (2013). A renewal theory approach to understanding interparticle coating variability. *Powder Technology*, *249*, 330–338.

Geldart, D. (1973). Types of Gas Fhidization. *Powder Technology*, *7*, 285–292.

Girardi, M., Radl, S., & Sundaresan, S. (2016). Simulating wet gas – solid fl uidized beds using coarse-grid CFD-DEM. *Chemical Engineering Science*, *144*, 224–238.

Gonzalez, R.C. and R.E. Woods, Morphological Image Processing, in Digital Image Processing. 2008, Pearson Prentice Hall.p.p 627-688.

Gonzalez, R. C., Woods, R. E., & Eddins, S. L. (2010). Morphological Reconstruction. *MATLAB Digest*, 517–522.

Good, R. J. (1992). *Contact-Angle, Wetting, and Adhesion - a Critical-Review*. *Journal of Adhesion Science and Technology* (Vol. 6).

Green, J., An investigation into the mechanism of spray coating of powders and particles in tumbling drums, University of Sheffield, 2016.

Haack, D., & Koeberle, M. (2014). Hot Melt Coating for Controlling the Stability , Release Properties and Taste of Solid Oral Dosage. *TechnoPharm 4*, *4*(5), 258–263.

Hagers, J. J. (1997). Basic Technical Considerations for Application of Spray Nozzles to Chemical Processing Basics of Spray Nozzles, (November).

Hapgood, K. P., Litster, J. D., White, E. T., Mort, P. R., & Jones, D. G. (2004). Dimensionless spray flux in wet granulation: Monte-Carlo simulations and experimental validation. *Powder Technology*, *141*(1–2), 20–30.

He, Y., Peng, W., Wang, T., & Yan, S. (2014). DEM Study of Wet Cohesive Particles in the Presence of Liquid Bridges in a Gas Fluidized Bed. *Mathematical Problems in Engineering*, *2014*, 1–14.

Hede, P. D., Bach, P., & Jensen, A. D. (2008a). Two-fluid spray atomisation and pneumatic nozzles for fluid bed coating/agglomeration purposes: A review. *Chemical Engineering Science*, *63*(14), 3821–3842.

Hede, P. D., Bach, P., & Jensen, A. D. (2008b). Validation of the flux number as scaling parameter for top-spray fluidised bed systems. *Chemical Engineering Science*, *63*(3), 815–828.

Hede, P. D., Bach, P., & Jensen, A. D. (2009a). Batch top-spray fluid bed coating: Scale-up insight using dynamic heat- and mass-transfer modelling. *Chemical Engineering Science*, *64*(6), 1293–1317.

Hede, P. D., Bach, P., & Jensen, A. D. (2009b). Tackiness and the Tack Stokes Number. *Industrial and Engineering Chemistry Research*, *48*, 1914–1920.

Heinämäki, J., Ruotsalainen, M., Lehtola, V. M., Antikainen, O., & Yliruusi, J. (1997). Optimization of aqueous-based film coating of tablets performed by a side-vented pan-coating system. *Pharmaceutical Development and Technology*, *2*(4), 357–364.

Hemati, M., Cherif, R., Saleh, K., & Pont, V. (2003). Fluidized bed coating and granulation: influence of process-related variables and physicochemical properties on the growth kinetics. *Powder Technology*, *130*(1–3), 18–34.

Henein, H., Brimacombe, J. K., & Watkinson, A. P. (1983). Experimental study of transverse bed motion in rotary kilns. *Metallurgical Transactions B*, *14*(2), 191–205.

Hilton, J. E., Ying, D. Y., & Cleary, P. W. (2013). Modelling spray coating using a combined CFD–DEM and spherical harmonic formulation. *Chemical Engineering Science*, *99*, 141–160.

Ho, L., Müller, R., Römer, M., Gordon, K. C., Heinämäki, J., Kleinebudde, P., Zeitler, J. a. (2007). Analysis of sustained-release tablet film coats using terahertz pulsed imaging. *Journal of Controlled Release*, *119*(3), 253–261.

Hogg, R., Cahn, D. S., Healy, T. W., & Fuerstenau, D. W. (1966). Diffusional mixing in an ideal system. *Chemical Engineering Science*, *21*(11), 1025–1038.

Hoornahad, H., Koenders, E., & Breugel, K. van. (2015). Wettability of particles and its effect on liquid bridges in wet granular materials. *Journal of Silicate Based and Composite Materials*, *67*(4), 139–142.

Hsiau, S. S., & Yang, S. C. (2003). Numerical simulation of self-diffusion and mixing in a vibrated granular bed with the cohesive effect of liquid bridges. *Chemical Engineering Science*, *58*(2), 339–351.

Iveson, S. M., & Litster, J. D. (1998). Growth regime map for liquid-bound granules. *AIChE Journal*, *44*(Compendex), 1510–1518.

Jacquot, M., & Pernette, M. (2004). Spray coating and drying processes. In V. Nedovic & R. Willaert (Eds.), *Fundamentals of Cell immobili sation Biotechnology* (pp. 343–356). Kluwer Academic Publishers.

Jarray, A., Magnanimo, V., & Luding, S. (2018). Wet granular flow control through liquid induced cohesion. *Powder Technology*, (2017).

Kalbag, A., & Wassgren, C. (2009). Inter-tablet coating variability: Tablet residence time variability. *Chemical Engineering Science*, *64*(11), 2705–2717.

Kalbag, A., Wassgren, C., Sumana Penumetcha, S., & Pérez-Ramos, J. D. (2008). Inter-tablet coating variability: Residence times in a horizontal pan coater. *Chemical Engineering Science*, *63*(11), 2881–2894.

Kandela, B., Sheorey, U., Banerjee, A., & Bellare, J. (2010). Study of tablet-coating

parameters for a pan coater through video imaging and Monte Carlo simulation. *Powder Technology*, *204*(1), 103–112.

Kantak, A. A., Galvin, J. E., Wildemuth, D. J., & Davis, R. H. (2005). Low-velocity collisions of particles with a dry or wet wall. *Microgravity Science and Technology*, *17*(1), 18–25.

Kariuki, W. I. J., Freireich, B., Smith, R. M., Rhodes, M., & Hapgood, K. P. (2013). Distribution nucleation: Quantifying liquid distribution on the particle surface using the dimensionless particle coating number. *Chemical Engineering Science*, *92*, 134–145.

Karlsson, S., Rasmuson, A., Björn, I. N., & Schantz, S. (2011). Characterization and mathematical modelling of single fluidised particle coating. *Powder Technology*, *207*(1–3), 245–256.

Kennedy, J. P., & Niebergall, P. J. (1997). Preliminary Assessment of an Image Analysis Method for the Evaluation of Pharmaceutical Coatings. *Pharmaceutical Development and Technology*, *2*(3), 205–212.

Khakhar, D. V., McCarthy, J. J., Shinbrot, T., & Ottino, J. M. (1997). Transverse flow and mixing of granular materials in a rotating cylinder. *Physics of Fluids*, *9*(1), 31–43.

Khan, W. A., Asghar, U., & Shamshad, I. (2016). Effect of Initial Static Bed Height and Liquid Superficial Velocity on the Minimum Fluidization Velocity (Umf) and Pressure Drop for the Bed of Semolina Particles in Liquid-Solid Fluidization. *Journal of Chemical Engineering & Process Technology*, *7*(5), 5–8.

Khoufech, A., Benali, M., & Saleh, K. (2015). Influence of liquid formulation and impact conditions on the coating of hydrophobic surfaces. *Powder Technology*, *270*, 599–611.

Kleinbach, E., & Riede, T. (1995). Coating of solids. *Chemical Engineering and Processing: Process Intensification*, *34*(3), 329–337.

Komossa, H., Wirtz, S., Scherer, V., Herz, F., & Specht, E. (2014). Transversal bed motion in rotating drums using spherical particles: Comparison of experiments with

DEM simulations. *Powder Technology*, *264*, 96–104.

Kumar, R., & Wassgren, C. (2014). Inter-particle coating variability in a continuous coater. *Chemical Engineering Science*, *117*, 1–7.

Lazghab, M., Saleh, K., Pezron, I., Guigon, P., & Komunjer, L. (2005). Wettability assessment of finely divided solids. *Powder Technology*, *157*(1–3), 79–91.

Lee, M.-J., Seo, D.-Y., Lee, H.-E., Wang, I.-C., Kim, W.-S., Jeong, M.-Y., & Choi, G. J. (2011). In line NIR quantification of film thickness on pharmaceutical pellets during a fluid bed coating process. *International Journal of Pharmaceutics*, *403*(1), 66–72.

Li, J., Freireich, B. J., Wassgren, C. R., & Litster, J. D. (2013). Experimental validation of a 2-D population balance model for spray coating processes. *Chemical Engineering Science*, *95*, 360–365.

Li, J., Wassgren, C., & Litster, J. D. (2013). Multi-scale modeling of a spray coating process in a paddle mixer/coater: the effect of particle size distribution on particle segregation and coating uniformity. *Chemical Engineering Science*, *95*, 203–210.

Lian, G., Thornton, C., & Adams, M. J. (1993). A theoretical study of the liquid bridge forces be- tween two rigid spherical bodies. *Journal of Colloid and Interface Science*, *161*, 138–147.

Liao, C. C. (2018). A study of the effect of liquid viscosity on density-driven wet granular segregation in a rotating drum. *Powder Technology*, *325*, 632–638.

Lim, C. N., Gilbertson, M. A., & Harrison, A. J. L. (2007). Bubble distribution and behaviour in bubbling fluidised beds. *Chemical Engineering Science*, *62*(1–2), 56–69.

Liu, P. Y., Yang, R. Y., & Yu, A. B. (2013a). DEM study of the transverse mixing of wet particles in rotating drums. *Chemical Engineering Science*, *86*, 99–107.

Liu, P. Y., Yang, R. Y., & Yu, A. B. (2013b). Self-diffusion of wet particles in rotating drums. *Physics of Fluids*, *63301*(2013).

Liu, X., Hu, Z., Wu, W., Zhan, J., Herz, F., & Specht, E. (2017). DEM study on the surface mixing and whole mixing of granular materials in rotary drums. *Powder Technology*, *315*, 438–444.

Malvern 2007, Mastersizer 2000 user manual Malvern Instruments Ltd. Malvern.

Maronga, S. (1998). *On the Optimization of the Fluidized Bed Particulate Coating Process*. royal institute of technology.

Marston, J. O., Thoroddsen, S. T., Ng, W. K., & Tan, R. B. H. (2010). Experimental study of liquid drop impact onto a powder surface. *Powder Technology*, *203*(2), 223–236.

Maurer, L., & Leuenberger, H. (2009). Terahertz pulsed imaging and near infrared imaging to monitor the coating process of pharmaceutical tablets. *International Journal of Pharmaceutics*, *370*(1–2), 8–16.

Mazzone, D. N., Tardos, G. I., & Pfeffer, R. (1987). The behavior of liquid bridges between two relatively moving particles. *Powder Technology*, *51*(1), 71–83.

McCarthy, J. J. (2003). Micro-modeling of cohesive mixing processes. *Powder Technology*, *138*(1), 63–67.

McLaughlin, L. J., & Rhodes, M. J. (2001). Prediction of fluidized bed behaviour in the presence of liquid bridges. *Powder Technology*, *114*(1–3), 213–223.

Mellmann, J. (2001). The transverse motion of solids in rotating cylinders—forms of motion and transition behavior. *Powder Technology*, *118*(3), 251–270.

Mitra, S., Sathe, M. J., Doroodchi, E., Utikar, R., Shah, M. K., Pareek, V., … Evans, G. M. (2013). Droplet impact dynamics on a spherical particle. *Chemical Engineering Science*, *100*, 105–119.

Mohan, B., Kloss, C., Khinast, J., & Radl, S. (2014). Regimes of liquid transport through sheared beds of inertial smooth particles. *Powder Technology*, *264*, 377–395.

Mozina, M., Tomazevic, D., Leben, S., Pernus, F., & Likar, B. (2010). Digital imaging as a process analytical technology tool for fluid-bed pellet coating process. *European Journal of Pharmaceutical Sciences : Official Journal of the European Federation for Pharmaceutical Sciences*, *41*(1), 156–62.

Muguruma, Y., Tanaka, T., & Tsuji, Y. (2000). Numerical simulation of particulate flow with liquid bridge between particles (simulation of centrifugal tumbling granulator). *Powder Technology*, *109*(1–3), 49–57.

Nafsun, A. I., Herz, F., Specht, E., Komossa, H., Wirtz, S., Scherer, V., & Liu, X. (2017). Thermal bed mixing in rotary drums for different operational parameters. *Chemical Engineering Science*, *160*, 346–353.

Nase, S. T., Vargas, W. L., Abatan, A. A., & McCarthy, J. J. (2001). Discrete characterization tools for cohesive granular material. *Powder Technology*, *116*(2–3), 214–223.

Naz, M. Y., & Sulaiman, S. A. (2016). Slow release coating remedy for nitrogen loss from conventional urea: A review. *Journal of Controlled Release*, *225*, 109–120.

Naz, M. Y., Sulaiman, S. A., Ariwahjoedi, B., Zilati, K., & Shaari, K. (2014). Characterization of Modified Tapioca Starch Solutions and Their Sprays for High Temperature Coating Applications. *The Scientific World Jounal*, *2014*, 10 pages.

Nienow, A. W. (1995). Fluidised Bed Granulation and Coating: Applications to Materials, Agriculture and Biotechnology. *Chemical Engineering Communications*, *139*(1), 233–253.

Niranjan, K. (1993). Fluidization and Its Applications to Food Processing. *Food Structure*, *12*(2), 199–215.

Norouzi, H. R., Zarghami, R., & Mostoufi, N. (2015). Insights into the granular flow in rotating drums. *Chemical Engineering Research and Design*, *102*, 12–25.

Pacheco, C., Piña, J., & Saleh, K. (2016). Molten materials' atomization for particle coating: prediction of mean droplet size for two-fluid nozzles. *Atomization and Sprays*, *26*(10), 1031–1050.

Palamanit, A., Prachayawarakorn, S., Tungtrakul, P., & Soponronnarit, S. (2016). Performance Evaluation of Top-Spray Fluidized Bed Coating for Healthy Coated Rice Production. *Food and Bioprocess Technology*, 1–10.

Palamanit, A., Soponronnarit, S., Prachayawarakorn, S., & Tungtrakul, P. (2013). Effects of inlet air temperature and spray rate of coating solution on quality attributes of turmeric extract coated rice using top-spray fluidized bed coating technique. *Journal of Food Engineering*, *114*(1), 132–138.

Panda, R. C., Zank, J., & Martin, H. (2001). Modeling the droplet deposition behavior on

a single particle in fluidized bed spray granulation process. *Powder Technology*, *115*(1), 51–57.

Pandey, P., Katakdaunde, M., & Turton, R. (2006). Modeling weight variability in a pan coating process using Monte Carlo simulations. *AAPS PharmSciTech*, *7*(4), 83.

Pandey, P., Turton, R., Joshi, N., Hammerman, E., & Ergun, J. (2006). Scale-up of a pan-coating process. *AAPS PharmSciTech*, *7*(4), 102.

Parker, D. J., Dijkstra, A. E., Martin, T. W., & Seville, J. P. K. (1997). Positron emission particle tracking studies of spherical particle motion in rotating drums. *Chemical Engineering Science*, *52*(13), 2011–2022.

Patnaik, K. S. K. R., & Sriharsha, K. (2010). Fluidization Principles for Three-Phase Fluidized Bed Bio-Reactor. *International Journal of Chemical Engineering and Applications*, *1*(3), 251–255.

Perfetti, G., Alphazan, T., van Hee, P., Wildeboer, W. J., & Meesters, G. M. H. (2011). Relation between surface roughness of free films and process parameters in spray coating. *European Journal of Pharmaceutical Sciences*, *42*(3), 262–272.

Perfetti, G., Casteele, E. Van de, Rieger, B., Wildeboer, W. J., & Meesters, G. M. H. (2010). X-ray micro tomography and image analysis as complementary methods for morphological characterization and coating thickness measurement of coated particles. *Advanced Powder Technology*, *21*(6), 663–675.

Pont, V., Saleh, K., Steinmetz, D., & Hémati, M. (2001). Influence of the physicochemical properties on the growth of solid particles by granulation in fluidized bed. *Powder Technology*, *120*(1–2), 97–104.

Rhodes, M. J. (2008). *Introduction to Particle Technology* (2nd ed.). Chichester: John Wiley.

Ribeiro, C., Vicente, A. A., Teixeira, J. A., & Miranda, C. (2007). Optimization of edible coating composition to retard strawberry fruit senescence. *Postharvest Biology and Technology*, *44*(1), 63–70.

Romero-Torres, S., Pérez-Ramos, J. D., Morris, K. R., & Grant, E. R. (2005). Raman spectroscopic measurement of tablet-to-tablet coating variability. *Journal of*

Pharmaceutical and Biomedical Analysis, *38*(2), 270–274.

Romero-Torres, S., Pérez-Ramos, J. D., Morris, K. R., & Grant, E. R. (2006). Raman spectroscopy for tablet coating thickness quantification and coating characterization in the presence of strong fluorescent interference. *Journal of Pharmaceutical and Biomedical Analysis*, *41*(3), 811–819.

Sahni, E., & Chaudhuri, B. (2011). Experiments and numerical modeling to estimate the coating variability in a pan coater. *International Journal of Pharmaceutics*, *418*(2), 286–296.

Sahni, E., & Chaudhuri, B. (2012). Experimental and modeling approaches in characterizing coating uniformity in a pan coater: A literature review. *Pharmaceutical Development and Technology*, *17*(2), 134–147.

Sahni, E., Yau, R., & Chaudhuri, B. (2011). Understanding granular mixing to enhance coating performance in a pan coater: Experiments and simulations. *Powder Technology*, *205*(1–3), 231–241.

Saleh, K., & Guigon, P. (2007a). Coating and encapsulation processes in powder technology. In A. Salman, M. Hounslow, & J. Seville (Eds.), *Granulation* (First, Vol. 11, pp. 323–375). Amsterdam, Netherlands: Elsevier B.V.

Saleh, K., & Guigon, P. (2007b). Influence of wetting parameters on particle growth in fluidized-bed coating and agglomeration processes. *Particle and Particle Systems Characterization*, *24*, 136–143.

Sanaei-Moghadam, M., Jahangiri, M., & Hormozi, F. (2017). An Experimental Study on the Spray Characteristics of Pressure Nozzle in a Fluid Bed Granulation. *Particulate Science and Technology*, *6351*(June), 1–8.

Sandadi, S., Pandey, P., & Turton, R. (2004). In situ, near real-time acquisition of particle motion in rotating pan coating equipment using imaging techniques. *Chemical Engineering Science*, *59*(24), 5807–5817.

Santomaso, A. C., Ding, Y. L., Lickiss, J. R., & York, D. W. (2003). Investigation of the granular behaviour in a rotating drum operated over a wide range of rotational speed. *Chemical Engineering Research and Design*, *81*(8), 936–945.

Santos, D. A., Dadalto, F. O., Scatena, R., Duarte, C. R., & Barrozo, M. A. S. (2014). Chemical Engineering Research and Design A hydrodynamic analysis of a rotating drum operating in the rolling regime, *4*(August), 204–212.

Senadeera, W., Wijesinghe, B., Young, G., & Bhandari, B. (2006). Fluidization characteristics of moist food particles. International Journal of Food Engineering, 2(1), 1-13.

Seville, J. P. K., Willett, C. D., & Knight, P. C. (2000). Interparticle forces in fluidisation: A review. *Powder Technology*, *113*(3), 261–268.

Sheritt, R. G., Chaouki, J., Mehrotra, A. K., & Behie, L. A. (2003). Axial dispersion in the three-dimensional mixing of particles in a rotating drum reactor. *Chemical Engineering Science*, *58*(2), 401–415.

Shi, D., & McCarthy, J. J. (2008). Numerical simulation of liquid transfer between particles. *Powder Technology*, *184*(1), 64–75.

Šikalo, Š., Marengo, M., Tropea, C., & Ganić, E. N. (2002). Analysis of impact of droplets on horizontal surfaces. *Experimental Thermal and Fluid Science*, *25*(7), 503–510.

Simons, S. J. ., & Fairbrother, R. . (2000). Direct observations of liquid binder–particle interactions: the role of wetting behaviour in agglomerate growth. *Powder Technology*, *110*(1–2), 44–58.

Simons, S. J. R., Seville, J. P. K., & Adams, M. J. (1994). An analysis of the rupture energy of pendular liquid bridges. *Chemical Engineering Science*, *49*(14), 2331–2339.

Smith, G. W., Macleod, G. S., & Fell, J. T. (2003). Mixing efficiency in side-vented coating equipment. *AAPS PharmSciTech*, *4*(3), E37.

Smith, P. G. (2007). *Applications of Fluidization to Food Processing. Applications of Fluidization to Food Processing.*

Smith, P. G., & Nienow, A. W. (1983). Particle growth mechanisms in fluidised bed granulation—I: The effect of process variables. *Chemical Engineering Science*, *38*(8), 1223–1231.

Sondej, F., Bück, A., Koslowsky, K., Bachmann, P., Jacob, M., & Tsotsas, E. (2015). Investigation of coating layer morphology by micro-computed X-ray tomography. *Powder Technology*, *273*, 165–175.

Sondej, F., Bück, A., & Tsotsas, E. (2016). Comparative analysis of the coating thickness on single particles using X-ray micro-computed tomography and confocal laser-scanning microscopy. *Powder Technology*, *287*, 330–340.

Song, C., Liu, D., Ma, J., & Chen, X. (2017). CFD-DEM simulation of flow pattern and particle velocity in a fluidized bed with wet particles. *Powder Technology*, *314*, 346–354.

Song, Y., & Turton, R. (2007). Study of the effect of liquid bridges on the dynamic behavior of two colliding tablets using DEM. *Powder Technology*, *178*, 99–108.

Soni, R. K., Mohanty, R., Mohanty, S., & Mishra, B. K. (2016). Numerical analysis of mixing of particles in drum mixers using DEM. *Advanced Powder Technology*, *27*(2), 531–540.

Srivastava, S., & Mishra, G. (2010). Fluid Bed Technology : Overview and Parameters for Process Selection. *International Journal of Pharmaceutical Sciences and Drug Research*, *2*(4), 236–246.

Ström, D., Karlsson, S., Folestad, S., Niklasson Björn, I., Laurell, T., Nilsson, J., & Rasmuson, A. (2005). A new device for coating single particles under controlled conditions. *Chemical Engineering Science*, *60*(16), 4647–4653.

Sudsakorn, K., & Turton, R. (2000). Nonuniformity of particle coating on a size distribution of particles in a fluidized bed coater. *Powder Technology*, *110*, 37–43.

Suzzi, D., Radl, S., & Khinast, J. G. (2010). Local analysis of the tablet coating process: Impact of operation conditions on film quality. *Chemical Engineering Science*, *65*(21), 5699–5715.

Tafreshi, Z. M., Kirpalani, D., Bennett, A., & McCracken, T. W. (2002). Improving the efficiency of fluid cokers by altering two-phase feed characteristics. *Powder Technology*, *125*(2–3), 234–241. https://doi.org/10.1016/S0032-5910(01)00511-3

Tatar, F., Tunç, M. T., Dervisoglu, M., Cekmecelioglu, D., & Kahyaoglu, T. (2014).

Evaluation of hemicellulose as a coating material with gum arabic for food microencapsulation. *Food Research International*, *57*, 168–175.

Teunou, E., & Poncelet, D. (2002). Batch and continuous fluid bed coating – review and state of the art. *Journal of Food Engineering*, *53*(4), 325–340.

Tobiska, S., & Kleinebudde, P. (2001). A simple method for evaluating the mixing efficiency of a new type of pan coater. *International Journal of Pharmaceutics*, *224*(1–2), 141–149.

Tobiska, S., & Kleinebudde, P. (2003). Coating uniformity and coating efficiency in a Bohle Lab-Coaterusing oval tablets. *European Journal of Pharmaceutics and Biopharmaceutics*, *56*(1), 3–9.

Toschkoff, G., & Khinast, J. G. (2013). Mathematical modeling of the coating process. *International Journal of Pharmaceutics*, *457*(2), 407–22.

Turchiuli, C. (2013). Fluidization in food powder production. In M. Z. and P. S. B. Bhandari, N. Bansal (Ed.), *Handbook of Food Powders* (First, pp. 178–199). Cambridge, UK: Woodhead Publishing Limited.

Turton, R. (2008). Challenges in the modeling and prediction of coating of pharmaceutical dosage forms. *Powder Technology*, *181*(2), 186–194.

Turton, R., & Cheng, X. X. (2005). The scale-up of spray coating processes for granular solids and tablets. *Powder Technology*, *150*, 78–85.

Valizadeh, H., Nokhodchi, A., Qarakhani, N., Zakeri-Milani, P., Azarmi, S., Hassanzadeh, D., & Löbenberg, R. (2004). Physicochemical Characterization of Solid Dispersions of Indomethacin with PEG 6000, Myrj 52, Lactose, Sorbitol, Dextrin, and Eudragit® E100. *Drug Development and Industrial Pharmacy*, *30*(3), 303–317.

Van Puyvelde, D. R., Young, B. R., Wilson, M. a., & Schmidt, S. J. (1999). Experimental determination of transverse mixing kinetics in a rolling drum by image analysis. *Powder Technology*, *106*(3), 183–191.

Vanderroost, M., Ronsse, F., Dewettinck, K., & Pieters, J. (2011). Modelling coating quality in fluidised bed coating: Spray sub-model. *Journal of Food Engineering*,

106(3), 220–227.

Vengateson, U., & Mohan, R. (2016). Experimental and modeling study of fluidized bed granulation: Effect of binder flow rate and fluidizing air velocity. *Resource-Efficient Technologies*, *2*, S124–S135.

Villa, M. P., Bertin, D. E., Cotabarren, I. M., Pina, J., & Bucala, V. (2016a). Fluidized-bed melt granulation: Coating and agglomeration kinetics and growth regime prediction. *Powder Technology*, *300*, 61–72.

Villa, M. P., Bertin, D. E., Cotabarren, I. M., Pina, P., & Bucala, V. (2016b). Fluidized-bed melt granulation: Coating and agglomeration kinetics and growth regime prediction. *Powder Technology*, *300*, 61–72.

Washino, K., Chan, E. L., Matsumoto, T., Hashino, S., Tsuji, T., & Tanaka, T. (2017). Normal viscous force of pendular liquid bridge between two relatively moving particles. *Journal of Colloid and Interface Science*, *494*, 255–265.

Washino, K., Miyazaki, K., Tsuji, T., & Tanaka, T. (2016). A New Contact Liquid Dispersion Model for Discrete Particle Simulation. *Chemical Engineering Research and Design*, *0*, 2–9.

Werner, S. R. L., Jones, J. R., Paterson, A. H. J., Archer, R. H., & Pearce, D. L. (2007a). Air-suspension coating in the food industry: Part II — micro-level process approach. *Powder Technology*, *171*(1), 34–45.

Werner, S. R. L., Jones, J. R., Paterson, A. H. J., Archer, R. H., & Pearce, D. L. (2007b). Air-suspension particle coating in the food industry: Part I — state of the art. *Powder Technology*, *171*(1), 25–33.

Werner, S. R. L., Jones, J. R., Paterson, A. H. J., Archer, R. H., & Pearce, D. L. (2007c). Droplet impact and spreading: Droplet formulation effects. *Chemical Engineering Science*, *62*(9), 2336–2345.

Wills, B. ., & Finch, J. . (2016). Particle Size Analysis. In B. . Wills & J. . Finch (Eds.), *Will's Mineral Processing Technology* (Eighth Edi, pp. 91–107). Elsevier.

Woodward, R. P. (2008). Surface Tension Measurements Using the Drop Shape Method. *First Ten Angstroms Inc Technical Information*, 1–6.

Wright, P. C., & Raper, J. A. (1998). Examination of dispersed liquid-phase three-phase fluidized beds Part 1 . Non-porous , uniform particle systems. *Powder Technology*, *97*, 208–226.

Yan Liu, X., & Specht, E. (2010). Predicting the fraction of the mixing zone of a rolling bed in rotary kilns. *Chemical Engineering Science*, *65*(10), 3059–3063.

Yang, C., & Leong, K. (2002). Influences of substrate wettability and liquid viscosity on isothermal spreading of liquid droplets on solid surfaces. *Experiments in Fluids*, *33*, 728–731.

Yang, R. Y., Yu, A. B., McElroy, L., & Bao, J. (2008). Numerical simulation of particle dynamics in different flow regimes in a rotating drum. *Powder Technology*, *188*(2), 170–177.

Yarin, a. L. (2006). DROP IMPACT DYNAMICS: Splashing, Spreading, Receding, Bouncing.... *Annual Review of Fluid Mechanics*, *38*(1), 159–192.

Zhao, T., & Jiang, L. (2018). Colloids and Surfaces B : Biointerfaces Contact angle measurement of natural materials. *Colloids and Surfaces B: Biointerfaces*, *161*, 324–330.

Zheng, C., Sun, D.-W., & Zheng, L. (2006). Recent developments and applications of image features for food quality evaluation and inspection – a review. *Trends in Food Science & Technology*, *17*(12), 642–655.

Zhou, Y., Shi, Q., Huang, Z., Wang, J., & Yang, Y. (2017). Particle agglomeration and control of gas-solid fluidized bed reactor with liquid bridge and solid bridge coupling actions. *Chemical Engineering Journal*, *330*, 840–851.

Zhou, Y., Shi, Q., Huang, Z., Wang, J., Yang, Y., Liao, Z., & Yang, J. (2013). Effects of interparticle forces on fluidization characteristics in liquid-containing and high-temperature fluidized beds. *Industrial and Engineering Chemistry Research*, *52*(47), 16666–16674.

Figure Permission Acknowledgements

The following figures have been republished by kind permission:

11 Appendix

11.1 Appendix A

A1. Particle Size Data

In this study, alumina beads were selected as a model material for each of the experimental works. The size distribution of the materials was determined using two techniques; sieving and laser diffraction. Table A.1 gives the raw particle size data for sieving analysis, while Table A.2 gives the raw data for laser diffraction analysis.

Sieve Method and Calculation

Procedure

First, the mass of the sample used was recorded. The sieves were then stacked in order from smallest to largest, starting at the bottom, with the pan below the smallest sieve. Then, the particles were poured into the top sieve. Before starting the sieve shaker, it was ensured that the sieve stack was held firmly in the shaker assembly. Finally, the sieve shaker was set to vibrate for 3 minutes.

Table A1. **Particle size data for alumina beads using sieve analysis**

Sieve size (µm)	Sieve interval (µm)	Sieve mass (g)	Sieve + sample retained mass (g)	Mass retained on sieve (g)	Frequency
0	300	348.63	348.66	0.03	0
600	655	288.19	288.35	0.16	0.003672167
710	780	334.8	336.4	1.6	0.028852743
850	925	349.48	363.02	13.54	0.22788858
1000	1090	301.55	324.23	22.68	0.31810149
1180	1290	358.65	360.25	1.6	0.01836084

A 1.1. Laser Diffraction Method

Table A.2   Particle size data for alumina beads using laser diffraction

Lower Size (µm)	Upper Size (µm)	In Size Range %
0.01	0.0114	0
0.0114	0.0129	0
0.0129	0.0147	0
0.0147	0.0167	0
0.0167	0.0189	0
0.0189	0.0215	0
0.0215	0.0244	0
0.0244	0.0278	0
0.0278	0.0315	0
0.0315	0.0358	0
0.0358	0.0407	0
0.0407	0.0463	0
0.0463	0.0526	0
0.0526	0.0597	0
0.0597	0.0679	0
0.0679	0.0771	0
0.0771	0.0876	0
0.0876	0.0995	0
0.0995	0.113	0
0.113	0.128	0
0.128	0.146	0
0.146	0.166	0
0.166	0.188	0
0.188	0.214	0
0.214	0.243	0
0.243	0.276	0
0.276	0.314	0
0.314	0.357	0
0.357	0.405	0
0.405	0.46	0
0.46	0.523	0
0.523	0.594	0
0.594	0.675	0
0.675	0.767	0
0.767	0.872	0
0.872	0.991	0
0.991	1.13	0
1.13	1.28	0

1.28	1.45	0
1.45	1.65	0
1.65	1.88	0
1.88	2.13	0
2.13	2.42	0
2.42	2.75	0
2.75	3.12	0
3.12	3.55	0
3.55	4.03	0
4.03	4.58	0
4.58	5.21	0
5.21	5.92	0
5.92	6.72	0
6.72	7.64	0
7.64	8.68	0
8.68	9.86	0
9.86	11.2	0
11.2	12.7	0
12.7	14.5	0
14.5	16.4	0
16.4	18.7	0
18.7	21.2	0
21.2	24.1	0
24.1	27.4	0
27.4	31.1	0
31.1	35.3	0
35.3	40.1	0
40.1	45.6	0
45.6	51.8	0
51.8	58.9	0
58.9	66.9	0
66.9	76	0
76	86.4	0
86.4	98.1	0
98.1	111	0
111	127	0
127	144	0
144	163	0
163	186	0
186	211	0
211	240	0
240	272	0

272	310	0
310	352	0
352	400	0
400	454	0
454	516	0
516	586	0
586	666	0
666	756	0.0005
756	859	0.0351
859	976	0.3112
976	1110	0.4747
1110	1260	0.1676
1260	1430	0.0104
1430	1630	0.0004
1630	1850	0
1850	2100	0
2100	2390	0
2390	2710	0

A2. Preparation of Coating Solutions

To prepare 50% PEG solutions (wt/wt) and 5% HPMC solutions (wt/wt), a 1 % dye solution was first prepared by weighing out 10 g of acid red powder. Then, 990 g distilled water was weighed out using a 1 L glass container. Whilst the distilled water was stirred on the magnetic stirrer, the acid red powder added until all the dye powder was completely dissolved in the solution.

This 1% dyed solution then was used to prepare 50% wt/wt dyed PEG solution and 5% HPMC solutions (wt/wt). For the PEG solutions 50 g of 1% dyed solution was weighed and stirred on the magnetic stirrer. While it was stirring, 50 g of the PEG was added until it was completely dissolved in the solution. A similar procedure was used to prepare 5% HPMC solutions (wt/wt), where 95 g of 1% dyed solution was weighed in a beaker, and approximately half of it was poured into a 100 mL bottle. This solution was then stirred on the magnetic stirrer and heated up to 80 °C. When the solution reached 80 °C, the heating was stopped. Then 5 g of HPMC powder was added slowly into the warm dyed solution while stirring. When the powder had nearly dissolved, the remaining dyed solution was added and stirred until the powder had completely dissolved. Once dissolved, the solution was de-foamed at room temperature before use.

11.2 Appendix B

B1. LabVIEW software

This section gives and its basic image processing functions. LabVIEW was initially developed for enabling easy interfacing between PCs and external instruments but has now expanded into a complete programming environment.

- **LabVIEW programming environment**

LabVIEW graphical programs are called Virtual Instruments (VI) and consist of two major components which include a Front Panel (FP) and a Block Diagram (BD):

- **Front panel (FP)**

The FP provides the user interface of a program like knobs, push buttons, graphs and many other controls (inputs) and indicators (outputs). Controls simulate instrument input devices and supply data to the BD of the VI whereas indicators simulate instrument output devices and display data generated from the BD.

- **Block diagram (BD)**

The BD is the VI's source code constructed in G and the actual executable program. FP objects appear as terminals on the block diagram and the terminals reflect the changes made to their corresponding FP objects and vice versa. Whenever a lower level VI is located in the BD of another VI, it is called sub-VI, and any VI or sub-VI can be run by itself. Wires establish the flow of data in a BD and structures are used to control the flow of a program such as repetitions or conditional executions. Figure B.1 shows an example of a typical FP and its BD in LabVIEW.
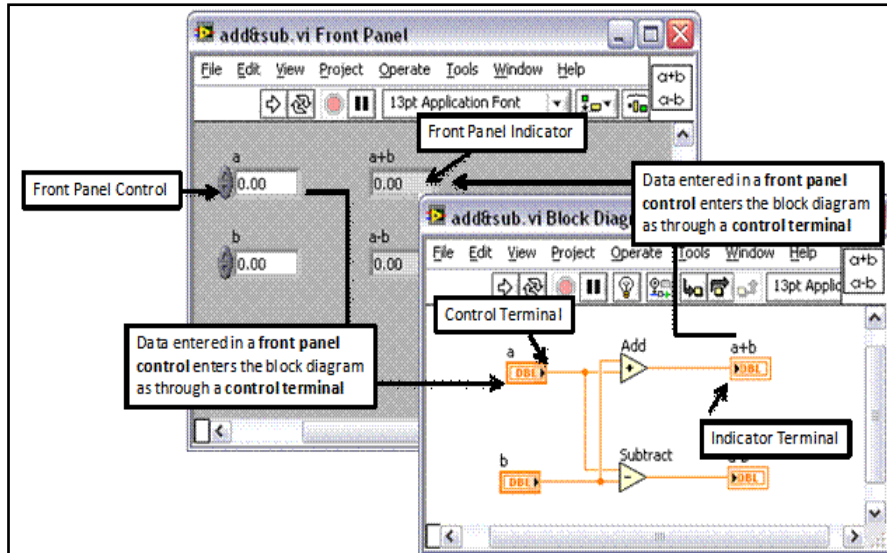
Figure B1. Typical front panel and its block diagram (National Instruments, 2015)

B2. Validating the image analysis system using coated materials from P&G.

The details of coated materials and previous experimental works which have been conducted at P&G are explained below.

- **Materials**

Coated Zirblast ceramic beads (Saint-Gobain ZirPro, France) were used as supplied by P&G. Each particle of Zirblast, with size range ca. 600 µm, had been coated with 33 % (wt/wt) of Polyethylene glycol (PEG) solution dyed with 0.3% (wt/wt) Acid Blue 80 (Sigma-Aldrich, UK). The samples had been coated in a tumbling drum and a sample taken at different times in the range from 0 – 15 seconds.

Figure B2: Uncoated Zirblast particles

- **Coating evolution of 33% PEG solution**
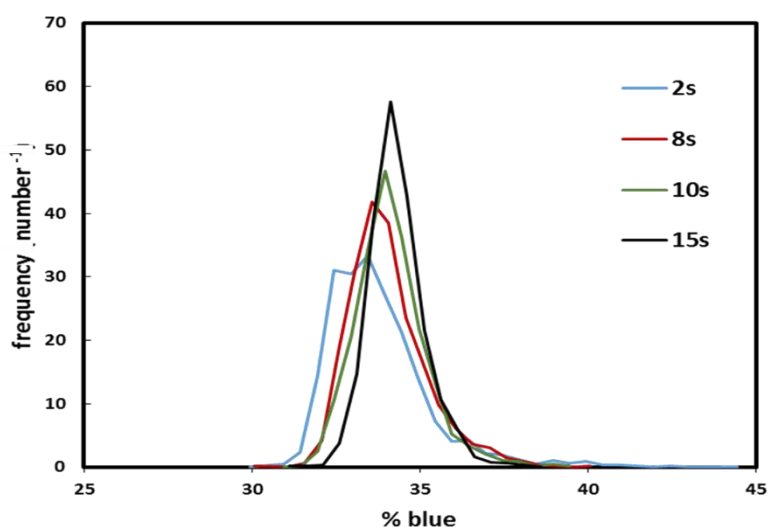
Figure B3: Coating evolution of Zirblast coated with 33% PEG solution

Analysed results for coating evolution of dyed blue coated Zirblast ceramic beads using developed LabVIEW software are shown in Figure B3, where the percentage blue is plotted as a function of frequency. This software sums the values for each pixel in a particle and returns the total value for each colour in a particle. Analytically, for perfect white particle or uncoated Zirblast, it will have 33.3% blue, 33.3% red and 33.3% green fraction whereas particles with blue dye will have a higher % blue value. From Figure B3, it can be observed that an increase in tumbling time (2-15s) produced a slightly higher percentage of blue dye and the distributions became sharper and narrower. This indicates a lower degree of coating variation and, therefore, more uniform inter-particle coating as the tumbling time is increased.
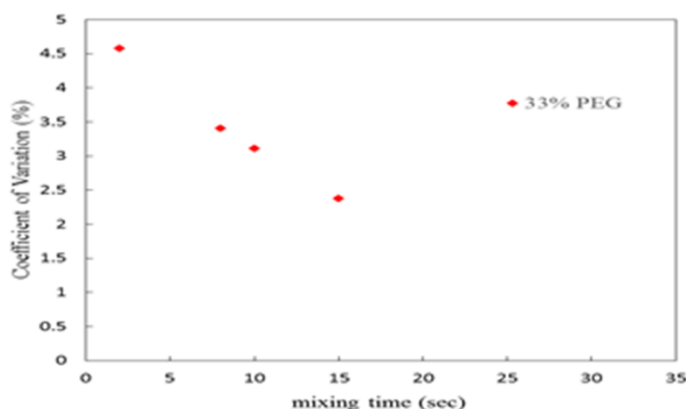
Figure B4: Coefficient of variation as a function of mixing time

274

Table B1: Images of coated Zirblast as a function of time

Time	Labelled images of Zirblast coated with 33% PEG
2 s	
8 s	
10 s	
15 s	
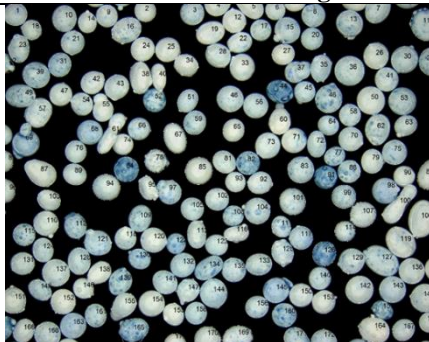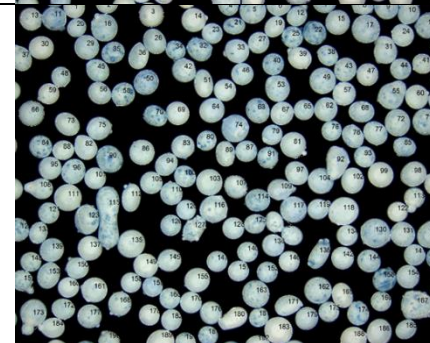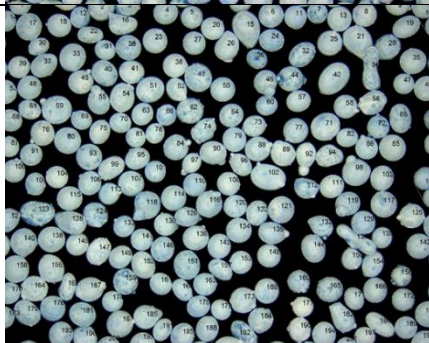
Figure B4 shows the coefficient of variation (C_oV) plotted as a function of tumbling time. The results show that the variability decreases with the mixing time. The images shown in Table B1 confirm this trend. The results obtained using coated Zirblast particles agrees well with previous experiments carried out in P&G and this suggests that the current new development imaging system and software are promising for characterization technique to measure the coating variability.

11.3 Appendix C

C1. Coating evolution as a function of mixing time for all data sets with different PEG solution viscosities:

1. **PEG 4000 MW (137 mPa.s):**
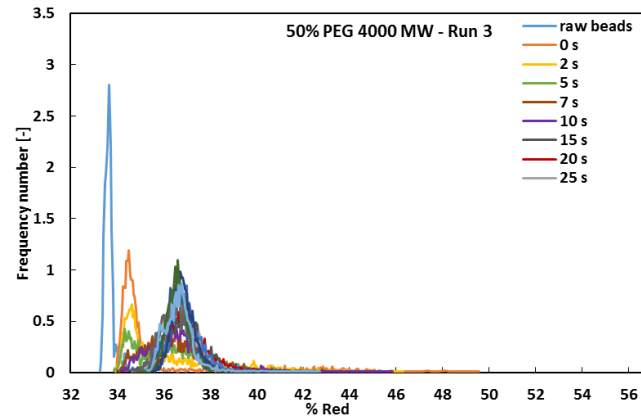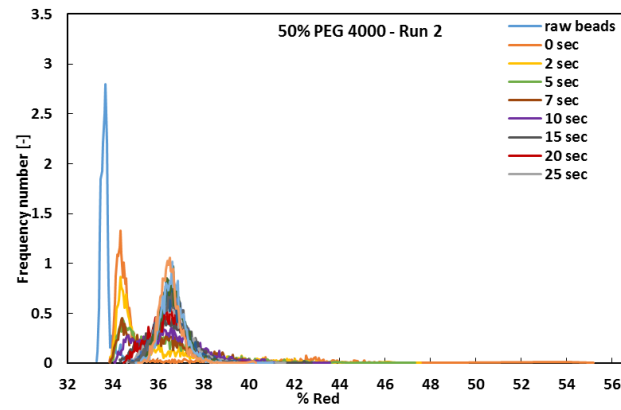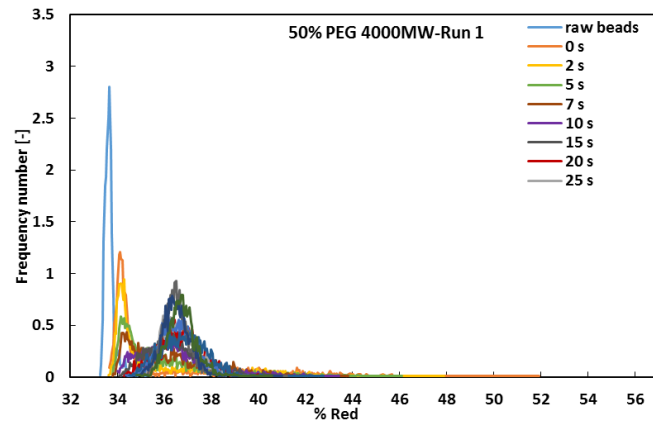
2. PEG 20000 MW (3115 mPa.s)
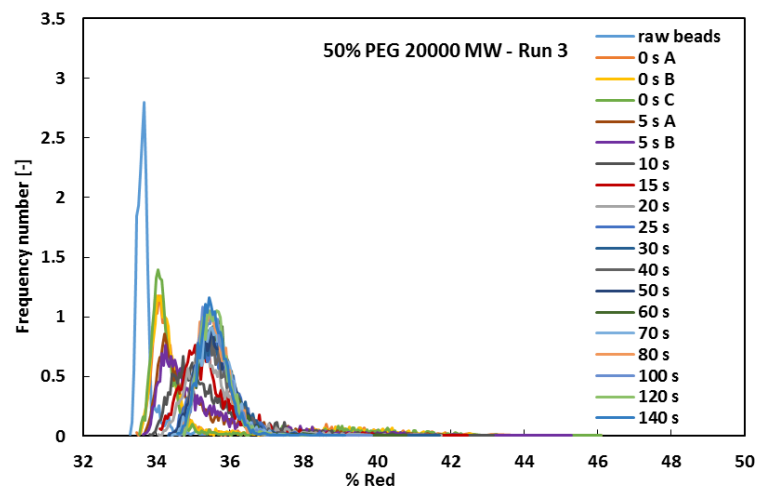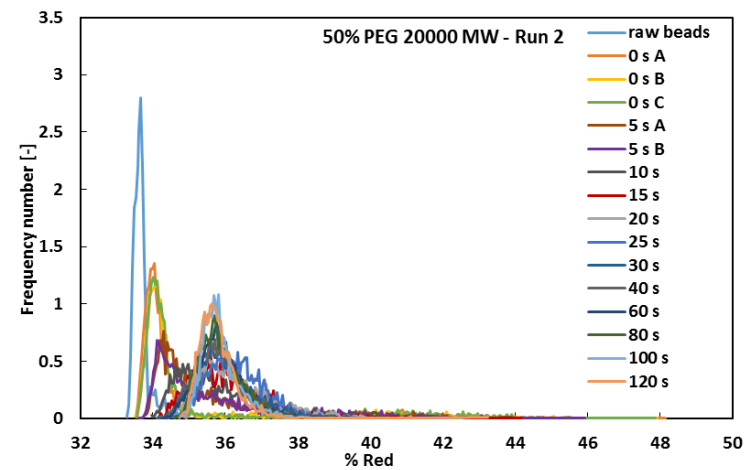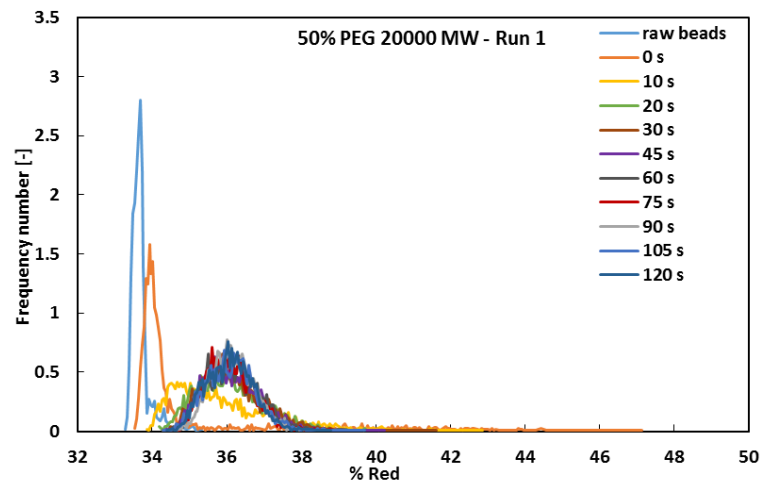
3. PEG 35000 MW (15489 mPa.s)
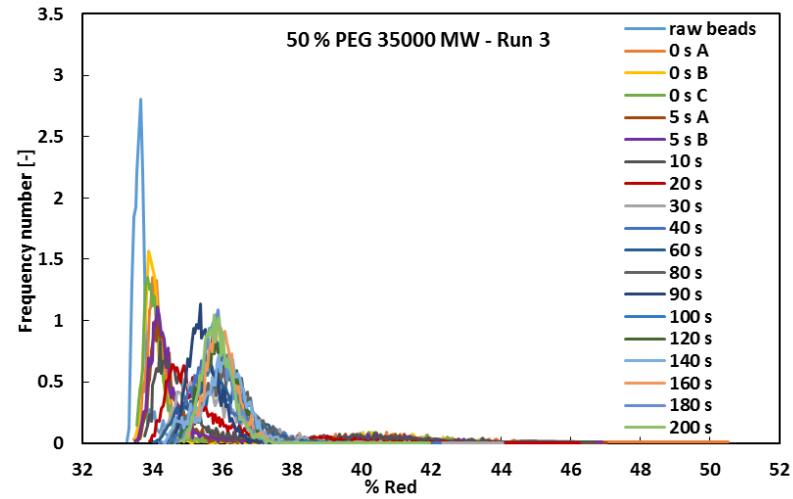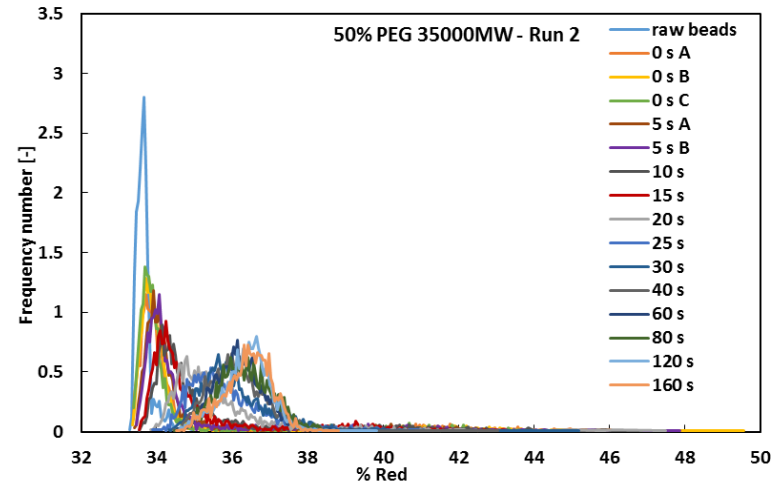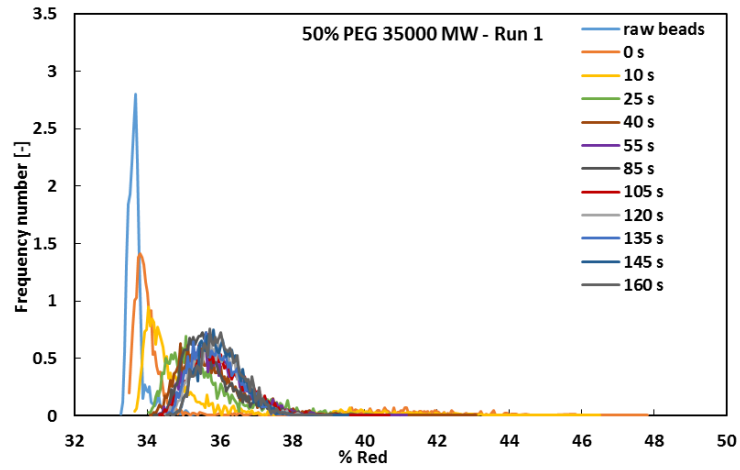
C2. Coating evolution as a function of mixing time for all data sets with different tumbling regimes:

1. PEG 4000 MW (137 mPa.s)
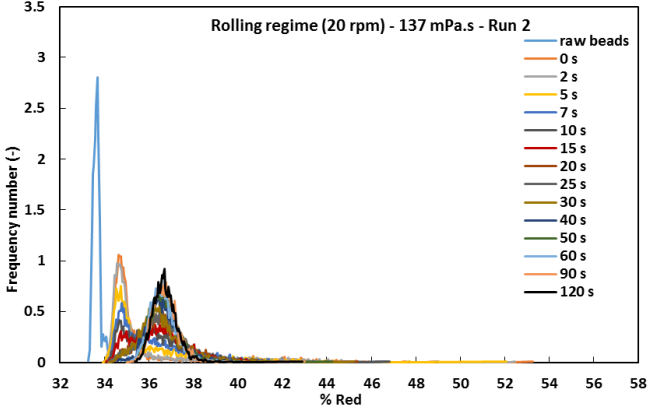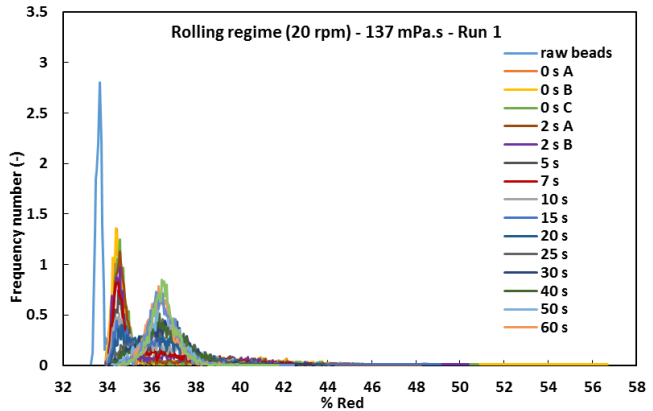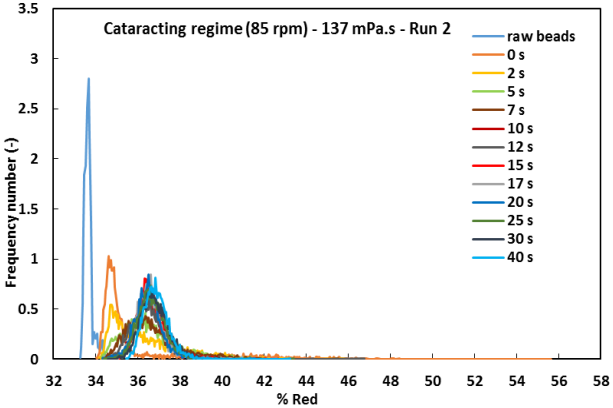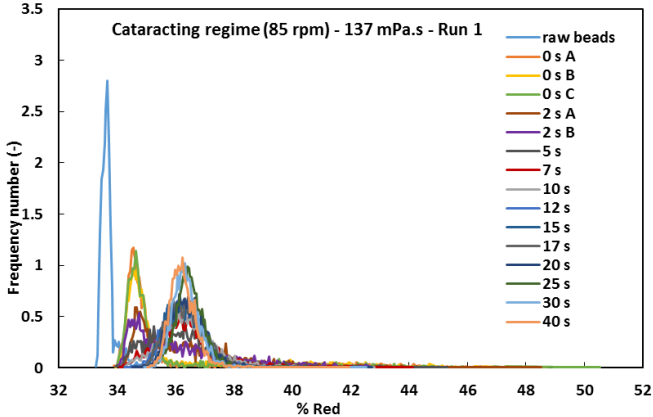
2. PEG 35000 MW (15489 mPa.s)

281
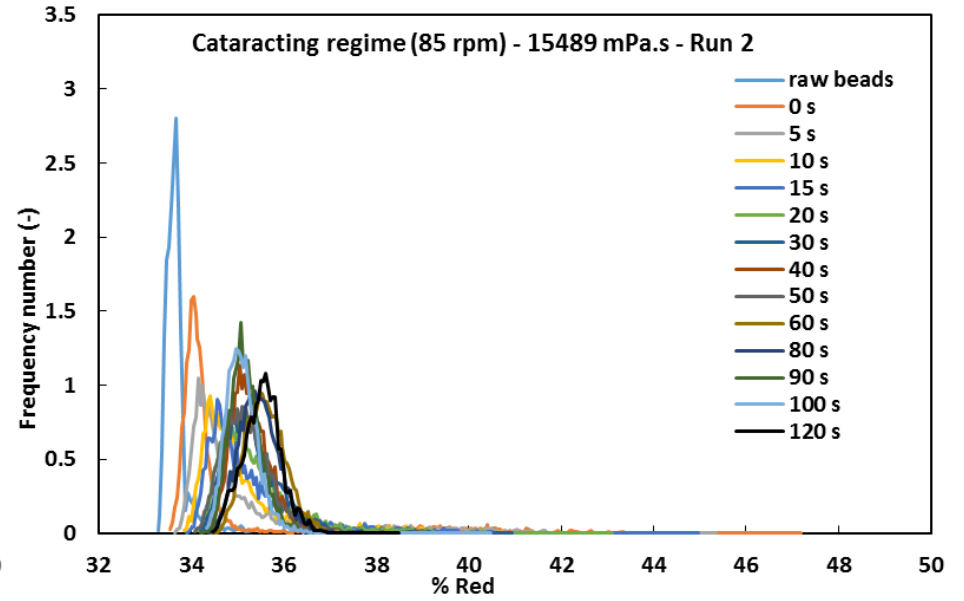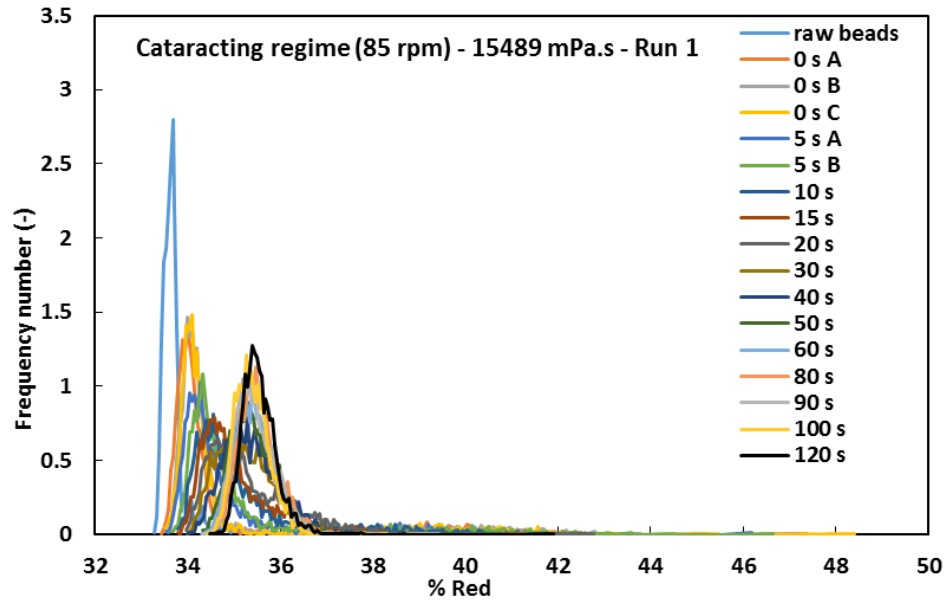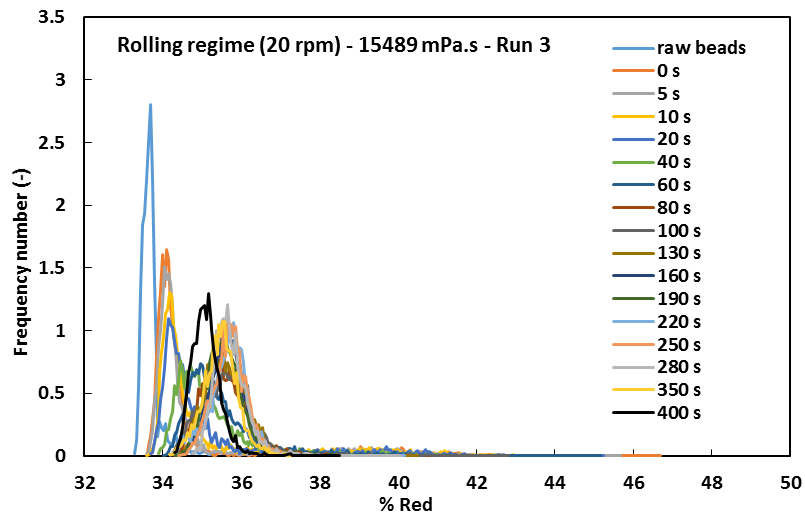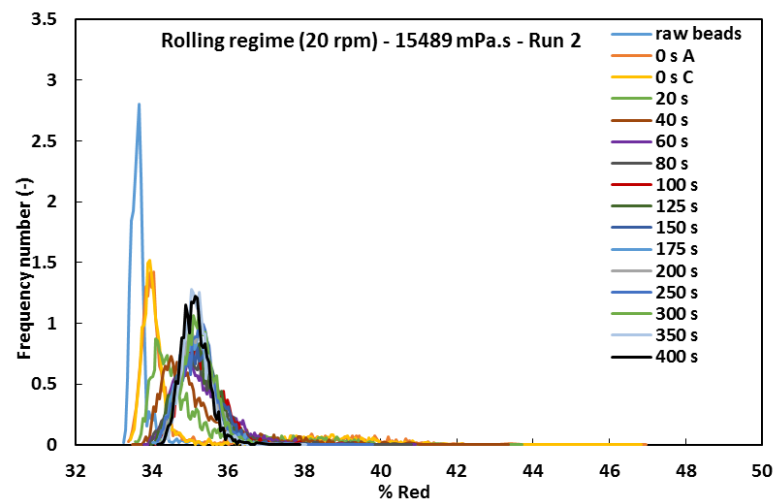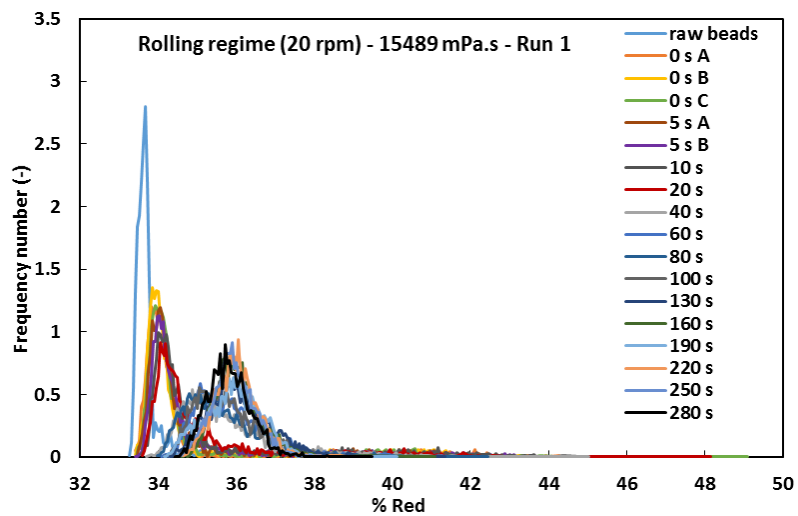
C3. Percentage mean red as a function of mixing time for different tumbling regimes:
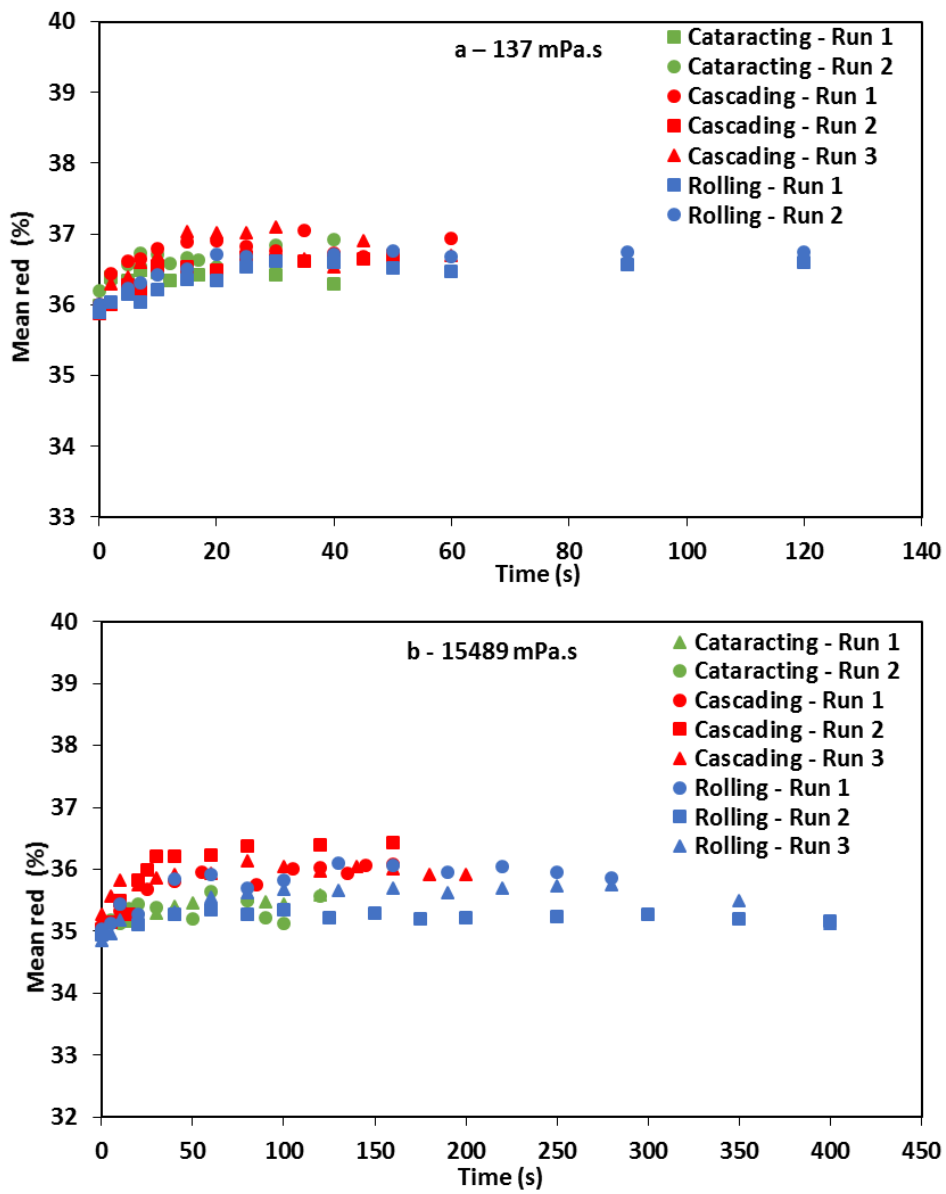
C4. Images of coated particles as a function of tumbling time for 137 mPa.s PEG solution at three different tumbling regimes

Rolling (20 rpm)	Cascading (50 rpm)	Cataracting (85 rpm)
CoV = 7.60 (0 s)	CoV = 7.14 (0 s)	CoV = 7.22 (0 s)
CoV = 4.06 (20 s)	CoV = 4.16 (10 s)	CoV = 3.95 (5 s)
CoV = 1.85 (60 s)	CoV = 1.86 (40s)	CoV = 1.97 (15 s)
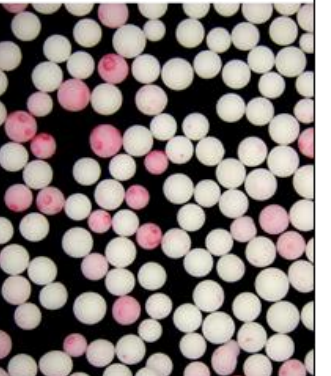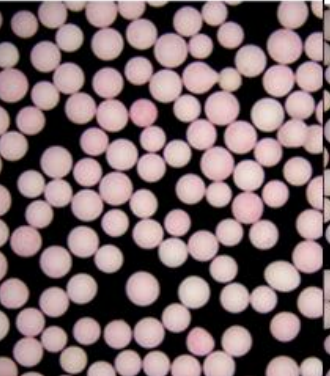
C5. Images of coated particles as a function of tumbling time for 15489 mPa.s PEG solution at three different tumbling regimes

Rolling (20 rpm)	Cascading (50 rpm)	Cataracting (85 rpm)
CoV = 6.98 (0 s)	CoV = 7.44 (0 s)	CoV = 6.34 (0 s)

CoV = 3.88 (40 s)	CoV = 3.43 (25 s)	CoV = 3.93 (10 s)
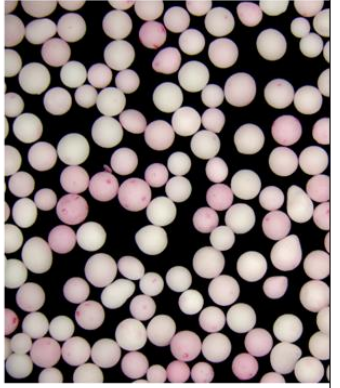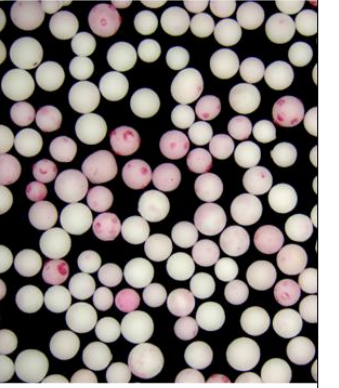
CoV = 1.54 (250 s)	CoV = 1.75 (120s)	CoV = 1.51 (50 s)
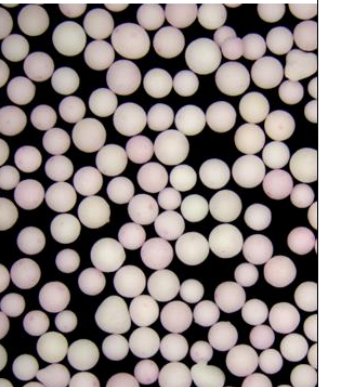
11.4 Appendix D

D1. Superficial velocity measurement

Superficial gas velocity, $U = \dfrac{Q}{A} = \dfrac{5.3 \, x \, 10^{-3}}{0.00636} = 0.838$ m/s

Bed cross-sectional area, $A = \dfrac{\pi D^2}{4} = \dfrac{\pi (0.09)^2}{4} = 0.00636$ m^2

Where, Q = air flowrate (320 L/min x 0.001/60 = 5.3 x 10^{-3} m^3/s)

D = internal diameter of the fluidised bed tube (0.09 m)

Air flow rate (L/min)	Air flowrate (m³/s)	Superficial velocity, U (m/s)	U-U$_{mf}$ (m/s)
50	0.00083	0.131	
100	0.00167	0.262	
150	0.00250	0.393	
180	0.00300	0.472	
200	0.00333	0.524	
220	**0.00367**	**0.576 (U$_{mf}$)**	**0**
250	0.00417	0.655	
260	0.00433	0.681	
280	0.00467	**0.733 (1.27 U$_{mf}$)**	**0.157**
300	0.00500	0.786	
320	0.00533	**0.838 (1.45 U$_{mf}$)**	**0.262**
350	0.00583	0.917	
380	0.00633	0.995	
400	0.00667	**1.048 (1.8 U$_{mf}$)**	**0.472**
420	0.00700	1.100	

D2. Minimum fluidisation theoretical measurement based on the Ergun equation:

Ergun equation:

$$\text{Ar} = \frac{d_p^{\,3}(\rho_p - \rho_g)g}{\mu^2}$$

$$U_{mf} = \frac{\mu_g}{\rho_g d_p}\{(1135.7 + 0.0408 \, Ar)^{\frac{1}{2}} - 33.7\} \text{ (m/s); } d_p > 100 \, \mu m$$

where ρ_g is the gas density (kg/m^3), ρ_p is the particle density (kg/m^3), d_p is the particle diameter (m), d_v is the diameter of the equivalent sphere (m), and μ is the gas viscosity (kg/m.s) (Dixit and Puthli, 2009).

Particle size, d_p [m]	Air density, ρ_g [kg/m^3]	Bulk density, ρ_p [kg/m^3]	Gravity acceleration, g [kg.m/s^2]	Air viscosity, μ [kg/m.s]	U_{mf} theory. [m/s]
0.00101	1.2	2064	9.81	0.00001983	0.448

D3. Coating evolution of all data sets for alumina coated with HPMC 603 (11 mPa.s) solution at different spray rates:
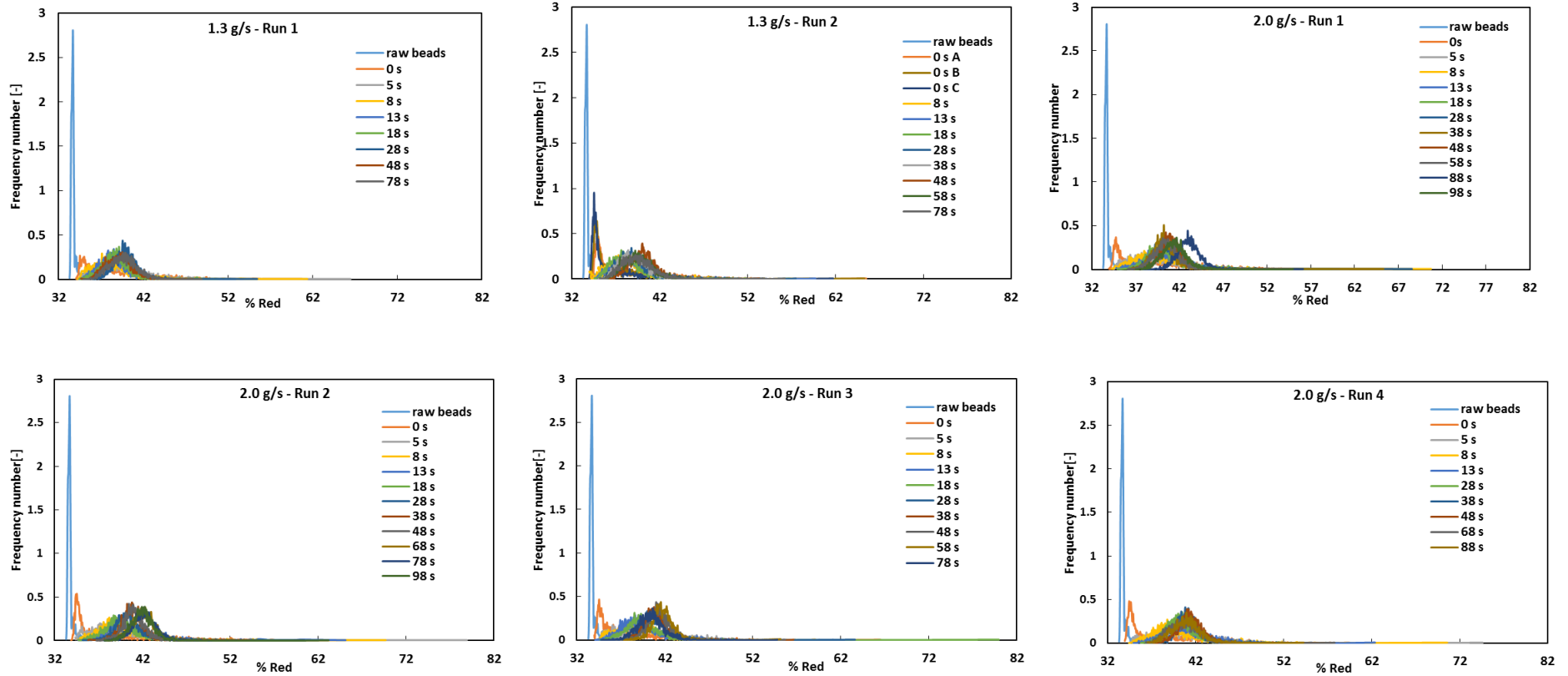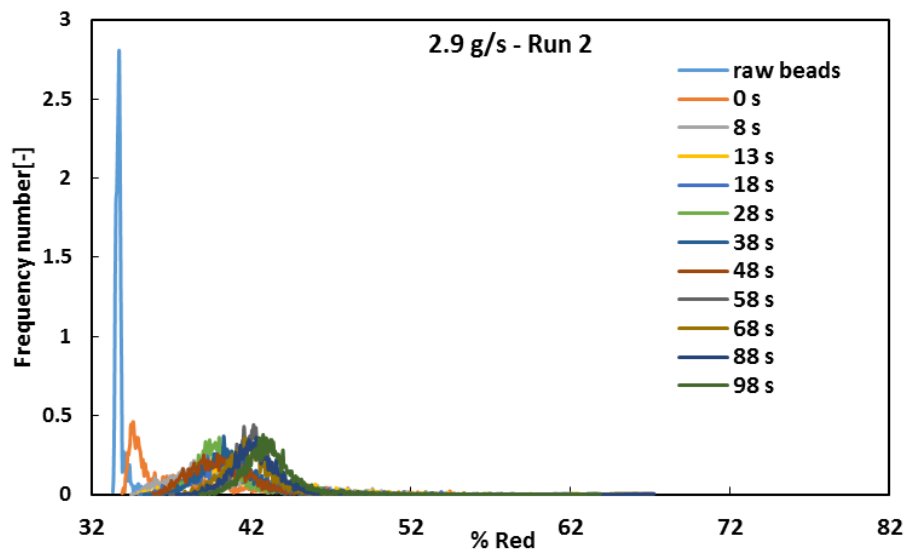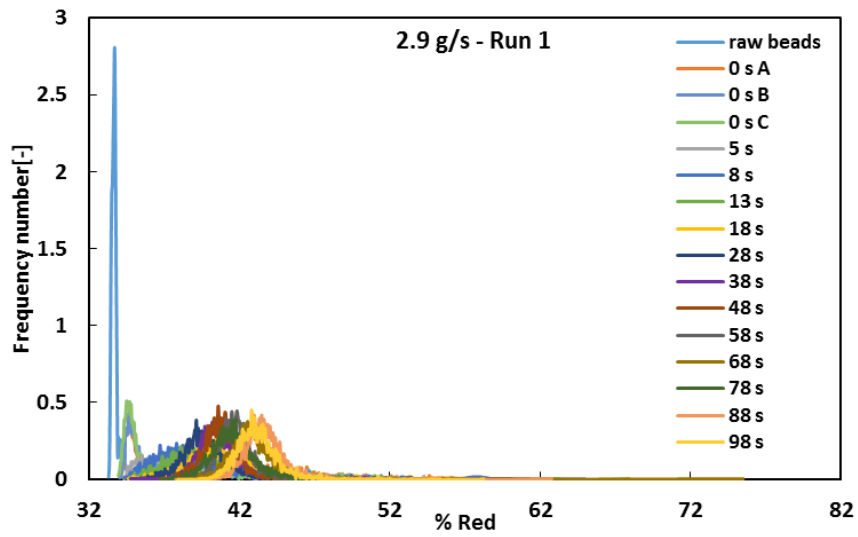
D4. Percentage mean red as a function of mixing time for HPMC 603 solution (11 mPa.s) at different spray rates:
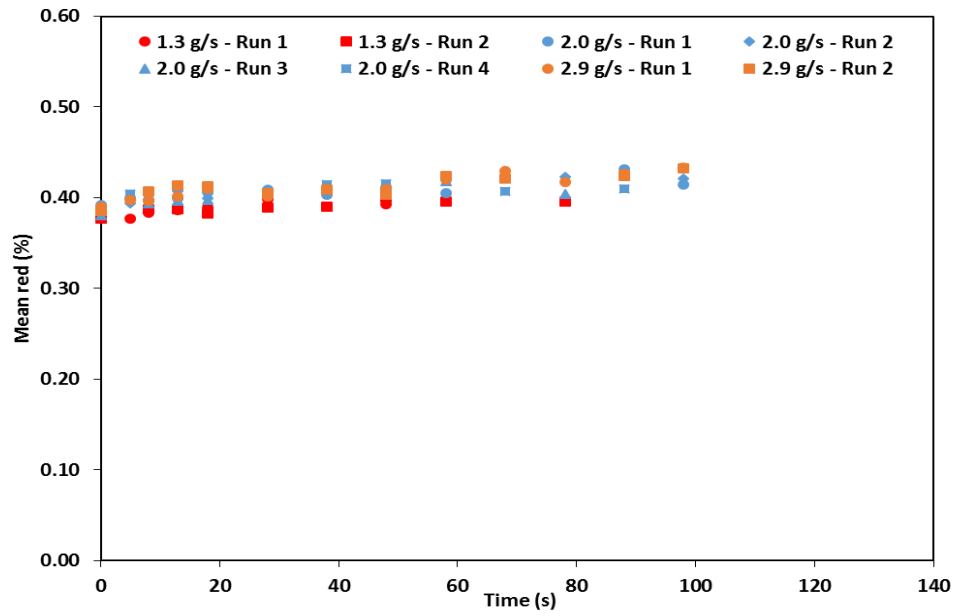
D5. Coating evolution of all data sets for alumina coated with HPMC 603 solution (11 mPa.s) at different fluidisation velocities:
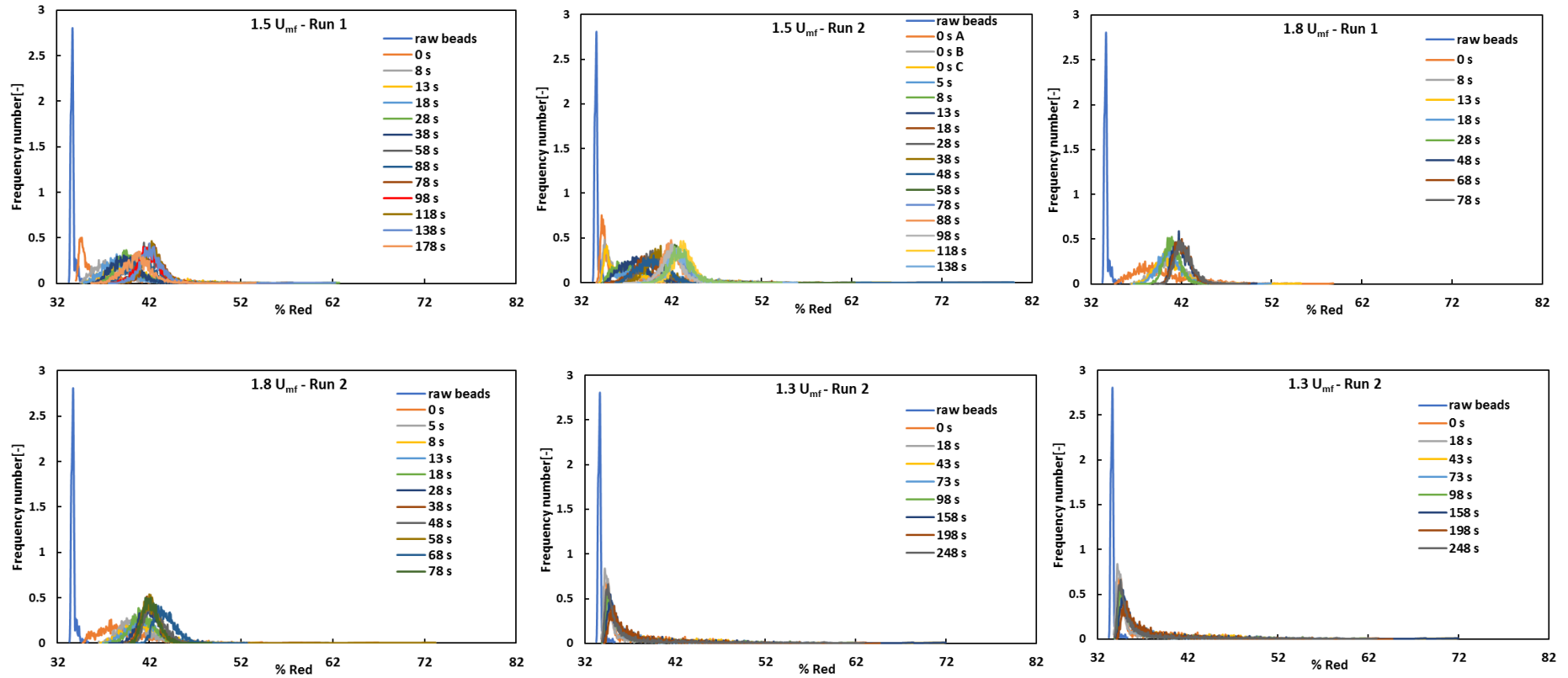
D6. Image comparison of coated particles with HPMC 603 solution (11 mPa.s) at different fluidisation velocities (1.3 U_{mf}, 1.5 U_{mf} and 1.8 U_{mf})
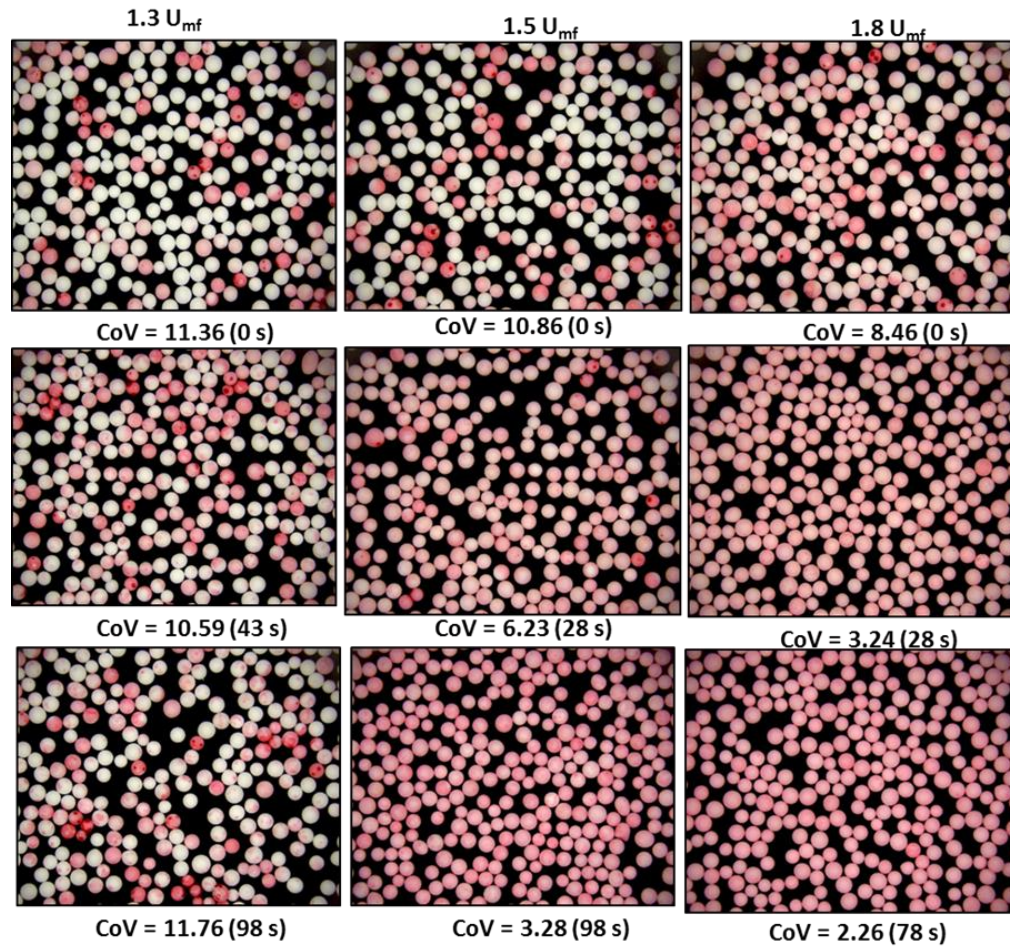
D7. Images of agglomerates formed at different fluidisation velocities and mixing times
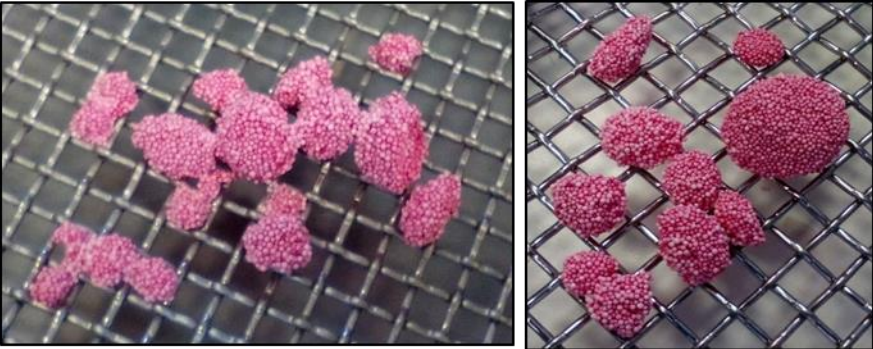
1.8 U$_{mf}$

1.5 U$_{mf}$

1.3 U$_{mf}$
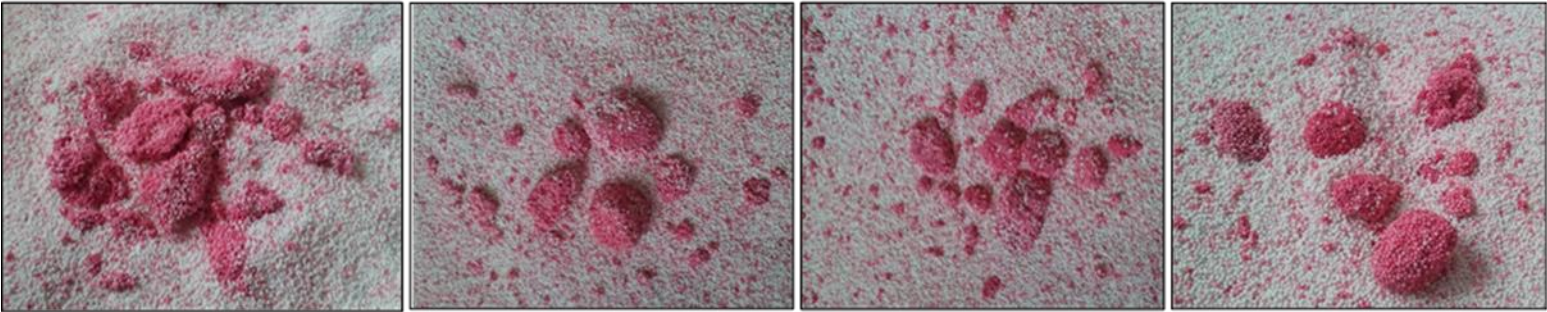
20 s

75 s

160 s

250 s

D8. Coating evolution of alumina coated with different viscosity HPMC solutions
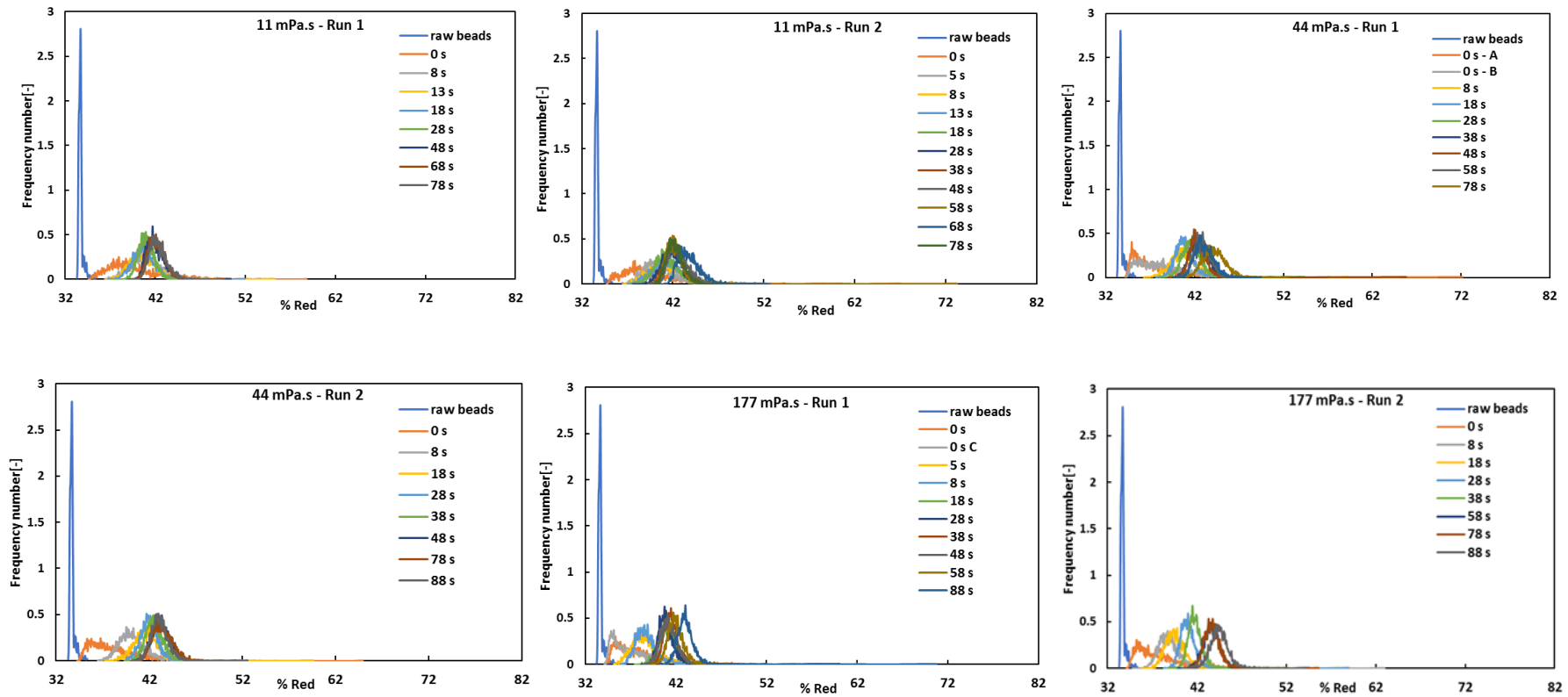
D9. Coating evolution of alumina coated with HPMC 603 solution (11 mPa.s) at different nozzle heights
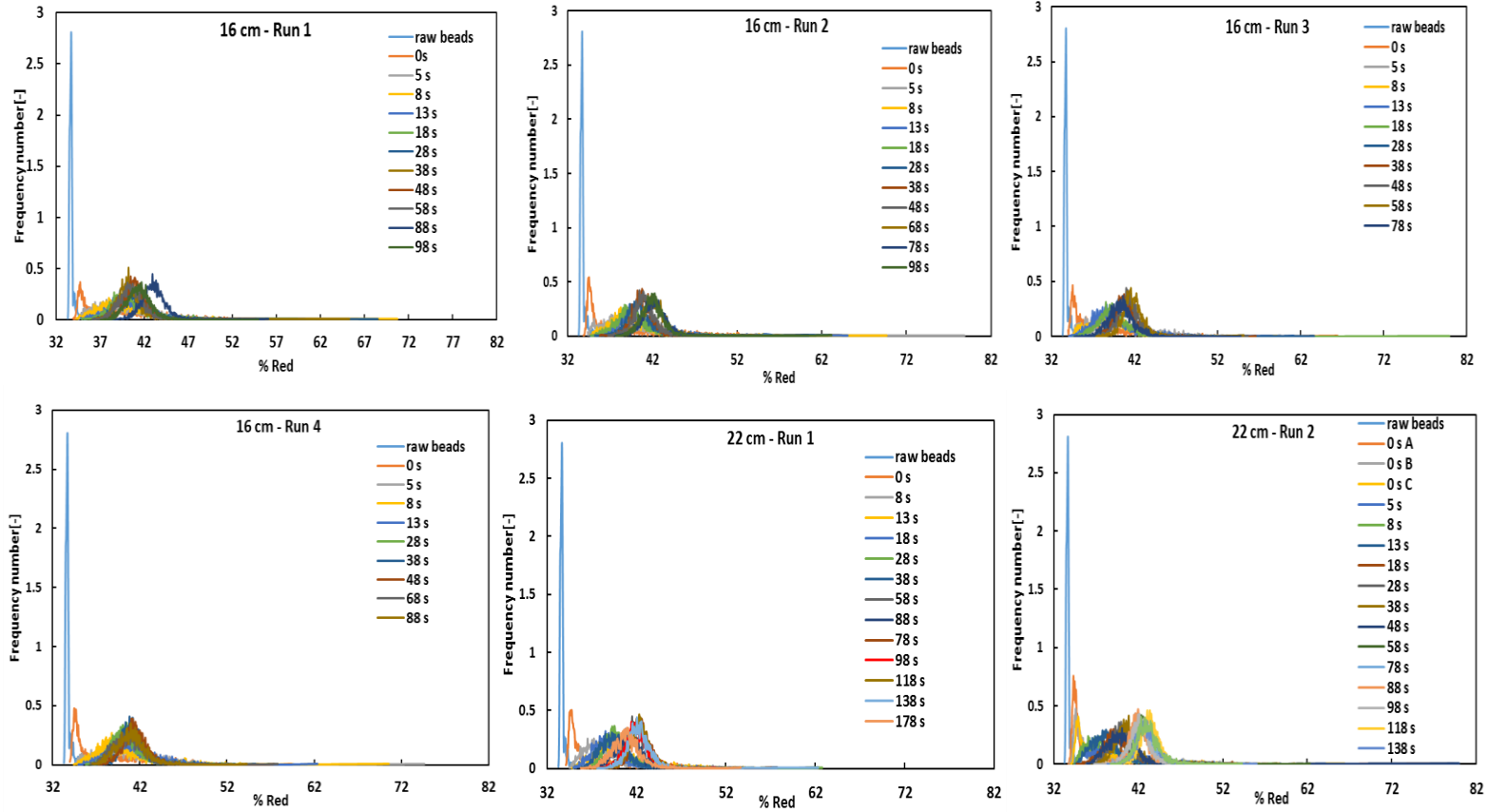
11.5 Appendix E

E1. Coating evolution of all data sets for alumina coated with HPMC solutions of different viscosities:
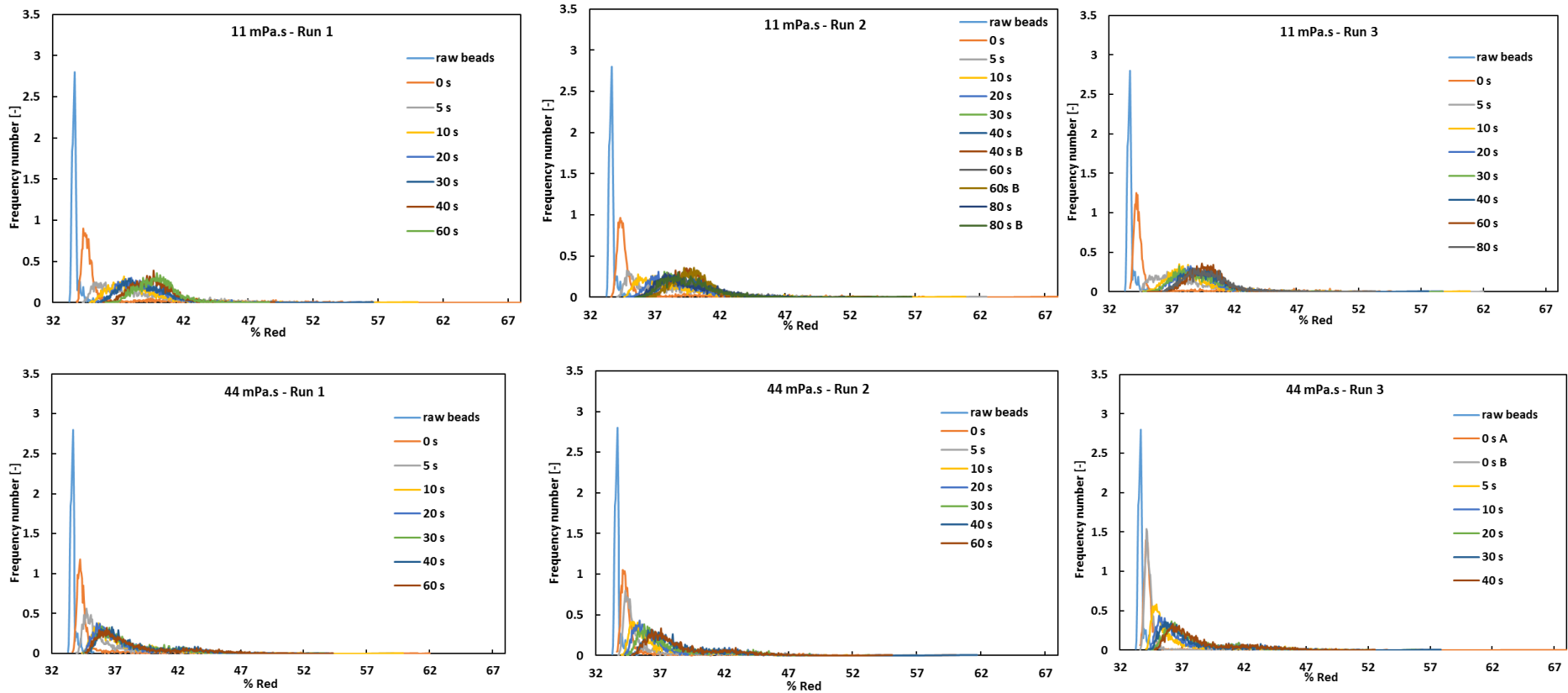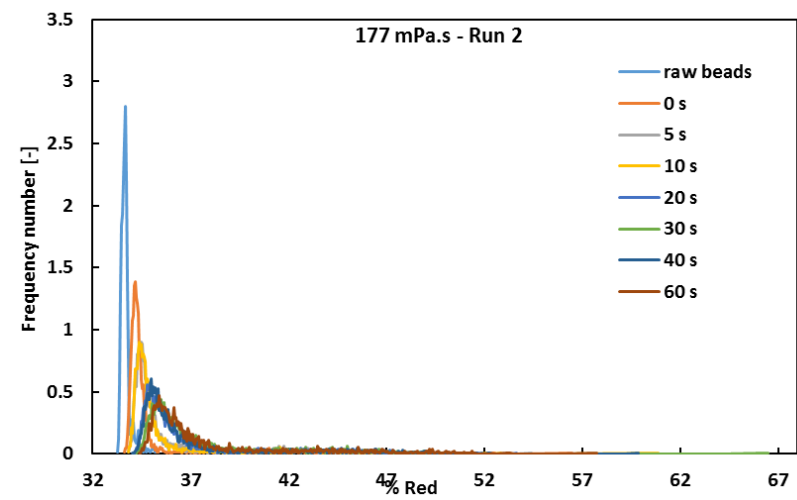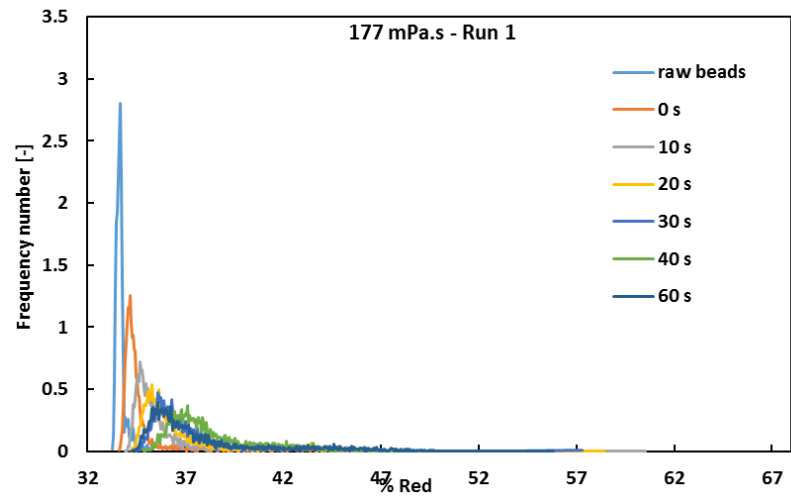
E2. Images of coated particles with different HPMC viscosities taken before sampling for image analysis
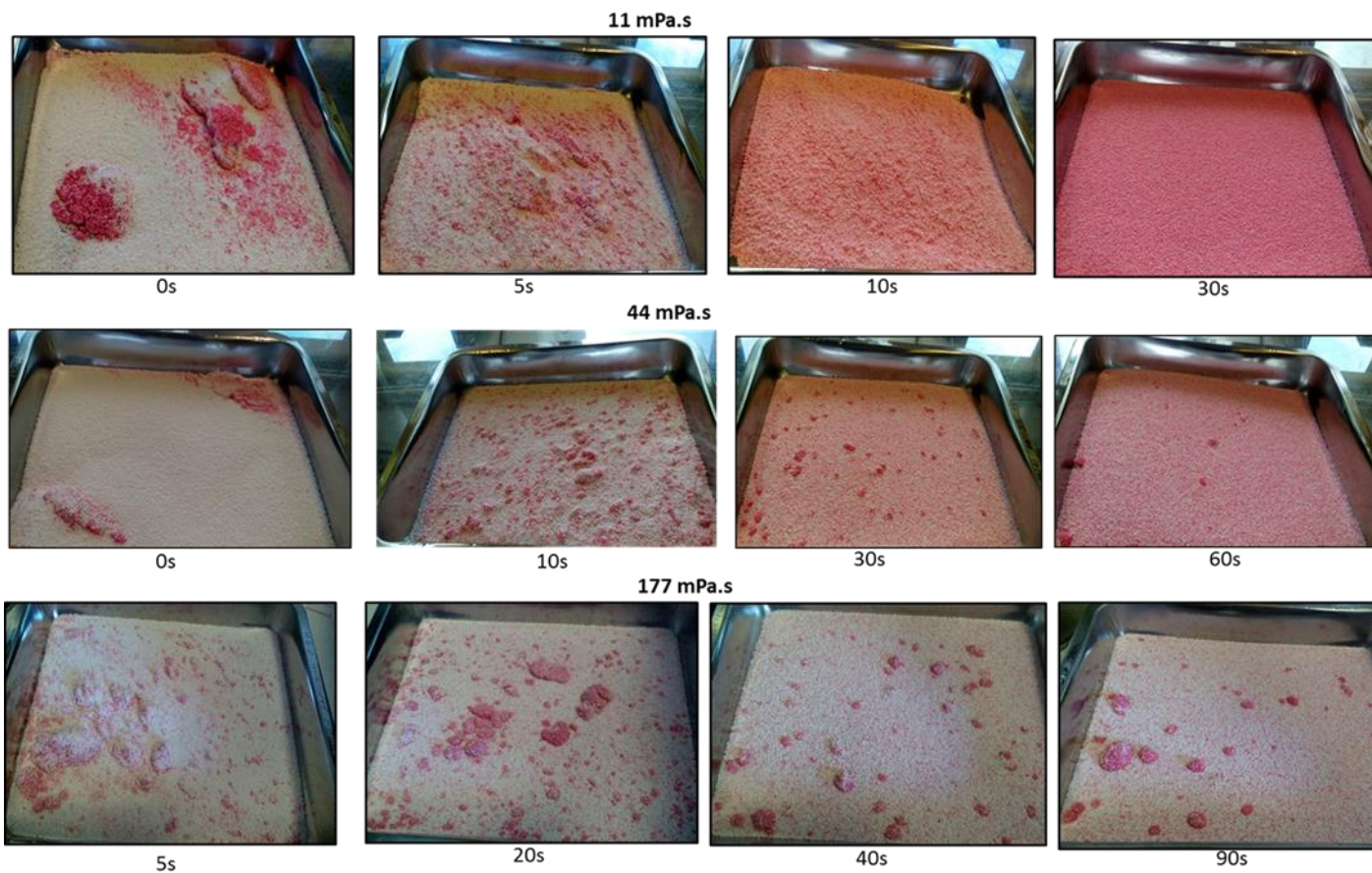
E3. Coating evolution of all data sets for alumina coated with 11 mPa.s HPMC solution at different fluidisation velocities:
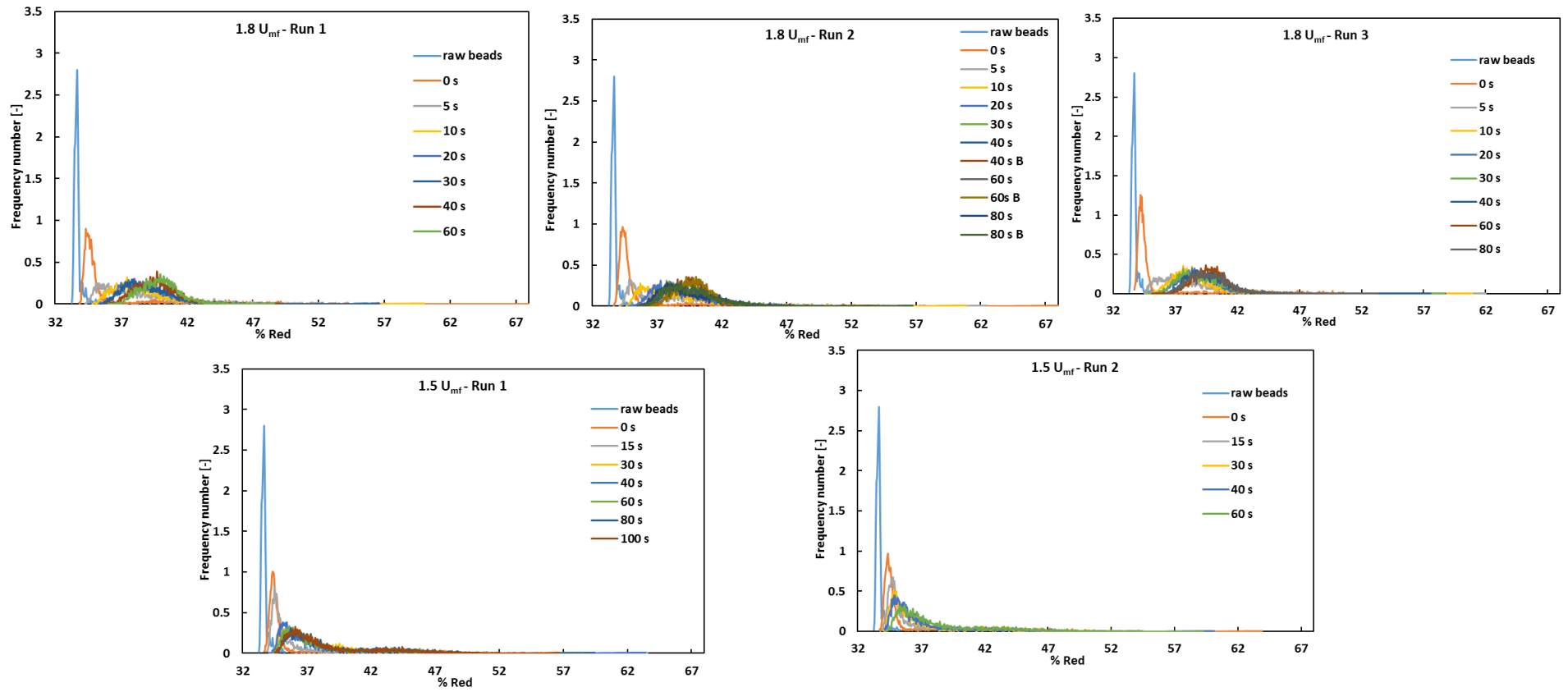
11.6 Appendix F

F1: Estimated determination of coating thickness

> • **Tumbling drum -precoated method**

The coating thickness, h_b for coated particles is measured based on the difference between the radius of dry particle, r_1, and dyed coated particles, r_2, as illustrated in Figure F1. Here, the measurement of coating thickness for particle coated with PEG solution of 137 mPa.s in the tumbling drum system using the pre-coated particles method is given as an example.

Volume of single particle, V_p

Volume of single pre-coated particle,
$V_c = V_p +$ volume liquid on coated particle
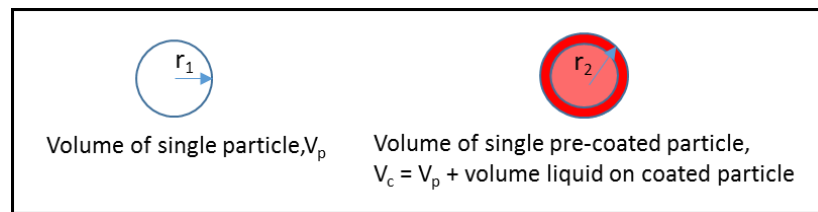
Figure F1. Schematic view of single uncoated and dye coated particles

i. Calculation related with the dry particle:

• Volume of single particle, V_p

$$V_p = \frac{4}{3}\pi r^3$$

• Surface are of single particle, A

$$A = 4\pi r^2$$

• Mass of single particle, m

$$m = V_p \rho_p$$

Here, ρ_p is particle envelope density $= 3260 \text{ kg/m}^3$

• Total mass of particles in tumbling drum at 10% fill level, $m_t = 2.323$ kg

• Total number of particles in 10% fill level, $n_p = 1320897$

$$n_p = \frac{m_t}{m} =$$

ii. Calculation of initial coating thickness, h_b:

The initial coating thickness is estimated by assuming that the liquid mass, m_L (0.005 kg) is evenly distributed on the 10% particles of 10% fill level (pre-coated particles).

- Total mass of 10% pre-coated particles from 10% fill level, $m_p = 0.1 m_t = 0.232$ kg

- Total number of 10% pre-coated particles, $n_t = 131919$

$$n_t = \frac{m_p}{m} =$$

- Total surface area of 10% pre-coated particle, $A_t = 0.42$ m^2

$$A_t = A n_t$$

- Total volume of 10% pre-coated particles, $V_t = 7.116 \times 10^{-5}$ m^3

$$V_t = V_p n_t$$

- Volume of liquid on single pre-coated particles, $V_L = 3.61 \times 10^{-11}$

$$V_L = \frac{m_L}{n_t} \rho_L$$

Here, ρ_L is liquid density. For 137 mPa.s viscosity solution is 1049 kg/m^3.

- Volume of liquid and volume of single particle, $V_c = 5.76 \times 10^{-10}$ m^3

$$V_c = V_p + V_L$$

- Radius of dyed coated particles, $r_2 = 0.000516$ m

$$r_2 = \sqrt[3]{\frac{3 V_c}{4\pi}}$$

- Coating thickness, $h_b = 1.103 \times 10^{-5}$ m

$$h_b = r_2 - r_1$$

iii. Calculation of final coating thickness, h_b

The final coating thickness is estimated by assuming that the liquid mass, m_L (0.005 kg) is evenly distributed on the 100% particles of 10% fill level.

- Volume of liquid on single coated particles, $V_L = 3.61 \times 10^{-12}$

$$V_L = \frac{m_L}{n_p} \rho_L$$

- Volume of liquid and volume of single particle, $V_c = 5.43 \times 10^{-10}$ m^3

$$V_c = V_p + V_L$$

- Radius of dyed coated particles, $r_2 = 0.000506$ m

$$r_2 = \sqrt[3]{\frac{3 V_c}{4\pi}}$$

- Coating thickness, $h_b = 1.123 \times 10^{-6}$ m

$$h_b = r_2 - r_1$$